REPORT SAMSO-TR-79-30
AFRPL-TR-78-60

LEVEL II

(12)

AD A068437

Inversion of Plume Radiance and Absorptance Data for Temperature and Concentration

S. J. YOUNG
Chemistry and Physics Laboratory
Laboratory Operations
The Aerospace Corporation
El Segundo, Calif. 90245

29 September 1978

Final Report

APPROVED FOR PUBLIC RELEASE;
DISTRIBUTION UNLIMITED

Prepared for
AIR FORCE ROCKET PROPULSION LABORATORY
Edwards Air Force Base, Calif. 93523

SPACE AND MISSILE SYSTEMS ORGANIZATION
AIR FORCE SYSTEMS COMMAND
Los Angeles Air Force Station
P.O. Box 92960, Worldway Postal Center
Los Angeles, Calif. 90009

79

This final report was submitted by The Aerospace Corporation, El Segundo, CA 90245, under Contract No. F04701-77-C-0078 with the Space and Missile Systems Organization, Deputy for Advanced Space Programs, P.O. Box 92960, Worldway Postal Center, Los Angeles, CA 90009. It was reviewed and approved for The Aerospace Corporation by S. Siegel, Director, Chemistry and Physics Laboratory. Lieutenant A. G. Fernandez, SAMSO/YCPT, was the project officer for Advanced Space Programs.

This report has been reviewed by the Information Office (OI) and is releasable to the National Technical Information Service (NTIS). At NTIS, it will be available to the general public, including foreign nations.

This technical report has been reviewed and is approved for publication. Publication of this report does not constitute Air Force approval of the report's findings or conclusions. It is published only for the exchange and stimulation of ideas.

Arturo G. Fernandez
Project Officer

George A. Kuck

GEORGE A. KUCK, Major, USAF
Chief, Technology Plans Division

FOR THE COMMANDER

LEONARD E. BALTZELL, Col, USAF
Deputy for Advanced Space Programs

UNCLASSIFIED

SECURITY CLASSIFICATION OF THIS PAGE (When Data Entered)

REPORT DOCUMENTATION PAGE	READ INSTRUCTIONS BEFORE COMPLETING FORM
1. REPORT NUMBER (18) SAMSO (19) TR-79-30 / AFRPL TR-78-69 — 2. GOVT ACCESSION NO.	3. RECIPIENT'S CATALOG NUMBER
4. TITLE (and Subtitle) (6) INVERSION OF PLUME RADIANCE AND ABSORPTANCE DATA FOR TEMPERATURE AND CONCENTRATION	5. TYPE OF REPORT & PERIOD COVERED (9) Final rept.
	6. PERFORMING ORG. REPORT NUMBER (14) TR-0078(3623)-2
7. AUTHOR(s) (10) Stephen J. Young	8. CONTRACT OR GRANT NUMBER(s) (15) F04701-77-C-0078
9. PERFORMING ORGANIZATION NAME AND ADDRESS The Aerospace Corporation El Segundo, Calif. 90245	10. PROGRAM ELEMENT, PROJECT, TASK AREA & WORK UNIT NUMBERS (12) 234p.
11. CONTROLLING OFFICE NAME AND ADDRESS Air Force Rocket Propulsion Laboratory Edwards Air Force Base Calif. 93523	12. REPORT DATE (11) 29 Sep[redacted]78
	13. NUMBER OF PAGES 229
14. MONITORING AGENCY NAME & ADDRESS (if different from Controlling Office) Space and Missile Systems Organization Air Force Systems Command Los Angeles Air Force Station, P.O. Box 92960 Worldway Postal Center, Los Angeles, Calif. 90009	15. SECURITY CLASS. (of this report) Unclassified
	15a. DECLASSIFICATION/DOWNGRADING SCHEDULE

16. DISTRIBUTION STATEMENT (of this Report)

Approved for public release; distribution unlimited

17. DISTRIBUTION STATEMENT (of the abstract entered in Block 20, if different from Report)

18. SUPPLEMENTARY NOTES

19. KEY WORDS (Continue on reverse side if necessary and identify by block number)

Rocket Plume Radiation
Temperature Retrieval
Concentration Retrieval
Inversion Methods

20. ABSTRACT (Continue on reverse side if necessary and identify by block number)

The usefulness of the inversion of rocket plume infrared emission and absorption profiles obtained experimentally in transverse scans across the nozzle exit plane in order to retrieve radial profiles of plume temperature and concentration is examined in detail. Principal aspects on the problem include: (1) the use of state-of-the-art band radiation models that account for highly nonuniform pl[illegible] and Doppler broadening effects; (2) the development of an iterative Abe[illegible]ersion algorithm that allows the application of the well-known Abel inversion to nonthin optical sources; and (3) the formulation of a — over

DD FORM 1473 (FACSIMILE)

409 383

UNCLASSIFIED

SECURITY CLASSIFICATION OF THIS PAGE (When Data Entered)

19. KEY WORDS (Continued)

20. ABSTRACT (Continued)

"quasi-objective" data smoothing procedure. The characteristics and error of inversion are determined for several synthetic data cases which approximate real rocket plumes and applied to actual data obtained from engine test firings.

CONTENTS

I. INTRODUCTION 11

A. Background 11

B. Review of Emission/Absorption Inversion 12

C. Scope of Present Work 15

PART 1. BAND MODEL RADIATION AND INVERSION MODELS

II. BAND MODEL RADIATION FORMULATION 19

A. Introduction 19

B. Radiance and Transmittance Equations 19

C. Derivative Functions 21

D. Transformation to Cylindrical Coordinates 29

III. INVERSION MODELS 35

A. General Considerations 35

B. Abel Inversion 36

C. Iterative Abel Inversion 38

D. Presmoothing 42

E. Quadrature Approximation 50

IV. PROGRAM EMABIC 53

A. Description of Code 53

B. Preparation of Input Data 57

CONTENTS (Cont.)

PART 2. APPLICATIONS AND ANALYSES

V. BAND MODEL PARAMETERS 69

VI. EMISSION/ABSORPTION PROFILE PREDICTIONS 79

VII. INVERSION CHARACTERISTICS 103

A. Introduction 103

B. Hypothetical Engine Test Case 103

C. Engine Test Case 4 116

D. Engine Test Case 12 116

VIII. RANDOM ERROR ANALYSIS 123

A. Introduction 123

B. Hypothetical Engine Test Case 123

C. Engine Test Case 4 130

D. Engine Test Case 12 133

E. Considerations on Presmoothing 137

IX. BIAS ERROR ANALYSES 145

A. Introduction 145

B. Effect of Band Model Parameter Uncertainty 145

C. Effect of Pressure Profile 150

D. Effect of Lineshape 152

E. Effect of Nonuniformity Approximation 152

F. Effect of Finite Field of View 155

CONTENTS (Cont.)

X. TRANSTAGE DATA INVERSION 159

A. Introduction 159

B. Data Preparation and Smoothing 159

C. Inversion Results 164

D. Random Error Analysis 165

E. Revised Inversions 168

XI. SUMMARY AND CONCLUSIONS 205

REFERENCES 211

APPENDIXES

A. CONSIDERATIONS ON OPTIMUM SPECTRAL REGIONS 215

B. PHILLIPS-TWOMEY INVERSION METHOD 219

C. WIDE BAND MODEL PARAMETERS 225

ACRONYMS 235

TABLES

1. Curve-of-Growth Functions for Statistical Doppler Line Band Model . . 25
2. Equivalent Width Derivative Function for Statistical Doppler Line Band Model 27
3. Pressure and Doppler Line Broadening Parameters for the H_2O and CO_2 Filter Bandpasses 78
4. Engine Test Cases for Emission/Absorption Profile Prediction 80
5. Source Conditions for Cases 1-7 81
6. Summary of Inversion Characteristics for Test Case 1 111
7. Summary of Inversion Characteristics for Test Case 2 115
8. Pressure Variation Results (Case 4) 151
9. Lineshape Variation Results — Case 4 Inversion 153
10. Transtage Engine Operating Conditions 160
11. Zero Levels for Correction of Transtage E/A Data 161
12. Smoothing Parameters for Transtage E/A Data 163
13. Smoothing Parameters for Revised Transtage E/A Data 169

FIGURES

1. Emission/Absorption Geometry 30

2. Iterative Abel Inversion Flow Diagram 41

3. EMABIC Program Control Card Formats 58

4. Input Card File Structure for Band Model Parameters 60

5. Input Card File Structure for Radial Profile Data 61

6. Input Card File Structure for Transverse Profile Data 63

7. Input Card File Structure for Radial Pressure Data 65

8. NERD H_2O Bandpass Filter Transmittance Curves 72

9. NERD CO_2 Bandpass Filter Transmittance Curve 73

10. Absorption Band Model Parameter $\bar{k}$ for H_2O Bandpasses 74

11. Line Density Band Model Parameter $1/\bar{\delta}$ for H_2O Bandpasses . . . 75

12. Absorption Band Model Parameter $\bar{k}$ for CO_2 Bandpasses 76

13. Line Density Band Model Parameter $1/\bar{\delta}$ for CO_2 Bandpasses . . . 77

14. Radial Profiles for Engine Case 8 83

15. Radial Profiles for Engine Case 9 84

16. Radial Profiles for Engine Case 10 85

17. Radial Profiles for Engine Case 11 86

18. Radial Profiles for Engine Case 12 87

19. Transverse Profiles for Engine Case 1 88

20. Transverse Profiles for Engine Case 2 89

21. Transverse Profiles for Engine Case 3 90

22. Transverse Profiles for Engine Case 4 91

23. Transverse Profiles for Engine Case 5 92

24. Transverse Profiles for Engine Case 6 93

25. Transverse Profiles for Engine Case 7 94

26. Transverse Profiles for Engine Case 8 95

27. Transverse Profiles for Engine Case 9 96

28. Transverse Profiles for Engine Case 10 97

29. Transverse Profiles for Engine Case 11 98

30. Transverse Profiles for Engine Case 12 99

31. Comparison of Transverse H_2O Profiles for Case 3 Generated with the RW and Modified NASA Voigt Line Models 110

32. Comparison of Transverse H_2O Profiles for Case 11 Generated with the RW and Modified NASA Voigt Line Models 101

33. Radial Profiles for Hypotehtical Engine Test Case 1. 104

34. Computed Transverse E/A Profiles for Hypothetical Engine Test Cases 105

35. Abel Inversion Results for Hypothetical Engine Test Case 1. 107

36. Profile Convergences for Hypothetical Engine Test Case 1 108

37. Profile Residuals for Hypothetical Engine Test Case 1 109

38. Abel Inversion Results for Hypothetical Engine Test Case 2 112

39. Profile Convergences for Hypothetical Engine Test Case 2 113

40. Profile Residuals for Hypothetical Engine Test Case 2 114

41. Abel Inversions for Engine Test Case 4 117

42. H_2O Profile Convergences for Engine Test Case 4 118

43. Temperature Inversions for Engine Test Case 12. 119

44. Concentration Inversions for Engine Test Case 12 120

45. Transverse E/A Profiles for Random Error Analysis (5% rms error) of Hypothetical Engine Test Case 2 124

46. Smoothing Curves for Hypothetical Engine Test Case 2. 125

47. Comparison between True and Inverted Profiles for 5% Error Analysis of Hypothetical Engine Test Case 2. 127

48. Transverse E/A Profiles for Random Error Analysis (10% rms error) of Hypothetical Engine Test Case 2 128

49. Comparison between True and Inverted Profiles for 10% Error Analysis of Hypothetical Engine Test Case 2 129

50. Transverse H_2O E/A Profiles for Random Error Analysis of Engine Test Case 4 131

51. Transverse CO_2 E/A Profiles for Random Error Analysis of Engine Test Case 4 132

52. Comparisons between True and Inverted Radial Profiles for Engine Test Case 4 134

53. Transverse CO_2 E/A Profiles for Random Error Analysis of Engine Test Case 12 135

54. Comparisons between True and Inverted Radial Profiles for Engine Test Case 12 136

55. Convergence Behavior for Engine Test Case 12 at 4.4 μm with 2% Random Errors 138

56. Absorptance Smoothing Curve for Engine Test Case 4 with 2% Random Errors 140

57. Transverse Transmittance Curves for Random Error Analysis (2% rms error) of Engine Test Case 4 141

58. Revised Comparison between True and Inverted Radial Profiles for Engine Test Case 4 143

59. Band Model Parameters for H_2O. 148

60. Inversions for Engine Test Case 11 with Three Band Model Parameter Sets 149

61. Effect of Nonuniformity Approximation on Inversions for Engine Test Case 11. 154

62. Convolutions of Transverse E/A Profiles with a Rectangular Field-of-View Slit Function 156

63. Effect of Field-of-View Convolution on Inversion 157
64. Transverse E/A Profiles for Transtage Case 1. 171
65. Transverse E/A Profiles for Transtage Case 2. 172
66. Transverse E/A Profiles for Transtage Case 3. 173
67. Transverse E/A Profiles for Transtage Case 4. 174
68. Transverse E/A Profiles for Transtage Case 5. 175
69. Transverse E/A Profiles for Transtage Case 6. 176
70. Transverse E/A Profiles for Transtage Case 7. 177
71. Transverse E/A Profiles for Transtage Case 8. 178
72. Transverse E/A Profiles for Transtage Case 9. 179
73. Transverse E/A Profiles for Transtage Case 10 180
74. Transverse E/A Profiles for Transtage Case 11 181
75. Transverse E/A Profiles for Transtage Case 12 182
76. Smoothing Curves for Transtage Cases 1, 2 and 3 183
77. Smoothing Curves for Transtage Cases 5, 6 and 7 184
78. Smoothing Curves for Transtage Cases 9, 10 and 11. 185
79. Smoothing Curves for Transtage Cases 4, 8 and 12 186
80. Pressure Profile for Transtage Inversions. 187
81. Transtage Inversion Results for Cases 1, 2 and 3 188
82. Transtage Inversion Results for Cases 5 and 6 189
83. Transtage Inversion Results for Cases 9 and 11 190
84. Transtage Inversion Results for Cases 4, 8 and 12 191
85. Radial Profiles for Transtage Random Error Analysis 192
86. Transverse E/A Profiles for Transtage Random Error Analysis . 193

87. Inversion Results for Transtage Random Error Analysis 194
88. Radial Error Curves for Transtage Inversion 195
89. Transverse E/A Profiles for Transtage Case 2 (Revised) 196
90. Transverse E/A Profiles for Transtage Case 8 (Revised) 197
91. Transverse E/A Profiles for Transtage Case 13 198
92. Smoothing Curves for Transtage Case 2 (Revised) 199
93. Smoothing Curves for Transtage Case 8 (Revised) 200
94. Smoothing Curves for Transtage Case 13 201
95. Inversion Results for Transtage Case 2 (Revised) 202
96. Inversion Results for Transtage Case 8 (Revised) 203
97. Inversion Results for Transtage Case 13 204
98. Final Inversion and Error Results for Transtage Cases 2 and 8 . . 210

I. INTRODUCTION

A. Background

The calculation of radiant intensity from rocket and jet-aircraft exhaust plumes requires a priori knowledge of the pressure p, temperature T, and active molecular species concentration c distributions (pTc distributions) throughout the whole plume flow field. Direct measurements of these distributions, particularly near the engine nozzle exit plane, are often impractical due to the harsh environment of the plume. In addition, direct measurements are intrusive and often disturb the flow field to such an extent that meaningless results are obtained. Accordingly, most plume flow-field determinations are based on computer modeling.[1,2] Computer codes that generate the downstream properties of the plume often require the radial pTc profiles at the nozzle as initial boundary conditions for the solution. These profiles are calculated with still other codes from the thermodynamics of the propellant combustion, nozzle expansion, and other engine characteristics. Although many of these codes are quite sophisticated and based on sound physical and chemical principles, there is a decided lack of experimental verification of their predictions.

In order to assess the accuracy of those code predictions, a series of experimental programs to infer radial pTc profiles from nonintrusive measurements of plume emission and absorption (E/A) characteristics was initiated by the Air Force Rocket Propulsion Laboratory (AFRPL). All of the data for these programs were obtained from engine test firings at the Arnold Engineering Development Center (AEDC) facility by ARO, Inc. Some results and analyses of data from the first two programs [High Altitude Plume Radiation Program (HAPRAP) and Emitted Radiation from Special Engines (ERASE) program] are reported in Ref. 3 and

Refs. 4 and 5, respectively. The present work was performed for the current Nozzle Exit Radiation Determination (NERD) program* and concerns the deduction of plume pTc properties from measured E/A data by mathematical inversion of the equations of radiative transfer.

B. Review of Emission/Absorption Inversion

The basic principle of emission/absorption inversion as applied to gases can be understood by considering a uniform optical path of length L, pressure p, mole fraction of active gas c, and temperature T. For given p and L, the two unknowns are c and T, and, consequently, a measurement of at least two independent properties of the gas sample will be required to determine these values. The radiance and absorptance (or transmittance) of the gas sample at a given wavelength (or within a small wavelength interval centered about the wavelength) are such independent properties. The temperature can be determined from the measured radiance and absorptance by application of Kirchhoff's law, and, once the temperature is known, the value of c can be derived from the absorptance measurement by use of appropriate transmission formulas.

The same principle can be applied to nonuniform optical paths, but its application is seriously compounded by the existence of both temperature and species concentration gradients. The general method of solution involves the assumption that the nonuniform path can be divided into a number of intervals, and that the properties within each interval can be considered as constants. If n intervals are used, the number of unknown quantities is now 2n (T and c of each interval). Thus, 2n independent quantities must be measured in order to extract a solution.

The two main approaches to measuring the requisite number of independent quantities are to measure the radiance and absorptance at either n different spectral positions (multi-color), or for n independent lines of sight (multi-position) through the gas sample. For an axisym-

*W. Bertrand, T. McRay and E. Kiech, Nozzle Exit Plane Radiation Diagnostics of Three Transtage Engine Injector Configurations, AEDC Technical Report, to be published (1978).

metric radiation source such as a rocket plume near the exit plane, either of these approaches is, in principle, applicable. Multi-color measurements could be made through the diameter of the plume or multi-path measurements at a fixed spectral position could be made by traversing across the lateral extent of the plume. The viewing direction for either of these measurements would be perpendicular to the plume axis so that the results pertain to a single axial station of the plume.

Techniques for performing both multi-color and multi-position measurements and inversion have been considered extensively with regard to the problem of atmospheric sounding by satellite-borne sensors.(6) Such passive techniques are able to yield altitude profiles for temperature and concentration of H_2O and O_3. Krakov,(7) Simmons et al.,(8) Buchele,(9) and Cutting and McC. Stewart(10) discuss multi-color techniques as applied to high temperature combustion gas problems. The technique of Krakov requires that radiance measurements be performed at spectral positions where the sample is described by strong absorption since his band model radiation formulation for transmittance is limited to this condition. The inversion algorithm employs the techniques of successive approximations and Lagrange undetermined multipliers. The use of the latter technique allows a solution to be obtained for the over-determined system of equations resulting from the use of measurements at more than n different spectral positions. The instabilities that often result from overdetermined systems and measurement errors in the input data is balanced by choosing multiplier values which sufficiently "smooth" the data to yield convergent iterations.

The techniques of Simmons et al. and Buchele are based on general band model formulations that do not require the limitation to strong absorption. The "inversion" involves the assumption of a priori species concentration and temperature profile functions which contain a few adjustable parameters. The parameters are varied until the spectrum generated from these profiles using the band model formulation best matches the observed spectrum. Justification for the use of a priori profile functions is based on the assumption that the physical restraints of most systems will indicate a good choice of profile. A principal advantage of this technique is that the problem of numerical instabilities inherent in other inversion techniques is essentially obviated. Moreover, if the functional form of the profiles is chosen general enough (i.e., it contains many parameters), this procedure approaches an "inversion" in the usually interpreted sense of the word.

The method of Cutting and McC. Stewart is very nearly a direct application of atmospheric sounding techniques to high-temperature furnace conditions.

The multi-position technique applied to high temperature combustion gas systems is discussed by Brewer and Limbaugh.[11] In this approach, the spatial radiance and absorptance of an axisymmetric cylindrical source are measured for a single wavelength interval $\Delta\lambda$ as a function of transverse distance across the source. The measured profiles thus represent results for all the possible independent lines of sight through the sample (for a perpendicular viewing geometry). The inversion technique assumes that the axisymmetric source is composed of n homogeneous annular zones. The edge of the measured profiles thus correspond to a line of sight passing through the single, outermost homogeneous zone. The center of the profiles corresponds to a line of sight through a series of 2n-1 homogeneous segments. By starting at the edge of the measured profiles and working toward the center, an inversion can be effected by iteratively determining the T and c of each new zone that is added to the lines of sight. This inversion method constitutes the primary diagnostic tool that has been used in the analysis of the HAPRAP and ERASE data and is presently being used by ARO, Inc. in the NERD program.

C. Scope of Present Work

The present work is an in-depth assessment of the multi-position inversion method for axisymmetric cylindrical plume sources. The fundamental goal is the inversion of profiles of plume radiance and absorptance obtained in transverse scans across the lateral extent of test engine plumes near the nozzle exit plane in order to obtain the radial profiles of temperature and species concentration, and, to estimate the accuracy with which these profiles can be obtained. The principal radiating species and spectral regions of interest are H_2O (2.44 - 2.63 μm) and CO_2 (4.17 - 4.55 μm).

An important aspect in the formulation of inversion diagnostic tools is the radiation transport model employed. The present work uses band model methods in which high spectral resolution is sacrificed in order to gain efficient computation of mean E/A values in spectral bandpasses encompassing several tens or hundreds of individual vibration-rotation lines of a molecular band. Use of such models is entirely consistent with the spectral resolution ($\sim$20 - 300 cm^{-1}) with which experimental E/A profiles are obtained in the AEDC measurements programs. The band model formulation used in the present work is a state-of-the-art model for application to combustion gas problems. The three principal features that distinguish this formulation from many previously used formulations are: (1) account of Doppler broadening effects in low pressure plumes through the use of Voigt line shape models; (2) the treatment of nonuniform source conditions (inhomogeneities and nonisothermalities) with approximations better suited than the traditional Curtis-Godson (CG) approximation to the sharp gradients encountered in many plumes, and (3) the use of band model parameters that are consistent over the temperature range from 200 K to 3000 K. A general outline of the radiation model is presented in Section II and considerations on band model parameters for the current applications are given in Section V.

Once the equations relating the E/A profiles to the radial pTc profiles are defined through the band model formulation, a means of inverting these radiation transport equations must be constructed. When the plume source is optically thin, the transport equations reduce to Abel integrals and standard techniques of inversion may be applied.[12] For nonthin sources, iteration methods must be used. For the present work, an iterative Abel inversion algorithm was formulated. The procedure is initiated with an Abel inversion (regardless of the source optical thickness) and the radial profile results iteratively corrected by performing Abel inversions on the difference profiles obtained by subtracting the input E/A profiles from intermediately computed E/A profiles.

A necessary procedure in any inversion of real data is some form of data smoothing. Regardless of the inversion method, experimental random noise on the input E/A profiles is amplified in the inversion process and can yield radial profiles so noisy that they are meaningless. The smoothing procedure adopted for this work is a straightforward pre-smoothing of the data. Both the iterative Abel inversion algorithm and the presmoothing method are presented in detail in Section III.

During the course of this work, a second inversion method (the Phillips-Twomey method) that provides implicit smoothing of the input data was formulated and compared with the iterative Abel/presmoothing method. The method was not found to be significantly better than the iterative Abel method. The formulation and one comparison are presented in Appendix B of this report. Aside from this appendix, all of the work of this report employed the iterative Abel inversion scheme.

This report is divided into two major parts. Part 1 contains the formulation of the general radiative (Section II) and inversion (Section III) models for axisymmetric plume radiation diagnostics. The incorporation of these models into a working computer code (EMABIC) is described in

Section IV. Part 2 of the report is an assessment and application of the overall formulation. Band model parameters appropriate to the present applications are discussed in Section V. Examples of E/A profile predictions from given pTc profiles for a variety of engine types are presented in Section VI. The inversion characteristics of the iterative Abel inversion method are assessed in Section VII, and the effects of random and bias data error are treated in Sections VIII and IX, respectively. An application of the formulation to the inversion of actual NERD E/A data is made in Section X. A summary and conclusions section (Section XI) completes the main text of the report. Three appendixes treat topics that do not fall easily into the mainstream of the report. Considerations on the selection of optimum spectral bandpasses for future E/A measurements programs is presented in Appendix A, the Phillips-Twomey inversion scheme is described in Appendix B, and a discussion on the construction of band model parameters for wide-band application is given in Appendix C.

PART 1

BAND MODEL RADIATION AND INVERSION MODELS

II. BAND MODEL RADIATION FORMULATION

A. Introduction

Radiation calculations are performed entirely within the statistical band model formulation for an array of lines distributed in strength according to the exponential-tailed inverse distribution. Derivations and discussions of the basic models and approximations that account for non-uniformities along optical paths and Doppler broadening effects are given in Refs. 13 through 16. Only the equations defining the models and methods of calculation are given here. In parts B and C of this section, the radiation formulations for a general, nonuniform optical path are reviewed. The coordinate transformation to the cylindrical geometry relevant to plume radiation is treated in part D.

B. Radiance and Transmittance Equations

Consider a general optical path along which the total pressure p(s), temperature T(s) and concentration (mole fraction) of active gas c(s) are known as a function of geometric path position s. The total length of the path is s_m, and the observation position is s = 0. The fundamental band model parameters $\overline{k}(s)$ (mean absorption coefficient), $\overline{\delta}(s)$ (mean line spacing) and $\overline{\gamma}(s)$ (mean line width) for the spectral interval $\Delta\nu$ and active gas species are also presumed known as a function of s. The first two parameters are functions of T(s) only, whereas $\overline{\gamma}(s)$ may depend additionally on c(s) and p(s). Explicit tabulations of these band model parameters for H_2O in the 2.5-μm region and CO_2 in the 4.4-μm region are given in Section V.

The mean value of radiance in the interval $\Delta\nu$ about ν is given by

$$\overline{N} = -\int_0^{s_m} N^*(s)\,\frac{d\overline{\tau}(s)}{ds}\,ds \qquad (1)$$

where $N^*(s)$ is the Planck radiation function evaluated at $T(s)$ and ν. $\bar{\tau}(s)$ is the mean transmittance in $\Delta\nu$ for the path segment between $s = 0$ and general position s. s_m is the total geometric length of the line of sight, and no source exists beyond s_m. Within the statistical band model formulation, the transmittance is given by

$$\bar{\tau}(s) = e^{-\overline{W}(s)/\delta} \tag{2}$$

where $\overline{W}(s)/\delta$ measures the ratio of the mean equivalent width (total integrated absorptance) of the lines in $\Delta\nu$ to the mean line spacing in $\Delta\nu$. The transmittance derivative is

$$\frac{d\bar{\tau}(s)}{ds} = -\bar{\tau}(s)\frac{1}{\delta}\frac{d\overline{W}(s)}{ds} \tag{3}$$

For all lineshapes and nonuniformity approximations, the equivalent width derivative and equivalent width are determined from

$$\frac{1}{\delta}\frac{d\overline{W}(s)}{ds} = c(s)p(s)\bar{k}(s)y(s) \tag{4}$$

and

$$\frac{\overline{W}(s)}{\delta} = \int_0^s c(s')p(s')\bar{k}(s')y(s')ds' \tag{5}$$

where only the derivative function $y(s)$ changes with model. These functions are considered in Section C. With the relationships (1) through (5), the total radiance and transmittance of the optical path may be written

$$\overline{N} = \int_0^{s_m} c(s)p(s)\bar{k}(s)\bar{\tau}(s)N^*(s)y(s)ds \tag{6}$$

$$\bar{\tau} = \exp\left[-\int_0^{s_m} c(s)p(s)\bar{k}(s)y(s)ds\right] \tag{7}$$

In order to simplify the notation, define

$$w(s) = \overline{\tau}(s)y(s) \tag{8}$$

$$K(s) = c(s)p(s)\overline{k}(s) \tag{9}$$

$$J(s) = N^*(s)K(s) \tag{10}$$

J(s) and K(s) are called the source function and absorption function, respectively. In terms of K, J and w, the fundamental relations for radiance and transmittance are

$$\overline{N} = \int_0^{s_m} J(s)w(s)ds \tag{11}$$

$$-\ln \overline{\tau} = \int_0^{s_m} K(s)y(s)ds \tag{12}$$

C. <u>Derivative Functions</u>

The preceding formulation fully defines the radiation and transmission of the optical path once the function y(s) is defined. These functions are now considered. In the traditional Curtis-Godson (CG) approximation for an array of Lorentz lines

$$y(s) = y[\pi x(s), \rho(s)] \tag{13}$$

where

$$y(\eta, \rho) = (2-\rho)\frac{dI(\eta)}{d\eta} + (\rho-1)\frac{I(\eta)}{\eta} \tag{14}$$

with

$$I(\eta) = \sqrt{1 + 2\eta} - 1 \tag{15}$$

$$\frac{dI(\eta)}{d\eta} = \frac{1}{\sqrt{1 + 2\eta}} \tag{16}$$

$$x(s) = \frac{u(s)\bar{k}_e(s)}{\beta_e(s)} \tag{17}$$

$$\rho(s) = \frac{\beta(s)}{\beta_e(s)} \tag{18}$$

$$u(s) = \int_0^s c(s')p(s')ds' \tag{19}$$

$$\bar{k}_e(s) = \frac{1}{u(s)}\int_0^s c(s')p(s')\bar{k}(s')ds' \tag{20}$$

$$\beta_e(s) = \frac{1}{u(s)\bar{k}_e(s)}\int_0^s c(s')p(s')\bar{k}(s')\beta(s')ds' \tag{21}$$

$$\beta(s) = \frac{2\pi\bar{\gamma}(s)}{\bar{\delta}(s)} \tag{22}$$

In this approximation, the relation (5) for $\overline{W}(s)/\delta$ can be integrated in closed form to give

$$\frac{\overline{W}(s)}{\delta} = \frac{\beta_e(s)}{\pi} I[\pi x(s)] \tag{23}$$

In the more sophisticated derivative (DR) approximation[15] for Lorentz lines,

$$y(s) = y[\pi x(s), \rho(s), q(s)] \tag{24}$$

where

$$y(\eta, \rho, q) = \frac{2}{\pi}\int_0^\infty \left[\int_0^1 \exp\left\{-\frac{2\eta u^q}{1+\rho^2 z^2}\right\} du\right] \frac{dz}{1+z^2} \tag{25}$$

A numerical procedure for computing this function is discussed in Ref. 15. Briefly, the procedure consists of rewriting $y(\eta, \rho, q)$ in an alternate form

$$y(\eta, \rho, q) = \frac{1}{q} y(\eta, \rho, 1) + \frac{q-1}{q} \int_0^1 y(xz^q, \rho, 1)dz \tag{26}$$

that relates $y(\eta, \rho, q)$ to its value at $q = 1$. The integral term of this alternate expression is evaluated numerically by Gaussian quadrature, and the function $y(\eta, \rho, 1)$ is approximated by

$$y(\eta, \rho, 1) = \frac{2\rho(1 + \eta) + (1 + \rho^2) \sqrt{1 + 2\eta}}{\sqrt{1 + 2\eta}\left[\rho + \sqrt{1 + 2\eta}\right]^2} \tag{27}$$

which is the derivative function within the Lindquist-Simmons (LS) approximation.[13,14] The additional parameter $q(s)$ of (24) is defined as

$$q(s) = \frac{\overline{\delta}_e(s)}{\overline{\delta}(s)} \tag{28}$$

where

$$\overline{\delta}_e(s) = \frac{1}{u(s)\overline{k}_e(s)} \int_0^s c(s')p(s')\overline{k}(s')\overline{\delta}(s')ds' \tag{29}$$

In this approximation, $\overline{W}(s)/\delta$ must be computed from (5).

For an array of Doppler lines, the formulation analogous to the CG approximation is

$$y(s) = y[\pi x(s), \rho(s)] \tag{30}$$

where

$$y(\eta, \rho) = (2 - \rho) \frac{dH(\eta)}{d\eta} + (\rho - 1) \frac{H(\eta)}{\eta} \tag{31}$$

and

$$H(\eta) = \frac{2}{\sqrt{\pi}} \int_0^\infty \ln\left[1 + \eta e^{-u^2}\right] du \tag{32}$$

The functions $H(\eta)$ and $dH(\eta)/d\eta$ are obtained by interpolation on the data of Table 1, from

$$H(\eta) = -\sum_{n=0}^{\infty} \frac{(-\eta)^{n+1}}{(n+1)^{3/2}} \tag{33}$$

$$\frac{dH(\eta)}{d\eta} = \sum_{n=0}^{\infty} \frac{(-\eta)^{n}}{\sqrt{n+1}} \tag{34}$$

for small η, and from the asymptotic series

$$H(\eta) \sim \frac{4}{3\sqrt{\pi}} (\ell n\eta)^{3/2} \left[1 + \frac{\pi^2/8}{(\ell n\eta)^2} + \frac{7\pi^4/640}{(\ell n\eta)^4} + \ldots\right] \tag{35}$$

$$\frac{dH(\eta)}{d\eta} \sim \frac{2}{\eta\sqrt{\pi}} (\ell n\eta)^{1/2} \left[1 - \frac{\pi^2/24}{(\ell n\eta)^2} - \frac{35\pi^4/1920}{(\ell n\eta)^4} + \ldots\right] \tag{36}$$

for large η. The arguments $x(s)$ and $\rho(s)$ are defined by (17) through (21) and with $\beta(s)$ defined by

$$\beta(s) = \sqrt{\frac{\pi}{\ell n2}} \frac{\gamma(s)}{\overline{\delta}(s)} \tag{37}$$

where $\gamma(s)$ is the Doppler line width. Within this approximation for the Doppler line shape (which will be referred to as the CG approximation for identification), $\overline{W}(s)/\delta$ is given in closed form by

$$\frac{\overline{W}(s)}{\delta} = \frac{\beta_e(s)}{\pi} H[\pi x(s)] \tag{38}$$

The derivative approximation for the Doppler line profile is

$$y(s) = y\left[\frac{\pi x(s)}{q(s)}, \rho(s)\right] \tag{39}$$

where

Table 1. Curve of Growth Functions for Statistical Doppler Line Band Model

η	H(η)	dH(η)/dη
0.1	0.09665	0.93460
0.2	0.18722	0.87828
0.4	0.35325	0.78593
0.6	0.50289	0.71310
0.8	0.63940	0.65398
1.0	0.76515	0.60490
2.0	1.28138	0.44564
4.0	2.00567	0.29978
6.0	2.52794	0.22935
8.0	2.94136	0.18717
10	3.28568	0.15883
20	4.47964	0.092598
40	5.84661	0.052199
60	6.71916	0.036911
80	7.36866	0.028752
100	7.88910	0.023642
200	9.59377	0.012759
400	11.4233	0.006813
600	12.5478	0.004702
800	13.3689	0.003609
1000	14.0187	0.002937

$$y(\eta, \rho) = \frac{2}{\sqrt{\pi}} \int_0^\infty \frac{e^{-z^2}}{\left[1 + \eta e^{-\rho^2 z^2}\right]} dz \tag{40}$$

$y(\eta, \rho)$ is the derivative function for Doppler lines in the LS approximation,[13, 14] and the modification of the optical depth argument from $\pi x(s)$ to $\pi x(s)/q(s)$ results from an application of the mean-line (ML) approximation for Lorentz lines[15] to Doppler lines. $y(\eta, \rho)$ is obtained by interpolation on the data of Table 2, from

$$y(\eta, \rho) = \sum_{n=0}^{\infty} \frac{(-\eta)^n}{\sqrt{1 + n\rho^2}} \tag{41}$$

for small η, or from

$$y(\eta, \rho) \simeq \frac{1}{\sqrt{(1 + \eta)[1 - \eta(\rho^2 - 1)]}} \tag{42}$$

for $\rho \lesssim 0.5$ (error $\lesssim 1\%$). For $\eta > 10^5$, $y(\eta, \rho)$ is set to zero.

For an array of Voigt lines, two approximations are used. The first is an heuristic adaptation of the approximation devised by Rodgers and Williams (RW) for isolated lines.[16, 17] The derivative function is

$$y(s) = A(s)y_L(s) + B(s)y_D(s) + C(s) \tag{43}$$

where

$$A(s) = \frac{\overline{W}_L(s)/\delta}{\overline{W}(s)/\delta} \left\{1 - \left(\frac{\overline{W}_D(s)/\delta}{\overline{W}_W(s)/\delta}\right)^2\right\} \tag{44}$$

$$B(s) = \frac{\overline{W}_D(s)/\delta}{\overline{W}(s)/\delta} \left\{1 - \left(\frac{\overline{W}_L(s)/\delta}{\overline{W}_W(s)/\delta}\right)^2\right\} \tag{45}$$

Table 2. Equivalent Width Derivation Function for Statistical Doppler Line Band Model

η	ρ						
	5.00E-1	1.00E+0	1.25E+0	1.50E+0	2.00E+0	3.00E+0	5.00E+0
1.0E-2	0.99114E+0	0.99299E+0	0.99380E+0	0.99450E+0	0.99556E-0	0.99686E-0	0.99805E-0
2.0E-2	0.98243E+0	0.98608E+0	0.98770E+0	0.98907E+0	0.99119E-0	0.99377E-0	0.99613E-0
5.0E-2	0.95723E+0	0.96603E+0	0.96995E+0	0.97329E+0	0.97844E-0	0.98474E-0	0.99053E-0
1.0E-1	0.91803E+0	0.93460E+0	0.94207E+0	0.94846E+0	0.95836E-0	0.97050E-0	0.98168E-0
2.0E-1	0.84868E+0	0.87828E+0	0.89190E+0	0.90367E+0	0.92200E-0	0.94464E-0	0.96560E-0
5.0E-1	0.69248E+0	0.74750E+0	0.77433E+0	0.79799E+0	0.83553E-0	0.88273E-0	0.92692E-0
1.0E+0	0.53069E+0	0.60490E+0	0.64392E+0	0.67937E+0	0.73706E-0	0.81132E-0	0.88198E-0
2.0E+0	0.36239E+0	0.44564E+0	0.49455E+0	0.54100E+0	0.61957E-0	0.72444E-0	0.82669E-0
5.0E+0	0.18622E+0	0.25945E+0	0.31182E+0	0.36593E+0	0.46452E-0	0.60548E-0	0.74932E-0
1.0E+1	0.10301E+0	0.15883E+0	0.20643E+0	0.25986E+0	0.36450E-0	0.52442E-0	0.69490E-0
2.0E+1	0.54426E-1	0.92598E-1	0.13195E+0	0.18053E+0	0.28411E-0	0.45506E-0	0.64664E-0
5.0E+1	0.22544E-1	0.43173E-1	0.70728E-1	0.10995E+0	0.20490E-0	0.38046E-0	0.59211E-0
1.0E+2	0.11408E-1	0.23642E-1	0.43542E-1	0.75384E-1	0.16102E-0	0.33469E-0	0.55672E-0
2.0E+2	0.57384E-2	0.12759E-1	0.26649E-1	0.51787E-1	0.12735E-0	0.29611E-0	0.52535E-0
5.0E+2	0.23038E-2	0.55566E-2	0.13871E-1	0.31709E-1	0.94277E-1	0.25368E-0	0.48873E-0
1.0E+3	0.11533E-2	0.29368E-2	0.84594E-2	0.21992E-1	0.75569E-1	0.22668E-0	0.46396E-0
2.0E+3	0.57700E-3	0.15432E-2	0.51628E-2	0.15322E-1	0.60853E-1	0.20319E-0	0.44126E-0
5.0E+3	0.23088E-3	0.65458E-3	0.26937E-2	0.95640E-2	0.45971E-1	0.17650E-0	0.41390E-0
1.0E+4	0.11546E-3	0.34067E-3	0.16503E-2	0.67263E-2	0.37322E-1	0.15906E-0	0.39491E-0
2.0E+4	0.57731E-4	0.17676E-3	0.10132E-2	0.47468E-2	0.30380E-1	0.14358E-0	0.37718E-0
5.0E+4	0.23093E-4	0.73960E-4	0.53344E-3	0.30083E-2	0.23224E-1	0.12570E-0	0.35546E-0
1.0E+5	0.11547E-4	0.38163E-4	0.32916E-3	0.21370E-2	0.18996E-1	0.11383E-0	0.34018E-0

$$C(s) = \frac{\overline{W}_W(s)/\delta}{\overline{W}(s)/\delta}\left(\frac{\overline{W}_L(s)/\delta}{\overline{W}_W(s)/\delta}\right)^2\left(\frac{\overline{W}_D(s)/\delta}{\overline{W}_W(s)/\delta}\right)^2 \tag{46}$$

$$\frac{\overline{W}(s)}{\delta} = \sqrt{\left[\frac{\overline{W}_L(s)}{\delta}\right]^2 + \left[\frac{\overline{W}_D(s)}{\delta}\right]^2 - \left[\frac{\overline{W}_L(s)}{\delta}\,\frac{\overline{W}_D(s)}{\delta}\Big/\frac{\overline{W}_W(s)}{\delta}\right]^2} \tag{47}$$

and

$$\frac{\overline{W}_W(s)}{\delta} = u(s)\overline{k}_e(s) \tag{48}$$

$\overline{W}_L(s)/\delta$ and $y_L(s)$ are, respectively, the equivalent width function and derivative function evaluated as though the lines were pure Lorentz lines (in either the CC or DR approximations). $\overline{W}_D(s)/\delta$ and $y_D(s)$ are the respective functions evaluated assuming a pure Doppler profile. This approximation is accurate to better than ~ 10%.

During the course of this work, a second approximation was constructed. It is essentially the same as the Voigt model employed in the NASA plume radiation code,[18] but uses the present methods for computing the curves of growth $\overline{W}_L(s)/\delta$ and $\overline{W}_D(s)/\delta$ rather than the methods prescribed in the NASA code. The derivative function y(s) is given by (43) where now

$$A(s) = \left[\frac{\overline{W}_L(s)/\delta}{\overline{W}(s)/\delta}\right] Y^{-3/2}(s)\left\{1 - \left[\frac{\overline{W}_L(s)/\delta}{\overline{W}_W(s)/\delta}\right]^2\right\}^{-3} \tag{49}$$

$$B(s) = \left[\frac{\overline{W}_D(s)/\delta}{\overline{W}(s)/\delta}\right] Y^{-3/2}(s)\left\{1 - \left[\frac{\overline{W}_D(s)/\delta}{\overline{W}_W(s)/\delta}\right]^2\right\}^{-3} \tag{50}$$

$$C(s) = \frac{\frac{\overline{W}(s)}{\delta} - A(s)\,\frac{\overline{W}_L(s)}{\delta} - B(s)\,\frac{\overline{W}_D(s)}{\delta}}{\frac{\overline{W}_W(s)}{\delta}} \tag{51}$$

$$\frac{\overline{W}(s)}{\delta} = \frac{\overline{W}_W(s)}{\delta}\sqrt{1 - 1/\sqrt{Y(s)}} \tag{52}$$

$$Y(s) = \left\{1 - \left[\frac{\overline{W}_L(s)/\delta}{\overline{W}_W(s)/\delta}\right]^2\right\}^{-2} + \left\{1 - \left[\frac{\overline{W}_D(s)/\delta}{\overline{W}_W(s)/\delta}\right]^2\right\}^{-2} - 1 \tag{53}$$

This approximation is accurate to better than $\sim 5\%$.

D. Transformation to Cylindrical Coordinates

Consider the geometric configuration of Fig. 1 in which measurements of radiance and absorptance are made on a cylindrical radiation source at a distance z from the cylinder diameter. The radiation formulation has been developed so far in terms of the optical path variable s. We wish to transform from s to the radial coordinate r with z retained as a parameter. This transformation is achieved through

$$r(z, s) = \sqrt{z^2 + \left[\frac{s_m(z)}{2} - s\right]^2} = \sqrt{s^2 + R^2 - 2s(R^2 - z^2)^{1/2}} \tag{54}$$

$$s(z, r) = \begin{cases} \frac{s_m(z)}{2} - \sqrt{r^2 - z^2} & \varphi \le 0 \\ \frac{s_m(z)}{2} + \sqrt{r^2 + z^2} & \varphi \ge 0 \end{cases} \tag{55}$$

$$ds = \begin{cases} -\frac{rdr}{\sqrt{r^2 - z^2}} & \varphi \le 0 \\ +\frac{rdr}{\sqrt{r^2 - z^2}} & \varphi \ge 0 \end{cases} \tag{56}$$

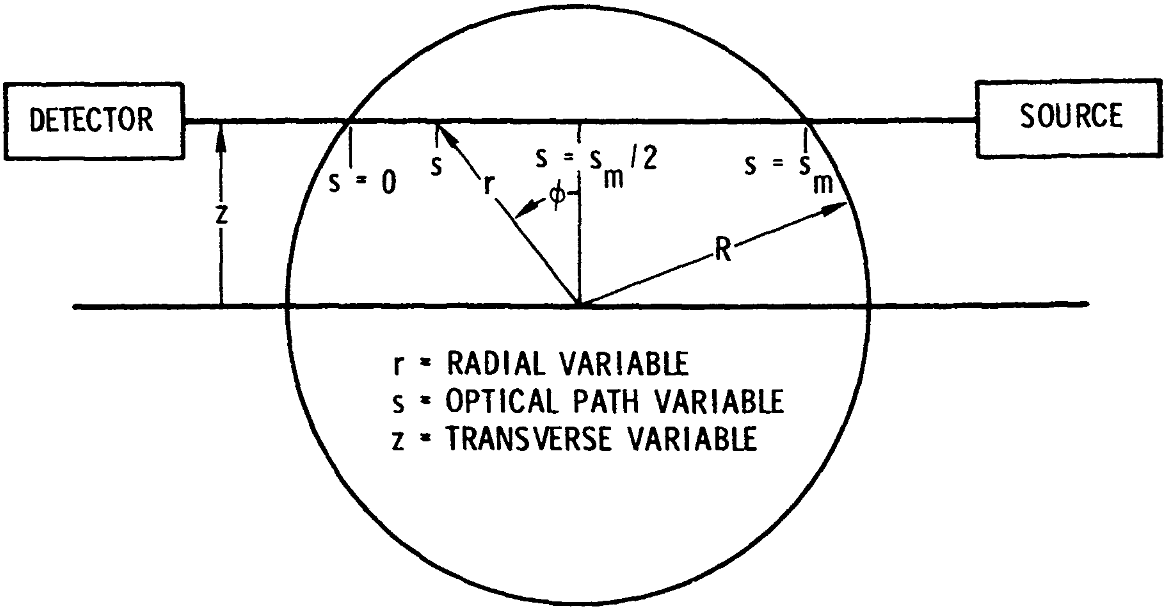

Fig. 1. Emission/Absorption Geometry

$$s_m(z) = 2\sqrt{R^2 - z^2} \tag{57}$$

Application of the radiation band model requires the evaluation of various integrals over the optical path coordinate s. It is these integrals that are transformed from s to r. Let g(z, s) be a general function of s for the line-of-sight chord at z, and

$$f(z, s) = \int_0^s g(z, s')ds' \tag{58}$$

Transformation of this general integral form to cylindrical coordinates with (54) through (57) gives

$$F(z, r) = \begin{cases} F^-(z, r) & \varphi \le 0 \\ F^+(z, r) & \varphi \ge 0 \end{cases} \tag{59}$$

where

$$F^-(z, r) = \int_r^R G^-(z, r') \frac{r'dr'}{\sqrt{r'^2 - z^2}} \tag{60}$$

$$F^+(z, r) = 2\int_z^R G^0(z, r') \frac{r'dr'}{\sqrt{r'^2 - z^2}} - \int_r^R G^-(z, r') \frac{r'dr'}{\sqrt{r'^2 - z^2}} \tag{61}$$

and

$$F(z, r) = f[z, s(r)] \tag{62}$$

$$G^-(z, r) = g\left[z, \frac{s_m(z)}{2} - \sqrt{r^2 - z^2}\right] \tag{63}$$

$$G^+(z, r) = g\left[z, \frac{s_m(z)}{2} + \sqrt{r^2 - z^2}\right] \tag{64}$$

$$G^0(z, r) = \frac{1}{2}\left[G^-(z, r) + G^+(z, r)\right] \tag{65}$$

For an integral over the entire line of sight, $s = s_m$, $\varphi > 0$, $r(z, s) = r(z, s_m) = R$ and $F(z, r)$ reduces to

$$F(z) \equiv F(z, R) = 2 \int_z^R G^0(z, r) \frac{r dr}{\sqrt{r^2 - z^2}} \tag{66}$$

Another simplification of the general result [(59) through (61)] occurs if $g(z, s)$ depends on z and s in the form (54), that is if $g(z, s)$ is a function of r only. Then $G(z, r)$ is a function only of r, $G^0 = G^+ = G^-$ and (59) through (61) reduce to

$$F(z, r) = \begin{cases} F^-(z, r) & \varphi \leq 0 \\ F^+(z, r) & \varphi \geq 0 \end{cases} \tag{67}$$

where

$$F^-(z, r) = \int_r^R G(r') \frac{r' dr'}{\sqrt{r'^2 - z^2}} \tag{68}$$

$$F^+(z, r) = 2 \int_z^R G(r') \frac{r' dr'}{\sqrt{r'^2 - z^2}} - F^-(z, r) \tag{69}$$

The significance of F^- and F^+ is that they represent integrals over the line of sight from $s = 0$ to the near and far intersections, respectively, of the line of sight and the circle r. For an integration over the entire line of sight with $G(z, r) = G(r)$, $F(z, r)$ reduces to the Abel integral

$$F(z) \equiv F(z, R) = 2 \int_z^R G(r) \frac{r dr}{\sqrt{r^2 - z^2}} \tag{70}$$

Transformation of the band model formulation in terms of the line-of-sight variables to cylindrical coordinates by use of (59) and (70) is as follows: The thermodynamic properties of the source are assumed to be functions of radius only. That is, $c = c(r)$, $p = p(r)$ and $T = T(r)$. The band model parameters are then also functions or r only, $\bar{k} = \bar{k}(r)$, $\bar{\delta} = \bar{\delta}(r)$, $\bar{\gamma} = \bar{\gamma}(r)$ and $\beta = \beta(r)$, as are the absorption (9) and source (10) functions, $K = K(r)$ and $J = J(r)$, respectively. Since the integrals appearing in (19) through (21) and (29) for the optical depth u and path averaged band model parameters $\bar{k}_e$, β_e and $\bar{\delta}_e$, respectively, all involve integrands which are functions of r only, the restricted transformation equations (67) through (69) can be applied to compute the "positive" and "negative" components

$$
\begin{array}{ll}
u^+(z, r) & u^-(z, r) \\
\bar{k}_e^+(z, r) & \bar{k}_e^-(z, r) \\
\beta_e^+(z, r) & \beta_e^-(z, r) \\
\bar{\delta}_e^+(z, r) & \bar{\delta}_e^-(z, r)
\end{array}
$$

from which the parameters

$$
\begin{array}{ll}
x^+(z, r) & x^-(z, r) \\
\rho^+(z, r) & \rho^-(z, r) \\
q^+(z, r) & q^-(z, r)
\end{array}
$$

can be found from (17), (18) and (28), respectively. These latter parameters define two components for the derivative function $y(x, \rho, q)$

$$y^{\pm}(z, r) = y[x^{\pm}(z, r), \rho^{\pm}(z, r), q^{\pm}(z, r)] \tag{71}$$

and the average

$$y^0(z, r) = \frac{1}{2}[y^+(z, r) + y^-(z, r)] \tag{72}$$

With $y^{\pm}(z, r)$ determined, the equivalent width (5) is determined by application of the general transformation equations (59) through (61) [since the integrand is now a function of both r and z through the appearance of $y^{\pm}(z, r)$ in the integrand] to obtain the two components of $\overline{W}/\delta$

$$\frac{\overline{W}^{\pm}(z, r)}{\delta} \tag{73}$$

These components are used with (2) to get the two components of transmittance

$$\bar{\tau}^{\pm}(z, r) = \exp\left\{-\frac{\overline{W}^{\pm}(z, r)}{\delta}\right\} \tag{74}$$

and the average

$$\bar{\tau}^{0}(z, r) = \frac{1}{2}\left[\bar{\tau}^{+}(z, r) + \bar{\tau}^{-}(z, r)\right] \tag{75}$$

The components (71) for y and (74) for $\bar{\tau}$ define the two components and average for the function w given by (8). That is

$$w^{\pm}(z, r) = \bar{\tau}^{\pm}(z, r) y^{\pm}(z, r) \tag{76}$$

$$w^{0}(z, r) = \frac{1}{2}\left[w^{-}(z, r) + w^{+}(z, r)\right] \tag{77}$$

With w(z, r) now determined, the general transformation equations for total path (59) through (61) can now be applied to obtain the transformed result for the radiance equation (11). It is

$$\overline{N}(z) = 2\int_{z}^{R} J(r) w^{0}(z, r) \frac{r\,dr}{\sqrt{r^{2} - z^{2}}} \tag{78}$$

The transformed equation for total transmittance at z is obtained from (12) as $\bar{\tau}^{+}(z, R)$ which, when written explicitly, is

$$-\ln \bar{\tau}(z) = 2\int_{z}^{R} K(r) y^{0}(z, r) \frac{r\,dr}{\sqrt{r^{2} + z^{2}}} \tag{79}$$

Equations (78) and (79) are the two basic equations required to compute the transverse profiles of $\overline{N}(z)$ and $\bar{\tau}(z)$ given the radial profiles of c(r), p(r) and T(r). The numerical quadrature approximation used to compute the integrals of (78) and (79), and also all of the integrals required in the intermediate steps, is treated in Section III. Equations (78) and (79) are also the basic equations on which the inversion algorithms of the following section are based.

III. INVERSION MODELS

A. General Considerations

The inversion procedures considered in this section are based on the radiative transfer equations (78) and (79) for transverse radiance and transmittance, respectively. With the definition

$$\overline{W}(z) = -\ln \overline{\tau}(z) \tag{80}$$

these equations are

$$\overline{N}(z) = 2 \int_z^R J(r) w^0(z, r) \frac{r\,dr}{\sqrt{r^2 - z^2}} \tag{81}$$

$$\overline{W}(z) = 2 \int_z^R K(r) y^0(z, r) \frac{r\,dr}{\sqrt{r^2 - z^2}} \tag{82}$$

The basic aim of inversion is to determine the radial functions J(r) and K(r) given the transverse functions $\overline{N}(z)$ and $\overline{W}(z)$. When this has been accomplished, the determination of the radial profiles of c, p and T proceeds directly from the definitions (9) and (10)

$$K(r) = c(r)p(r)\overline{k}(r) \tag{83}$$

$$J(r) = K(r)N^*(r) \tag{84}$$

The ratio J(r)/K(r) is the Planck function $N^*(r)$. Thus, the radial temperature profile is determined as

$$T(r) = \frac{C_2}{\ln\left[C_1 \frac{K(r)}{J(r)} + 1\right]} \tag{85}$$

where $C_1 = 1.129 \times 10^{-13}\ \nu^3\ \text{cm}^3\ \text{W/cm}^2\text{-sr-}\mu\text{m}$ and $C_2 = 1.4389\ \nu$ cm K. With T(r) known, $\overline{k}(r)$ is known. Then, the partial pressure c(r)p(r) is obtained from

$$c(r)p(r) = \frac{K(r)}{\bar{k}(r)} \qquad (86)$$

Note that the inversion solves only for the product c(r)p(r) and not the two profiles c(r) and p(r) individually. Even though the product is usually the final result desired in the inversion, it is significant that the individual profiles cannot be determined. In all but the Abel inversion, an iterative procedure is employed wherein (81) and (82) are alternately used for inversion and for generating intermediate transverse profiles. While the inversion gives only c(r)p(r), the individual variables are required in the profile generation through the calculation of $\bar{\gamma}$ (see Section V). The mathematical reason for this problem is that by inverting only two independent profiles, that is $\overline{N}(z)$ and $\overline{W}(z)$, we are allowed to obtain only two radial profiles, that is T(r) and c(r)p(r). In practice, inversions are carried out with a pressure profile which is assumed to be close to the true pressure profile. A test inversion is presented in Section IX, in which p(r) is varied about a known true profile. The inversion results for c(r), of course, vary with p(r), but the partial pressure profile c(r)p(r) is relatively insensitive to the variation.

B. Abel Inversion

For a source that is optically thin, the derivative function y(s), the transmittance $\bar{\tau}(s)$, and the product $w(s) = y(s)\bar{\tau}(s)$ approach unity. In this limit, the radiative transfer functions (81) and (82) approach

$$\overline{N}(z) = 2\int_z^R J(r)\frac{rdr}{\sqrt{r^2 - z^2}} \qquad (87)$$

$$\overline{W}(z) = 2\int_z^R K(r)\frac{rdr}{\sqrt{r^2 - z^2}} \qquad (88)$$

In both cases, the equations are of the Abel integral form

$$f(z) = 2\int_z^R g(r)\frac{r\,dr}{\sqrt{r^2 - z^2}} \tag{89}$$

for which the well-known inversion is

$$g(r) = -\frac{1}{2\pi r}\frac{dF(r)}{dr} \tag{90}$$

$$F(r) = 2\int_r^R f(z)\frac{z\,dz}{\sqrt{z^2 - r^2}} \tag{91}$$

Thus, solutions for $J(r)$ and $K(r)$ are immediately obtained by application of (90) and (91) to (87) and (88) and the radial profiles obtained as outlined in part A of this section.

An alternate form of the Abel inversion is

$$g(r) = -\frac{1}{\pi}\int_r^R \frac{df(z)}{dz}\frac{dz}{\sqrt{z^2 - r^2}} \tag{92}$$

Although apparently simpler than the form of (90) and (91), the latter is used because it expresses the integration portion (91) of the Abel transform in exactly the same form as all the previous integrals that have been considered and thus the same quadrature approximation (see part E of this section) can be employed. In application the differentiation portion (90) of the Abel transform is handled with a central difference approximation except at $r = R$ where a backward difference is used, and at $r = 0$ where a symmetric (about $r = 0$) quadratic fit to $F(r)$ values in the vicinity of r is used to obtain $g(r)$ at $r = 0$.

The Abel inversion method can be used to obtain meaningful results only for optically thin sources. Generally, this means that the transverse transmittance profile $\overline{\tau}(z)$ be greater than ~ 0.90 for all z. For smaller transmittance, some iterative procedures must be employed. One such procedure is considered next in this section. The Abel inversion, however, plays two important roles in this iterative method; it is used to start the iteration process and to continue the process by performing inversions of "difference" profiles obtained by subtracting intermediate calculated transverse profiles from the input transverse profiles.

C. Iterative Abel Inversion

In order to obtain inversions for radiation sources that are not optically thin, it is necessary to use an iteration scheme. The method presented here was inspired by a scheme devised by Elder et al.[19] for the inversion of monochromatic emission/absorption data, but is substantially modified to apply to band model radiation formulations and to provide a rational test for convergence. (That the formulation used by Elder et al. can give convergence to the correct answer is highly suspect.)

The starting points for the method are the radiative transfer equations (81) and (82). Suppose that we have some estimate of the radial functions c(r), p(r), and T(r). Denote these profiles and any functions computed from them by the subscript i. Then we can write from (81) and (82) that

$$\overline{N}_i(z) = 2\int_z^R J_i(r) w_i^0(z,r) \frac{rdr}{\sqrt{r^2 - z^2}} \tag{93}$$

$$\overline{W}_i(z) = 2\int_z^R K_i(r) y_i^0(z,r) \frac{rdr}{\sqrt{r^2 - z^2}} \tag{94}$$

The difference profiles obtained by subtracting $\overline{N}_i(z)$ and $\overline{W}_i(z)$ from the known profiles $\overline{N}(z)$ and $\overline{W}(z)$ are

$$\Delta\overline{N}_i(z) = \overline{N}(z) - \overline{N}_i(z) = 2\int_z^R \left[J(r)w^0(z,r) - J_i(r)w_i^0(z,r) \right] \frac{rdr}{\sqrt{r^2 - z^2}} \tag{95}$$

$$\Delta\overline{W}_i(z) = \overline{W}(z) - \overline{W}_i(z) = 2\int_z^R \left[K(r)y^0(z,r) - K_i(r)y_i^0(z,r)\right] \frac{rdr}{\sqrt{r^2 - z^2}} \quad (96)$$

where $J(r)$, $K(r)$, $w^0(z,r)$, and $y^0(z,r)$ are functions of the true radial profiles $c(r)$, $p(r)$, and $T(r)$. The standard procedure for obtaining an iteration formulation is to assume that the true functions will obtain in the next iteration. Thus, we add the subscript $i + 1$ to all nonsubscripted variables on the right-hand side of (95) and (96) to obtain

$$\Delta\overline{N}_i(z) = 2\int_z^R \left[J_{i+1}(r)w_{i+1}^0(z,r) - J_i(r)w_i^0(z,r)\right] \frac{rdr}{\sqrt{r^2 - z^2}} \quad (97)$$

$$\Delta\overline{W}_i(z) = 2\int_z^R \left[K_{i+1}(r)y_{i+1}^0(z,r) - K_i(r)y_i^0(z,r)\right] \frac{rdr}{\sqrt{r^2 - z^2}} \quad (98)$$

Despite the fact that the coordinate z appears in the integrands of (97) and (98), we now apply an Abel transformation to $\Delta\overline{N}_i(z)$ and $\Delta\overline{W}_i(z)$ and denote the results by $\Delta J_i(r)$ and $\Delta K(r)$, respectively. In some sense, we then have

$$\Delta J_i(r) = J_{i+1}(r)w_{i+1}^0(z,r) - J_i(r)w_i^0(z,r) \quad (99)$$

$$\Delta K_i(r) = K_{i+1}(r)y_{i+1}^0(z,r) - K_i(r)y_i^0(z,r) \quad (100)$$

or

$$J_{i+1}(r) = \frac{1}{w_{i+1}^0(z,r)}\left[J_i(r)w_i^0(z,r) + \Delta J_i(r)\right] \quad (101)$$

$$K_{i+1}(r) = \frac{1}{y_{i+1}^0(z,r)}\left[K_i(r)y_i^0(z,r) + \Delta K_i(r)\right] \quad (102)$$

Equations (101) and (102) define an iteration procedure for J and K, but not yet in a usable form. In order to extract a usable form, we assume *a priori* that the algorithm converges. Then, as the iteration progresses $w^0_{i+1} \rightarrow w^0_i$ and $y^0_{i+1} \rightarrow y^0_i$. Thus

$$J_{i+1} = J_i(r) + \frac{1}{w^0_{i+1}(z, r)} \Delta J_i(r) \tag{103}$$

$$K_{i+1} = K_i(r) + \frac{1}{y^0_{i+1}(z, r)} \Delta K_i(r) \tag{104}$$

Further, since we have assumed that the algorithm will converge, we have that $\Delta J_i(r) \rightarrow 0$ and $\Delta K_i(r) \rightarrow 0$. Thus, it will make no difference in the limit whether we correct the $i^{\underline{th}}$ iteration for J and K by $\Delta J_i/w^0_{i+1}$ and $\Delta K_i/y^0_{i+1}$ or by these correction values multiplied by some constant. Choosing w^0_{i+1} and y^0_{i+1}, respectively, as the multiplying factors for the J and K increments, we obtain the final iteration formula as

$$J_{i+1}(r) = J_i(r) + \Delta J_i(r) \tag{105}$$

$$K_{i+1}(r) = K_i(r) + \Delta K_i(r) \tag{106}$$

where $\Delta J_i(r)$ is the Abel transform of $\overline{N}(z) - \overline{N}_i(z)$, $\Delta K_i(r)$ is the Abel transform of $\overline{W}(z) - \overline{W}_i(z)$; $\overline{N}_i(z)$ is obtained from (93), and $\overline{W}_i(z)$ is obtained from (94). The iteration is initiated by obtaining "first guess" profiles of c(r) and T(r) by Abel inversion. The iteration is continued until some convergence criteria is met. Generally, the criterion is used that the $i^{\underline{th}}$ and $i + 1^{\underline{st}}$ radial profiles differ by no more than some preset, small increment.

Although this iteration scheme has been derived heuristically, it is shown by example in Section VII that the scheme is rapidly convergent and unique. A summary of the method is presented as a computational flow diagram in Fig. 2. Note that in the scheme, the pressure profile is entered as a known profile.

One aspect of the scheme diagramed in the figure has not yet been discussed — the testing of J(r) and K(r) for nonnegative values. If the input

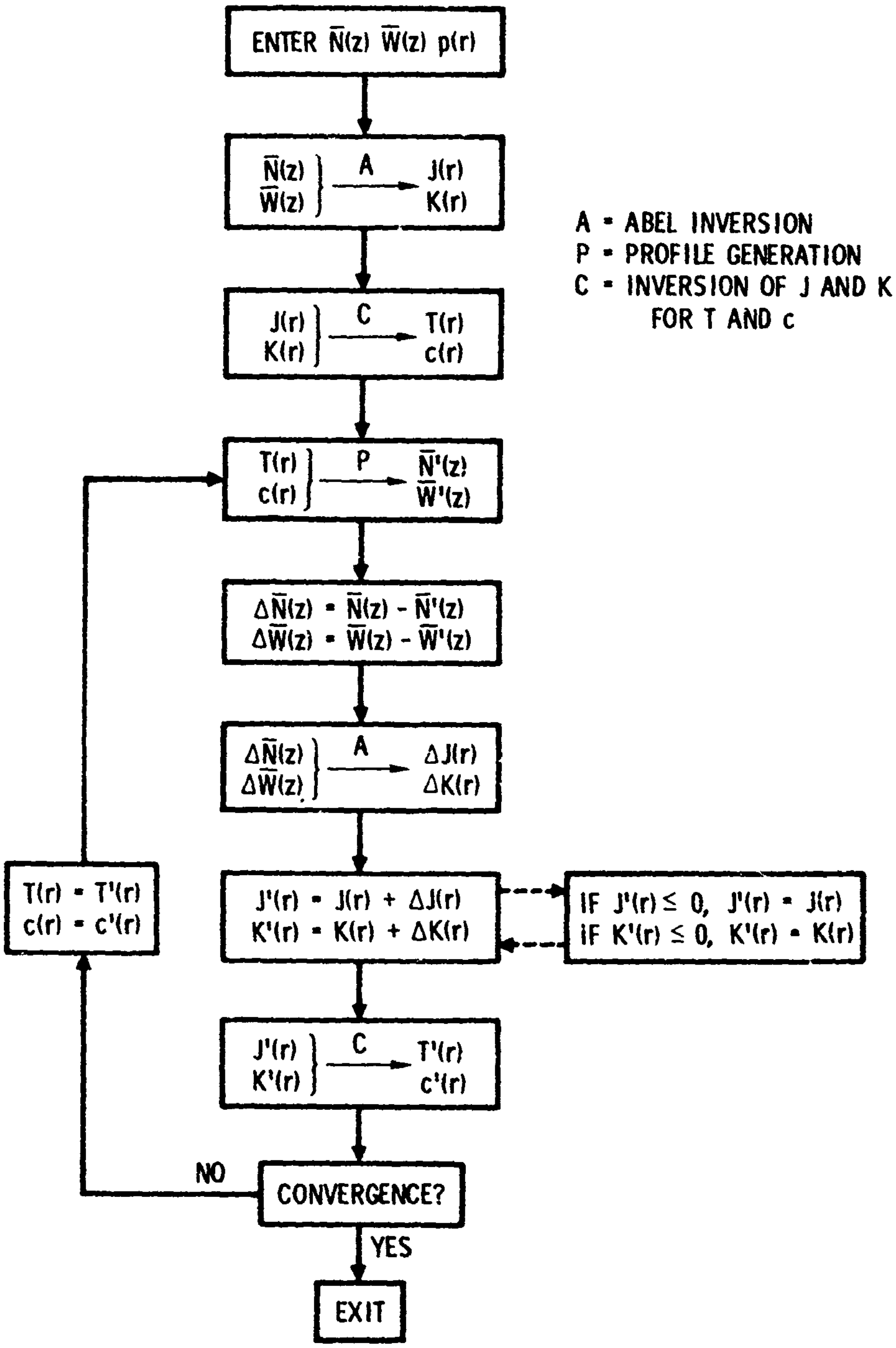

Fig. 2. Iterative Abel Inversion Flow Diagram

data profiles $\overline{N}(z)$ and $\overline{\tau}(z)$ are noisy (i.e., random noise fluctuations), it is possible for intermediate results for the iterated J(r) and K(r) profiles to be negative If they are so, the inversion of J(r) and K(r) for c(r) and T(r) is suspect if not indeterminate. In the inversion scheme, therefore, J(r) and K(r) are tested at each discrete value of r used in the numerical approximation routines and, if found to be nonpositive, replaced by their value from the preceding iteration. This procedure cannot be used, of course, if negative or zero values of J(r) or K(r) occur in the initiating Abel inversion. In this case, the input transverse profiles must be smoothed to such an extent that this condition does not arise. Smoothing of the input data is the subject of the following part of this section.

D. Presmoothing

The integral equations (81) and (82) can be classed as Fredholm integral equations of the first kind. The solution of such equations is known to be highly sensitive to irregularities in the input functions $\overline{N}(z)$ and $\overline{W}(z)$. Even very small fluctuations (such as random experimental noise) in the input functions can be dramatically amplified in the inversion process and yield essentially meaningless results. Additionally, there is the possibility that an inversion cannot even be effected if the fluctuations are large enough to cause negative or zero values of the radial functions J(r) and K(r). Several methods have been devised to handle this fluctuation problem. Here we consider a straightforward presmoothing of the input data to be inserted into the Abel or iterative Abel inversion routines.

The presmoothing scheme used here is inspired by the inversion schemes of Phillips[20] and Twomey.[21] Consider a function g(z) defined on an equal interval grid $z_n = (n - 1)\Delta z$ $(n = 1, 2, \ldots, N + 1)$ consisting of N intervals of width Δz. Define $g_n = g(z_n)$. The array g_n represents either of the unsmoothed transverse profiles $\overline{N}(z)$ or $\overline{W}(z)$, and $\Delta z = R/N$. Let the array f_n $(n = 1, 2, \ldots, N + 1)$ represent the smoothed version of g_n. The Phillips-Twomey approach to smoothing is to select that set of f_n which minimizes the curvature function

$$C(f_1, \ldots, f_{N+1}) = \sum_{i=1}^{N+1} (f_{n-1} - 2f_n + f_{n+1})^2 \tag{107}$$

subject to certain constraints. Clearly, some restraint must be imposed since the set that minimizes C without constraint is the trivial set f_n = Constant for all n. The constraint imposed here is that the root-mean-square (rms) difference between the smoothed and unsmoothed functions be of the order of the estimated experimental rms error ϵ. We will write this constraint as

$$S(f_1, \ldots, f_{N+1}) = \sum_{i=1}^{N+1} (f_n - g_n)^2 \simeq (N + 1)\epsilon^2 \tag{108}$$

The method of Lagrange undetermined multiplier indicates that we should then minimize the function $C - \lambda S$ with respect to the f_n and then vary λ until the constraint (108) is satisfied. Rather than λ, we use $\gamma = -1/\lambda$ and minimize

$$\begin{aligned} H(f_1, \ldots, f_{N+1}) &= \gamma C(f_1, \ldots, f_{N+1}) + S(f_1, \ldots, f_{N+1}) \\ &= \gamma \sum_{n=1}^{N+1} (f_{n-1} - 2f_n + f_{n+1})^2 + \sum_{n=1}^{N+1} (f_n - g_n)^2 \end{aligned} \tag{109}$$

Minimization of H with respect to the f_n is obtained by solving the system of N + 1 equations

$$\begin{aligned} \frac{\partial H}{\partial f_1} &= 0 \\ \frac{\partial H}{\partial f_2} &= 0 \\ &\vdots \\ \frac{\partial H}{\partial f_{N+1}} &= 0 \end{aligned} \tag{110}$$

Differentiation of (109) with respect to f_j, use of

$$\frac{\delta f_n}{\delta f_j} = \delta_{nj} \tag{111}$$

and equating the result to zero gives

$$\gamma f_{j-2} - 4\gamma f_{j-1} + (6\gamma + 1)f_j - 4\gamma f_{j+1} + \gamma f_{j+2} = g_j \tag{112}$$

This result is the form of the equations (110) for $j = 3, 4, \ldots, N - 2$. For j in the end regions $j = 1, 2$ and $j = N - 1, N, N + 1$, the form of the equations will depend on how f_n is defined for $n \le 0$ and $n \ge N + 2$. The transverse profiles $\overline{N}(z)$ and $\overline{W}(z)$ are symmetric about $z = 0$ and fall (ideally) to zero at $z = R$. It seems appropriate to define

$$f_j = f_{2-j} \qquad j \le 0 \tag{113}$$

$$f_{N+1} = 0$$

$$f_j = -f_{2(N+1)-j} \qquad j \ge N + 2 \tag{114}$$

A common approach is to substitute the conventions directly into (112) to obtain the special end zone equations. However, this procedure is not strictly correct because then we are assuming a dependence between f_n values <u>after</u> we have already used the independence relation (111). The correct procedure is to use (113) and (114) in H before the partial differentiations are taken. Thus,

$$H = \gamma\left[(-2f_1 + 2f_2)^2 + \sum_{n=2}^{N-1} (f_{n-1} - 2f_n + f_{n+1})^2\right.$$

$$\left. + (f_{N-1} - 2f_N)^2 + (0)^2\right] + \sum_{n=1}^{N} (f_n - g_n)^2 + g_{N+1}^2 \tag{115}$$

From this expression for H, the following system equations result

$$
\begin{aligned}
j &= 1 & (5\gamma + 1)f_1 - 6\gamma f_2 + \gamma f_3 &= g_1 \\
j &= 2 & -6\gamma f_1 + (9\gamma + 1)f_2 - 4\gamma f_3 + \gamma f_4 &= g_2 \\
j &= N - 1 & \gamma f_{N-3} - 4\gamma f_{N-2} + (6\gamma + 1)f_{N-1} - 4\gamma f_N &= g_{N-1} \\
j &= N & \gamma f_{N-2} - 4\gamma f_{N-1} + (5\gamma + 1)f_N &= g_N
\end{aligned}
\tag{116}
$$

Note that because f_{N+1} has been specifically set to zero, the system contains only N equations. With (112) and (116), the system of equations can be written in the matrix form

$$(\gamma\overline{H} + \overline{I})\overline{f} = \overline{g} \tag{117}$$

where $\overline{f}$ and $\overline{g}$ are the column matrices

$$\overline{f} = \begin{bmatrix} f_1 \\ f_2 \\ \cdot \\ \cdot \\ \cdot \\ f_N \end{bmatrix} \qquad \overline{g} = \begin{bmatrix} g_1 \\ g_2 \\ \cdot \\ \cdot \\ \cdot \\ g_N \end{bmatrix} \tag{118}$$

$\overline{I}$ is the identity matrix

$$\overline{I} = \begin{bmatrix} 1 & & & & \bigcirc \\ & 1 & & & \\ & & \ddots & & \\ & & & 1 & \\ \bigcirc & & & & 1 \end{bmatrix} \tag{119}$$

and $\overline{H}$ is the banded, N x N, symmetric matrix

$$\overline{H} = \begin{bmatrix} 5 & -6 & 1 & & & & & & & \\ -6 & 9 & -4 & 1 & & & & \bigcirc & & \\ 1 & -4 & 6 & -4 & 1 & & & & & \\ & 1 & -4 & 6 & -4 & 1 & & & & \\ & & & & \ddots & & & & & \\ & & \bigcirc & & & 1 & -4 & 6 & -4 & 1 \\ & & & & & & 1 & -4 & 6 & -4 \\ & & & & & & & 1 & -4 & 5 \end{bmatrix} \tag{120}$$

The formal solution for the smoothed array f_n is then, from (117)

$$\overline{f} = (\gamma\overline{H} + \overline{I})^{-1}\,\overline{g} \tag{121}$$

The smoothing parameter γ controls the degree of smoothing. For $\gamma = 0$, $\overline{f} = \overline{I}^{-1}\overline{g} = \overline{I}\,\overline{g} = \overline{g}$ and no smoothing is effected. As $\gamma \longrightarrow \infty$, $\overline{f} \longrightarrow \gamma^{-1}\overline{g} \longrightarrow 0$. In practice, γ is varied until the constraint (108) is met. Application of this smoothing method requires a computation of the inverse of $\gamma\overline{H} + \overline{I}$. A standard inversion routine[22] based on the Gauss elimination algorithm is employed. Characteristics of this smoothing routine in application to real data are discussed in Section VIIIE.

For some applications, it is necessary to smooth data defined on an irregular grid. The generalization of the method considered above to a general grid is straightforward, but tedious. Only an outline of the derivation and the final result are reported here. The unsmoothed (and smoothed) profiles are taken to be defined on the general grid z_i, i = 1, N + 1 with $z \equiv 0$ and $z_{N+1} \equiv R$. Define the interval weighting functions

$$\begin{aligned} d_1 &= z_2 - z_1 \\ d_i &= z_{i+1} - z_{i-1} \qquad i = 2, 3, \ldots, N \\ d_{N+1} &= z_{N+1} - z_N \end{aligned} \tag{122}$$

The generalization of (109) for the function to be minimized is

$$H(f_1, \ldots, f_{N+1}) = \gamma \sum_{n=1}^{N+1} [a_n f_{n-1} - b_n f_n + c_n f_{n+1}]^2$$

$$+ \sum_{n=1}^{N+1} (f_n - g_n)^2 d_n \tag{123}$$

where the second-derivative coefficients a_n, b_n and c_n are

$$\left. \begin{aligned} a_n &= \frac{1}{(z_{n+1} - z_{n-1})(z_n - z_{n-1})} \\ b_n &= \frac{1}{(z_{n+1} - z_n)(z_n - z_{n-1})} \\ c_n &= \frac{1}{(z_{n+1} - z_{n-1})(z_{n+1} - z_n)} \end{aligned} \right\} \quad n = 1, 2, \ldots, N \tag{124}$$

with the convention that $z_0 \equiv -z_2$ and $z_{N+2} \equiv 2R - z_N$. Carrying the derivation through as before, we find the smoothed profile to be given by

$$\overline{f} = \overline{K}^{-1} \overline{g}' \tag{125}$$

where $\overline{g}'$ is the column matrix

$$\overline{g}' = \begin{bmatrix} d_1 g_1 \\ d_2 g_2 \\ \cdot \\ \cdot \\ \cdot \\ d_N g_N \end{bmatrix} \tag{126}$$

and $\overline{K}$ is the banded, $N \times N$, symmetric matrix

$$
\overline{K} = \begin{bmatrix}
k_1 & k_2 & k_3 & & & & & & & \\
k_4 & k_5 & k_6 & k_7 & & & & & & \\
k_8 & k_9 & k_{10} & k_{11} & k_{12} & & & & & \\
 & k_{13} & k_{14} & k_{15} & \cdots & & & & & \\
 & & k_{18} & \cdots & & & & & & \\
 & & & & & & \cdots & k_{5N-23} & & \\
 & & & & & & & \cdots & k_{5N-18} & \\
 & & & & & k_{5N-17} & k_{5N-16} & k_{5N-15} & k_{5N-14} & k_{5N-13} \\
 & & & & & & k_{5N-12} & k_{5N-11} & k_{5N-10} & k_{5N-9} \\
 & & & & & & & k_{5N-8} & k_{5N-7} & k_{5N-6}
\end{bmatrix} \tag{127}
$$

with

$$
\begin{aligned}
k_1 &= (a_2^2 + b_1^2)\gamma + d_1 \\
k_2 &= -(a_2 b_2 + 2b_1 c_1)\gamma \\
k_3 &= a_2 c_2 \gamma \\
\\
k_4 &= k_2 \\
k_5 &= (a_3^2 + b_2^2 + 4c_1^2)\gamma + d_2 \\
k_6 &= -(a_3 b_3 + b_2 c_2)\gamma \\
k_7 &= a_3 c_3 \gamma
\end{aligned}
$$

$$
\left.
\begin{aligned}
k_{5n-7} &= a_{n-1} c_{n-1} \gamma \\
k_{5n-6} &= -(a_n b_n + b_{n-1} c_{n-1})\gamma \\
k_{5n-5} &= (a_{n+1}^2 + b_n^2 + c_{n-1}^2)\gamma + d_n \\
k_{5n-4} &= -(a_{n+1} b_{n+1} + b_n c_n)\gamma \\
k_{5n-3} &= a_{n+1} c_{n+1} \gamma
\end{aligned}
\right\} \quad n = 3,\ N - 1
$$

$$
\begin{aligned}
k_{5N-8} &= a_{N-1} c_{N-1} \gamma \\
k_{5N-7} &= (a_N b_N + b_{N-1} c_{N-1})\gamma \\
k_{5N-6} &= (b_N^2 + c_{N-1}^2)\gamma + d_N
\end{aligned}
\tag{128}
$$

E. Quadrature Approximation

All of the integrals required in radiation computation and inversion can be written in the general form

$$F(y, P) = 2 \int_P^R G(y, x) \frac{x\,dx}{\sqrt{x^2 - y^2}} \tag{129}$$

with

$$y \le P \le R \tag{130}$$

For integrals over only a portion of an optical path [such as (19) through (21) and (28) to compute path averaged band model parameters], we set $x = r$, $y = z$ and $P = r$. For integrals along an entire optical path [such as (6) and (7) which compute the radiance and transmittance from the chord at transverse coordinate z], we set $x = r$, $y = z$ and $P = z$. For the Abel inversion, we set $x = z$, $y = r$ and $P = r$.

The quadrature approximation for (129) is patterned on the method of Barr.[23] Divide the interval $x = 0$ to $x = R$ into N equal size subintervals. The subinterval size is then

$$\Delta = \frac{R}{N} \tag{131}$$

The coordinate x and parameters y and P are discretized as

$$\begin{aligned} x_n &= (n - 1)\Delta & n &= 1, 2, \ldots, N + 1 \\ y_k &= (k - 1)\Delta & k &= 1, 2, \ldots, N + 1 \\ P_q &= (q - 1)\Delta & q &= 1, 2, \ldots, N + 1 \end{aligned} \tag{132}$$

where, because of (130) and the integration limits on (129)

$$1 \le k \le q \le n \le N + 1 \tag{133}$$

Define the discrete function values

$$
\begin{aligned}
F_{kq} &= F(y_k, P_q) \\
G_{kn} &= G(y_k, x_n)
\end{aligned}
\tag{134}
$$

Within the subinterval $x_n \le x \le x_{n+1}$, the kernal function $G(y, x)$ is approximated by the symmetric quadratic form

$$
G(y, x) = a_{kn} + b_{kn} x^2 \tag{135}
$$

The coefficients a_{kn} and b_{kn} are determined by forcing $G(y, x)$ to be equal to G_{kn} and $G_{k, n+1}$ at the interval end points x_n and x_{n+1}, respectively. The solutions are

$$
\begin{aligned}
a_{kn} &= \frac{1}{(2n - 1)} \left[n^2 G_{kn} - (n - 1)^2 G_{k, n+1} \right] \\
b_{kn} &= \frac{1}{\Delta^2 (2n - 1)} \left[G_{k, n+1} - G_{kn} \right]
\end{aligned}
\tag{136}
$$

With the relationships so far established, (129) is written as

$$
F_{kq} = 2 \sum_{n=q}^{N} \int_{(n-1)\Delta}^{n\Delta} \left[a_{kn} + b_{kn} x^2 \right] \frac{x dx}{\sqrt{x^2 - y_k^2}} \tag{137}
$$

Evaluation of the integrals over x and a straightforward but tedious manipulation of the resulting expressions gives the final result

$$
F_{kq} = \Delta \left[\alpha_1(k, q) G_{kq} + \sum_{n=q+1}^{N} \alpha_2(k, n) G_{kn} + \alpha_3(k) G_{k, N+1} \right] \tag{138}
$$

where the quadrature coefficients are

$$\alpha_1(k,q) = \frac{4}{3}\left[\frac{\left|q^2 - (k-1)^2\right|^{3/2}}{2q - 1} - \frac{3}{2}\sqrt{(q-1)^2 - (k-1)^2} - \frac{\left|(q-1)^2 - (k-1)^2\right|^{3/2}}{2q - 1}\right] \tag{139}$$

$$\alpha_2(k,n) = \frac{4}{3}\left[\frac{\left|n^2 - (k-1)^2\right|^{3/2}}{2n - 1} - \frac{4(n-1)\left|(n-1)^2 - (k-1)^2\right|^{3/2}}{(2n-1)(2n-3)} + \frac{\left|(n-2)^2 - (k-1)^2\right|^{3/2}}{2n - 3}\right] \tag{140}$$

$$\alpha_3(k) = \frac{4}{3}\left[\frac{\left|(N-1)^2 - (k-1)^2\right|^{3/2}}{2N - 1} + \frac{3}{2}\sqrt{N^2 - (k-1)^2} - \frac{\left|N^2 - (k-1)^2\right|^{3/2}}{2N - 1}\right] \tag{141}$$

The only qualifications required for application of (138) are the index relation of (133), the convention that the summation term be omitted if $q = N$ and the obvious result that $F_{kq} = 0$ if k or $q = N + 1$.

IV. PROGRAM EMABIC

A. Description of Code

A computer code, EMABIC,* has been written which incorporates the band model radiation formulation of Section II and the inversion and smoothing formulations of Section III into a general usage program. The code is written in Fortran IV compatible with The Aerospace Corporation CDC 7600 and the AFRPL CDC 6400 computer systems.

The code operates in one of four modes, a transverse profile generation mode, a data smoothing mode, and two data inversion modes. The specification of mode and data to be analyzed is treated in part B of this section. Here, a brief description of the operation of the code in each of these modes is given.

A routine common to all modes is the input of relevant data. This input is accomplished by calls to the two subroutines INPUT and DAT-PREP. The first subroutine simply reads in all data required for a computational run, stores the data, and provides a preliminary output listing summarizing the calculation conditions and data. The second subroutine prepares the input data for use by the main program EMABIC. The two most important preparations are the fitting of input profiles to an equal-interval grid on the coordinate r or z in the range zero to R and smoothing of input transverse data profiles. The former is accomplished by a call to subroutine ZONEFIT which fits the input profile (defined on an arbitrary coordinate grid) by linear interpolation to the grid $(i - 1) R/N$, $i = 1, 2, \ldots, N + 1$ where N is the number of zones used in the computations. Smoothing is performed by a call to subroutine SMOOTH which

*EMABIC is an acronym for Emission/Absorption Inversion Code. Requests for this code by interested users should be directed to AFRPL/CE in writing.

employs the formalism of Section IIID. The matrix inversion of (121) is handled by subroutine GELB.* Provisions are also made in subroutine DATPREP for the removal of finite field-of-view effects on transverse profiles by a call to subroutine DCONVLV.**

A second common routine is the computation of the quadrature weighting coefficients (139-140) by a call to subroutine COEFF. These coefficients are subsequently used in any call to subroutine QUAD which applies the quadrature approximation of (138) whenever a numerical integration is called for.

Profile Generation Mode. The profile generation mode accepts input radial profiles of pressure, temperature and concentration and computes transverse profiles of radiance and transmittance according to the band model radiation formulation of Section II. Both $\overline{N}(z)$ and $\overline{\tau}(z)$ are computed by a single call to subroutine PROFILS. Depending on the approximation used to treat optical path nonuniformities and the spectral lineshape, one or more of the following routines may be called by PROFILS.

YCGL Compute the derivative function y for the CG approximation and Lorentz lineshape.

YDRL Compute the derivative function y for the DR approximation and Lorentz lineshape. YDRL calls the subprogram YLSL which computes y for the LS approximation and Lorentz lineshape.

*Subroutines GELB and GELS are taken from the IBM Scientific Subroutine Package (Reference 22).

**DCONVLV has not yet been coded and at present an immediate return to the main program takes place in a call to DCONVLV.

YCGD	Compute the derivative function y for the CG approximation and Doppler lineshape.
YMLD	Compute the derivative function y for the ML derivative approximation and Doppler lineshape. YMLD calls the subprogram YLSD which computes y for the LS approximation and Doppler lineshape.
YMIX	Compute the derivative function y for the Voigt lineshape.
F	Compute the curve-of-growth function for a band of Lorentz lines
G	Compute the curve-of-growth function for a band of Doppler lines
WMIX	Compute the curve-of-growth function for a band of Voigt lines.

Band model parameters required for generation of transverse profiles are obtained from a call to subroutine KDPARAM which interpolates linearly in temperature on a table of parameters entered as part of the input. The results of a profile generation run are listed by subroutine LIST1.

Profile Smoothing Mode. For an inversion run using the Abel or iterative Abel method, the input transverse profile data must first be smoothed. For the actual inversion run, this smoothing is part of the data preparation performed by subroutine DATPREP and uses smoothing parameters entered as part of the input. In order to determine the proper smoothing parameters for the inversion, a prior run of EMABIC in the variable smoothing mode is generally required. In this mode, the transverse profiles are smoothed according to the procedure of Section IIID for a wide range of smoothing parameter γ. Inspection of the degree of smoothing performed as a function of γ allows the selection of proper γ values for the actual inversion. The principle subroutine used in this mode is subroutine GAMMA which calls the smoothing subroutine SMOOTH for a range of γ values specified in the input.

Abel Inversion Mode. When operating in this mode, EMABIC inverts the input transverse profiles $\overline{N}(z)$ and $\overline{\tau}(z)$ for c(r) and T(r) according to the Abel inversion routine of Section IIIB. The first step of the inversion is the computation of the radial source and absorption functions J(r) and K(r). These calculations are effected by a call to subroutine ABEL. The radial profiles T(r) and c(r) are obtained from J(r) and K(r) according to (85) and (86) in subroutine CTSOLVE. If the solution for c(r) and T(r) is indeterminate because J(r) is negative, an error message is written. Generally, this indeterminacy can be removed by a higher degree of data smoothing. The results of an Abel inversion are written out by subroutine LIST3.

Iterative Abel Inversion Mode. In this mode, inversion of transverse profiles is carried out with the iterative Abel inversion method derived in Section IIIC. The successive Abel inversions on the difference profiles and profile generations using updated radial profiles (see Fig. 2) are carried out with subroutines ABEL and PROFILES, respectively. At each iteration, the source functions J(r) and K(r) are used to obtain c(r) and T(r) as in the Abel inversion. Testing for convergence is made in subroutine CONVERGE. Convergence criteria are set as part of the input data and provide for testing on the maximum absolute difference or root-mean-square difference between successive iterations of any or all of the four profiles c(r), T(r), $\overline{N}(z)$ or $\overline{\tau}(z)$. Results of a successful inversion (and, optionally, the results of intermediate iterations) are written by subroutine LIST2. Optionally, intermediate iteration results for J(r) and K(r) may be listed by subroutine LIST4.

B. Preparation of Input Data

A computational run of program EMABIC requires a set of program control cards to specify the mode of computation and to supply input data. Some program control cards simply specify a computation mode, some specify a computation mode and supply data, while others signal the code that blocks of auxiliary data are now to be read in. Each type of control card contains an alphanumeric name in the first ten card columns. These names must be spelled correctly and must be left-justified. If data are specified on a program control card, they must be entered in accordance with the format specification indicated in the detailed description of each card given below. All fields of the program control cards are 10 columns wide. In general, integer and alphanumeric data must be right-justified in their fields. Non-integer numerical data may be entered in either F or E formats (with decimal point and, for the latter, the exponential symbol E). E-formated data must be right-justified in their field. These same rules apply to data entered on auxiliary card decks. The types of control cards and the data contained on them are illustrated in Fig. 3. A description of each type follows.

1. Title Card. The card name is TITLE. Columns 11-80 of this card may be used for any identification title desired. This title will appear on the final listing of the computation run.

2. Lineshape Card. The card name is LINESHAPE. The variable SHAPE (format A10) defines the lineshape that will be used in the statistical band model radiation calculations and must have one of the three alphanumeric values LORENTZ, DOPPLER or VOIGT.

3. Nonuniformity Approximation Card. The card name is INHOM (for inhomogeneous). The variable APPROX (format A10) specifies the approximation that will be used to treat nonuniformities along an optical line of sight. If APPROX has the value CG, the Curtis-Godson approximation will be used. If the value is DR, the derivative approximation will be used.

10	20	30	40	50	60	70	80
TITLE							
LINESHAPE	SHAPE						
INHOM	APPROX						
ZONES	NZONES						
PARAM	PRINT						
PROFILES	PRINT						
SPECIE	SPECIE						
INVERSION	PRINT	SAME	MODE	G1	G2		
PRESSURE	PRINT						
LIST	JKLIST						
NOLIST							
CONVERGE	CTEST	IMAX	TRRMS	CTRMS	TRMAX	CTMAX	
RUN							

Fig. 3. EMABIC Program Control Card Formats

4. Integration Grid Card. The card name is ZONES. The variable NZONES (format I10) defines the number of equal size radial and transverse zones that will be used in the various numerical routines of EMABIC. The maximum allowed value is 50.

5. Band Model Parameter Card. The card name is PARAM. This card calls for the read-in of band model parameters for the active species and spectral bandpass being considered. The auxiliary data defining the band model parameters must follow the PARAM card immediately in the card input stream and must be structured as shown in Fig. 4. If the variable PRINT (format A10) has the value PRINT, the band model parameters will be listed.

6. Transverse Profile Mode Card. The card name is PROFILES. This card is used to operate EMABIC in the profile generation mode. That is, transverse profiles of radiance and transmittance will be generated from input radial profiles of pressure, temperature and species concentration. This input data must immediately follow the PARAM card and be structured as illustrated in Fig. 5. If the variable PRINT (format A10) on the PROFILES card has the value PRINT, these radial data will be listed. The auxiliary radial data deck allows for the specification of profiles for H_2O, CO_2 and CO. In order for the program to know which species to work with, a SPECIE control card (type 7) must be used with a PROFILES card.

7. Species Card. The card name is SPECIE. This card must be included as part of the control card sequence whenever EMABIC is operating in the transverse profile generation mode. The variable SPECIE (format A10) must have one of the three alphanumeric values H2O, CO2 or CO. Note that this control card only tells the program where to find the correct concentration data in the radial input data deck. It does not set band model parameters, for example. Thus, the band model parameters entered with a PARAM card (type 5) must be consistent with the species called for by the SPECIE card.

Legend

All field formats are E10 or F10 except the PARAMID field which is A10.

PARAMID	Any 10-character identification name.
ν	Spectral position (cm^{-1}).
$\Delta\nu$	Spectral resolution (cm^{-1}).
$\overline{Y}$	Pressure broadening coefficient (cm^{-1}/atm for non-resonant self-broadening at STP).
α_1	Ratio of resonant self-broadening parameter to $\overline{Y}$ at STP.
α_2	Ratio of foreign-gas broadening parameter to $\overline{Y}$ at STP.
α_3	Atomic weight of active gas species (amu).
T(i)	Temperature array ($^{\circ}K$). The T(i) array must be T(i) = 100i, i = 1, 2, ..., 40.
$\bar{k}$(i)	Absorption coefficient for ν, $\Delta\nu$ and T(i) (cm^{-1}/atm).
D(i)	Line density parameter for ν, $\Delta\nu$ and T(i) (lines/cm^{-1}). Note, D = $1/\bar{\delta}$.

10	20	30	40	80
PARAMID	ν	$\Delta\nu$		
$\overline{Y}$	α_1	α_2	α_3	
T(1)	$\bar{k}$(1)	D(1)		
T(2)	$\bar{k}$(2)	D(2)		
T(39)	$\bar{k}$(39)	D(39)		
T(40)	$\bar{k}$(40)	D(40)		

Fig. 4. Input Card File Structure for Band Model Parameters

Legend

All field formats are E10 or F10 except the DATAID field which is A10 and the NPOINTS field which is I10.

DATAID	Any 10-character identification name.
NPOINTS	Number of radial positions at which data are given (maximum value = 101).
R	Source cylinder radius (cm).
r(i)	Radial positions at which data are given (cm). The value of r(1) must be zero, the value of r(NPOINTS) must be R, and r(i) must increase with increasing i .
p(i)	Pressure at r(i) (atm).
T(i)	Temperature at r(i) (^{o}K).
c_{H2O}	Concentration of H_2O at r(i) (mole fraction)
c_{CO2}	Concentration of CO_2 at r(i) (mole fraction).
c_{CO}	Concentration of CO at r(i) (mole fraction).

10	20	30	40	50	60	80
DATAID	NPOINTS	R				
r(1)	p(1)	T(1)	$c_{H2O(1)}$	$c_{CO2(1)}$	$c_{CO(1)}$	
r(2)	p(2)	T(2)	$c_{H2O(2)}$	$c_{CO2(2)}$	$c_{CO(2)}$	
r(NPOINTS)	p(NPOINTS)	T(NPOINTS)	$c_{H2O(NPOINTS)}$	$c_{CO2(NPOINTS)}$	$c_{CO(NPOINTS)}$	

Fig. 5. Input Card File Structure for Radial Profile Data

8. Inversion Mode Card. The card name is INVERSION. An encounter of this card in the input stream signals EMABIC that an inversion run is to be made. Usually, a card deck of data defining the transverse radiance and transmittance profiles that are to be inverted must follow this card immediately in the input stream. The deck structure for these data is shown in Fig. 6. If the variable PRINT (format A10) on the INVERSION card has the value PRINT, these input data will be listed. The exception to the requirement that an auxiliary data deck immediately follow the INVERSION card occurs if the variable SAME (format A10) has the value SAME. In this case, the transverse profiles data that were used in the immediately preceding run will be used unchanged. The variable MODE (format A10) specifies which of two inversion methods will be used. If MODE has the value ABEL, the optically thin Abel inversion will be employed. If the value is INVERSION, the iterative Abel method will be used. The variables G1 and G2 (each format E10) are smoothing parameters for the absorption and radiance input profiles, respectively. For an iterative Abel inversion, these smoothing parameters are presmoothing parameters and are determined from a prior run of EMABIC in the smoothing mode (following paragraph).

A fourth value is possible for the variable MODE. If the value is SMOOTH, no inversion of the input profiles is made, but rather EMABIC performs a variable smoothing of the input transverse radiance and transmission curves. Both profiles are smoothed using values of γ starting at G1 and increasing by factors of two up to and including G2. The output of EMABIC operating in this mode allows the selection of G1 and G2 for operation in the iterative Abel inversion mode.

9. Pressure Profile Card. The card name is PRESSURE. An encounter of this card indicates that a card deck specifying the radial pressure profile that will be used in an inversion computation follows immediately in the data input stream. This card, and the data it calls

Legend

All field formats are E10 or F10 except the DATAID field which is A10, the NPOINTS field which is I10, and the C2 field which is I10.

DATAID	Any 10-character identification name.
NPOINTS	Number of transverse positions at which data are given (maximum value = 101).
R	Source cylinder radius (cm).
Δz	Transverse spatial resolution of data (i.e., instrument FOV resolution) (cm).*
C1	A constant that converts by multiplication the $\overline{N}(i)$ emission data to units of W/cm^2-sr-cm^{-1}. (If C1 is zero or blank, C1 = 1 is assumed).
C2	A flag that indicates whether the "absorption" data is absorptance or transmittance. Blank or zero (normal mode) implies transmittance. C2 = 1 implies absorptance.
z(i)	Transverse positions at which data are given (cm). The value of z(1) must be zero, the value of z(NPOINTS) must be $R + \Delta z/2$ and z(i) must increase with increasing i .
$\overline{N}(i)$	Emission data at z(i). (Nominal unit is W/cm^2-sr-cm^{-1}, see use of C1). The value of $\overline{N}$(NPOINTS) must be zero.
$\overline{\tau}(i)$	Absorption data at z(i). (Nominal variable is transmittance, see use of C2). The value of $\overline{\tau}$(NPOINTS) must be unity if the data are transmittance and zero if absorptance. $\overline{\tau}(i)$ must not be either zero or unity for any other value of i.

*$\Delta z = 0$ is the only value that can presently be used.

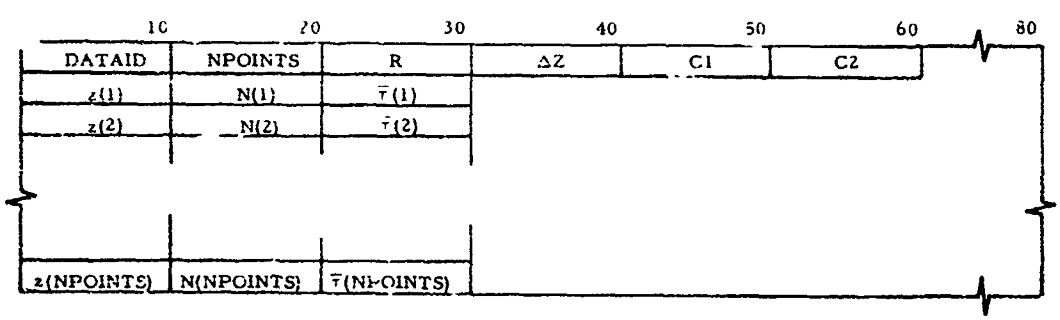

Fig. 6. Input Card File Structure for Transverse Profile Data

for must be included whenever an inversion mode is specified. That is, whenever an INVERSION card is used and MODE ≠ SMOOTH. The card file structure for the pressure data is given in Fig. 7. If the variable PRINT (format A10) has the value PRINT on the PRESSURE Control card, the radial pressure profile will be listed.

10. List Control Cards. Two cards with the names LIST and NOLIST control the printout of transverse and radial profiles generated during successive iterations in an inversion mode computation run. If a LIST card is never encountered, the printout of intermediate profiles is suppressed. If a LIST card is encountered, the intermediate profiles will be listed. A NOLIST card can be used to again suppress the listing on a run subsequent to a run in which the listing was called for. If the variable JKLIST (format A10) on the LIST card has the value LIST, the emission and absorption functions $J(r)$ and $K(r)$ are also listed for each iteration.

11. Convergence Card. The card name is CONVERGE and contains data specifying the convergence criteria that must be met in order to terminate an inversion computation. The variable CTEST (format A10) must have one of the two values TC or RT. The former value indicates that convergence testing will be done on the radial temperature-concentration profiles while the latter indicates that the tests will be made on the transverse radiance-transmittance profiles.

The variable IMAX (format I10) specifies the maximum number of iterations that will be allowed. If convergence is not achieved within this number of iterations, a message to this effect is printed, the radial and transverse profiles of the last iteration are printed, and the program moves on to the next run.

If CTEST has the value TC, the variables TRRMS, CTRMS, TRMAX and CTMAX (all format E10) have the following meaning:

Legend

All fields are E10 or F10 except the PPROFID field which is A10 and the NPOINTS field which is I10.

PPROFID	Any 10-character identification name.
NPOINTS	Number of radial points at which pressure is defined (maximum value = 101).
R	Source cylinder radius (cm).
$r(i)$	Radial positions at which pressures are given (cm). The value of $r(1)$ must be zero, the value of $r(\text{NPOINTS})$ must be R, and $r(i)$ must increase with increasing i. The $r(i)$ array need not (and, in fact, cannot unless $\Delta z = 0$) correspond with the transverse input data grid $z(i)$.
$p(i)$	Pressure at $r(i)$ (atm).

10	20	30	80
PPROFID	NPOINTS	R	
r(1)	p(1)		
r(2)	p(2)		
r(NPOINTS)	p(NPOINTS)		

Fig. 7. Input Card File Structure for Radial Pressure Profile

The absolute value of the maximum difference (at any radial position) between two successive temperature profiles must be less than TRMAX (unit = K) for convergence to be assumed. The absolute value of the radially computed root mean square difference (rms) between the two profiles must be less than TRRMS (unit = K). Similarly, the maximum absolute difference between successive concentration profiles must be less than CTMAX and the rms difference must be less than CTAVE.

If CTEST has the value RT, TRRMS and TRMAX correspond to the rms and maximum absolute differences, respectively, allowed between two successively computed transverse radiance profiles. In this case, the unit of TRRMS and TRMAX is W/cm^2-sr-cm^{-1}. CTRMS and CTMAX now correspond to tests made on successively computer transmittance profiles.

The most stringent convergence testing occurs when all four variables (TRRMS, TRMAX, CTRMS, and CTMAX) have small but non-zero values. A zero value for any of the variables indicates that testing on that value is not made. If all four variables are specified to be zero, no convergence testing is made and the results are assumed to converge after the first iteration.

12. Execution Card. The card name is RUN. When this card is encountered, computations are begun using the data entered up to that point, and an output listing of the results is made. When the computation and results listing is completed, the program continues to read program control cards until a new RUN card is encountered. A new computation is then begun for all of the conditions and data of the first run except those which have been changed by the intervening program control cards and auxiliary data decks. This process is repeated until an end-of-file card is encountered. With this feature, a large number of related runs can be made with one job submission.

Other than the requirement that all required data be specified before a RUN card is encountered and that auxiliary data immediately follow the control card that calls for them, the program control cards may be arranged in any order.

Great care should be taken in the preparation of input data since very few checks of data consistency and setting of default values are provided. A general feature of data preparation is that, if particular data on a card are not required, they need not be specified. If none of the data on a control card is needed, that card need not be included.

PART 2

APPLICATIONS AND ANALYSES

V. BAND MODEL PARAMETERS

Application of EMABIC for either transverse emission/absorption profile generation or inversion requires the specification of band model parameters for the active species of interest. The basic band model parameters used here for H_2O and CO_2 are those constructed by Young[23-25] explicitly for use in combustion gas problems in which a high degree of nonisothermality obtains. Briefly, the parameters were constructed by combining the high-temperature parameters from the NASA Handbook[18] with low-temperature parameters derived from the optical line data of the AFGL compilation.[26] The former parameters are quite adequate for temperatures above $\sim$1500 K but fail for some lower temperatures. The parameters derived from the AFGL compilation, on the other hand, are very good below $\sim$500 K, but fail at some higher temperatures because of the lack of hot-line data in the compilation. The combined parameters represent the state-of-the-art parameters for H_2O and CO_2 for application to the temperature range 200 to 3000 K.

The combined parameters $\bar{k}(T, \nu)$, $\bar{\delta}(T, \nu)$ for H_2O in the 2.7-μm region are tabulated in Ref. 23 and 24 for T = 100, 200, 300, 500, 750, 1000, 1500, 2000, 2500, 3000 K and ν = 2500 to 4500 cm^{-1} in steps of 25 cm^{-1}. The spectral resolution of the data is 25 cm^{-1}. The same parameters for CO_2 in the 4.3-μm region are tabulated in Ref. 25 for the same temperature array and for ν = 2000 to 2400 cm^{-1} in steps of 5 cm^{-1}. The spectral resolution is 5 cm^{-1}. For both species and both parameters, a linear extrapolation of $\log \bar{k}$ or $\log \bar{\delta}$ with T is used to obtain values at T > 3000 K.

The line width band model parameter for pressure (Lorentz) broadening is taken from the NASA handbook, but simplified to allow only a single foreign gas broadening component. The form is

$$\bar{\gamma}_L(\nu, c, p, T) = \gamma_0(\nu) p \left[\alpha_1 c \left(\frac{273}{T}\right) + c\sqrt{\frac{273}{T}} + \alpha_2 (1 - c)\sqrt{\frac{273}{T}}\right] \tag{142}$$

$\gamma_0(\nu)$ is the broadening parameter at standard temperature and pressure for non-resonant self-broadening. α_1 is the efficiency (relative to γ_0) for resonant self-broadening and α_2 is the efficiency for foreign gas broadening. These efficiency factors are assumed to be independent of ν and are $\alpha_1 = 6.53$, $\alpha_2 = 1.0$ for H_2O in the 2.7-μm region and $\alpha_1 = 0.111$ $\alpha_2 = 0.778$ for CO_2 in the 4.3-μm region. $\gamma_0(\nu)$ for the two species is tabulated in Ref. 23 for the same spectral grid and resolution as $\bar{k}$ and $\bar{\delta}$.

For velocity (Doppler) broadening,

$$\bar{\gamma}_D(\nu, T) = 3.56817 \times 10^{-7} \, \nu \sqrt{\frac{T}{\alpha_3}} \tag{143}$$

where ν is in cm^{-1}, T in °K, and α_3 is the molecular weight of the active species in a.m.u. For H_2O, $\alpha_3 = 18$ and for CO_2, $\alpha_3 = 44$.

For use in the present work, these parameters are convolved with an instrument filter function in order to obtain parameters appropriate to various simulation and measurement conditions. Let $f(\nu)$ be a general filter function that falls to zero at ν_1 and ν_2 ($\nu_1 < \nu_2$) and is normalized such that

$$\int_{\nu_1}^{\nu_2} f(\nu)\, d\nu = 1$$

Within the statistical band model formulation, the appropriate effective parameters for the bandpass $f(\nu)$ are defined by (see Appendix C)

$$\bar{k}(T) = \int_{\nu_1}^{\nu_2} f(\nu)\, \bar{k}(\nu, T)\, d\nu \tag{144}$$

$$\bar{Y}_0 = \int_{\nu_1}^{\nu_2} f(\nu)\, \bar{Y}_0(\nu)\, d\nu \tag{145}$$

$$\frac{1}{\bar{\delta}(T)} = \frac{1}{\bar{k}(T)\bar{Y}_0} \left[\int_{\nu_1}^{\nu_2} f(\nu) \sqrt{\frac{k(\nu, T)\, \bar{Y}_0(\nu)}{\bar{\delta}(\nu, T)}} \right]^2 \tag{146}$$

The effective Doppler width is obtained from (143) with ν replaced by $\bar{\nu}$ where

$$\bar{\nu} = \int_{\nu_1}^{\nu_2} \nu\, f(\nu)\, d\nu \tag{147}$$

Three H_2O and two CO_2 filter bandpasses are used in the current work. Two of the H_2O bandpasses are the actual filters used in the NERD emission/absorption measurements program and are illustrated in Fig. 8. $f(\nu)$ is obtained by properly normalizing these filter transmittance curves. The third H_2O filter is used for simulation work and is a simple rectangular function of width $\Delta\nu = 25\ cm^{-1}$ centered on $\nu = 4000\ cm^{-1}$. The CO_2 filter used in the NERD measurements program is shown in Fig. 9. A second CO_2 bandpass used in simulation calculations is rectangular with width $\Delta\nu = 25\ cm^{-1}$ and centered on $\nu = 2272.7\ cm^{-1}$.

The effective band model parameters $\bar{k}$ and $\bar{\delta}$ obtained from (144)-(146) for the three H_2O filters are shown in Figs. 10 and 11. The effective parameters for the two CO_2 filters are shown in Figs. 12 and 13. The $\bar{Y}_0$ and $\bar{\nu}$ parameters for the five filters are tabulated in Table 3.

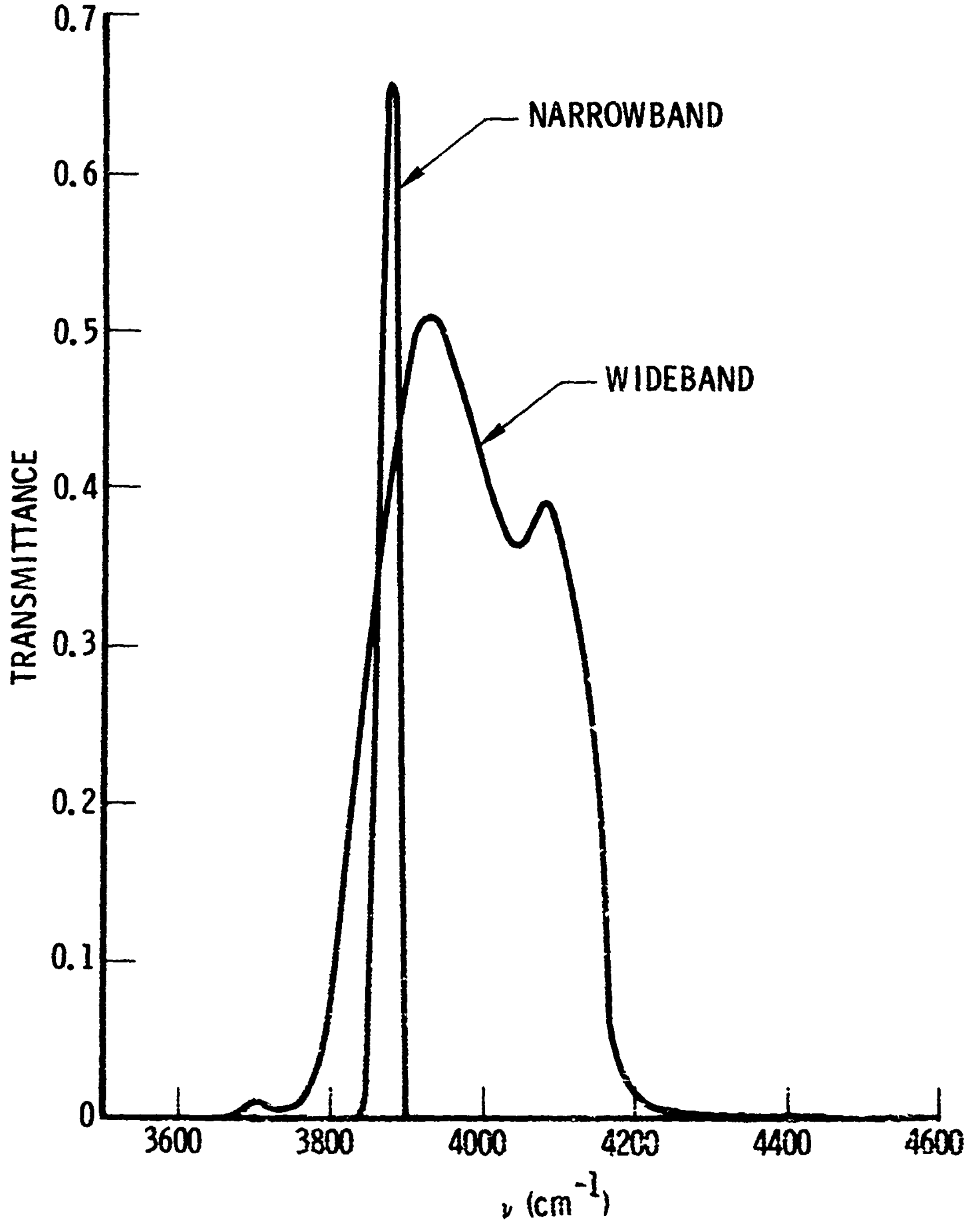

Fig. 8. NERD H_2O Bandpass Filter Transmittance Curves

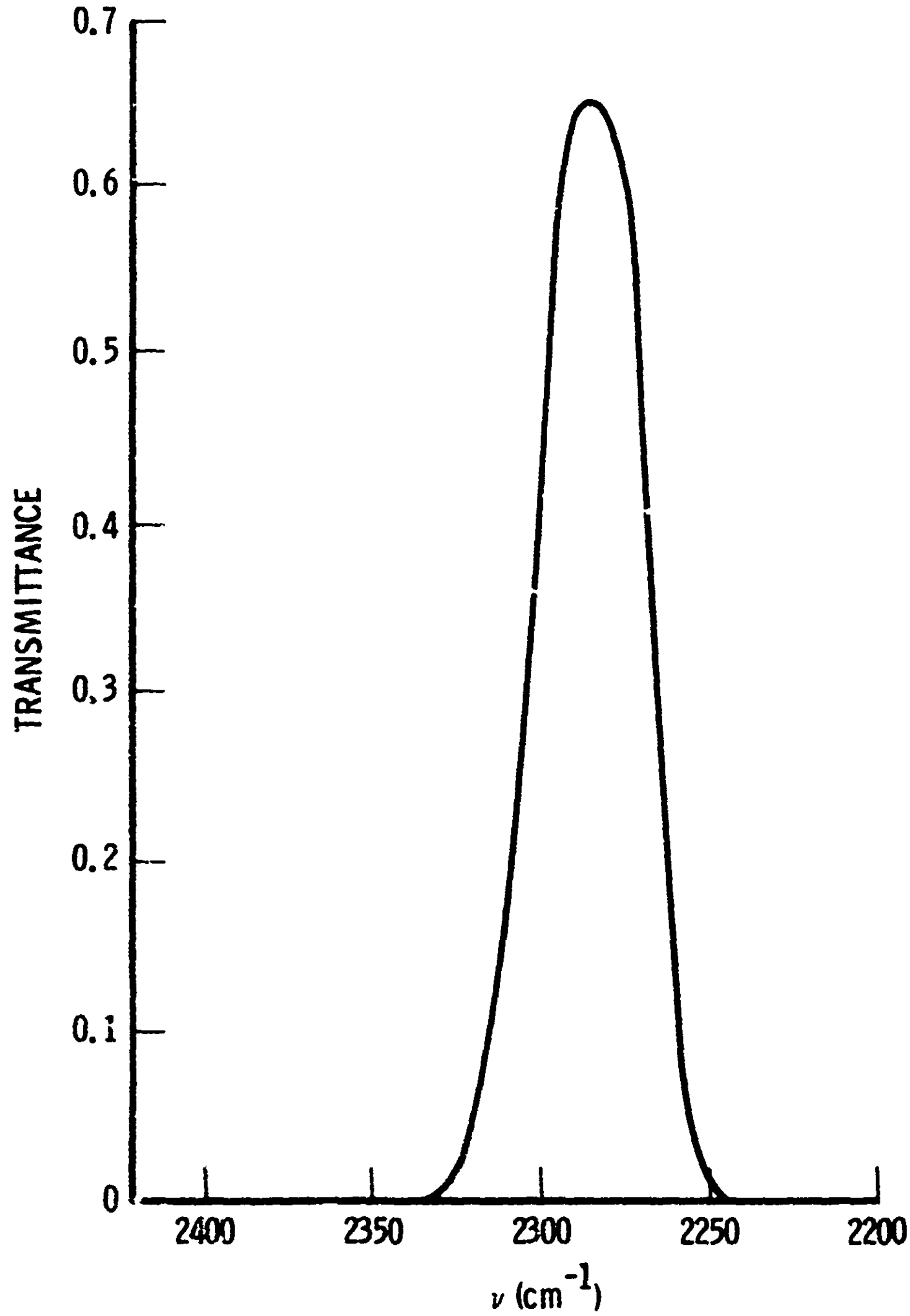

Fig. 9. NERD CO_2 Bandpass Filter Transmittance Curve

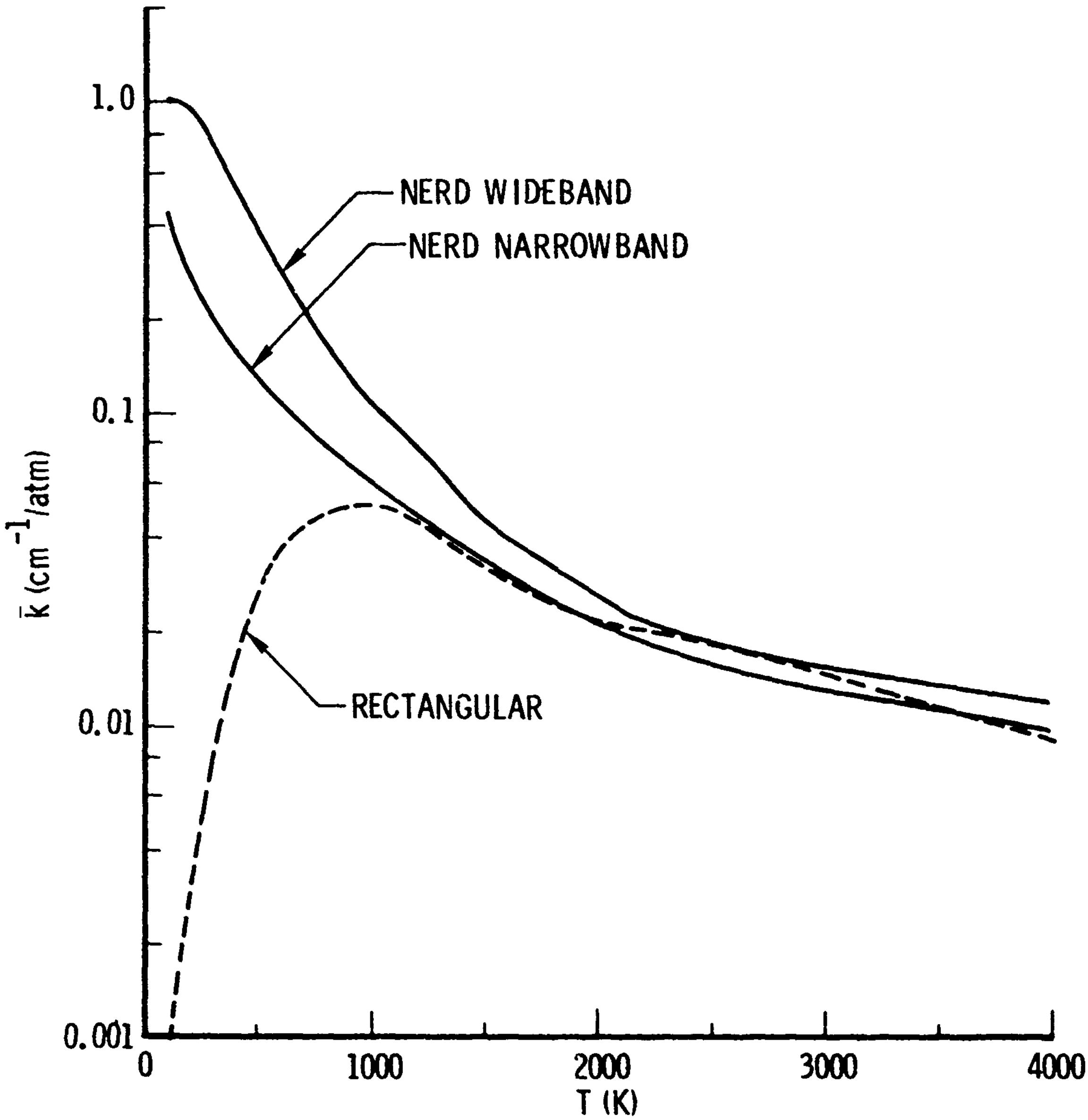

Fig. 10. Absorption Band Model Parameter $\bar{k}$ for H_2O Bandpasses

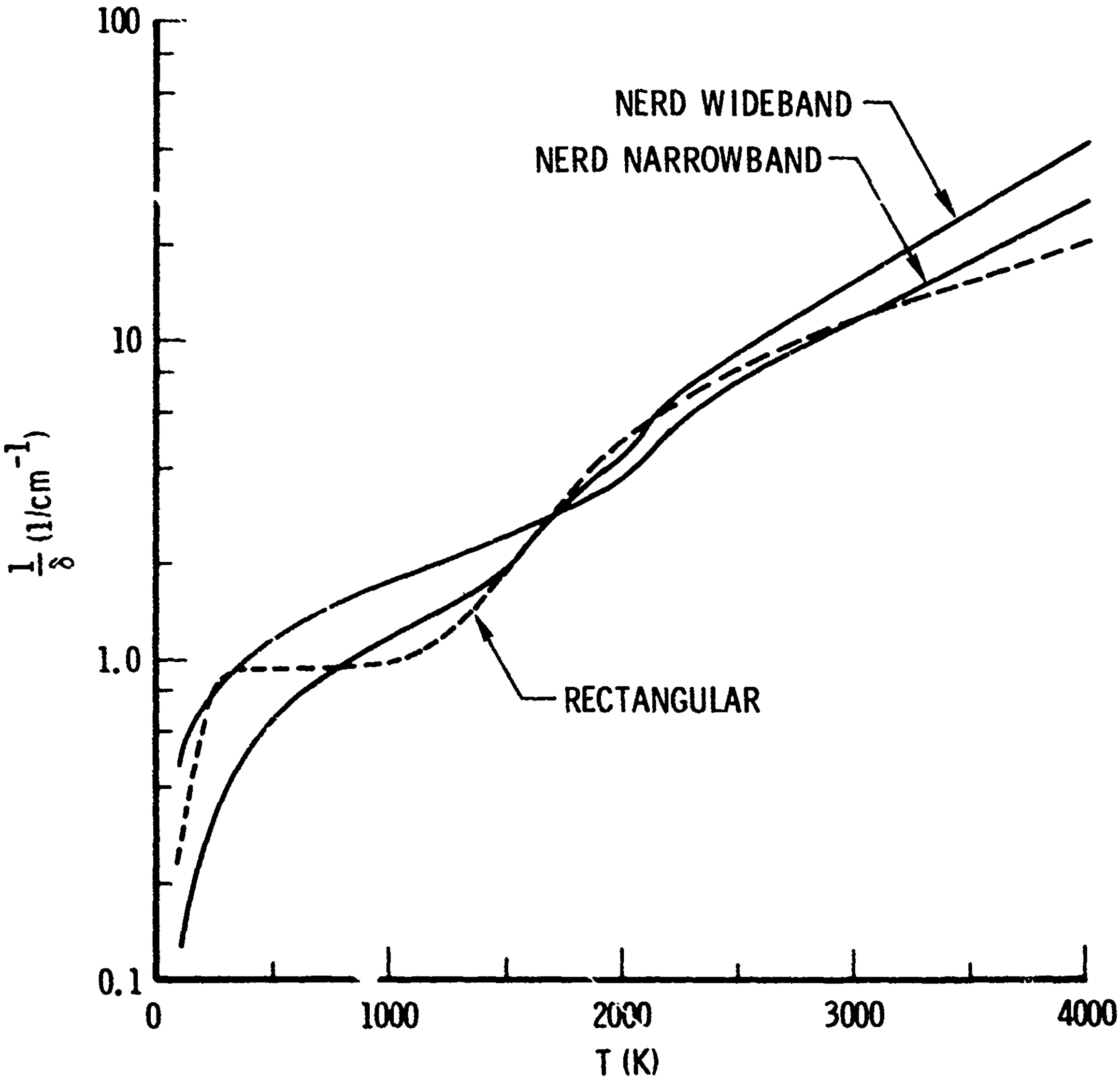

Fig. 11. Line Density Band Model Parameter $1/\bar{\delta}$ for H_2O Bandpasses

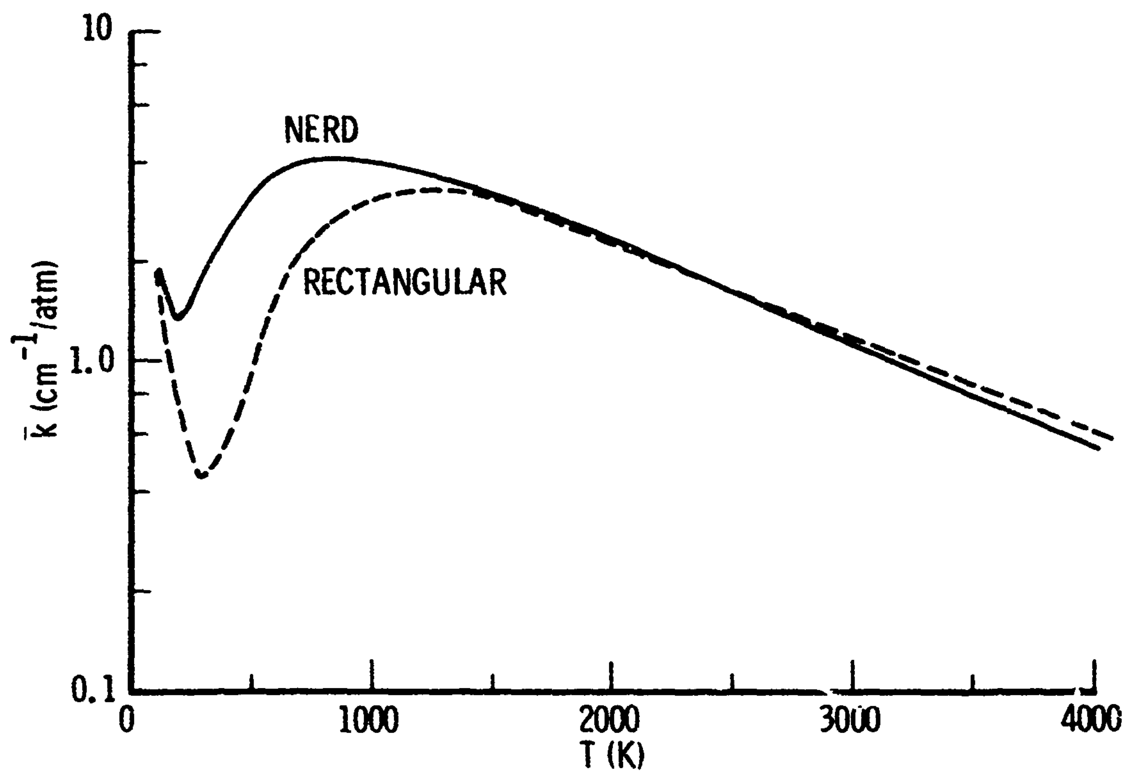

Fig. 12. Absorption Band Model Parameter $\bar{k}$ for CO_2 Bandpasses

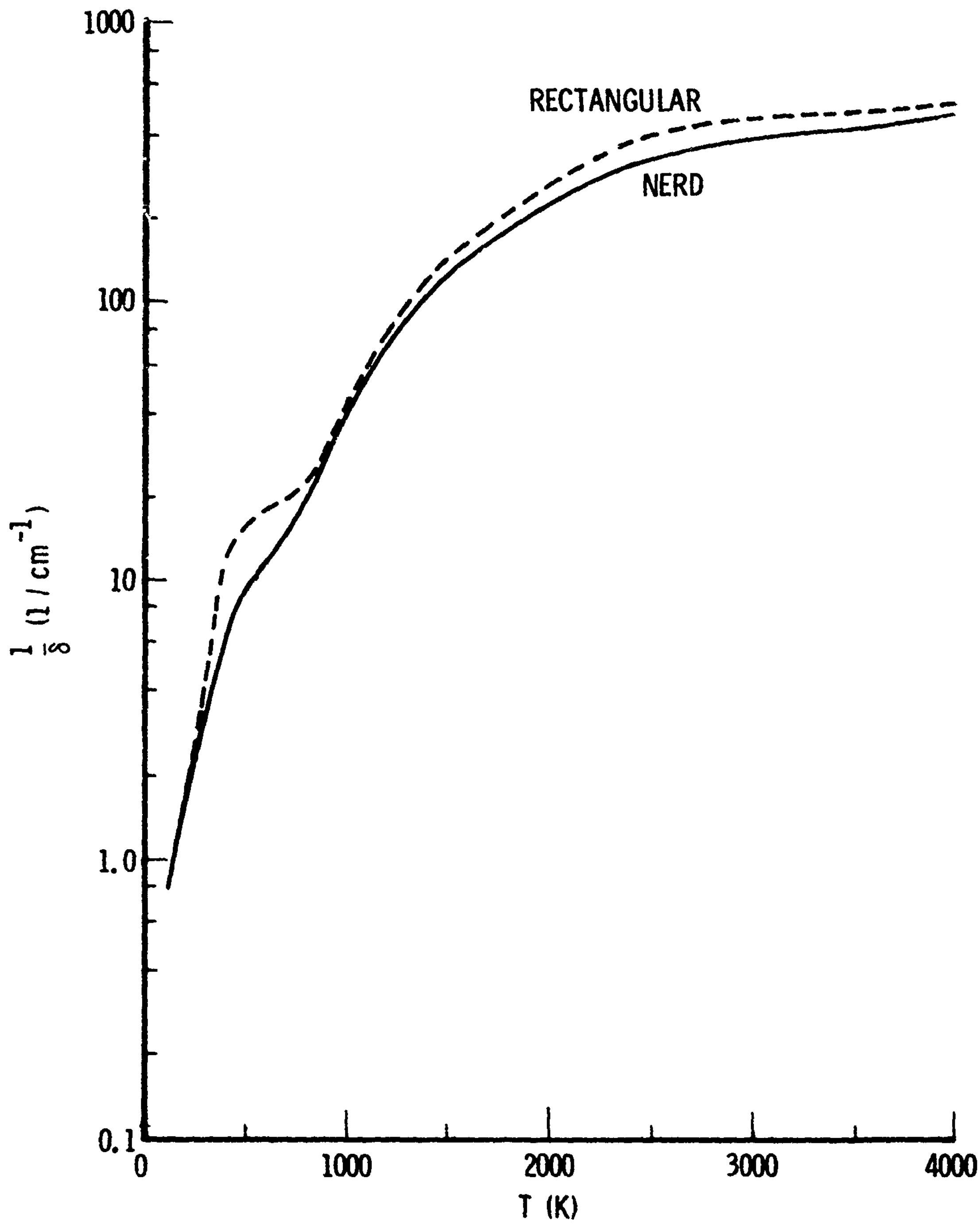

Fig. 13. Line Density Band Model Parameter $1/\bar{\delta}$ for CO_2 Bandpasses

Table 3. Pressure and Doppler Line Broadening Parameters for the H_2O and CO_2 Filter Bandpasses

Filter Bandpass	$\bar{\gamma}_0$ (cm^{-1}/atm)	$\bar{\nu}$ (cm^{-1})
NERD H_2O Narrowband	0.0739	3865.5
NERD H_2O Wideband	0.0739	3985.0
H_2O Rectangular	0.0674	4000.0
NERD CO_2	0.0958	2282.5
CO_2 Rectangular	0.0941	2272.7

VI. EMISSION/ABSORPTION PROFILE PREDICTIONS

Program EMABIC was used to generate transverse radiance and absorptance profiles for twelve engine test cases. These cases were chosen to represent a wide range of engine conditions (e.g., thrust, pressure, nozzle contour). For all cases, the radial profiles of pressure, temperature, and concentration (pTc profiles) at the nozzle exit plane were obtained with standard combustion/nozzle codes.* The engine designations, type of exit-plane calculation, and case numbering are listed in Table 4. For the first seven cases (the 1-dimensional, constant oxidizer-to-fuel ratio calculation cases), the source conditions are uniform across the exit plane. These source conditions are tabulated in Table 5. The last five cases represent nozzle exit planes with varying degrees of nonuniform source conditions. The pTc profiles for these cases are shown in Figs. 14-18.

Transverse profiles were generated for both H_2O at 2.5-μm and CO_2 at 4.4-μm with the parameters for the 25 cm^{-1} wide rectangular filter bandpasses discussed in Section V. Calculations were performed for both the Lorentz and Voigt lineshapes and (for the nonuniform source cases) for both the CG and DR nonuniformity approximations. Voigt lineshape calculations were performed with the RW approximation. A spatial resolution corresponding to N = 50 zones was used in all cases. The results for the transverse radiance and absorptance profiles are presented in Figs. 19-30.

For two of the test cases (Cases 3 and 11), profiles were generated with the modified NASA Voigt line model also. A comparison of the results obtained for the two models is shown in Figs. 31 and 32. The difference between the models amounts to only ~10% in radiance and absorptance.

The primary reason for the generation of these profiles was to obtain a familiarity with the magnitudes and shapes of profiles that are likely to occur in test measurements on typical engines. Some of the significant features will be pointed out in latter sections where inversions of a limited

---

*These profiles were provided by J.D. Stewart, AFRPL.

Table 4. Engine Test Cases for Emission/Absorption Profile Predictions

Engine Designation	1-D Constant O/F	2-D Constant O/F	2-D Variable O/F
	CASE	CASE	CASE
Titan II/Stage 1	1		
Titan IIIC/Stage 2	2	8	10
Transtage Baseline	3		11
ERASE 1,000 lb (6:1 Cone)	4		
ERASE 500 lb (25:1 Cone)	5		
ERASE 500 lb (25:1 Bell)	6	9	12
300 lb MM Bus	7		

Table 5. Source Conditions for Cases 1-7

Case	Engine Description	Nozzle Radius R (cm)	T (K)	p (atm)	c_{H_2O} (mole fraction)	c_{CO_2} (mole fraction)
1	Titan II/Stage 1	54.53	1883	0.937	0.458	0.0819
2	Titan IIIC/Stage 2	81.15	1027	0.0449	0.417	0.0675
3	Transtage Baseline	60.10	1079	0.0133	0.419	0.0793
4	ERASE 1,000 lb (6:1 Cone)	4.178	1728	0.790	0.373	0.0597
5	ERASE 500 lb (25:1 Cone)	5.779	1124	0.1091	0.368	0.0578
6	ERASE 500 lb (25:1 Bell)	5.779	1044	0.0813	0.369	0.0563
7	300 lb MM Bus	4.023	891	0.0195	0.330	0.0413

set of these profiles will be made in order to determine how closely the known "true" radial profiles can be retrieved.

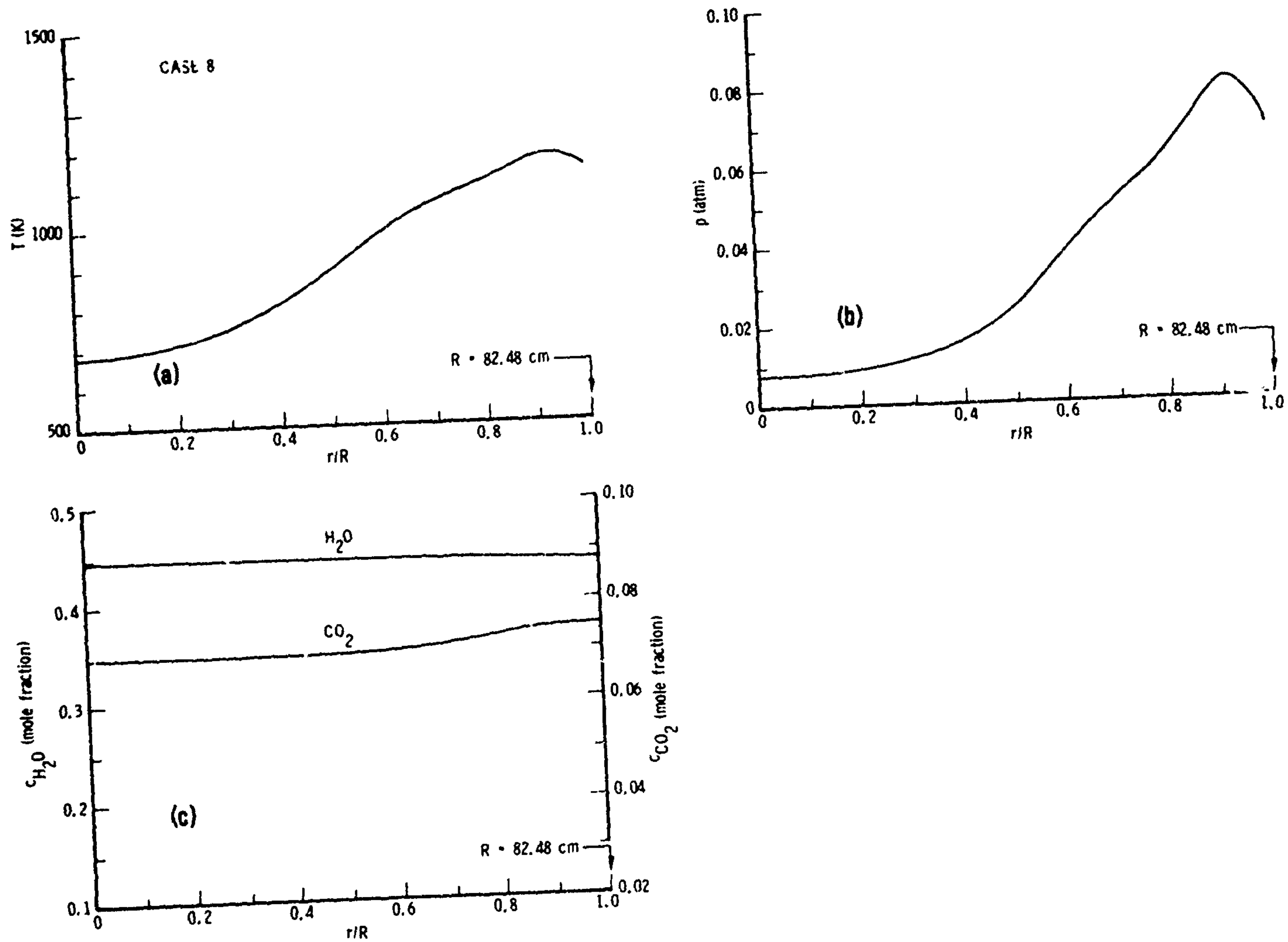

Fig. 14. Radial Profiles for Engine Case ?. (a) Temperature; (b) Pressure; (c) H_2O and CO_2 concentrations.

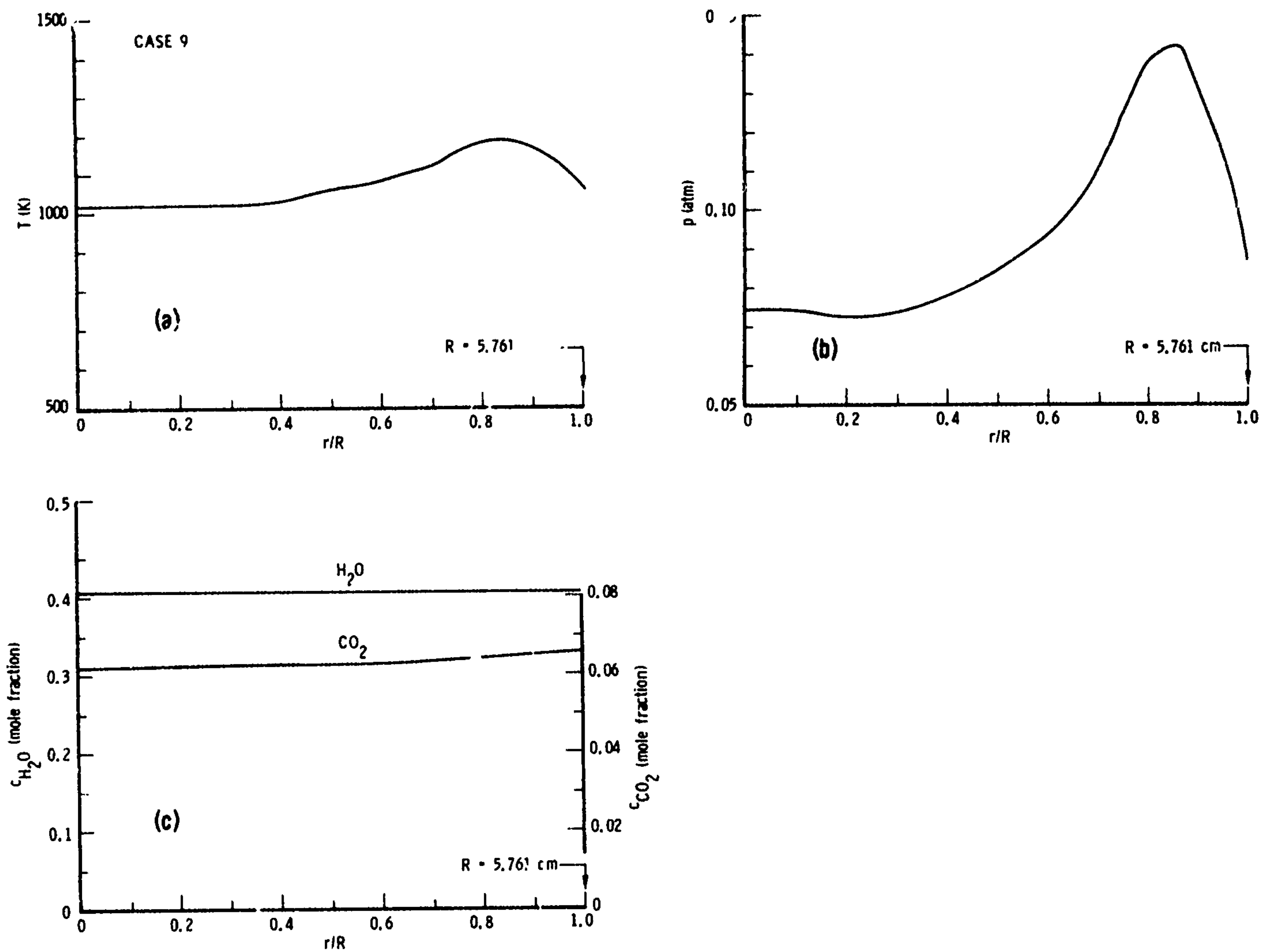

Fig. 15. Radial Profiles for Engine Case 9. (a) Temperature; (b) Pressure; (c) H_2O and CO_2 concentrations.

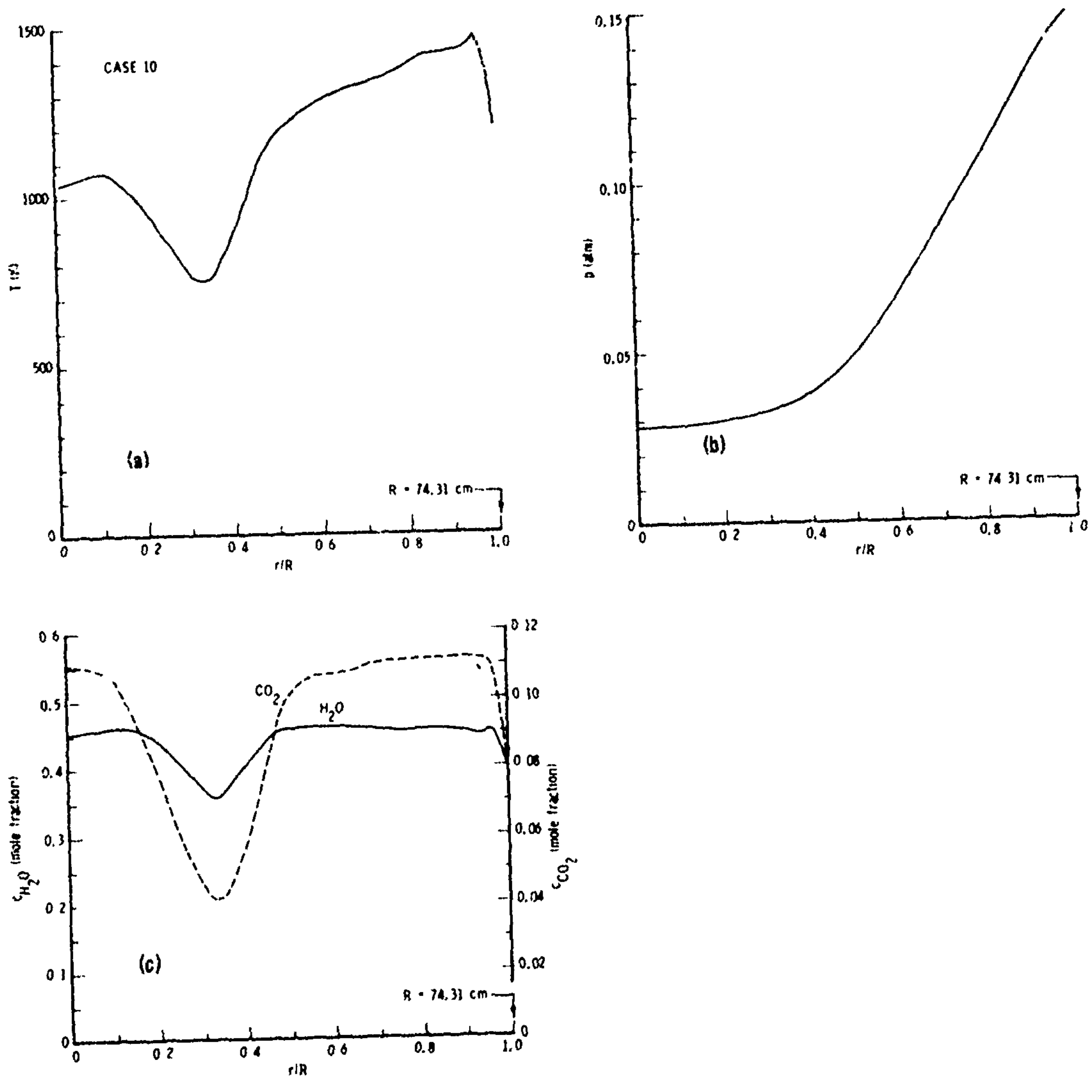

Fig. 16. Radial Profiles for Engine Case 10. (a) Temperature; (b) Pressure; (c) H_2O and CO_2 concentrations.

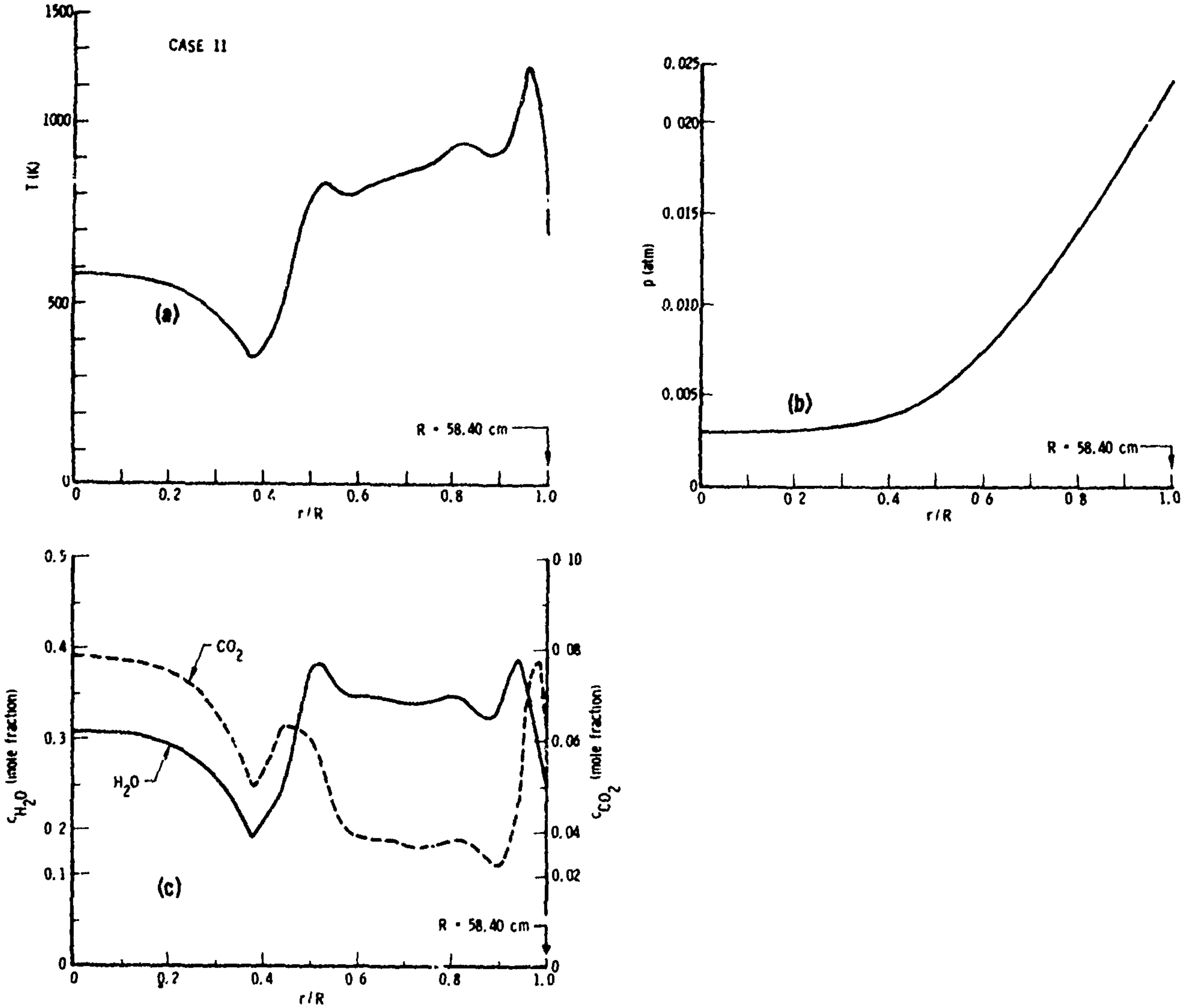

Fig. 17. Radial Profiles for Engine Case 11. (a) Temperature; (b) Pressure; (c) H_2O and CO_2 concentrations.

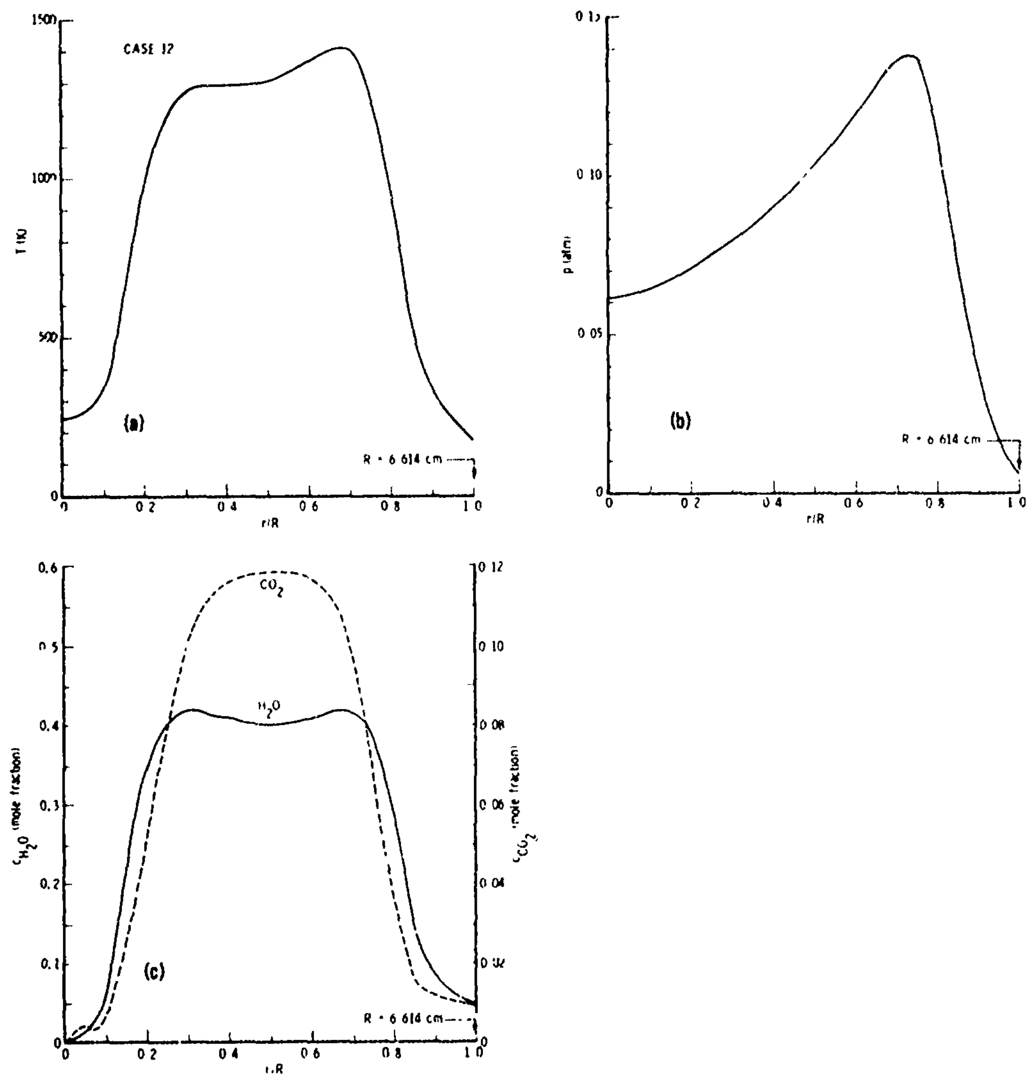

Fig. 18. Radial Profiles for Engine Case 12. (a) Temperature; (b) Pressure; (c) H_2O and CO_2 concentrations.

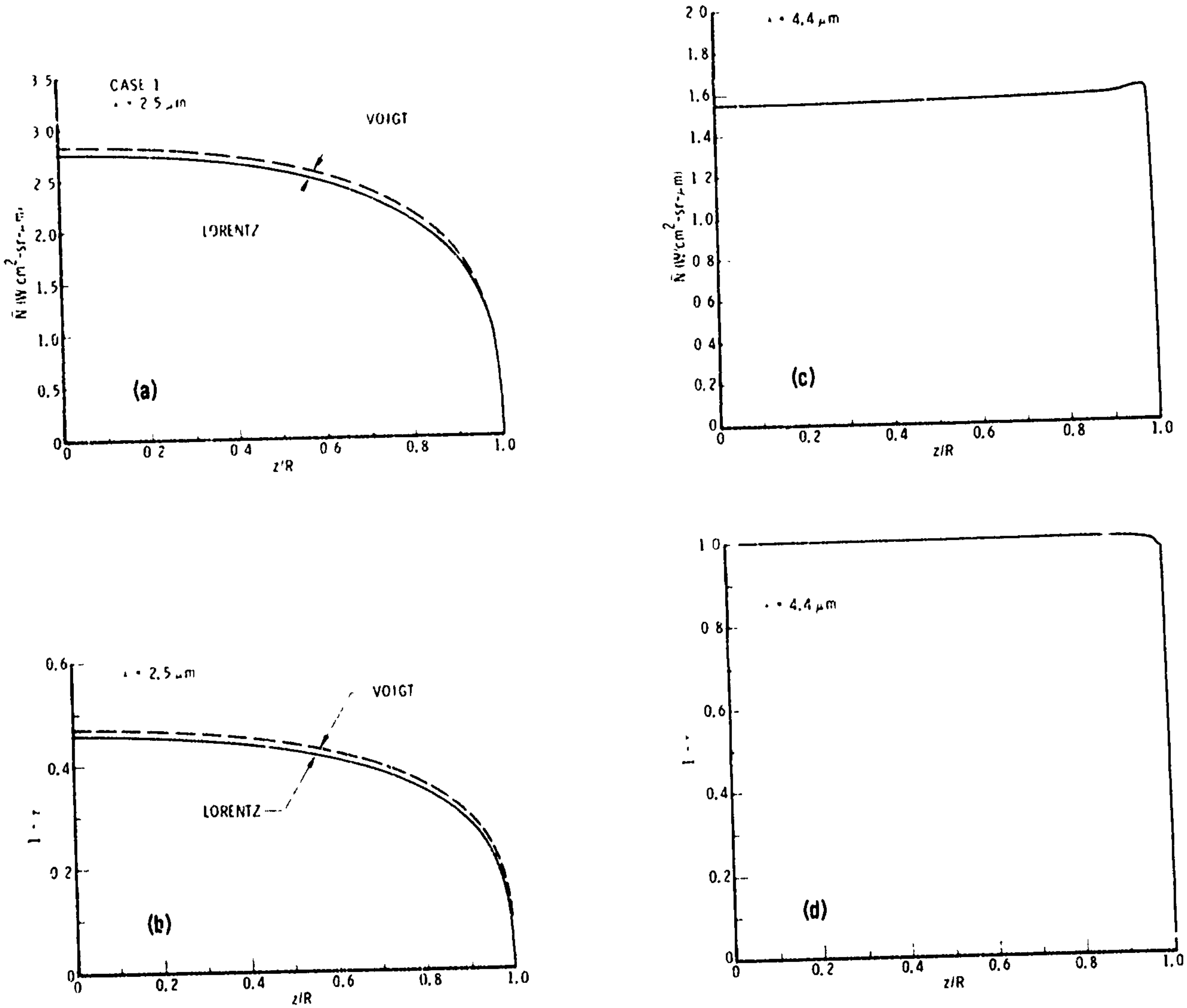

Fig. 19. Transverse Profiles for Engine Case 1. (a) H_2O Radiance; (b) H_2O Absorptance; (c) CO_2 Radiance; (d) CO_2 absorptance.

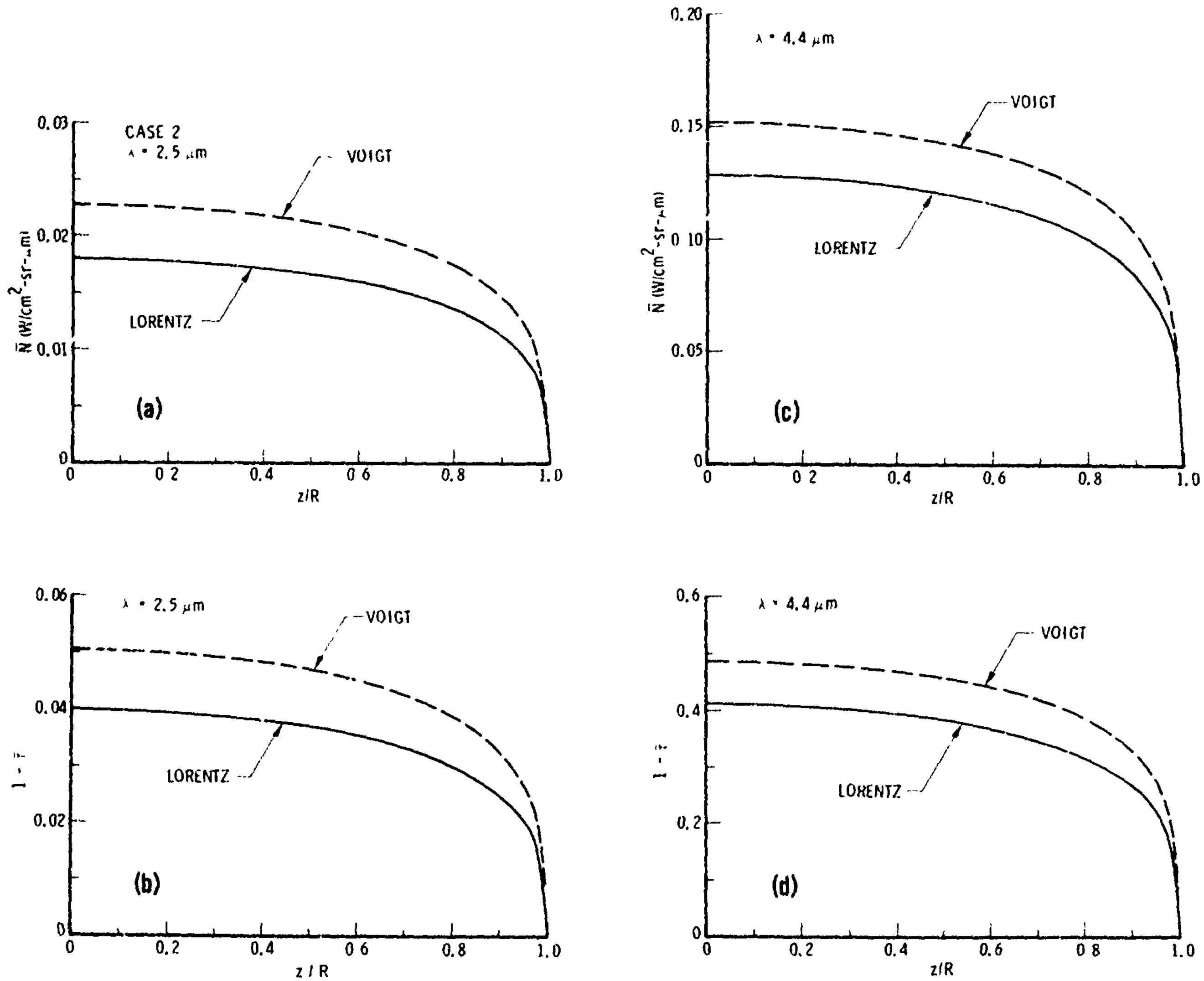

Fig. 20. Transverse Profiles for Engine Case 2. (a) H_2O Radiance; (b) H_2O Absorptance; (c) CO_2 Radiance; (d) CO_2 absorptance.

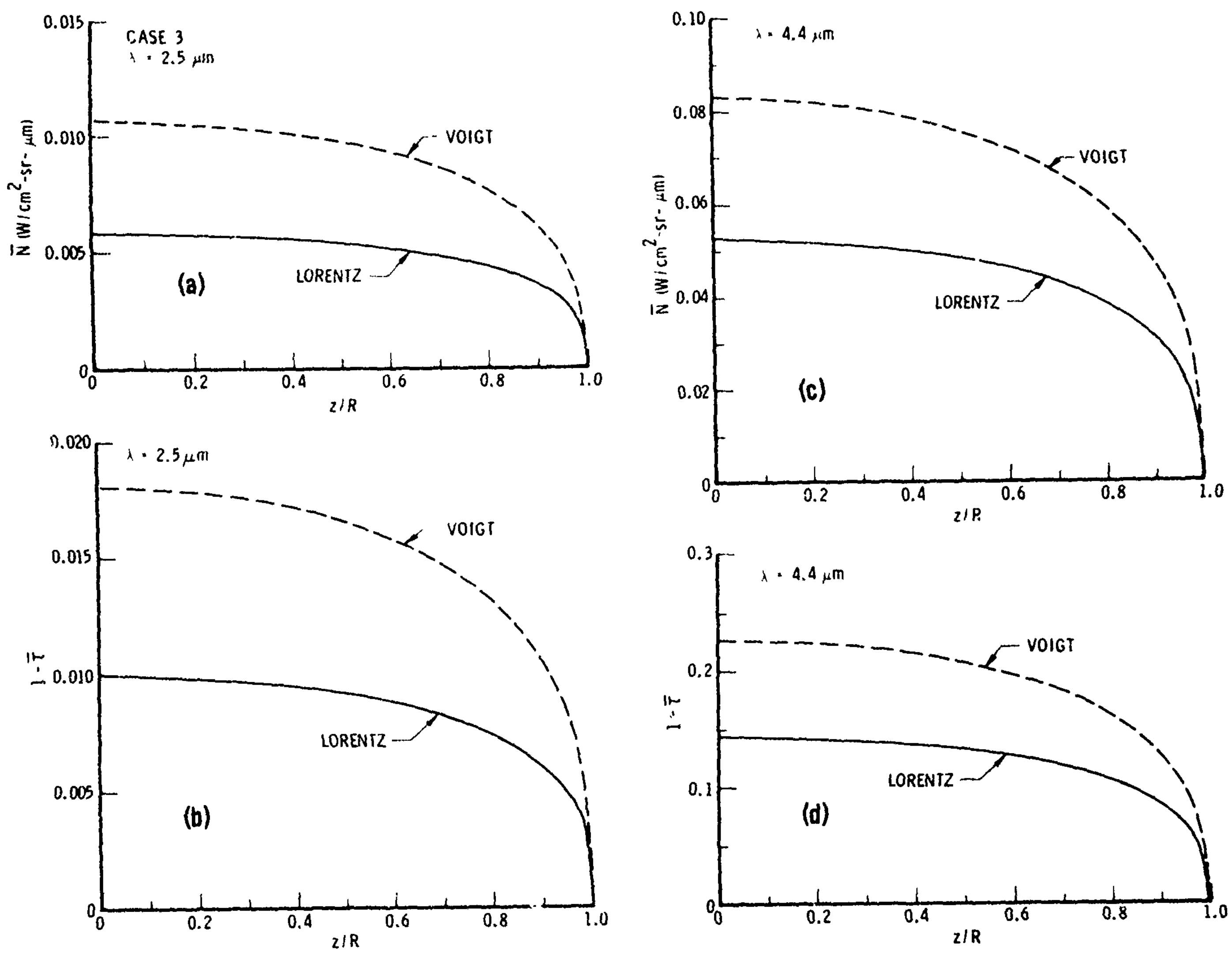

Fig. 21. Transverse Profiles for Engine Case 3. (a) H_2O Radiance; (b) H_2O Absorptance; (c) CO_2 Radiance; (d) CO_2 absorptance.

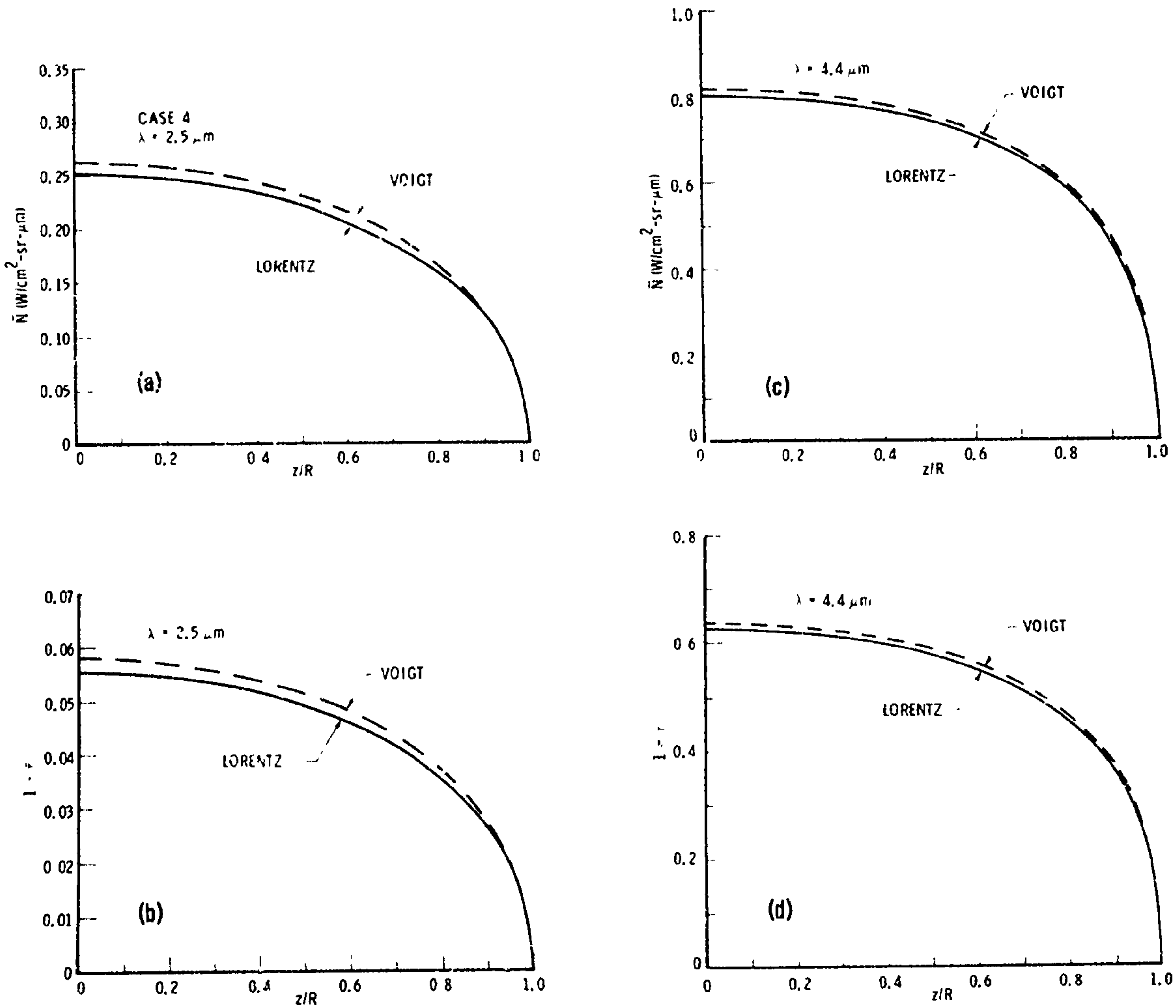

Fig. 22. Transverse Profiles for Engine Case 4. (a) H_2O Radiance; (b) H_2O Absorptance; (c) CO_2 Radiance; (d) CO_2 absorptance.

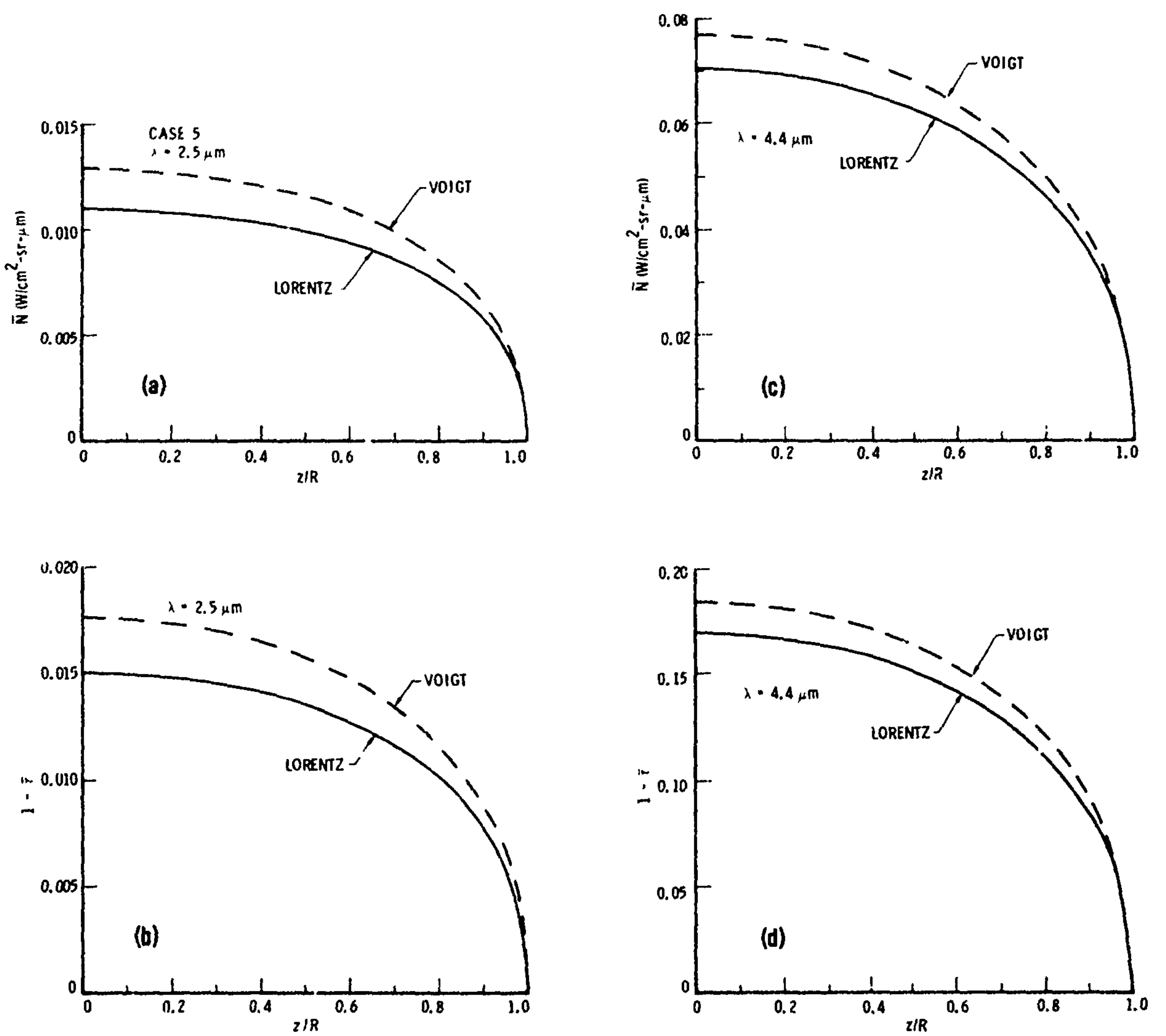

Fig. 23. Transverse Profiles for Engine Case 5. (a) H_2O Radiance; (b) H_2O Absorptance; (c) CO_2 Radiance; (d) CO_2 absorptance.

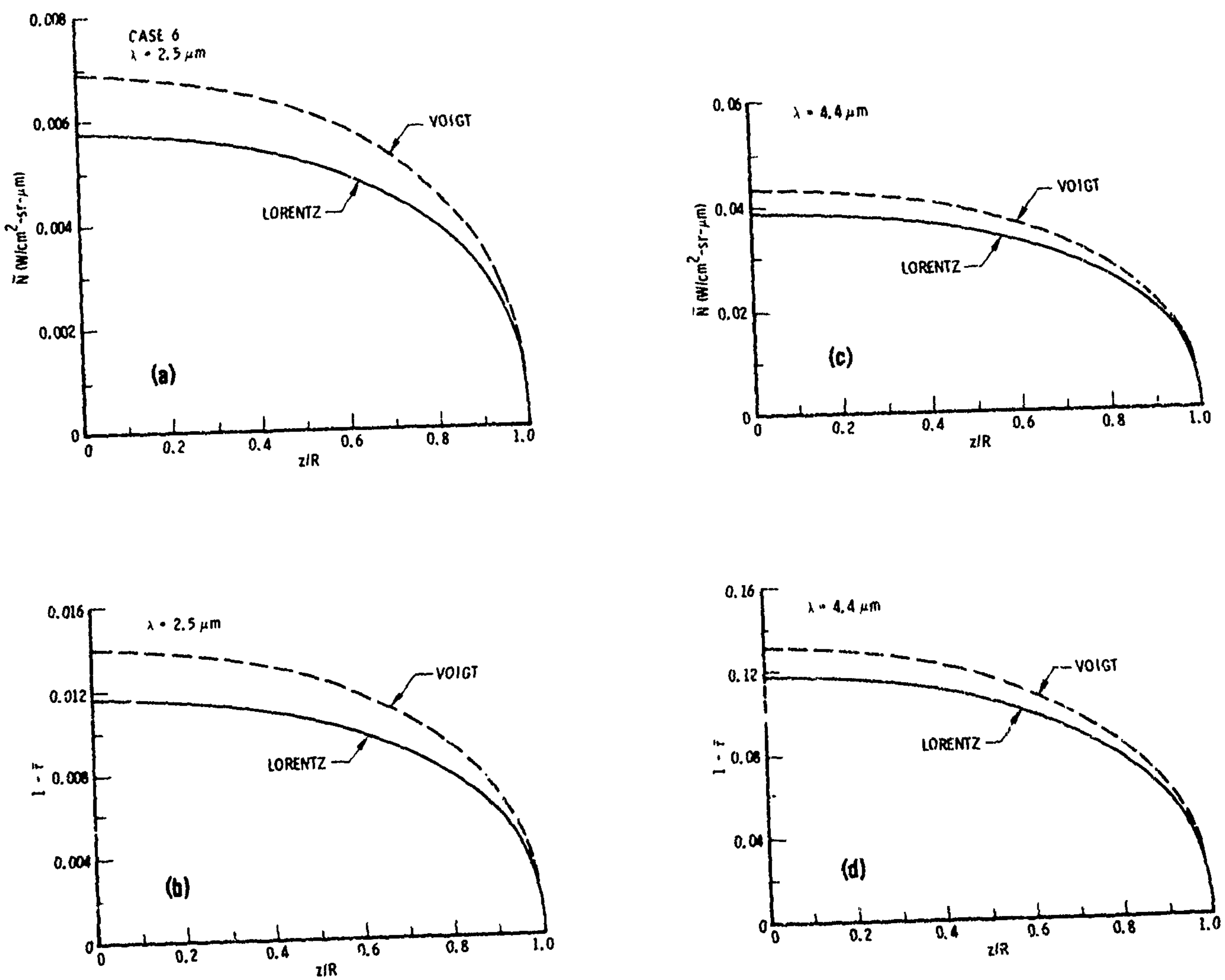

Fig. 24. Transverse Profiles for Engine Case 6. (a) H_2O Radiance; (b) H_2O Absorptance; (c) CO_2 Radiance; (d) CO_2 absorptance.

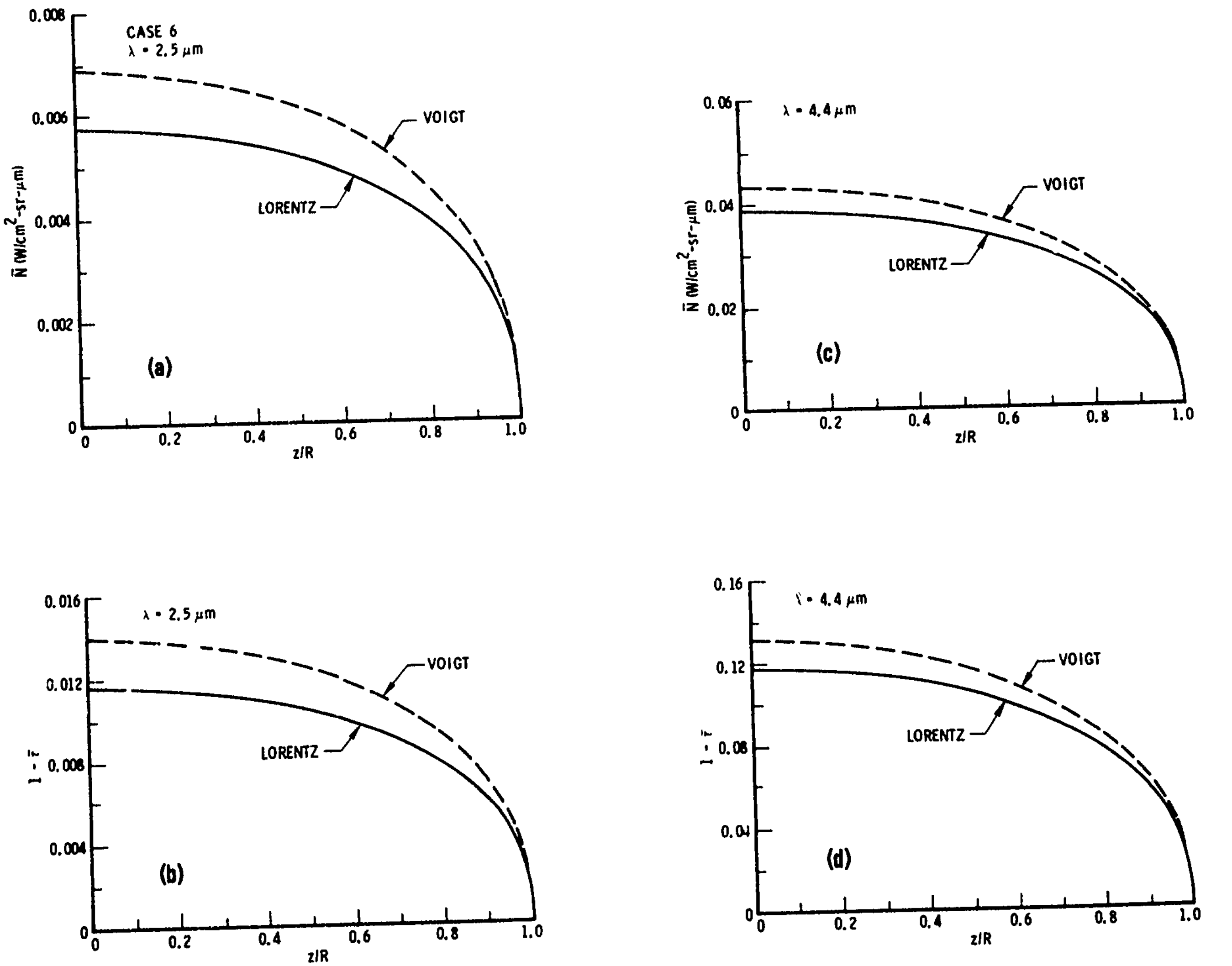

Fig. 24. Transverse Profiles for Engine Case 6. (a) H_2O Radiance; (b) H_2O Absorptance; (c) CO_2 Radiance; (d) CO_2 absorptance.

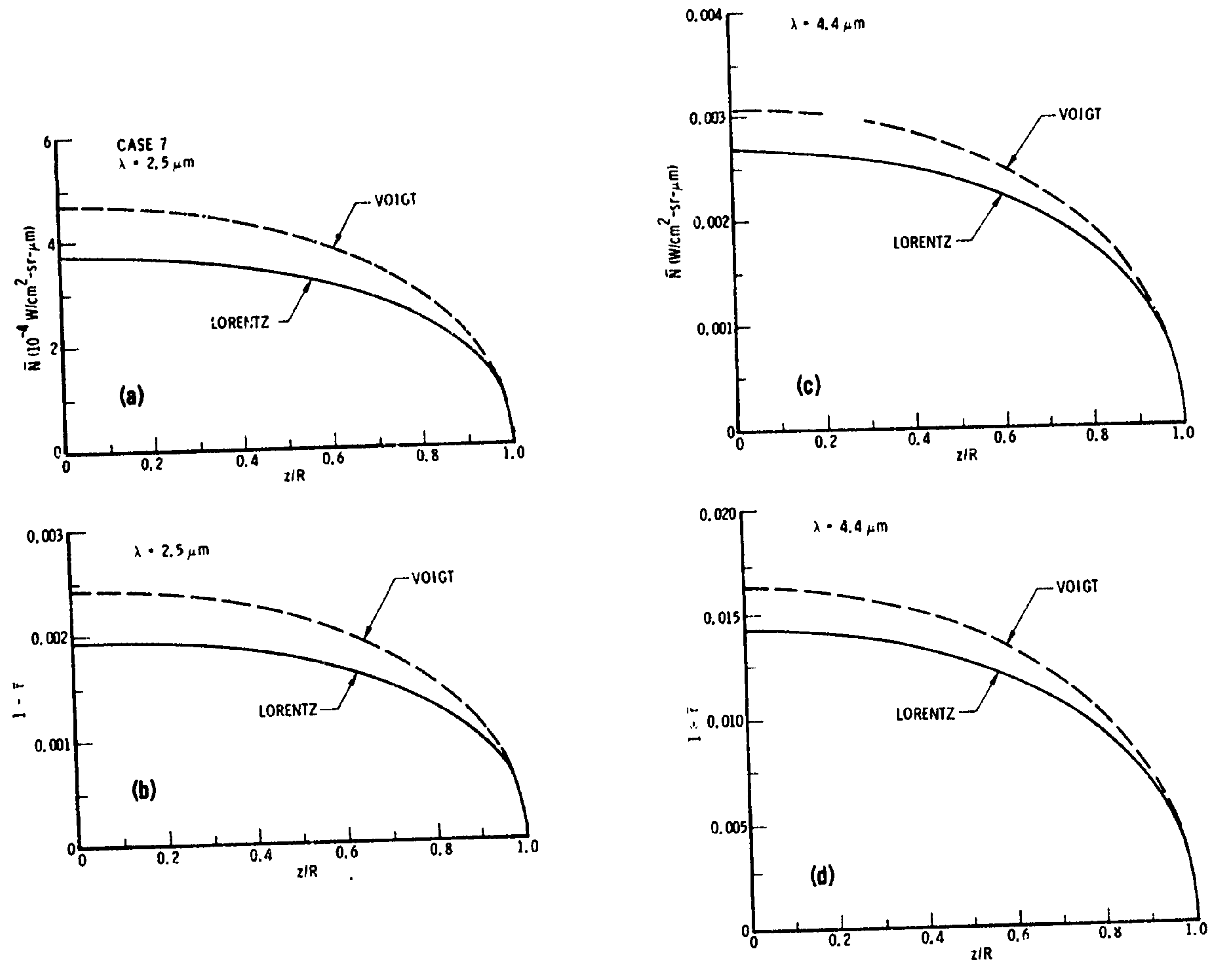

Fig. 25. Transverse Profiles for Engine Case 7. (a) H_2O Radiance; (b) H_2O Absorptance; (c) CO_2 Radiance; (d) CO_2 absorptance.

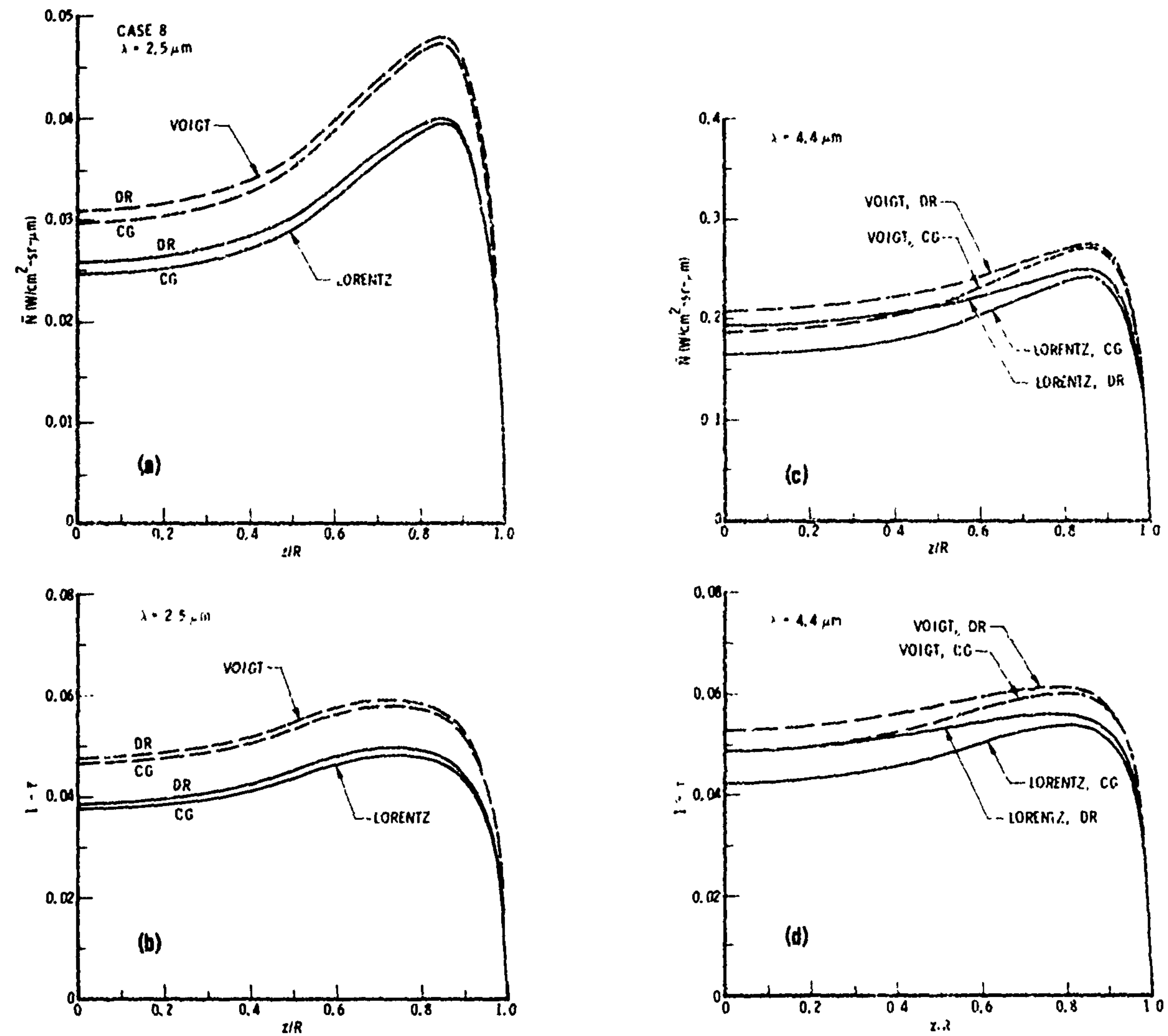

Fig. 26. Transverse Profiles for Engine Case 8. (a) H_2O Radiance; (b) H_2O Absorptance; (c) CO_2 Radiance; (d) CO_2 absorptance.

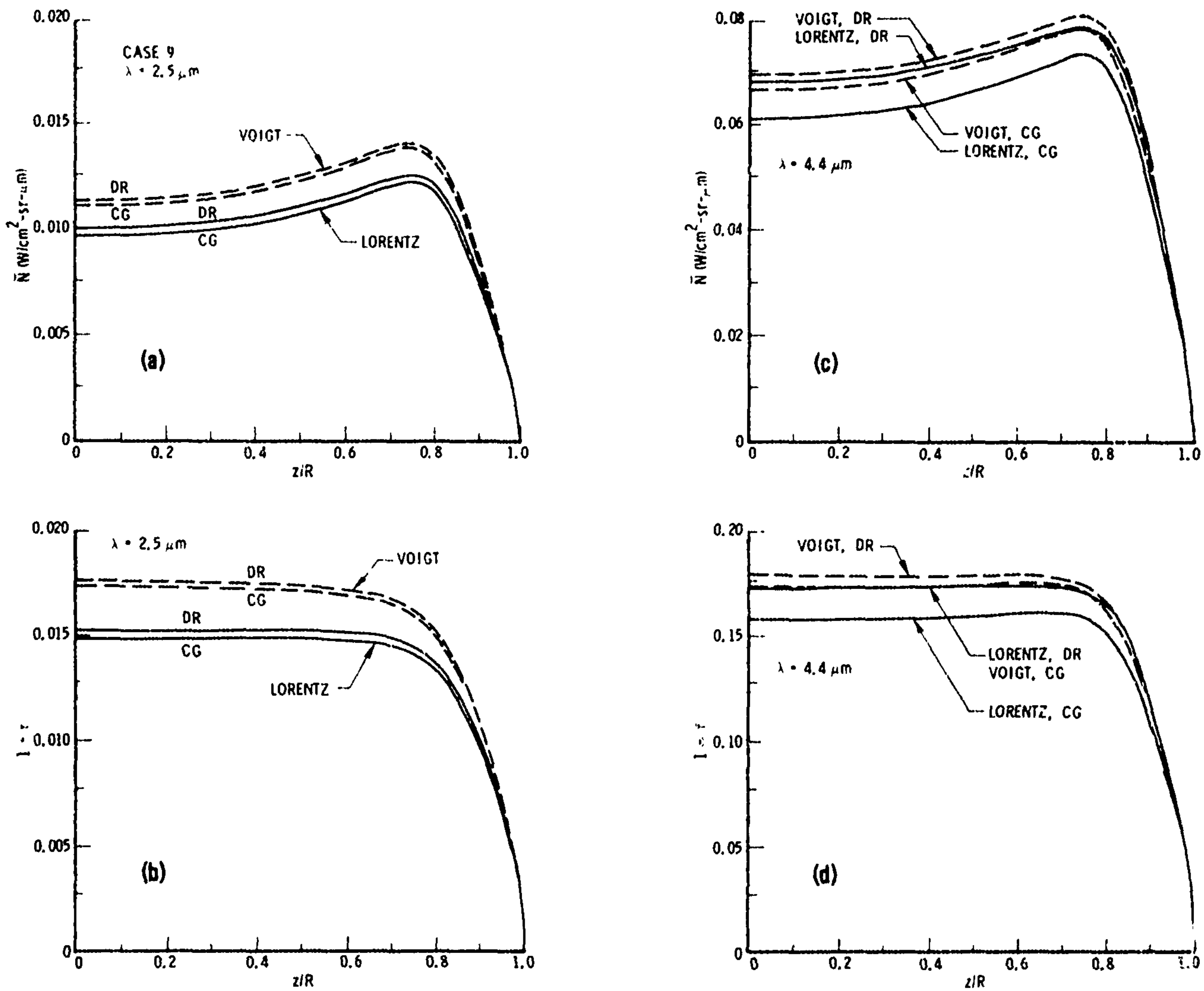

Fig. 27. Transverse Profiles for Engine Case 9. (a) H_2O Radiance; (b) H_2O Absorptance; (c) CO_2 Radiance; (d) CO_2 absorptance.

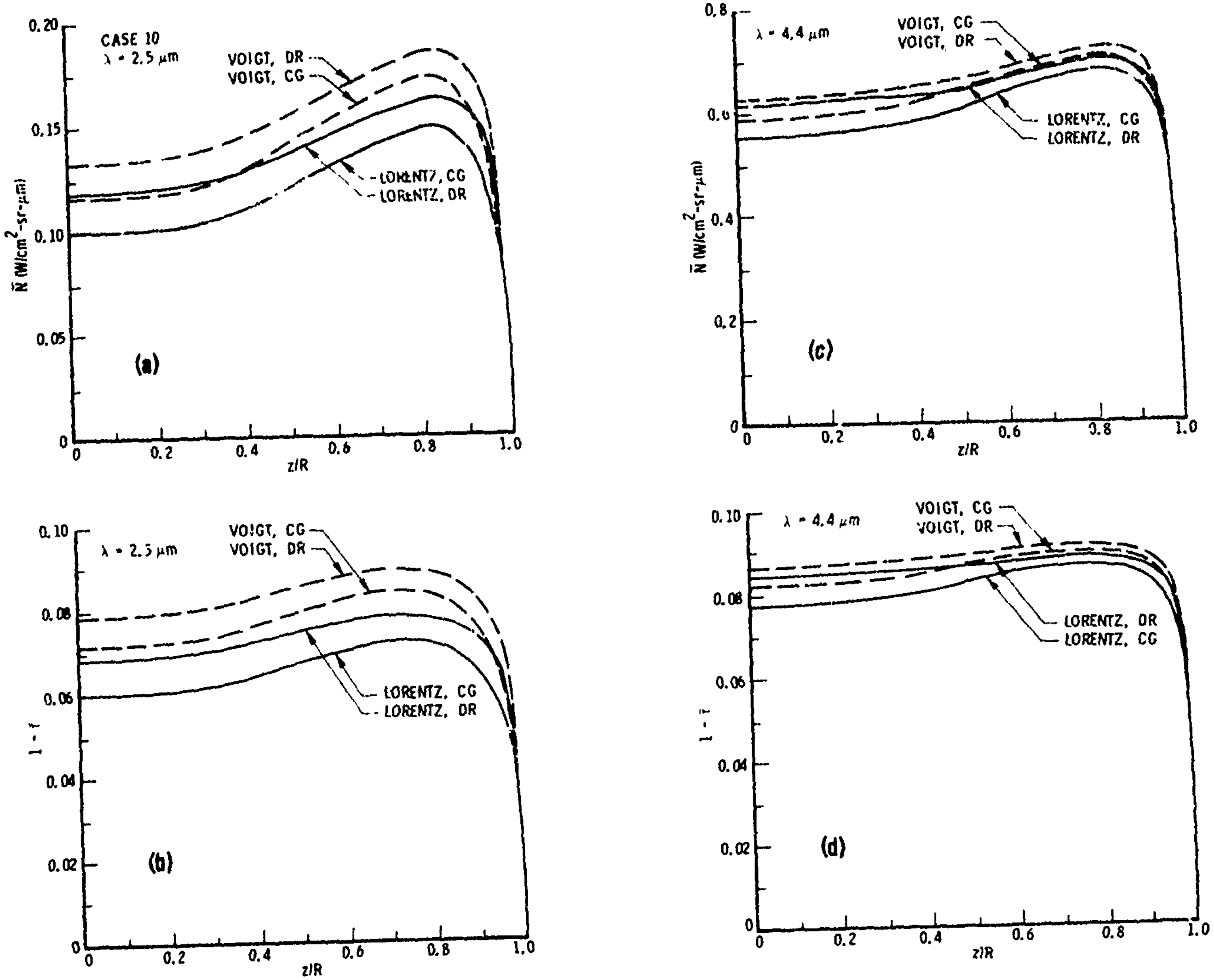

Fig. 28. Transverse Profiles for Engine Case 10. (a) H_2O Radiance; (b) H_2O Absorptance; (c) CO_2 Radiance; (d) CO_2 absorptance.

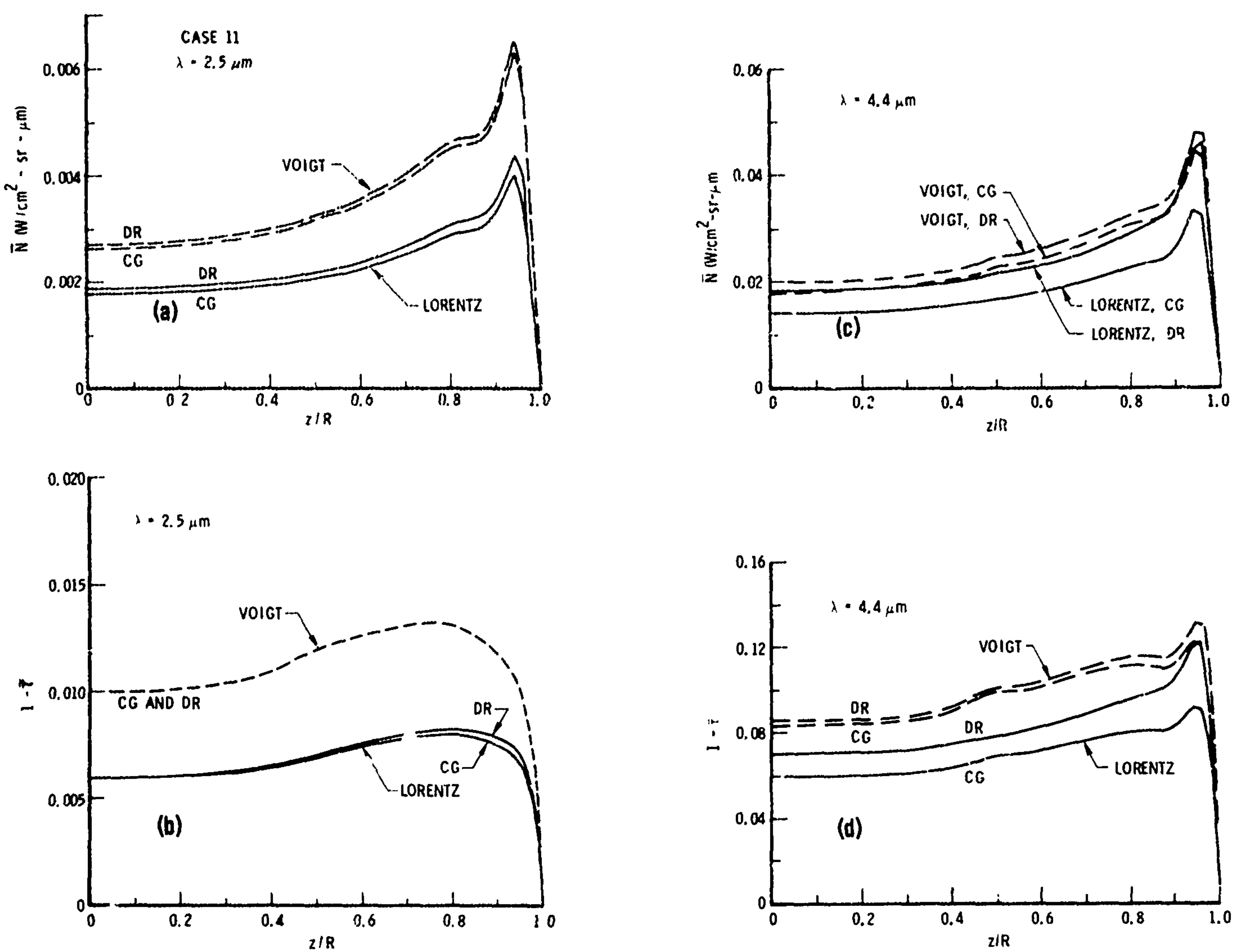

Fig. 29. Transverse Profiles for Engine Case 11. (a) H_2O Radiance; (b) H_2O Absorptance; (c) CO_2 Radiance; (d) CO_2 absorptance.

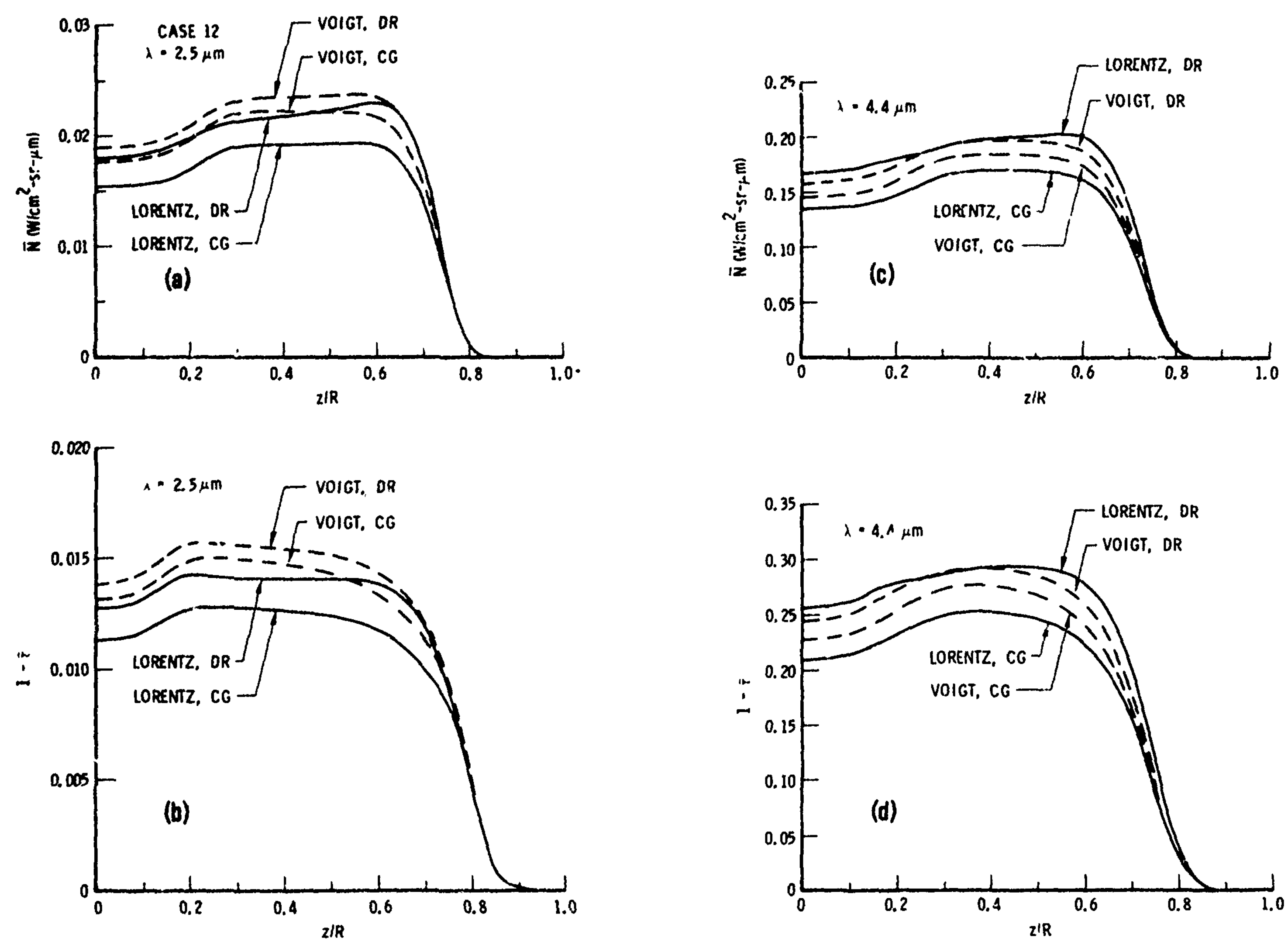

Fig. 30. Transverse Profiles for Engine Case 12. (a) H_2O Radiance; (b) H_2O Absorptance; (c) CO_2 Radiance; (d) CO_2 absorptance.

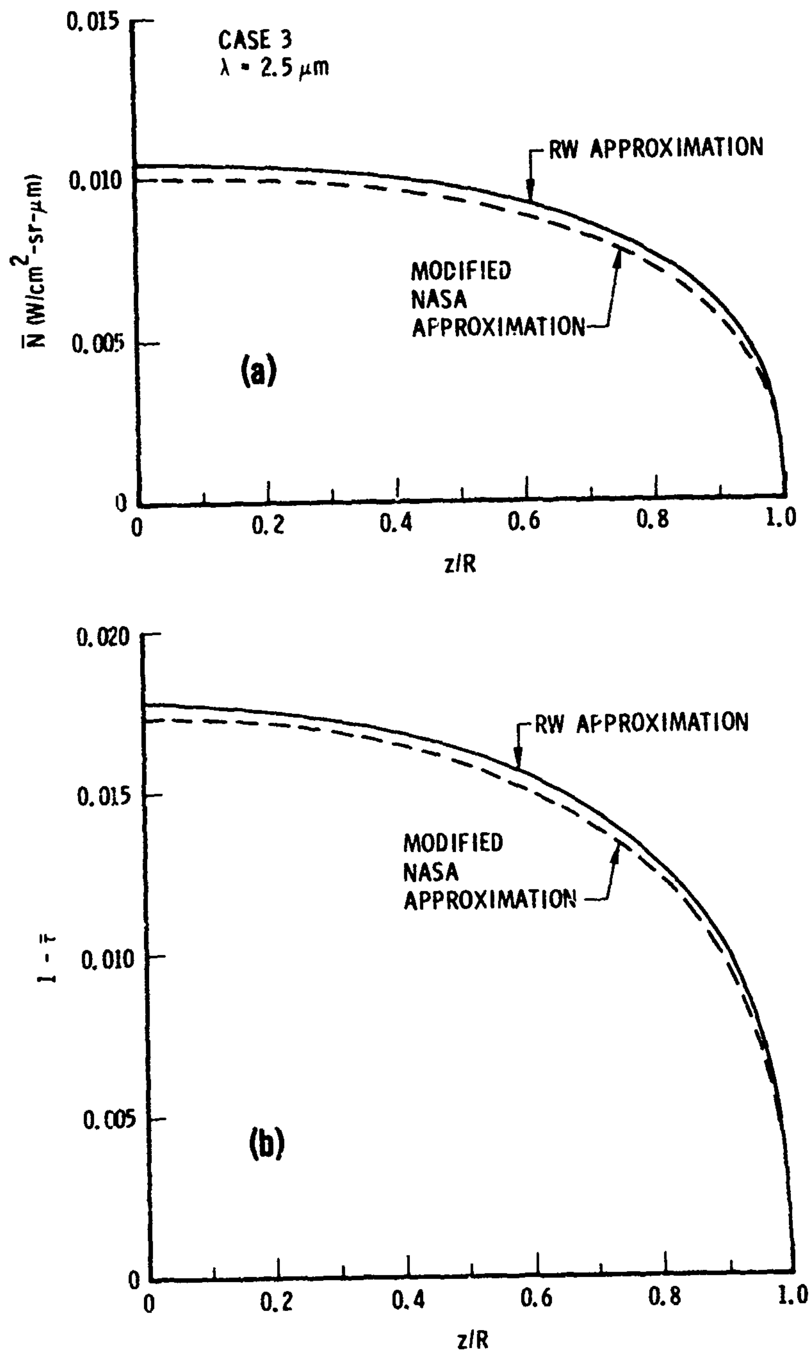

Fig. 31. Comparison of Transverse H_2O Profiles for Case 3 Generated with the RW and Modified NASA Voigt Line Models. (a) Radiance; (b) Absorptance.

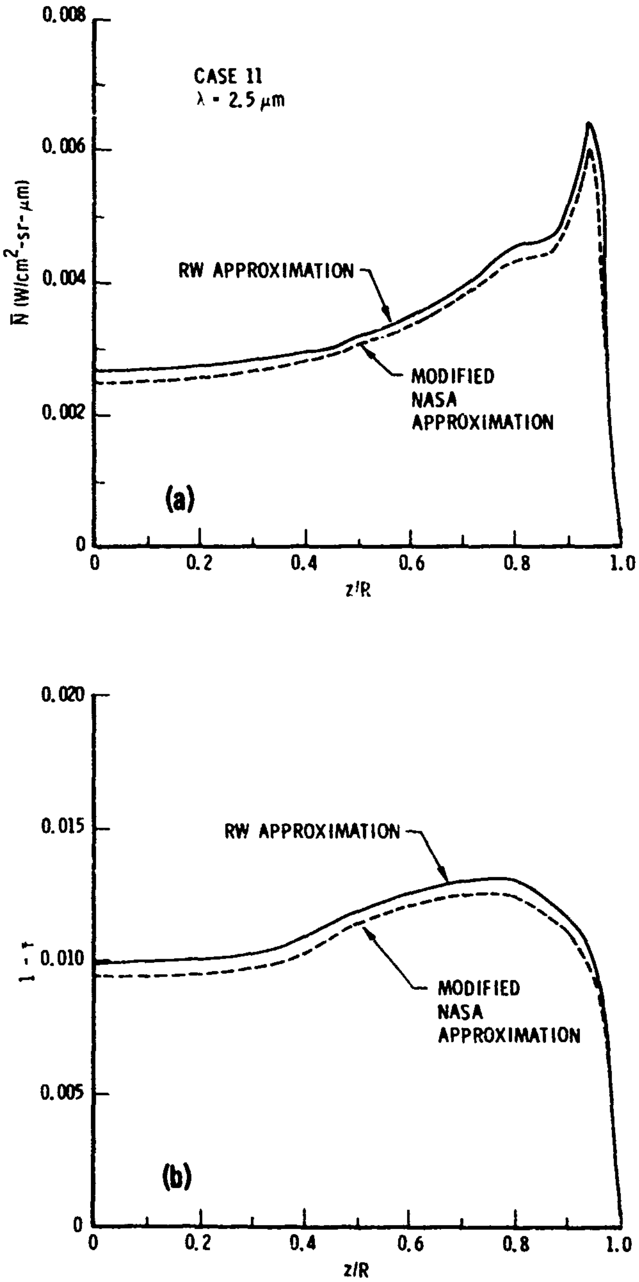

Fig. 32. Comparison of Transverse H_2O Profiles for Case 11 Generated with the RW and Modified NASA Voigt Line Models. (a) Radiance; (b) Absorptance.

VII. INVERSION CHARACTERISTICS

A. Introduction

The intrinsic inversion characteristics of the iterative Abel inversion algorithm are considered in this section. The basic method involves: (1) the assumption of radial pTc profiles; (2) generation of transverse emission/absorption profiles from these radial profiles; (3) an immediate inversion of these transverse profiles to retrieve the radial profiles, and (4) a comparison of the retrieved and true radial profiles. No consideration is made here on the effect of random or bias error in the "synthetic data" (the transverse profiles generated in step 2) on inversion (except for that introduced by rounding the output of step 2 to a finite number of significant digits before inserting it into step 3). Thus, this analysis assesses only the convergence and uniqueness aspects of the inversion model. Some effects of random and bias data error are treated in Sections VIII and IX, respectively.

Three test cases are treated in the present analysis. The first is a purely hypothetical engine case. The second and third are the engine test cases 4 and 12 considered in the previous section.

B. Hypothetical Engine Test Case

Two cases involving hypothetical radial profiles were considered. The assumed radial pTc profiles for the first (Test Case 1) are shown in Fig. 33. The radial profiles for the second (Test Case 2) are identical in shape, but the nozzle radius is increased an order of magnitude from 5 to 50 cm and the concentration is increased from 0.3 to 1.0. For both cases, the assumed active species is H_2O, and the 25 cm^{-1} wide rectangular filter centered on 4000 cm^{-1} is used. Transverse emission/absorption profiles were generated with a spatial resolution grid corresponding to N = 20 zones, the Lorentz lineshape, and the CG nonuniformity approximation.* (All of these calculation conditions were duplicated in inversion). The results are shown in Fig. 34.

*A slightly different line-broadening model from that described in Section V was used in these calculations, but this same model was used in the subsequent inversions.

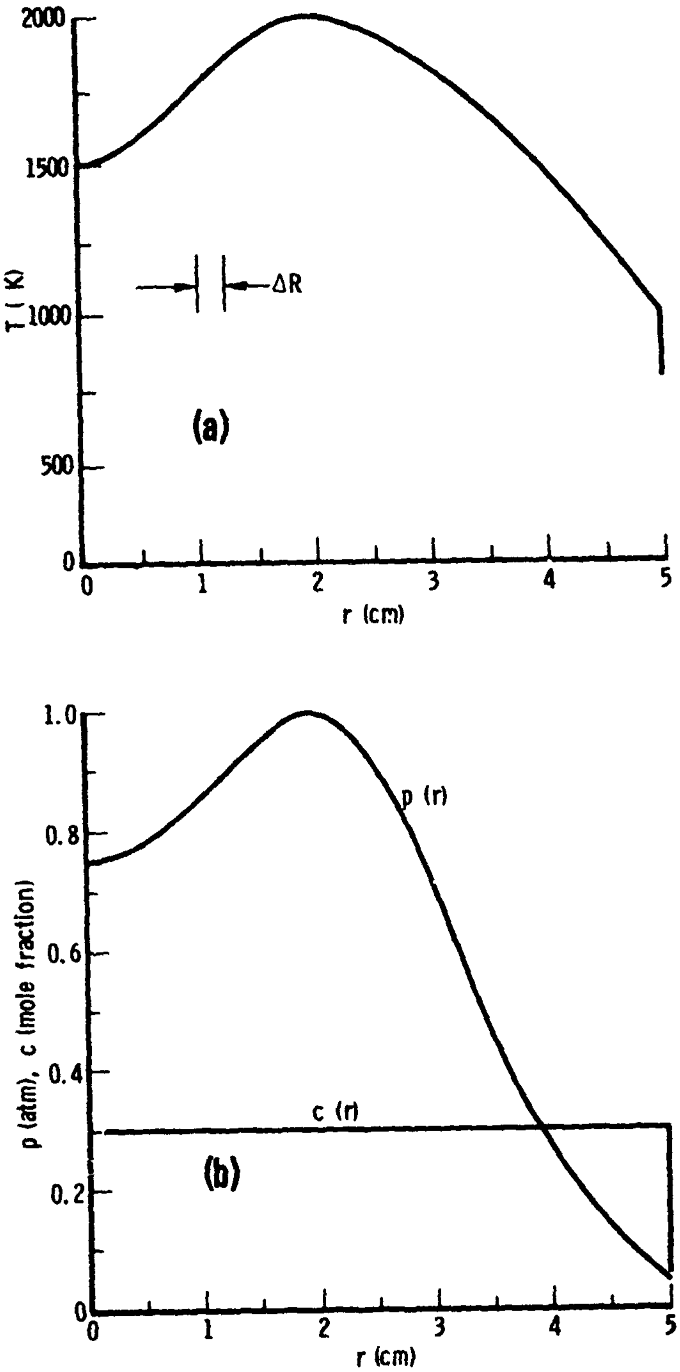

Fig. 33. Radial Profiles for Hypothetical Engine Test Case 1. (a) Temperature; (b) Concentration and pressure.

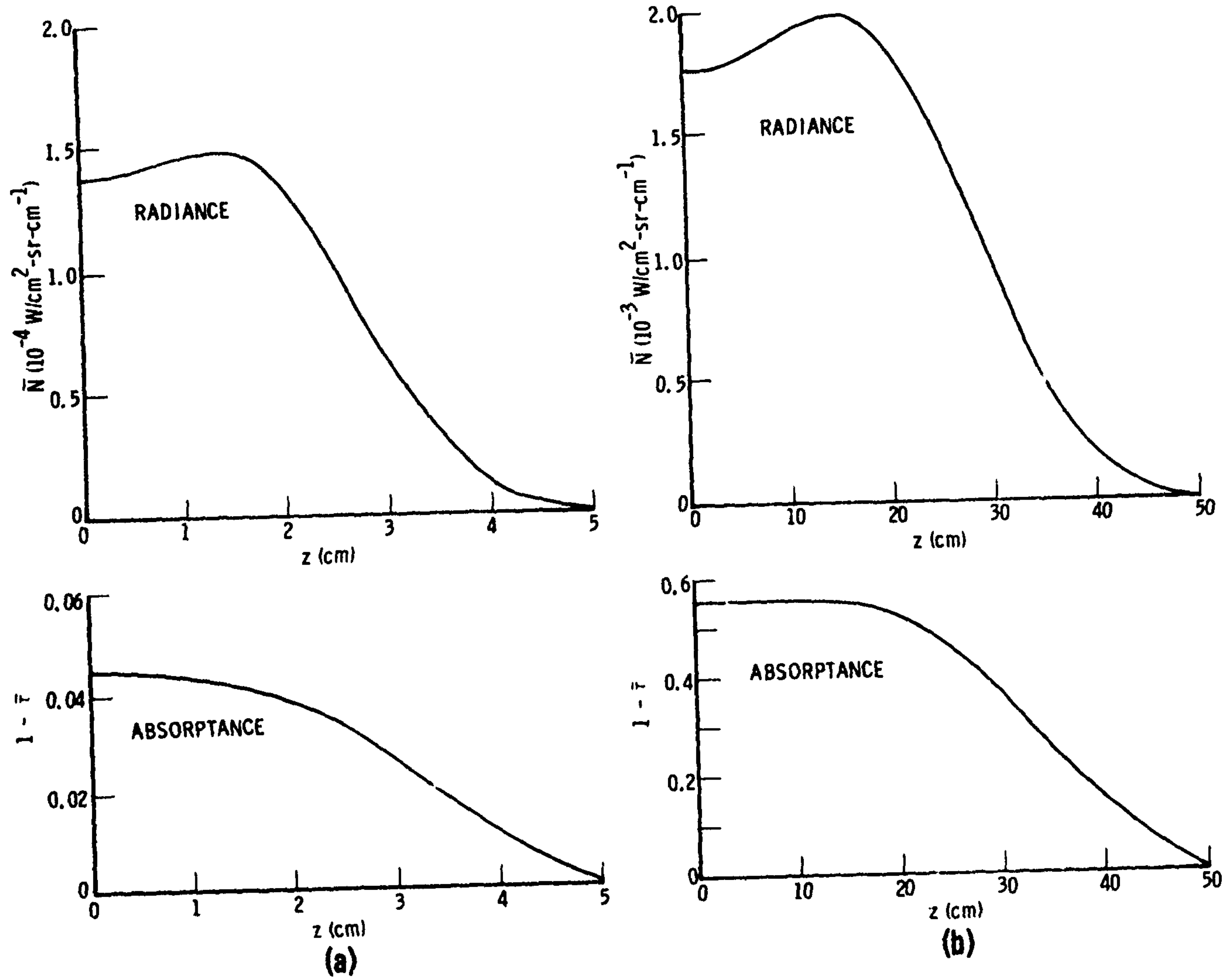

Fig. 34. Computed Transverse E/A Profiles for Hypothetical Engine Test Cases. (a) Case 1 (thin source); (b) Case 2 (thick source).

From the degree of centerline absorptance for these two cases, we can describe Test Case 1 as representing a "relatively thin" source condition and Test Case 2 as a "moderately thick" source condition.

Inversion of Test Case 1. Figure 35 shows the Abel inversion results for Test Case 1. Since the source is relatively thin, these results are fairly close to the "true" radial profiles.

A measure of the improvement upon the simple Abel inversion by successive iterations is shown in Fig. 36. Figure 36a is a plot of the root-mean-square (rms) difference between successive iterations for T and c for increasing iteration number. If f is either T or c, then

$$\Delta f_{rms} \equiv \left[\frac{1}{R} \int_0^R [f_i(r) - f_{i-1}(r)]^2 \, dr \right]^{\frac{1}{2}} \tag{148}$$

The curve for ΔT indicates convergence near $i = 6$ with a final convergence residual of $\Delta T \simeq 0.2$ K. The concentration curve indicates convergence near $i \simeq 11$ with a residual value of $\Delta c \simeq 6 \times 10^{-6}$. Both of these residual values are very small compared to the absolute values of the true T and c profiles. It is conjectured that finite, rather than zero, values of the residuals occur because only four significant figures are retained from the generated transverse profiles for input into the inversion process.

A more significant test for convergence is illustrated in Fig. 36b. Here, the rms differences between the input transverse profiles and transverse profiles generated from successive iterations for T and c are plotted. Both the curves for radiance ($\overline{N}$) and transmittance ($\overline{\tau}$) show a convergence at $i \simeq 5$ with residuals of $\Delta\overline{N} \simeq 3 \times 10^{-8}$ and $\Delta\overline{\tau} \simeq 1.5 \times 10^{-5}$.

The detailed difference between the inverted T and c profiles and the true T and c profiles are shown for $i = 5$ in Fig. 37a. Note that this display is not related to Fig. 36a which was a measure of difference between successive iterations for T and c. The deviations of Fig. 37a display a random distribution of positive and negative deviations in $0 \leq r \leq R = 5$ cm.

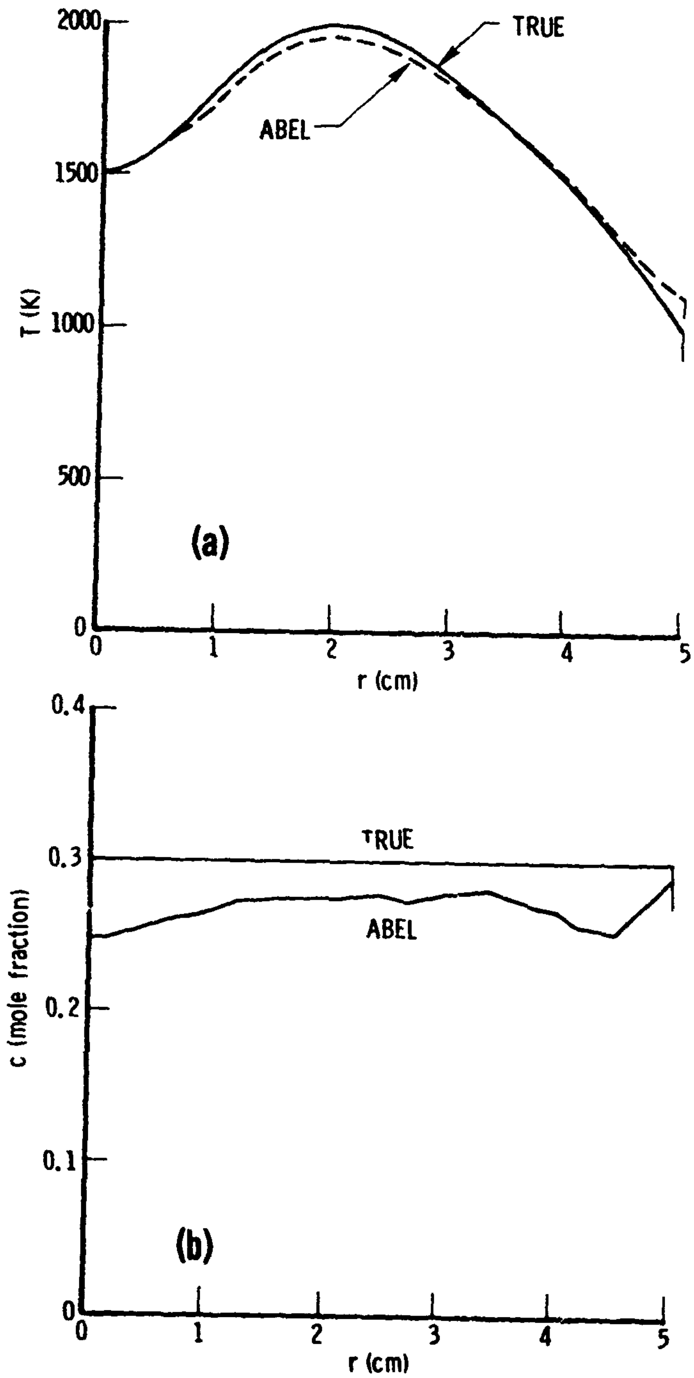

Fig. 35. Abel Inversicn Results for Hypothetical Engine Test Case 1. (a) Temperature; (b) Concentration.

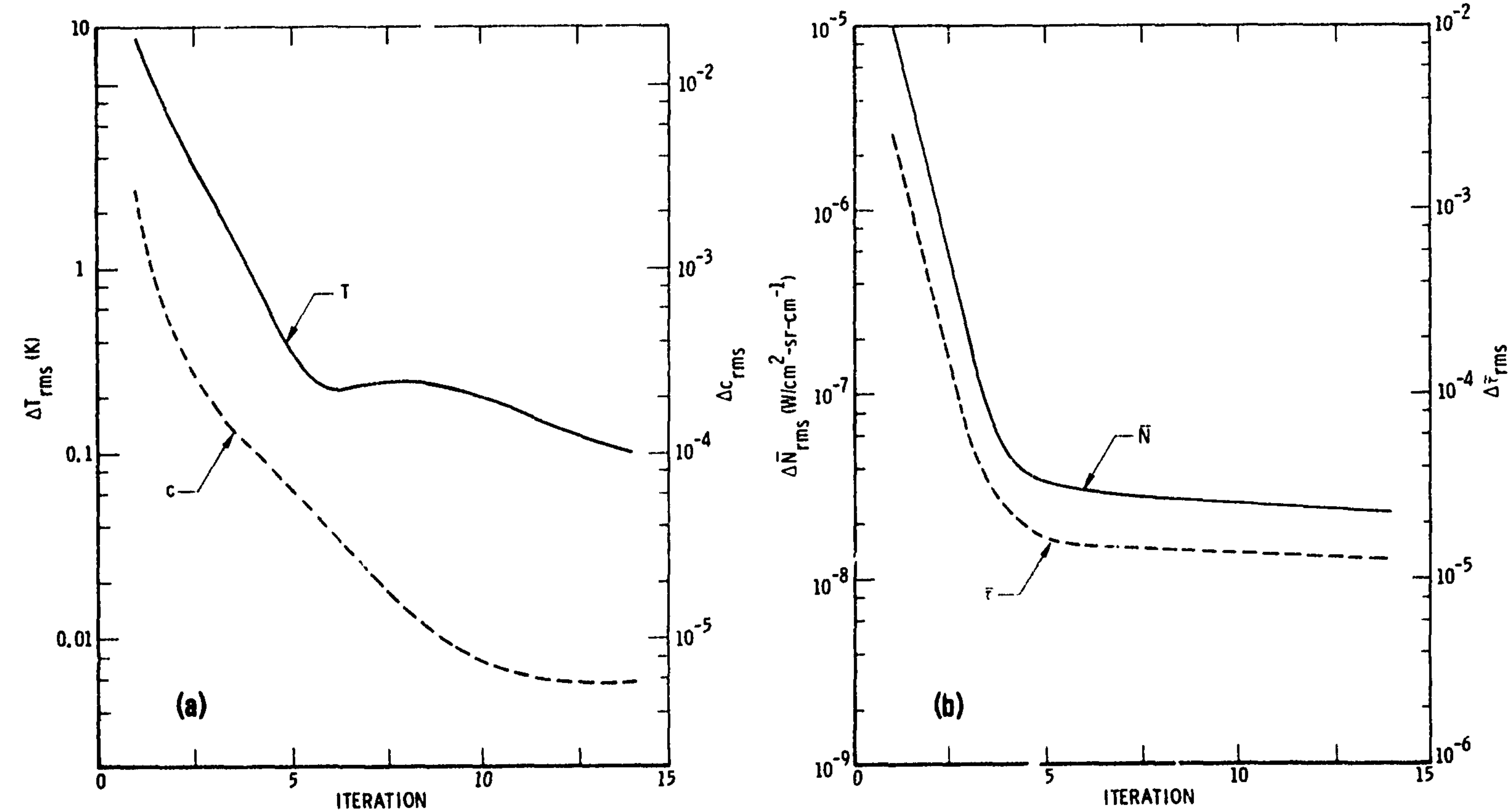

Fig. 36. Profile Convergences for Hypothetical Engine Test Case 1. (a) Radial temperature and concentration; (b) Transverse radiance and transmittance.

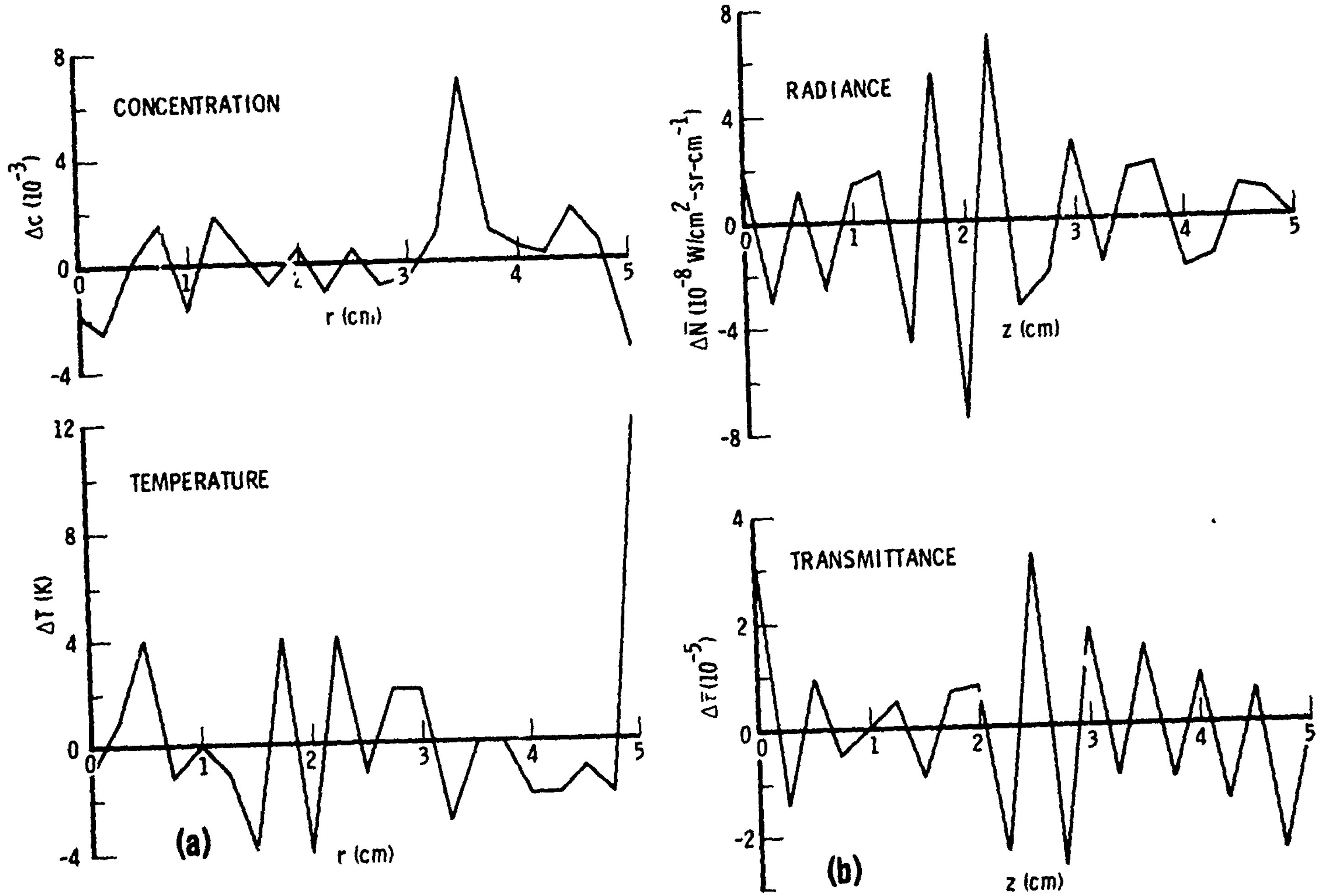

Fig. 37. Profile Residuals for Hypothetical Engine Test Case 1. (a) Radial temperature and concentration; (b) Transverse radiance and transmittance. In all cases, i = 5.

The magnitude of the deviations also appear to be normally distributed. The only conspicuous behavior is a tendency for the maximum deviations to occur at the end point r = R. This behavior can be traced to the numerical differentiation algorithm of the Abel inversion routine. Over most of r, a central-difference formula is used; at r = R, a backward difference formula is used.

Figure 37b is similar to Fig. 37a, but shows the detailed difference between the input transverse profiles and the transverse profiles generated from the fifth iteration for T and c. A summary of Fig. 37 is given in Table 6. The totality of these results indicate a unique convergence to the true radial profiles

Inversion of Test Case 2. Simple Abel inversions of the transverse profiles of Fig. 34b yield the T and c profiles of Fig. 38. Here, because the source is not even approximately thin, the Abel inversion results are not at all close to the true radial profiles. Convergence effected by successive iterations is shown in Fig. 39. Figure 39a is similar to Fig. 36a for Test Case 1 and shows the convergence between successive radial profiles. Figure 39b is similar to Fig. 36b for Test Case 1 and shows the convergence between the input transverse profiles and profiles generated from successive c and T profiles. Both Figs. 39a and 39b indicate convergence near i = 30. Details of the radial and transverse profiles at i = 30 are shown in Fig. 40. The discussion of this figure is the same as the discussion of Fig. 37 for Test Case 1. A summary of the results of Fig. 40 is given in Table 7. As for Test Case 1, these results indicate a unique convergence.

The only significant difference between the Test Case 1 and Test Case 2 inversions is the number of iterations required for "ultimate" convergence, that is, convergence to the point where the transverse profiles generated from successive iterations for c and T do not become closer to the input transverse profiles. For Test Case 1, five iterations were required while for the thicker source of Test Case 2, thirty iterations were required. Although this latter number may appear excessive, the inversion routines are reasonably efficient, and thirty iterations are completed in less than 1.5 seconds of computing time on the CDC 7600 computer.

Table 6. Summary of Inversion Characteristics for Test Case 1

Variable	Maximum Profile Value	Deviation Results at i = 5		
		Mean	rms*	Maximum**
T	2000 K	0.33	3.5	4.0
c	0.30	0.0024	0.0021	0.0068
$\overline{N}$	1.5(-4)W/cm^2-sr-cm^{-1}	2.9(-10)	3.3(-8)	7.4(-8)
1-$\overline{\tau}$	0.044	3.3(-7)	1.7(-5)	3.4(-5)

* from true

**except endpoint at r = R

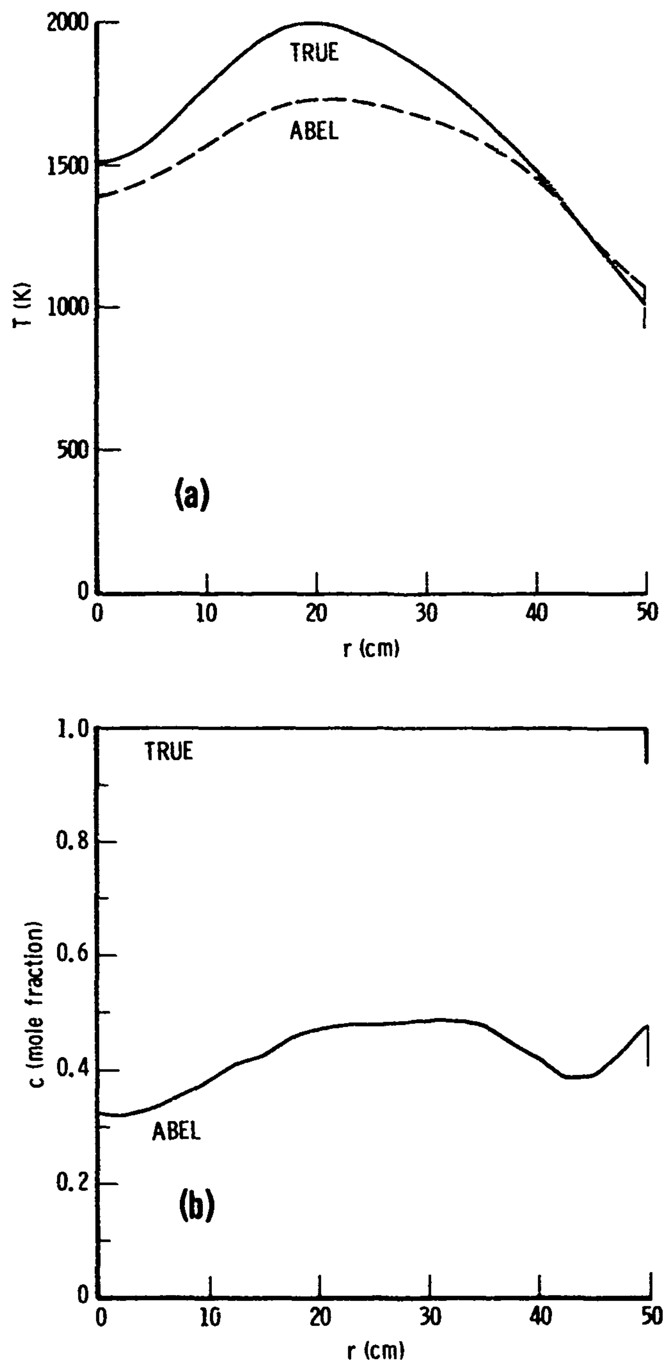

Fig. 38. Abel Inversion Results for Hypothetical Engine Test Case 2. (a) Temperature; (b) Concentration.

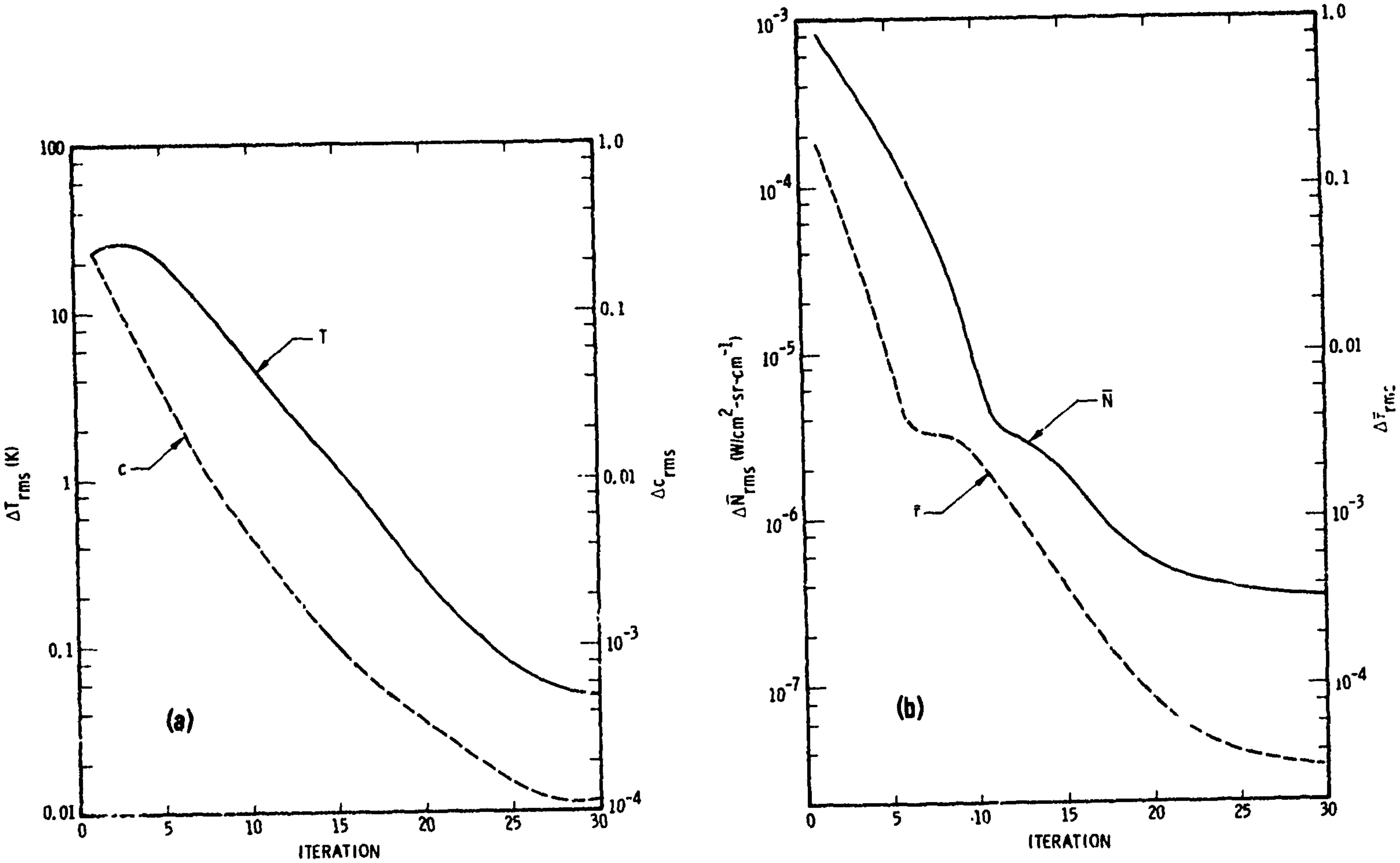

Fig. 39. Profile Convergences for Hypothetical Engine Test Case 2. (a) Radial temperature and concentration; (b) transverse radiance and transmittance.

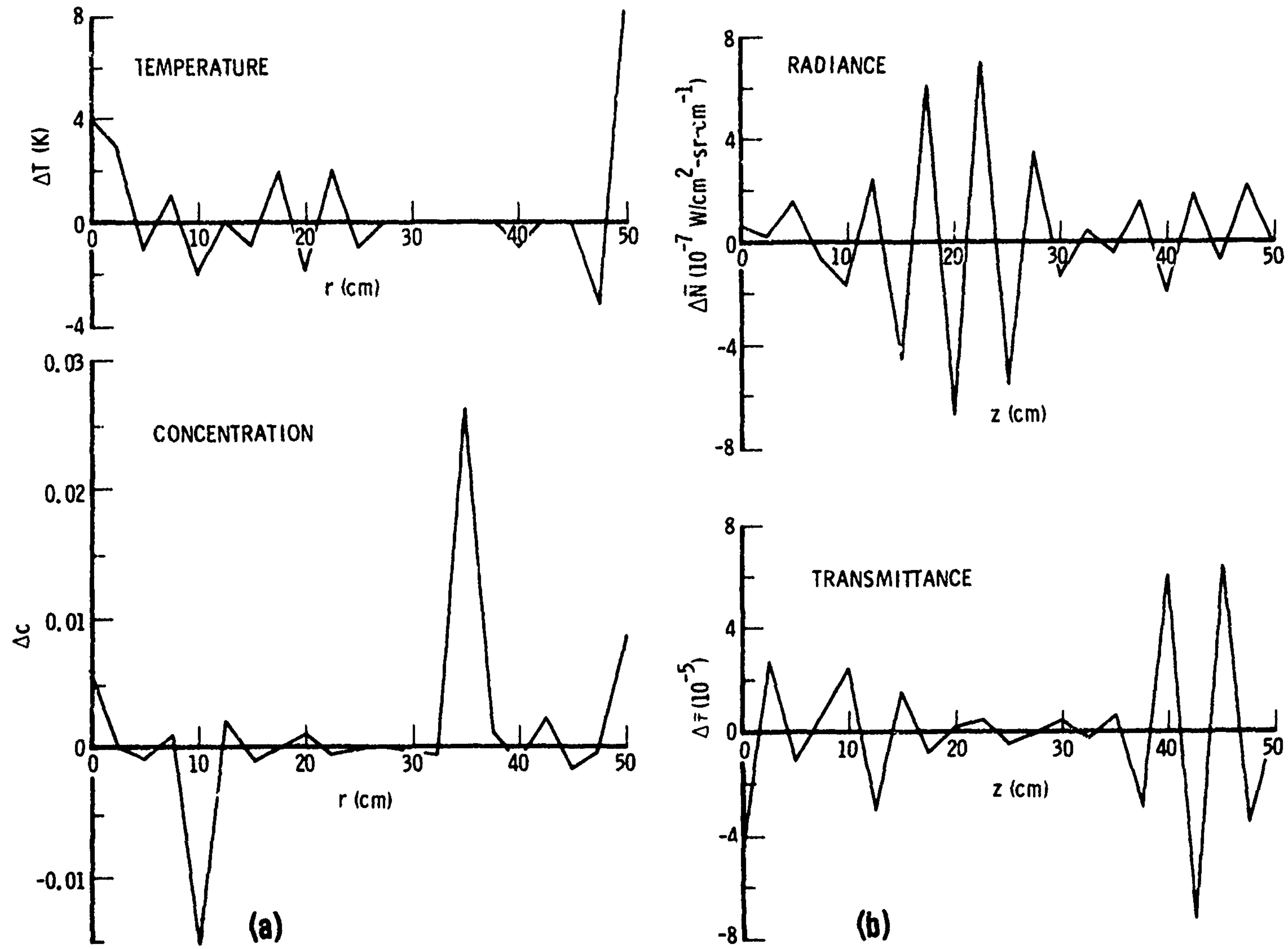

Fig. 40. Profile Residuals for Hypothetical Engine Test Case 2. (a) Radial temperature and concentration; (b) Transverse radiance and transmittance. In all cases, i = 5.

Table 7. Summary of Inversion Characteristics for Test Case 2

Variable	Maximum Profile Value	Deviation Results at i = 30		
		Mean	rms*	Maximum**
T	2000 K	0.43	2.4	4.0
c	1.00	0.0012	0.0071	0.026
$\overline{N}$	$2.0(-3) W/cm^2$-sr-cm^{-1}	1.5(-8)	3.3(-7)	7.0(-7)
$1 - \overline{\tau}$	0.45	-1.6(-6)	3.2(-5)	7.4(-5)

* from true

**except endpoint r = R

C. Engine Test Case 4

Engine Test Case 4 represents a uniform source with R = 4.178 cm, p = 0.790 atm, T = 1728 K, c_{H_2O} = 0.373, and c_{CO_2} = 0.0597. Transverse profiles generated from these conditions for the Voigt lineshape (RW approximation) and N = 50 are shown in Fig. 22. Inversions of these profiles were performed with these same conditions. Abel inversion results for T and c are shown in Fig. 41. The temperature profile retrieved from the H_2O data at 2.5-μm is very close to the true value of 1728 K because the source is optically thin in this spectral region. The profile obtained from inversion of the CO_2 profiles at 4.4-μm is substantially different from the true value because the source is not thin in this spectral region. Similarly, the Abel inversion for the H_2O concentration profile is closer to the true H_2O profile than the result for the CO_2 profile is to its true profile.

The convergence of the inverted profiles in the iterative Abel scheme is shown for H_2O in Fig. 42. Figure 42a displays the convergence of successive radial profiles and Fig. 42b shows the convergence of successive transverse profiles to the input profiles.

These results are qualitatively similar to those of the hypothetical engine test case and again confirm the convergence and uniqueness of the iterative inversion scheme.

D. Engine Test Case 12

Engine Test Case 12 represents a highly nonuniform radiation source. The radial pTc profiles are given in Fig. 18 and the calculated transverse profiles in Fig. 30. The transverse profiles generated with the Voigt lineshape and DR nonuniformity approximation were used as input to the inversion (and, of course, inverted with these same conditions). Inversion results for temperature and concentration are shown in Figs. 43 and 44, respectively.

Explanations for the results in the region below $r/R \leq 0.2$ and $r/R \geq 0.8$ are required. Near the edge of the source, both the temperature and concentration profiles plunge rapidly to low values (see Fig. 18). Consequently, the

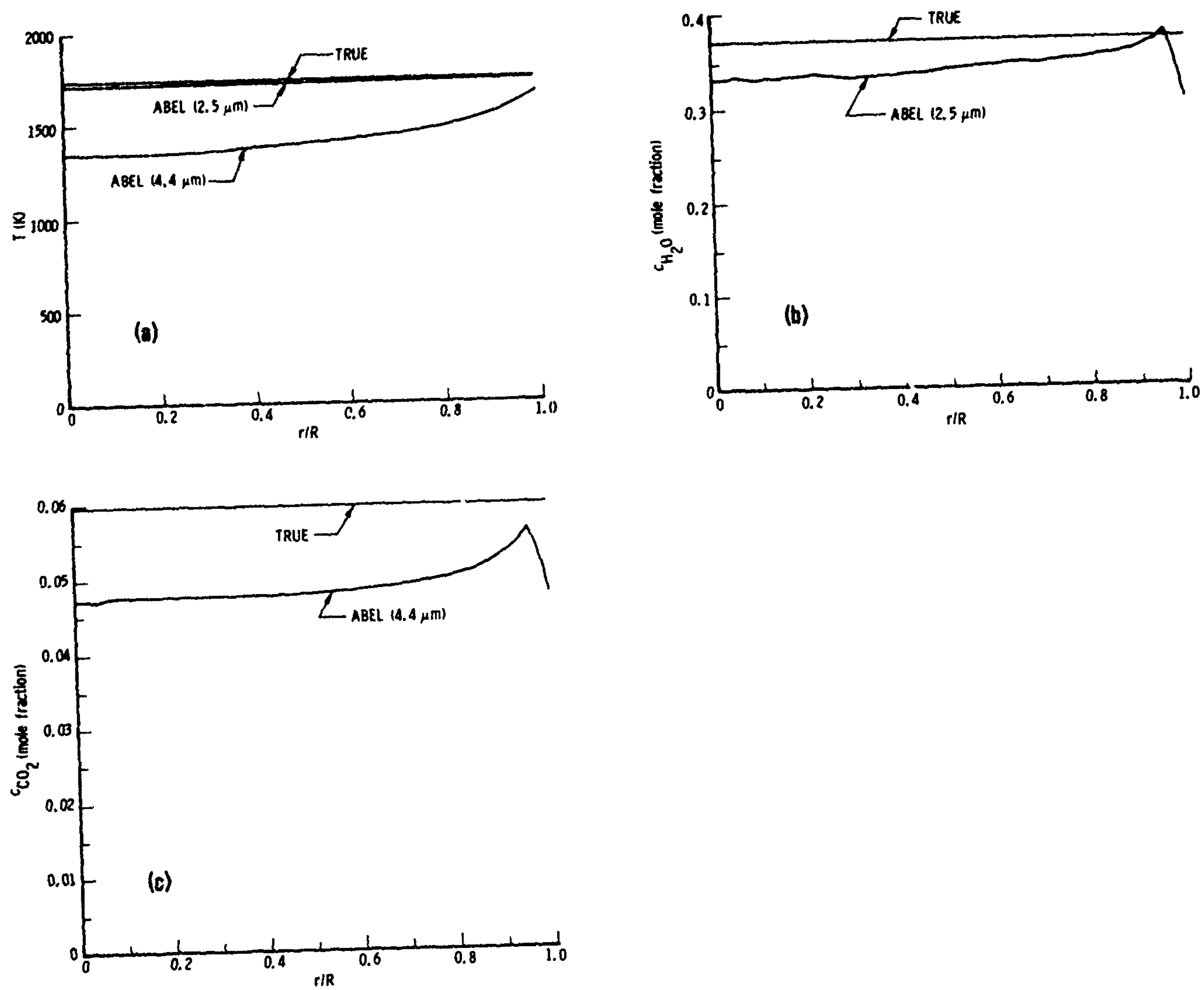

Fig. 41. Abel Inversions for Engine Test Case 4. (a) Temperature; (b) H_2O concentration; (c) CO_2 concentration.

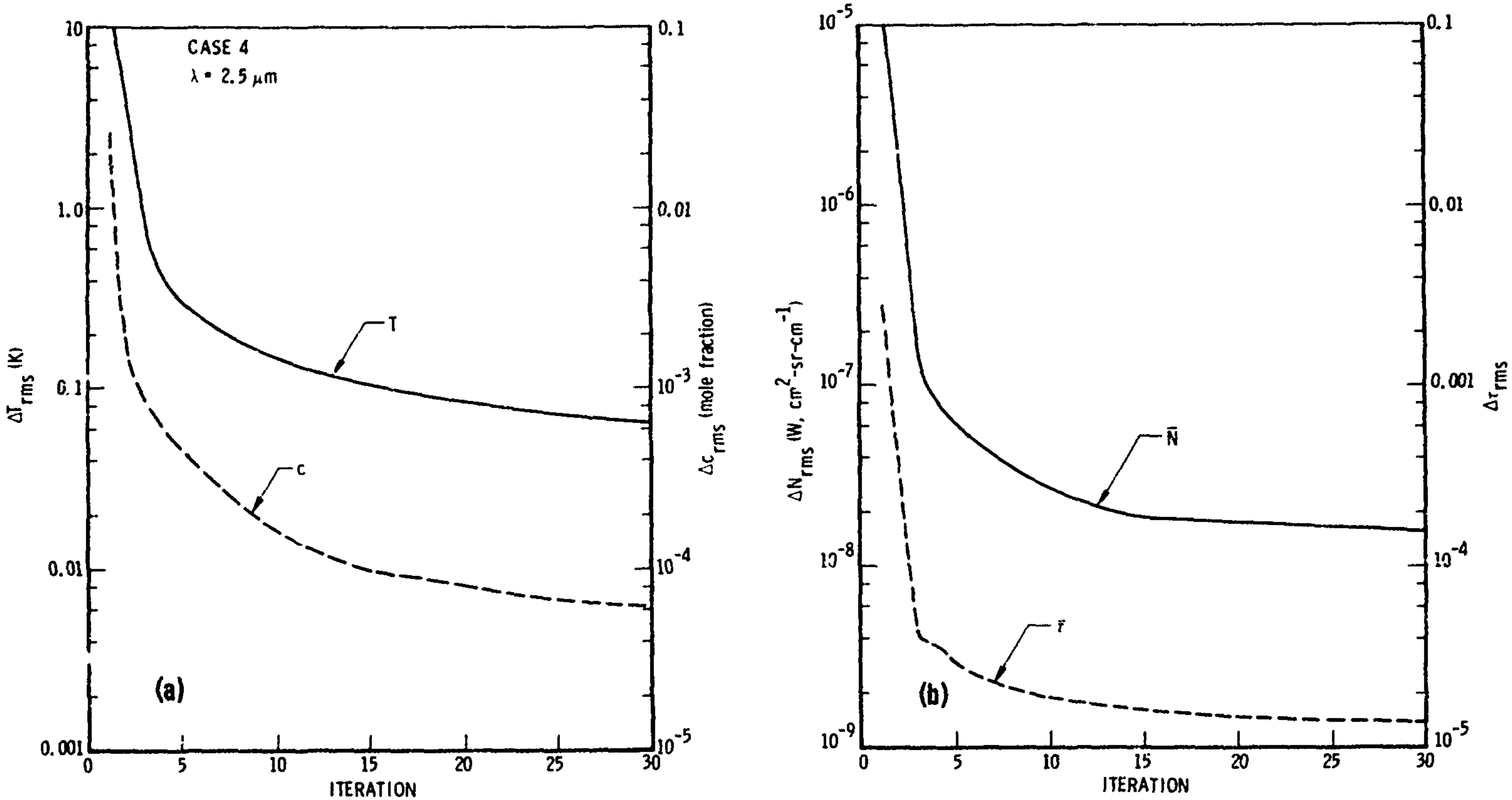

Fig. 42. H_2O Profile Convergences for Engine Test Case 4. (a) Radial temperature and concentration; (b) Transverse radiance and transmittance.

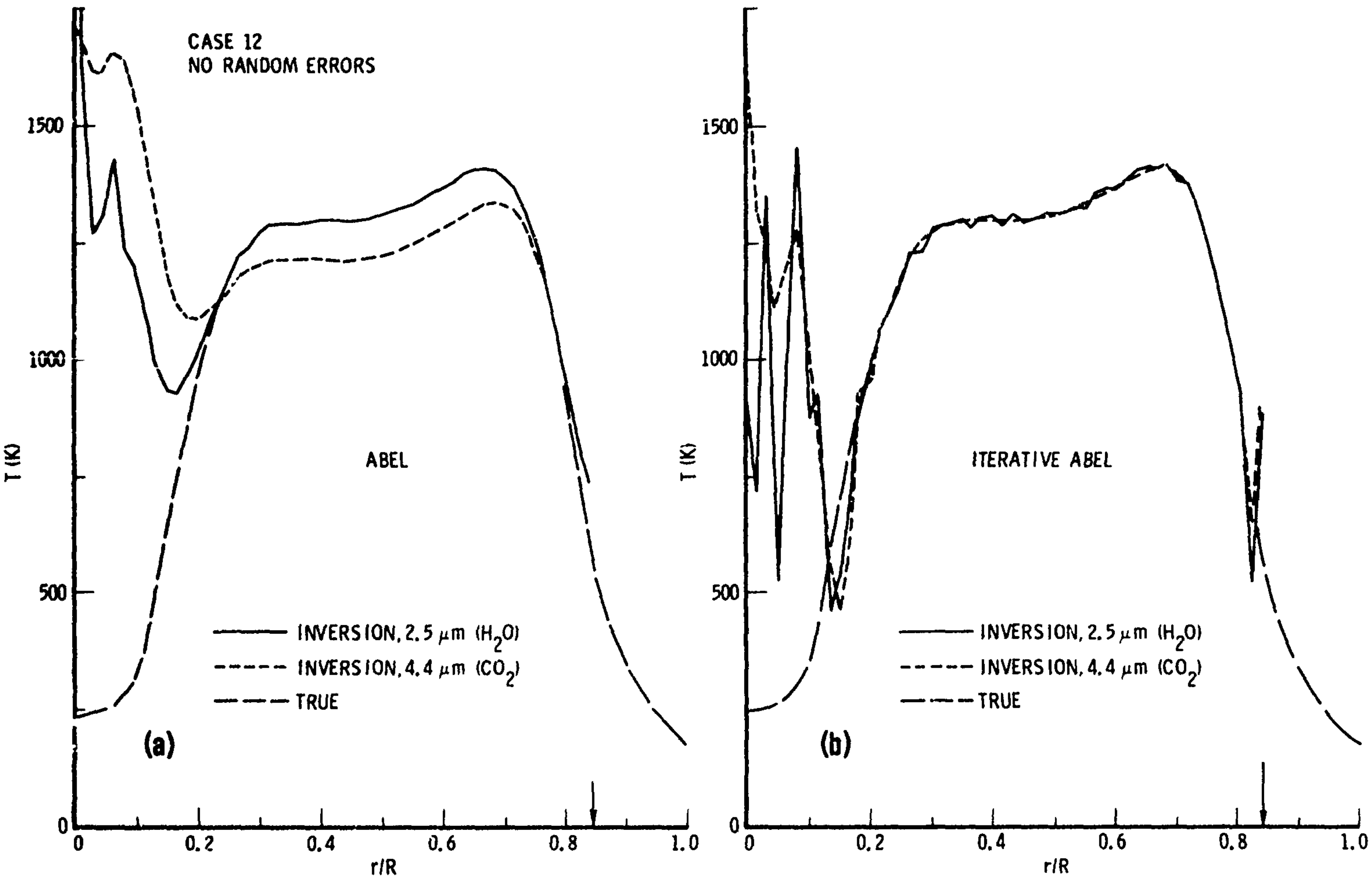

Fig. 43. Temperature Inversions for Engine Test Case 12. (a) Abel Inversion; (b) Iterative Abel Inversion.

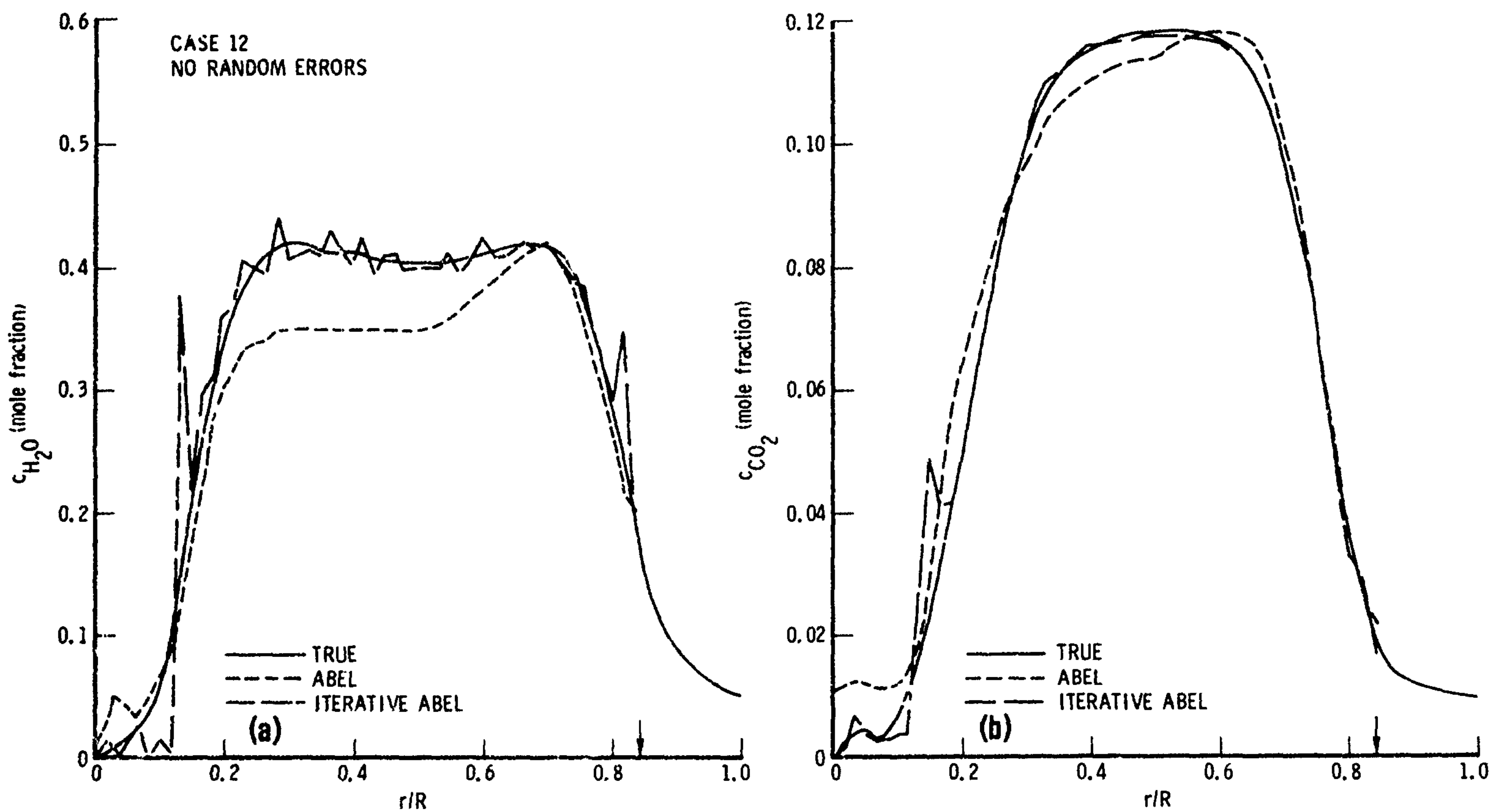

Fig. 44. Concentration Inversions for Engine Test Case 12. (a) H_2O; (b) CO_2.

resulting transverse profiles of radiance and transmittance are nearly zero and unity, respectively, near the edge (above ~ 0.80)(see Fig. 30). Since essentially no information is contained in this region, no inversion for radial profiles can be made. The inversions were carried out by redefining the source radius to be 0.84 of the true source radius.

Below $r/R \simeq 0.2$, the temperature and concentration again plunge to low values. Here, the interpretation of the inversion problem takes several forms. An important effect in the present case is that the transverse profiles were generated with only four significant digits in radiance and transmittance. Since the transmittance is so high, the effect of using only this number of significant digits is to produce a random error in the input data simply through the process of round off.

However, results obtained with the retention of many more significant digits displayed the same spurious results in this region. An explanation of the results can be made with the physical picture provided by the "onion-peel" method. As we work in from the outer edge and determine T and c for each concentric zone, we reach a point where we must start to subtract two large radiance values in order to determine a small radiance (because temperature is low) caused by an inner zone. An inspection of the emission function J (r) indicates that in order to perform this subtraction accurately, more than ~ 20 significant digits must be retained throughout the inversion. This interpretation is consistent with the interpretation that inversion can be performed only if the transverse profiles maintain a spatial gradient sensibly different from zero. Inspection of case 12 profiles show that the transverse profiles are essentially constant for $r/R \lesssim 0.1$. (Note that this same interpretation can be applied to $r/R \gtrsim 0.8$). This feature is not to be interpreted as a failing of the inversion method, but rather a confirmation of the fact that an inversion can be made only if information is available.

Outside of these two regions, the application of the iterative inversion method provides adequate inversion convergence.

VIII. RANDOM ERROR ANALYSIS

A. Introduction

The effects of random experimental error on the accuracy of inversion was investigated for the three test cases considered in the previous section. The approach is the same as used to investigate the intrinsic inversion characteristics: transverse profiles were generated from known radial profiles, inverted to obtain radial profiles, and the results compared with the starting radial profiles. Here, the added steps were taken of superimposing artificial random fluctuations onto the transverse profiles and smoothing these profiles before performing the inversion. Since the inversion has been determined to be convergent and unique in the absence of random fluctuations, any significant discrepancy between the inverted and starting radial profiles can be attributed directly to the random errors or the smoothing routine used to suppress them or both.

B. Hypothetical Engine Test Case

The moderately deep (Test Case 2) test case considered in Section VIIA was used for this random error analysis. The assumed radial profiles are shown in Fig. 33 (except that the nozzle radius is R = 50 cm and $c_{H_2O} = 1$).

The transverse emission/absorption profiles are shown in Fig. 34b and again here in Fig. 45. Random errors with a $\pm 5\%$ rms deviation of the peak value were superimposed on both the radiance and absorptance profiles at the N = 20 transverse zone positions in order to simulate experimental random fluctuations. The magnitude of the individual fluctuations was obtained from tables of random normal numbers, and different tables were used for each profile so that the errors would be uncorrelated between the profiles. These transverse "error profiles" are shown in Fig. 45 along with the true transverse profiles.

The results of variable pre-smoothing of the data according to the routine described in Section IIID are shown in Fig. 46 for the transverse

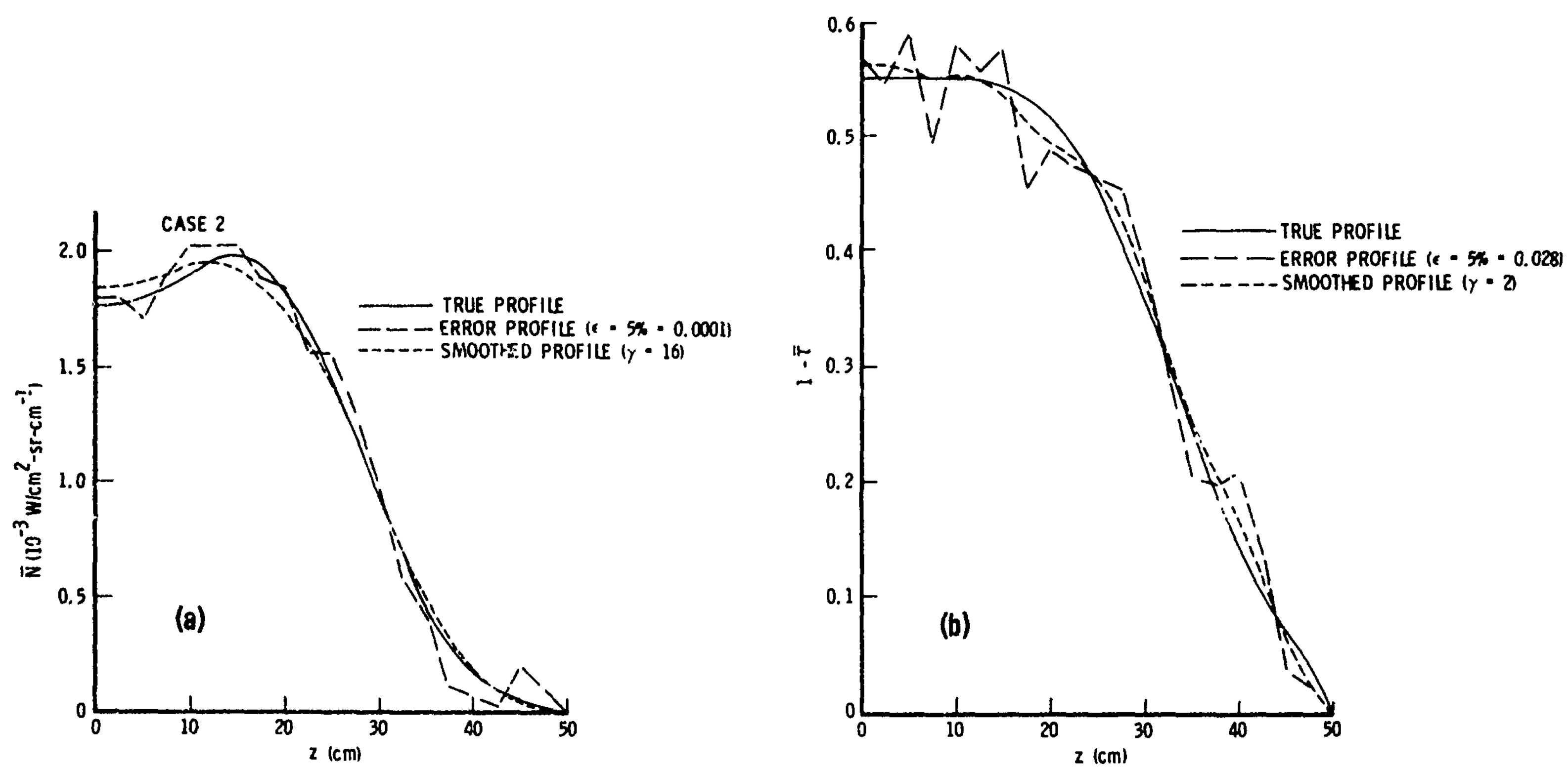

Fig. 45. Transverse E/A Profiles for Random Error Analysis (5% rms error) of Hypothetical Engine Test Case 2. (a) Radiance; (b) Absorptance.

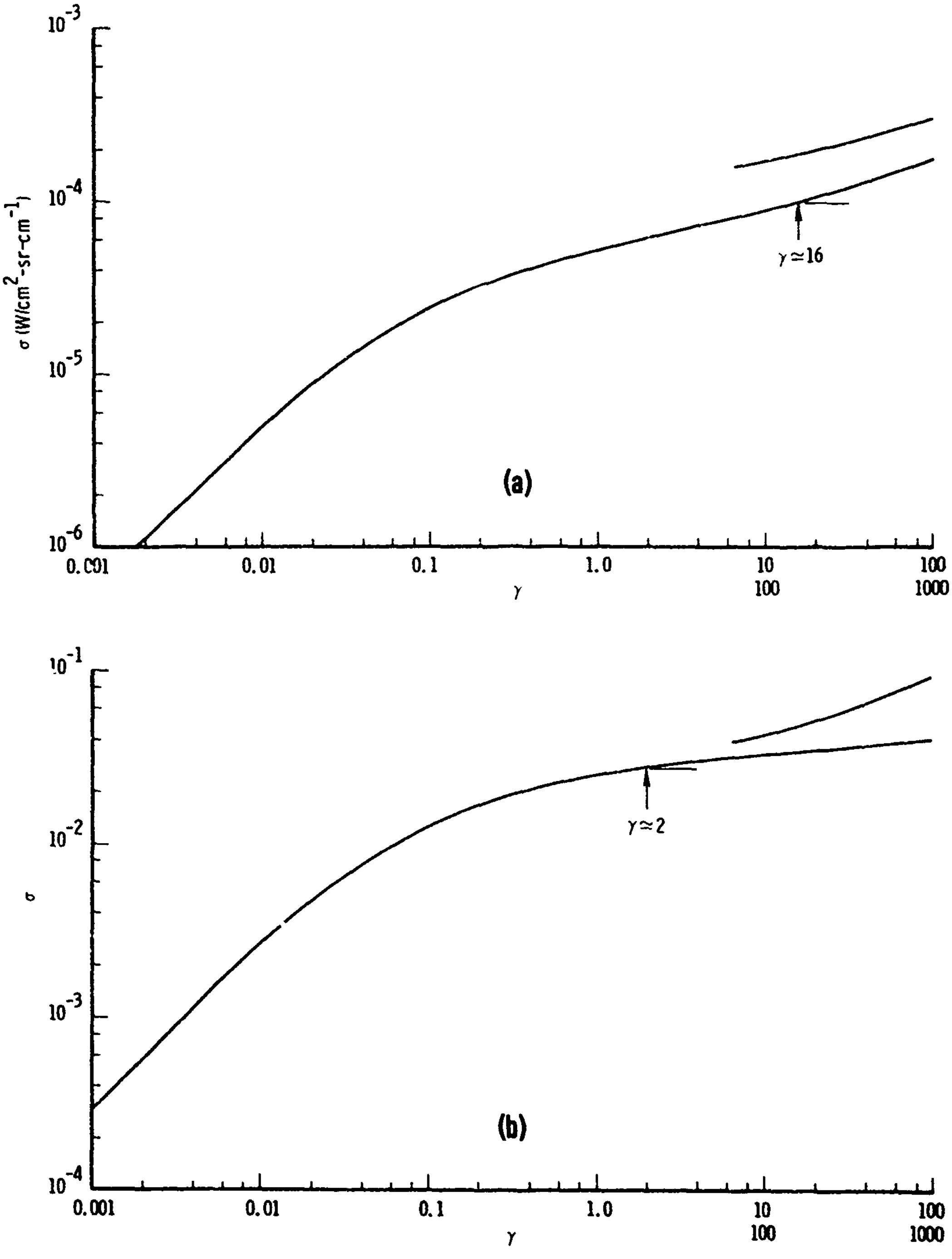

Fig. 46. Smoothing Curves for Hypothetical Engine Test Case 2. (a) Radiance smoothing; (b) Absorptance smoothing.

radiance and absorptance profiles, respectively. Each figure is a plot of the rms difference between the smoothed and unsmoothed profile σ versus the smoothing parameter γ. A criterion for selecting γ is to choose that value which makes σ about equal to the estimated rms fluctuations in the data ϵ. The estimated rms fluctuations in radiance is 10^{-4} W/cm^2-sr-cm^{-1} (i.e., 5% of peak value), and the appropriate value of γ is seen to be ~ 16. For absorptance, the estimated rms fluctuations is 10^{-2} and the corresponding γ value is ~ 2. The smoothed profiles resulting from these choices for γ are shown in Fig. 45 along with the true and error profiles.

Finally, the radial profiles resulting from an inversion of the pre-smoothed transverse profiles are shown in Fig. 47. The temperature profile is quite respectable and displays only a 81 K rms deviation from the "true" profile. The concentration profile, on the other hand, is not as good and displays an rms difference from the "true" concentration profile of over 20%. These results are based on the use of γ = 16 and 2, respectively, for radiance and absorption. An attempt was made to further smooth the concentration result by increasing the γ value for absorption, but little was gained. Since the inversion for concentration is not governed solely by the absorption profile but is coupled with the radiance profile, an increased smoothing of the radiance profile may also be needed in order to smooth the concentration result.

A second analysis of this case was run under somewhat different conditions. The spatial grid resolution was reduced to 1 cm by use of N = 50 zones, and random errors of $\pm 10\%$ rather than $\pm 5\%$ were superimposed on the transverse radiance and absorptance profiles. Also, the example was run with the consistent use of the DR rather than CG nonuniformity approximation. The true, synthesized experimental, and appropriately presmoothed transverse radiance and absorptance profiles are shown in Fig. 48. The comparison between exact and inverted radial profiles for temperature and concentration are shown in Fig. 49. The comparisons apparent in these latter two figures are qualitatively the same as the comparisons reported for the 5% random error example. However, the quality of the comparison is

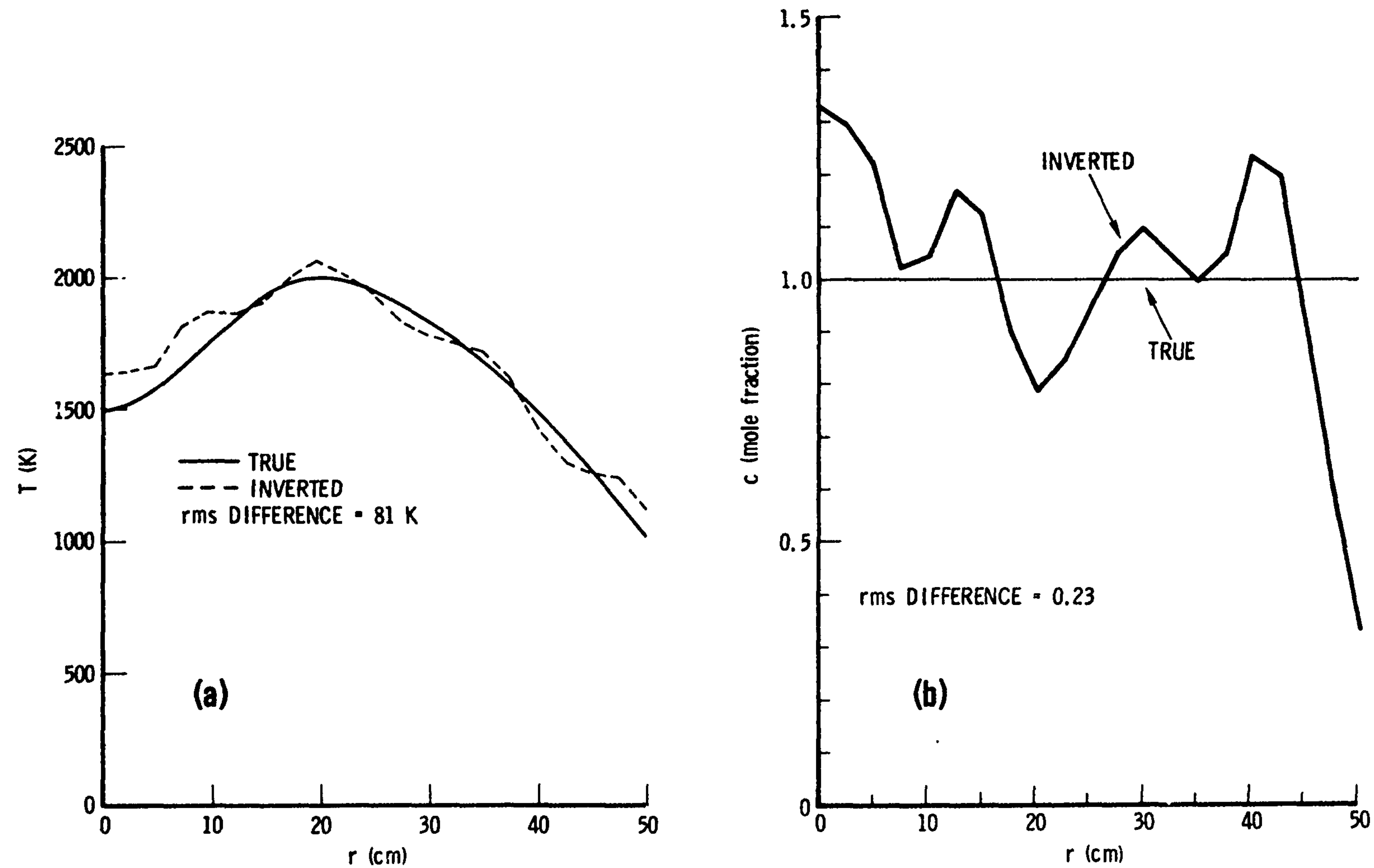

Fig. 47. Comparison between True and Inverted Profiles for 5% Error Analysis of Hypothetical Engine Test Case 2. (a) Temperature comparison; (b) Concentration comparison.

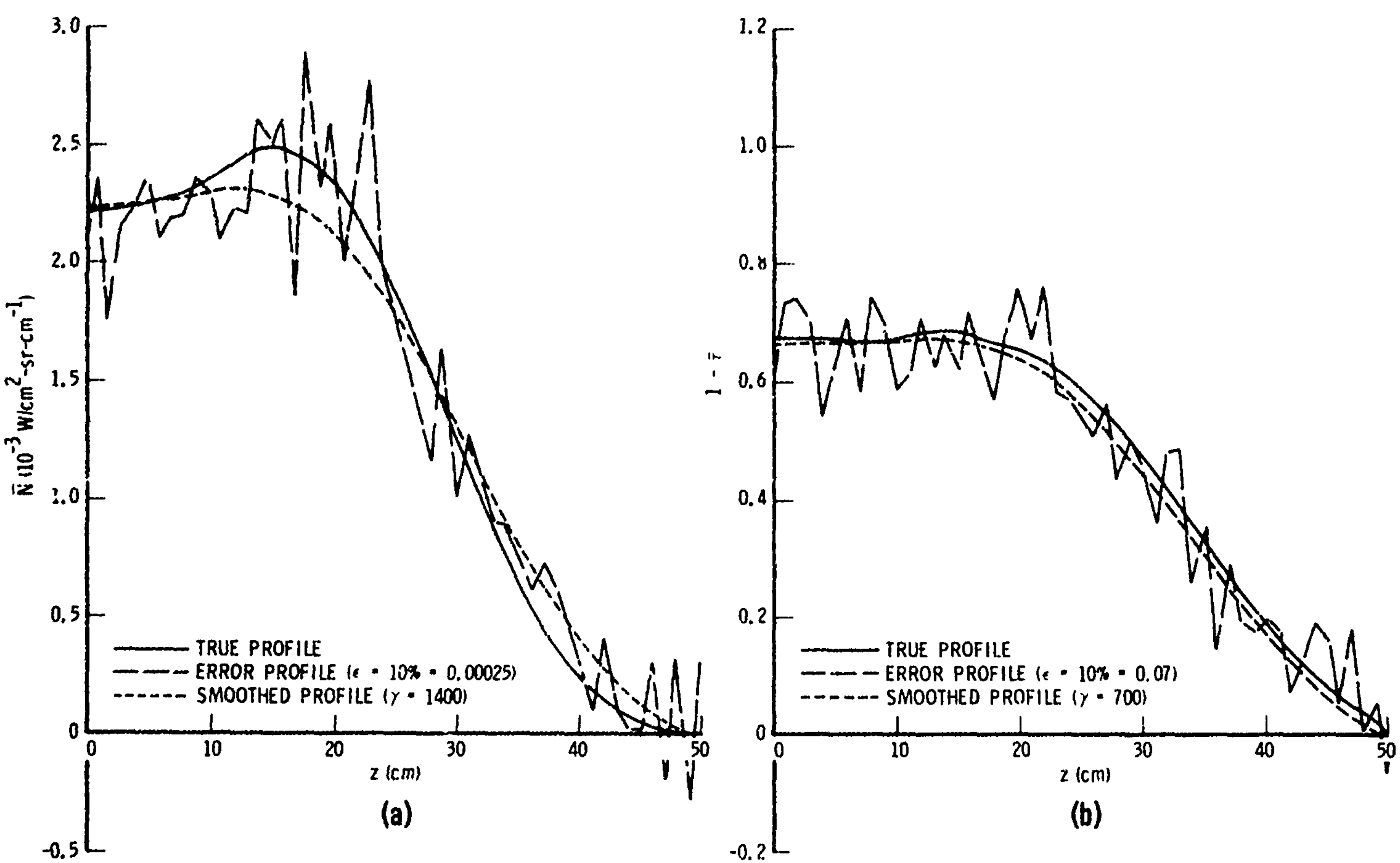

Fig. 48. Transverse E/A Profiles for Random Error Analysis (10% rms error) of Hypothetical Engine Test Case 2. (a) Radiance; (b) Absorptance.

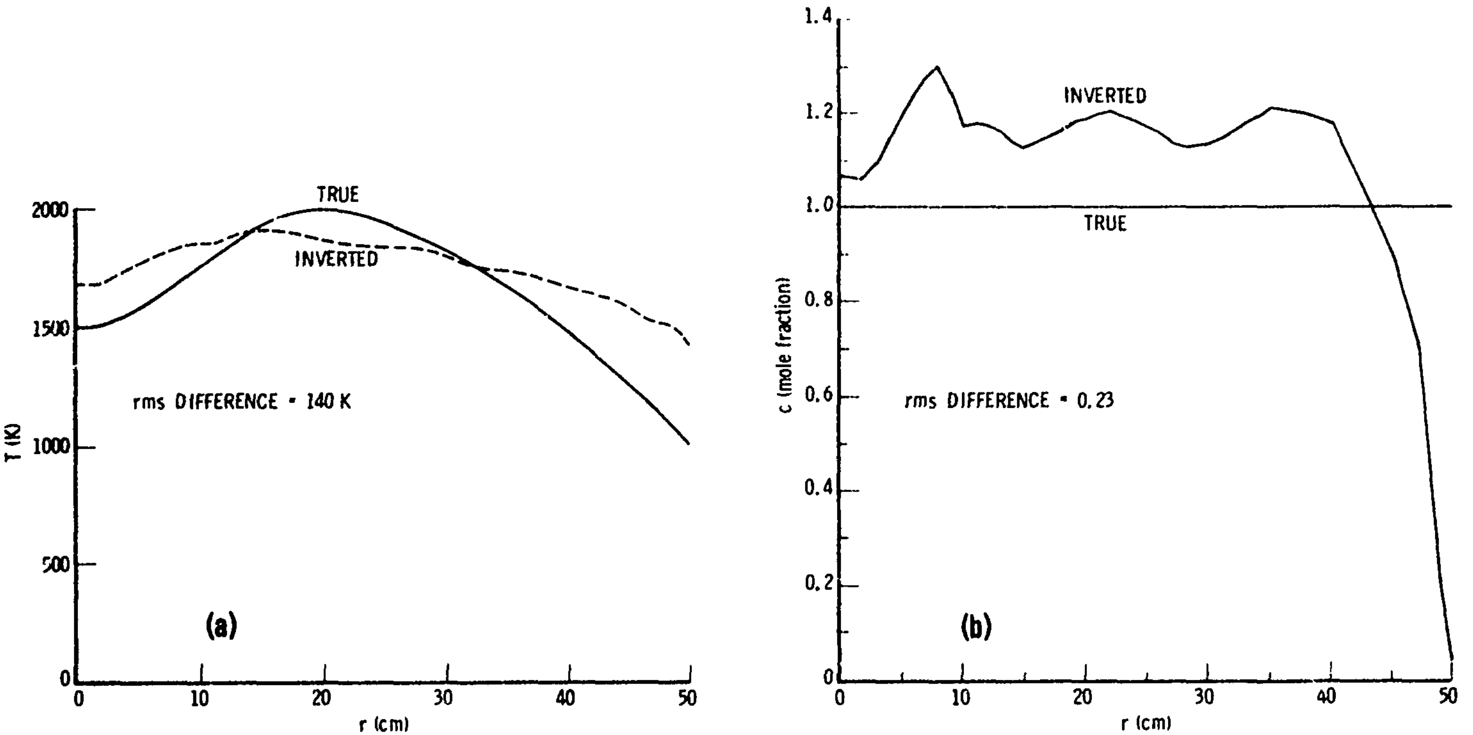

Fig. 49. Comparison between True and Inverted Profiles for 10% Error Analysis of Hypothetical Engine Test Case 2. (a) Temperature comparison; (b) Concentration comparison.

worse. This is to be expected, of course, since the input data is at least twice as noisy as the ±5% error example. In the present case, the rms difference between the true and inverted temperature profiles is 140° K, up from 81° K for the 5% error case. In addition, the temperature profile appears to be over-smoothed yet is based on the same quantitative pre-smoothing criteria used for the 5% example. The inverted concentration profile, on the other hand, displays the same ~23% rms difference from the true profile (c = 1) that was obtained in the 5% error example, but here the error is all in one direction (higher) than the true value rather than distributed around the true value.

C. Engine Test Case 4

The true radial profiles for this case are given in Table 5 and the transverse profiles in Fig. 22. Random fluctuations of ±2% rms of peak profile value were superimposed on the radiance and transmittance profiles. These error profiles are shown in Fig. 50 for H_2O and Fig. 51 for CO_2. Although the rms error magnitude is only 2%, the fact that it is superimposed on transmittance corresponds to a superposition of ~30% errors on the H_2O absorptance profile and ~6% on the CO_2 absorptance profile. Presmoothing of these profiles gave the following optimum values for γ (that is, these values gave rms differences between the smoothed and unsmoothed profiles equal to the superimposed errors).

H_2O radiance : $\gamma = 0.58$

H_2O absorptance: $\gamma = 1.35$

CO_2 radiance: $\gamma = 0.40$

CO_2 absorptance: $\gamma = 0.53$

The CO_2 profiles smoothed with these CO_2 values for γ are shown in Fig. 51. The smoothed profiles for H_2O shown in Fig. 50 were obtained with γ values eight times larger than these optimum H_2O values. The reason for this

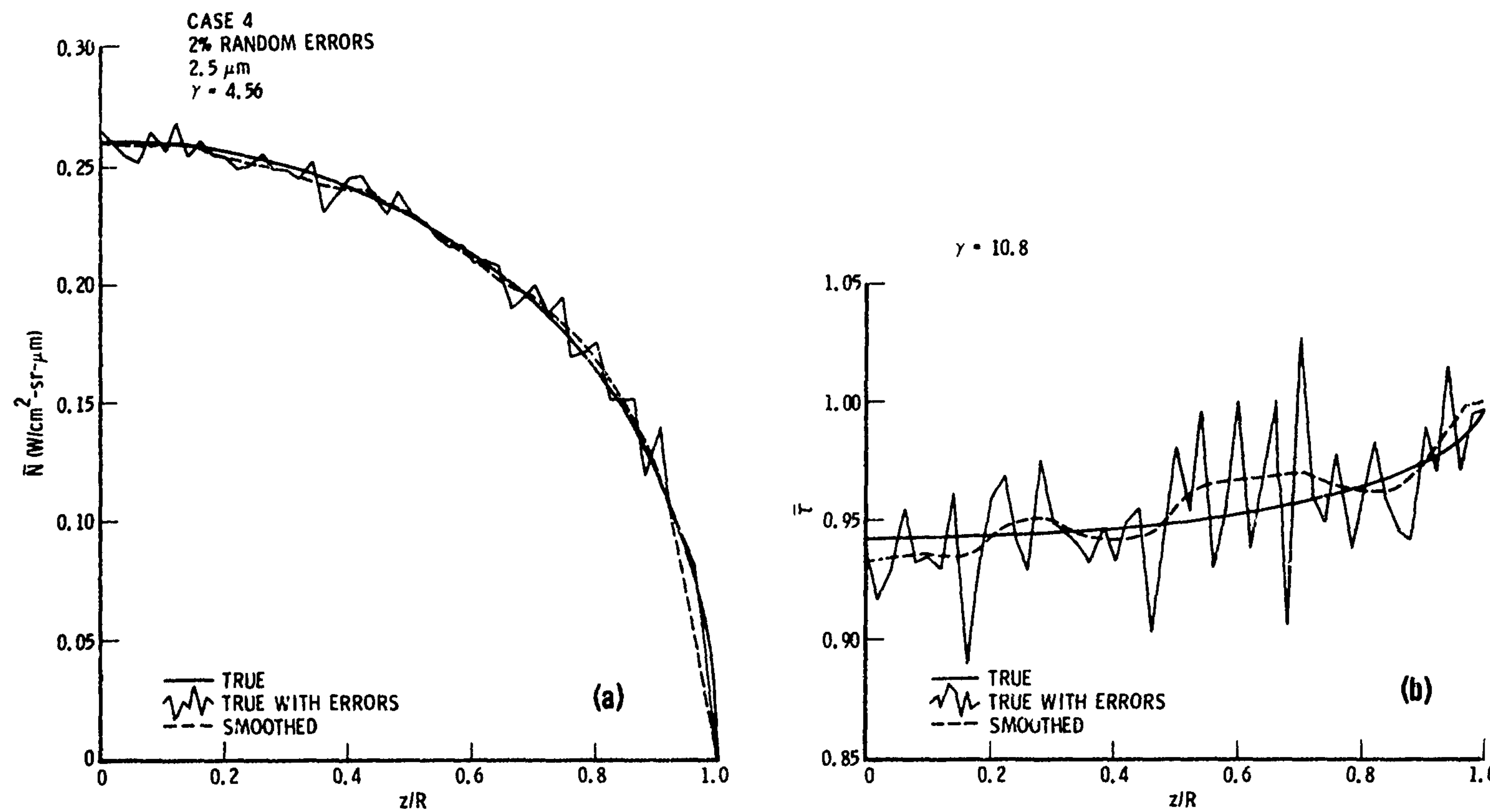

Fig. 50. Transverse H_2O E/A Profiles for Random Error Analysis of Engine Test Case 4. (a) Radiance; (b) Transmittance.

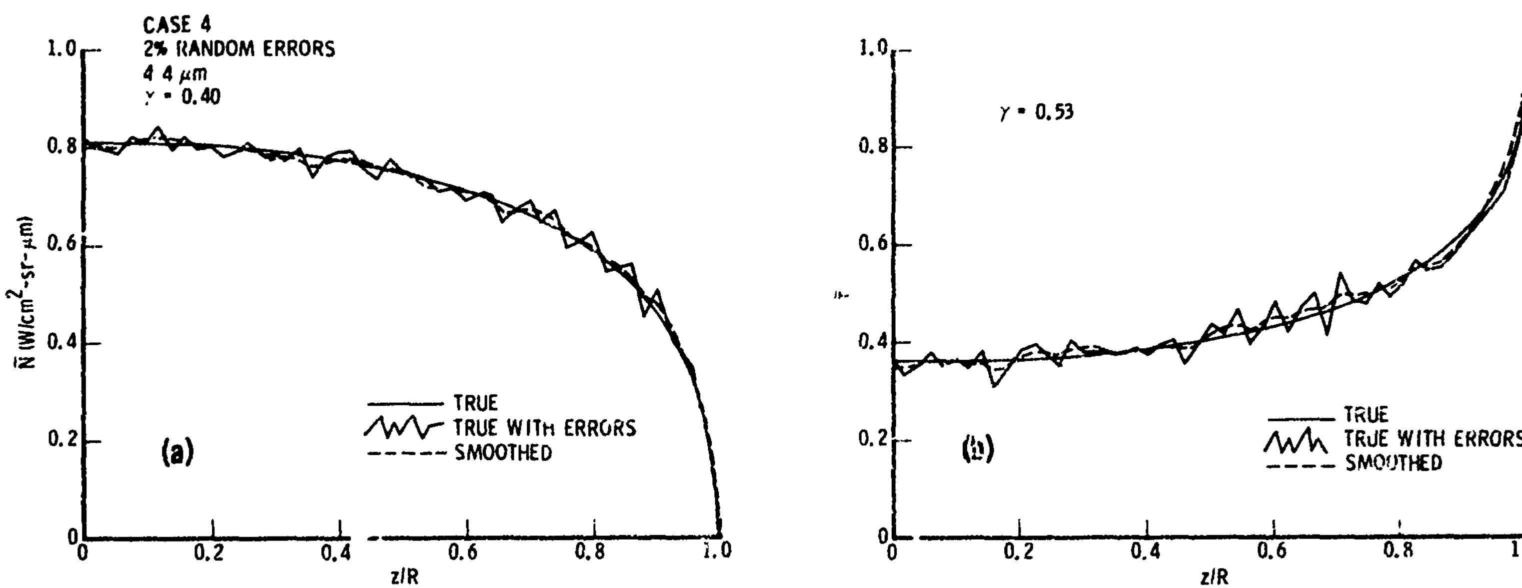

Fig. 51. Transverse CO_2 E/A Profiles for Random Error Analysis of Engine Test Case 4. (a) Radiance; (b) Transmittance.

increase in γ was that for smaller γ, the error curves were still too rough to allow the inversion algorithm to operate without generating indeterminate conditions in the starting Abel inversion.

The resulting inversions for T and c are shown in Fig. 52. In all cases, the results display severe fluctuations about the true profiles. The magnitude of fluctuations is so bad that, except for the temperature result obtained from inverting the 4.4-μm CO_2 profiles, the results are nearly meaningless.

The reason for these poor results is due to the heretofore used smoothing criterion that the optimum γ is that for which the rms difference between the smoothed and unsmoothed transverse profiles is equal to the superimposed rms error. This criterion is too severe. A reanalysis of Case 4 is made in Section VIIIE.

D. Engine Test Case 12

The radial pTc profiles and transverse emission/absorption profiles for Case 12 are shown in Figs. 18 and 30, respectively. The inversion of this case with superimposed 2% rms random errors was carried out only for the 4.4-μm profiles. In the 2.5-μm region, the transmittance is never smaller than ~0.98. Thus, the imposition of 2% errors on transmittance converts to a 100% rms error in absorptance. Since absorptance is the basic data used in inversion, it was felt that inversion of this case would be meaningless. The true, randomized, and smoothed 4.4-μm transverse profiles are shown in Fig. 53. The smoothing parameters were increased to four times their optimum value in order to avoid indeterminate results.

Inversion results for the Abel and iterative Abel methods are shown in Fig. 54. As for the case with no errors (see Section VIIID), inversion results for r/R below 0.4 and above 0.85 are meaningless; otherwise, the inversion display the expected behavior.

The iterative Abel inversion displayed a new behavior not seen in any previous inversions. With increasing iteration, the rms difference between successive radial profiles at first fluctuates around a generally decreasing

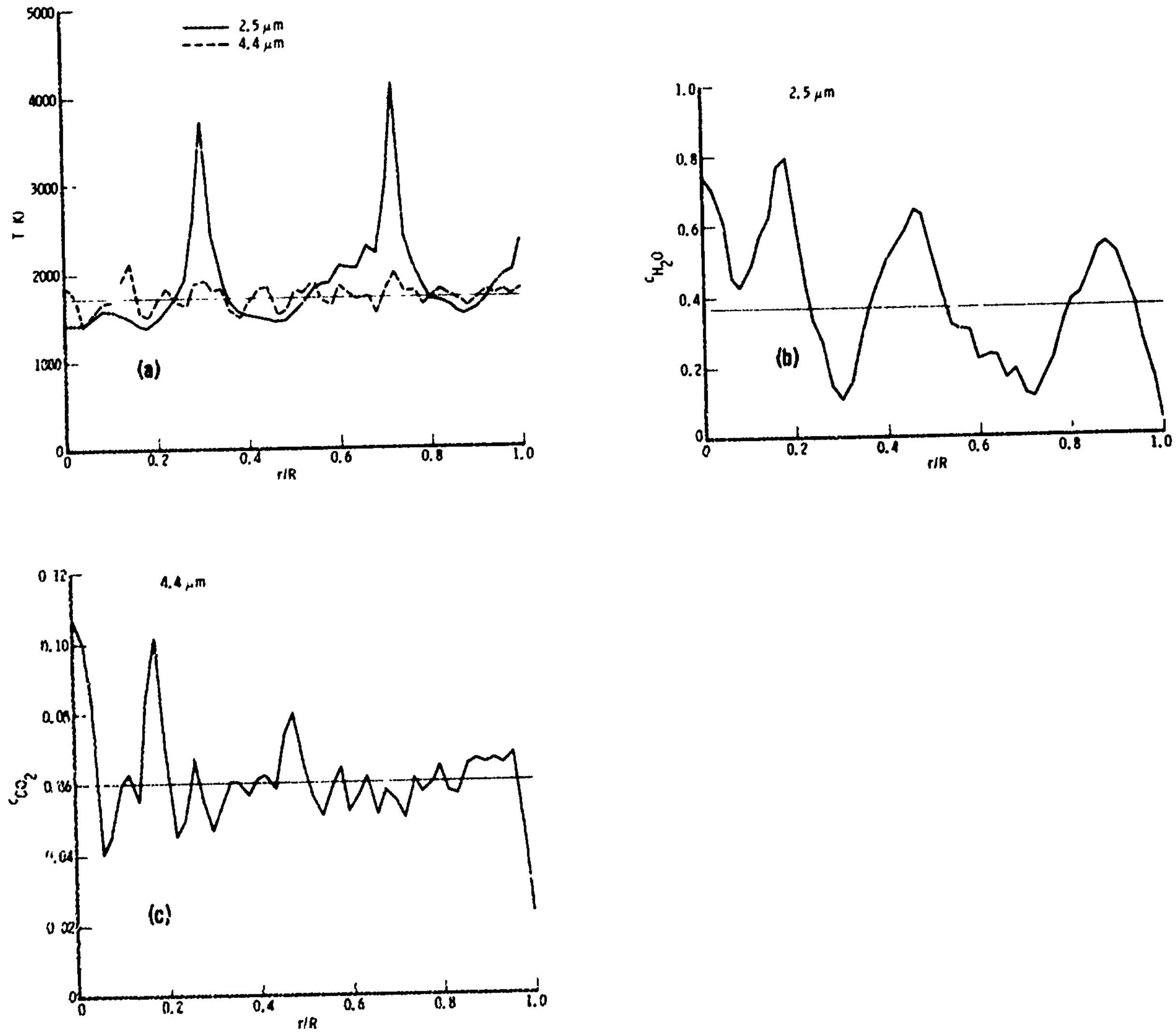

Fig. 52. Comparisons between True and Inverted Radial Profiles for Engine Test Case 42. (a) Temperature; (b) H_2O concentration; (c) CO_2 concentration.

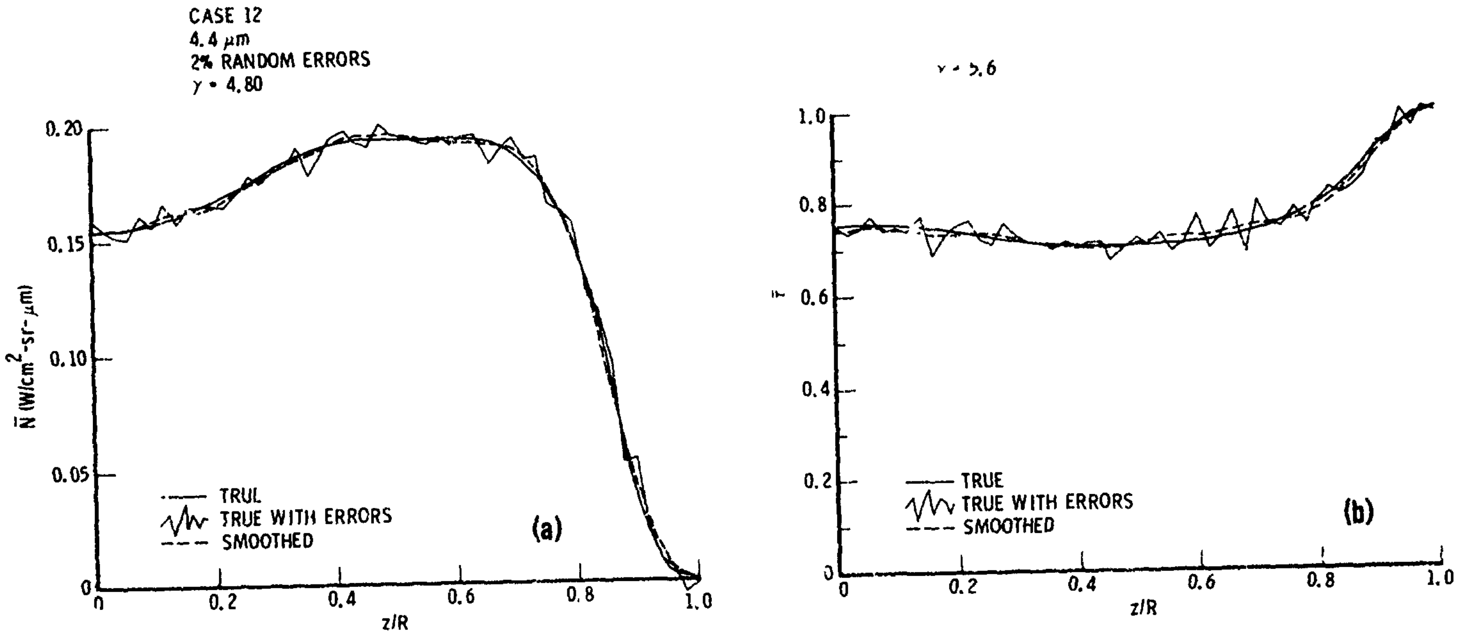

Fig. 53. Transverse CO_2 E/A Profiles for Random Error Analysis of Engine Test Case 12. (a) Radiance; (b) Transmittance.

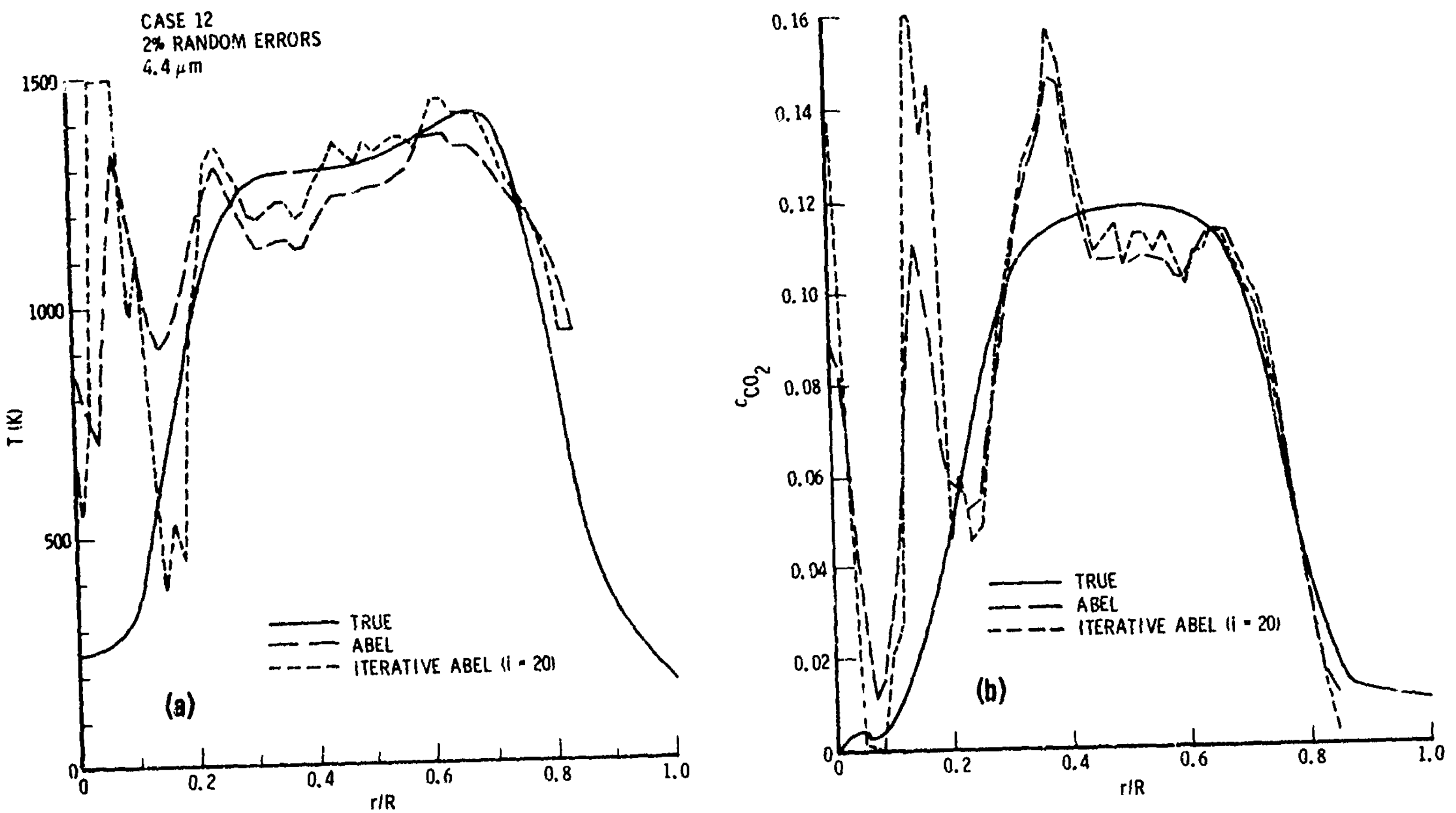

Fig. 54. Comparisons between True and Inverted Radial Profiles for Engine Test Case 12. (a) Temperature; (b) CO_2 concentration.

value before maintaining a steady decrease at about i = 10 (Fig. 55). However, the decrease, at least for temperature, continues only out to $\sim$i = 20 at which point an instability develops which results in an increase of ΔT_{rms} with i. The inversion results of Fig. 54 were taken from the 20th iteration.

E. Considerations on Presmoothing

The results obtained so far indicate that random fluctuations in input transverse emission/absorption profiles can produce serious error in the inverted radial profiles even when the random fluctuations are dampened by presmoothing of the transverse profiles. The criterion applied so far to the degree of smoothing allowed on the transverse profiles is that the rms difference σ between the smoothed and unsmoothed profiles should be about equal to the estimated experimental rms error ϵ of the data (or, in the case of the data error simulation tests, equal to the rms value of the artifically imposed fluctuations). Reconsideration of the smoothing procedure suggests that this criterion is too severe in most cases and that a higher degree of smoothing can be tolerated without introducing any significant error, that is, without seriously "over-smoothing" the profiles.

Consider the σ versus γ curves of Fig. 46. These curves are typical for most of the smoothing performed so far. The shape of the curve is linear for small γ. As γ increases, the curve levels off somewhat to form a plateau region before again increasing sharply with γ. The appropriate values of γ based on estimated (actually, in this case, known) rms fluctuations occur in this plateau region. Presumably, the shape of the curve in the linear region corresponds to increased smoothing of the random errors with no distortion of the underlying profile, the plateau region corresponds to complete smoothing of the random errors with no profile distortion (i.e., oversmoothing), and the sharp increase of σ with γ beyond the plateau corresponds to an increase smoothing and distortion of their underlying profile. Although not shown in Fig. 46, with increased smoothing beyond the upswing at the end of the plateau, the curve again levels off at a value near the mean value of radiance (or absorptance). This condition reflects a complete smoothing

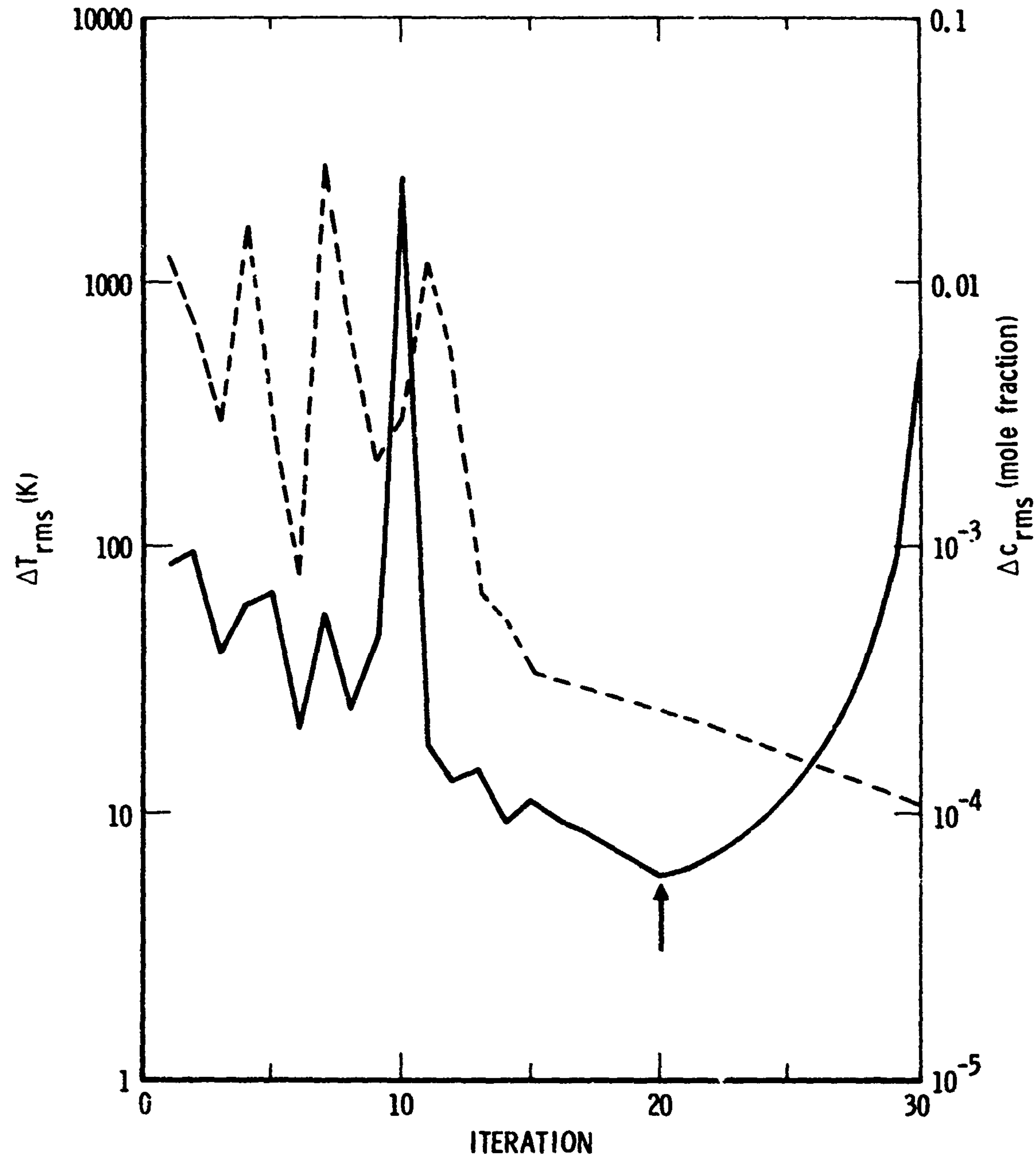

Fig. 55. Convergence Behavior for Engine Test Case 12 at 4.4 μm with 2% Random Errors

(errors and underlying profile) to some constant value, that is, to the point where the curvature of the smoothed profile reaches its absolute minimum value of zero.

The usual condition that obtains in these analytic cases is that the value of γ that makes σ equal to the superimposed rms error ϵ occurs near the left hand side of the plateau. In application to real data, ϵ is only an estimate and such an exact selection of γ could not be made. However, since σ does not vary much with γ in the plateau region, its selection is not critical. Thus, a second criterion for the selection of γ can be imposed by requiring it to be in the plateau region (if it can be identified in the σ vs γ plot). However, even this is not enough. Consider the σ versus γ curve for the Case 4 Engine Test shown in Fig. 56. Here, the plateau region extends over an enormous range from ~ 1 to beyond 1000 (the upswing is still not evident at $\gamma = 1000$). The optimum value of γ determined by requiring $\sigma = \epsilon = 0.02$ is $\gamma \sim 1$. But, σ is not much greater than 0.02 even for γ as large as 1000. Consequently, smoothing of the profile with $\gamma = 1000$ does <u>not</u> constitute a significant oversmoothing. In Fig. 57 are shown the unsmoothed transmittance profile and the smoothed profile for $\gamma \sim 1$ and $\gamma = 1000$. For either of these cases, $\sigma \sim 0.02$, yet the curve for $\gamma = 1000$ is decidedly smoother. The question remains, how can two drastically different values of γ give significantly different degrees of smoothing yet give the same result for the rms difference between the smoothed and unsmoothed curves? The answer lies partially in the distribution of differences between the smoothed and unsmoothed curves. When γ is taken from the left end of the plateau, the deviations making up σ are all about the same size. When γ is taken from the right end of the plateau, the deviations are more randomly distributed (i.e., both small and large deviations occur). Clearly, the latter case is the condition desired since this is how the deviations were superimposed in the first place. The result of this analysis is a new criterion for selecting γ; γ should be taken as the rightmost value of the plateau region. This ensures that $\sigma \sim \epsilon$ and that the deviations are randomly distributed.

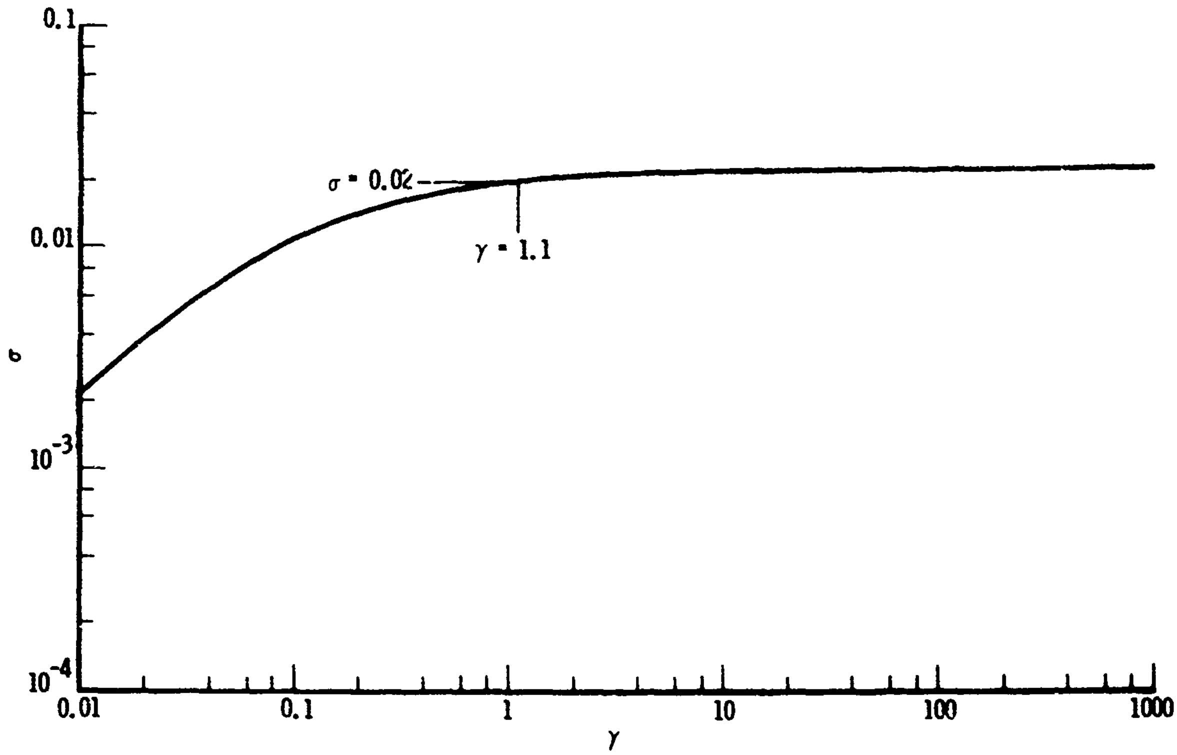

Fig. 56. Absorptance Smoothing Curve for Engine Test Case 4 with 2% Random Errors

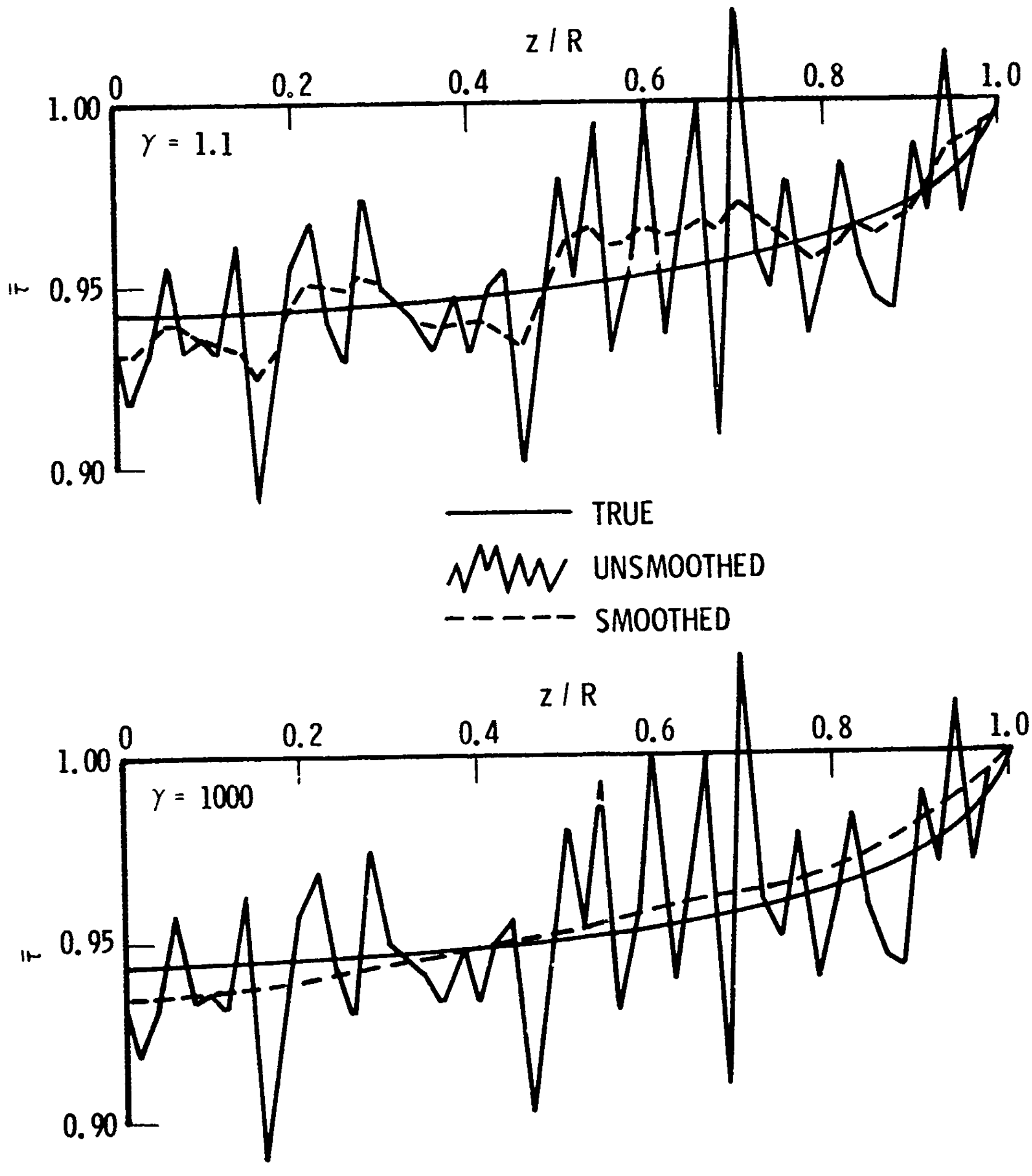

Fig. 57. Transverse Transmittance Curves for Random Error Analysis (2% rms error) of Engine Test Case 4

The Case 4 inversion for H_2O was rerun with increased smoothing. The critical variable here is the degree of noise on the transmittance or absorptance profile. The effect on increased smoothing on this profile has already been shown in Fig. 57. Inversions were made for smoothing parameters of γ_a = 10, 100, 1000 (the value γ_a = 10 is near the value used in the inversion of Section VIIB). The radiance profile was smoothed with corresponding values γ_r = 5, 50, 100.

The temperature inversion results for these increasing values of γ are shown in Fig. 58a. The large spikes for the previous inversion (γ_a = 10) are substantially reduced for γ_a = 100 and are essentially nonexistent for γ_a = 1000. In the last case, the maximum deviation of the inverted temperature profile from the true profile is only ~ 200 K. The inversion results for H_2O concentration are shown in Fig. 58b where again the enhancement of smoothing results in a much better inversion, although not as good as for temperature. Here, even for γ_a = 1000, a 30% discrepancy occurs between the inverted and true profile. However, this discrepancy cannot be critisized since the errors of the original absorptance curve are also ~ 30%.

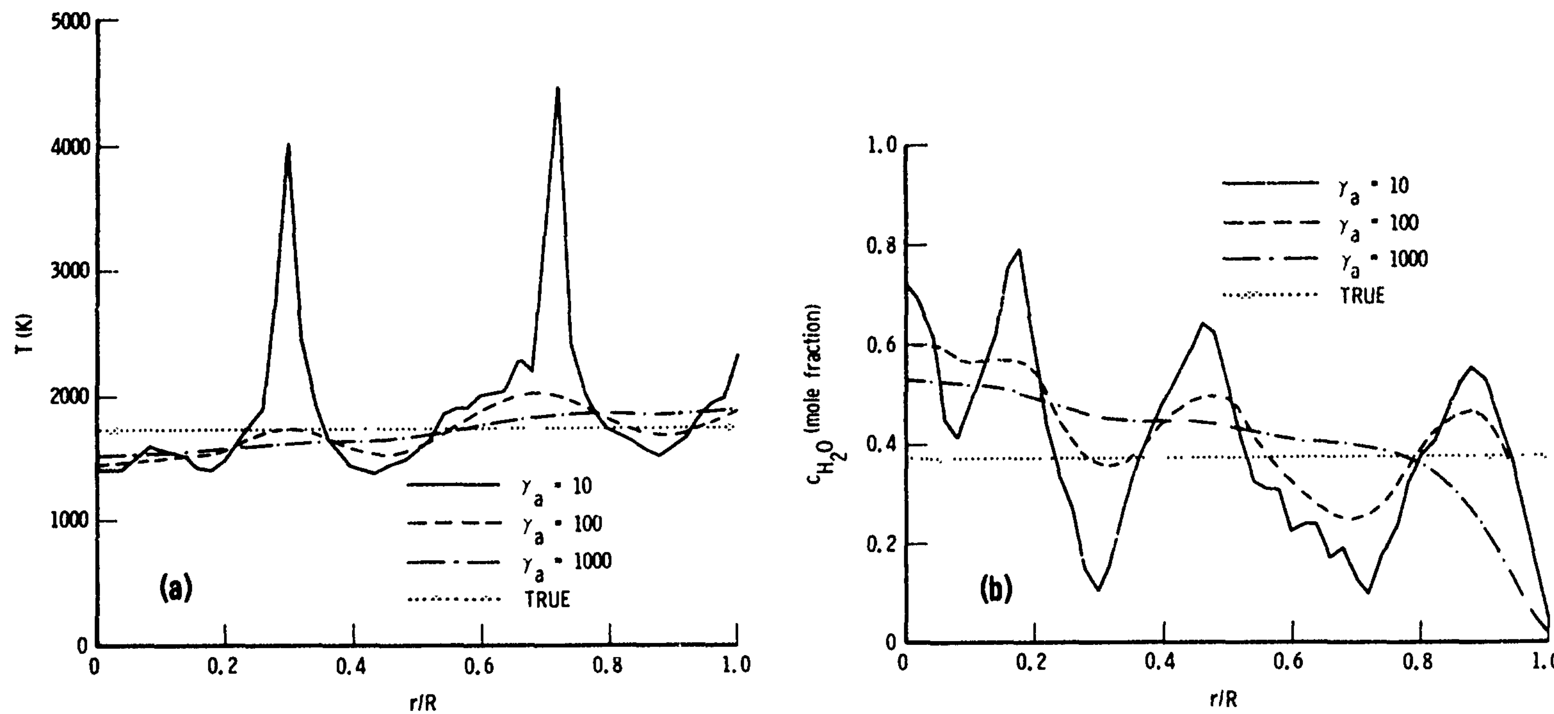

Fig. 58. Revised Comparison between True and Inverted Radial Profiles for Engine Test Case 4. (a) Temperature; (b) H_2O concentration.

IX. BIAS ERROR ANALYSIS

A. Introduction

A variety of calculations were performed in order to assess the effects of bias error on the accuracy of radial pTc profile retrieval. With the exception of assuming an infinitesimal field of view on data collection, bias error in the input data itself (e.g., errors due to radiometer calibration error, instrument zero line drift and optical alignment errors) were not considered because they are generally very much smaller than the random error of the data and essentially masked by the latter. (An exception to this is presented in the next section where the effect of correcting the radiance profile for background radiation is considered.) The bias errors considered here are those that may be introduced by the radiation and inversion models used in the analysis, that is, those introduced by the modelling assumptions.

B. Effect of Band Model Parameter Uncertainty

The effect of the uncertainty in band model parameters on inversion is considered in two ways. First, a simple-minded analytical treatment is presented. Second, the results of some actual inversion in which parameter variations were introduced are discussed.

Analytical Analysis

In any band model for an array of arbitrary lines and a uniform optical path, the weak and strong absorption limits for absorptance are

$$\bar{\alpha} \to \begin{cases} \bar{k}u & \text{weak} \\ 1 & \text{strong} \end{cases}$$

These limits simply display the linear dependence of $\bar{\alpha}$ on $\bar{k}$ for weak ($\bar{\alpha} \to 0$) absorption and the independence of $\bar{\alpha}$ on any band model parameter for strong absorption. Consider then, only the weak absorption case. The fractional change in $\bar{\alpha}$ due to changes in $\bar{k}$ is simply

$$\frac{\Delta\bar{\alpha}}{\bar{\alpha}} = \frac{\Delta\bar{k}}{\bar{k}}$$

and similarly, since $\bar{N} = N^*\bar{\alpha}$, the fractional change in radiance and N^* is also

$$\frac{\Delta N^*}{N^*} = \frac{\Delta\bar{N}}{\bar{N}} = \frac{\Delta\bar{k}}{\bar{k}}$$

The change in inversion temperature to changes in N^* is related through the Planck radiation law. In the extremes of low and high temperature we have, respectively

$$N^* = \begin{cases} C_1 e^{-C_2/T} & T \to 0 \\ \dfrac{C_1}{C_2} T & T \to \infty \end{cases}$$

where C_1 and C_2 are radiation constants. From these limiting relations we find

$$\frac{\Delta T}{T} \to \begin{cases} \dfrac{\Delta N^*}{N^*} \dfrac{T}{C_2} = \dfrac{\Delta\bar{k}}{\bar{k}} \dfrac{T}{C_2} & T \to 0 \\ \dfrac{\Delta N^*}{N^*} = \dfrac{\Delta\bar{k}}{\bar{k}} & T \to \infty \end{cases}$$

For all practical purposes, $T < C_2 = (1.439\ \text{K cm}^{-1})\nu$ so that the worst case variation is

$$\left|\frac{\Delta T}{T}\right| \simeq \left|\frac{\Delta\bar{k}}{\bar{k}}\right|$$

A similar result for concentration error can be obtained from the thin source relation $\alpha = ku = kcpL$. It is easily established that

$$\left|\frac{\Delta c}{c}\right| = \left|\frac{\Delta \bar{k}}{\bar{k}}\right|$$

Thus, we conclude that an estimate of maximum fractional temperature and concentration inversion error is of the order of the fractional error in the absorption band model parameter $\bar{k}$.

Inversion Analysis

The band model parameters used in EMABIC are constructed by combining the high temperature NASA parameters with low temperature parameters derived from the AFGL atmospheric absorption line data compilation (see Section V). These three sets of parameters for H_2O at $\nu = 4000\ cm^{-1}$ with $\Delta\nu = 25\ cm^{-1}$ are shown in Fig. 59. The effect of band model parameter variation is demonstrated by inverting H_2O transverse radiance and absorptance profiles generated with the combined parameters using the three parameter sets. Case 11 of the engine test cases was used since this case displayed the highest degree of temperature variation across the plume. Aside from the variation of parameter set, all the inversions employed the Voigt line shape, the DR approximation, and N = 50. The original transverse profiles were generated with these same conditions.

The inversions for temperature are shown in Fig. 60a. The garbage below r/R = 0.45 is known to be an implicit failure of inversion due to the lack of information content in the flat transverse profiles and should be ignored here (see Section VIID). Above r/R = 0.45, the solid line reproduces the true radial temperature profile as expected. The inversion using the line-averaged parameters also reproduces the true profile. This result is also expected since up to the highest temperature of the optical path (~ 1100 K), the line-averaged and combined parameters are essentially identical (see Fig. 59). The inversion using the NASA parameters displays a large deviation from the true profile in the region $0.45 \leq r/R \leq 0.70$.

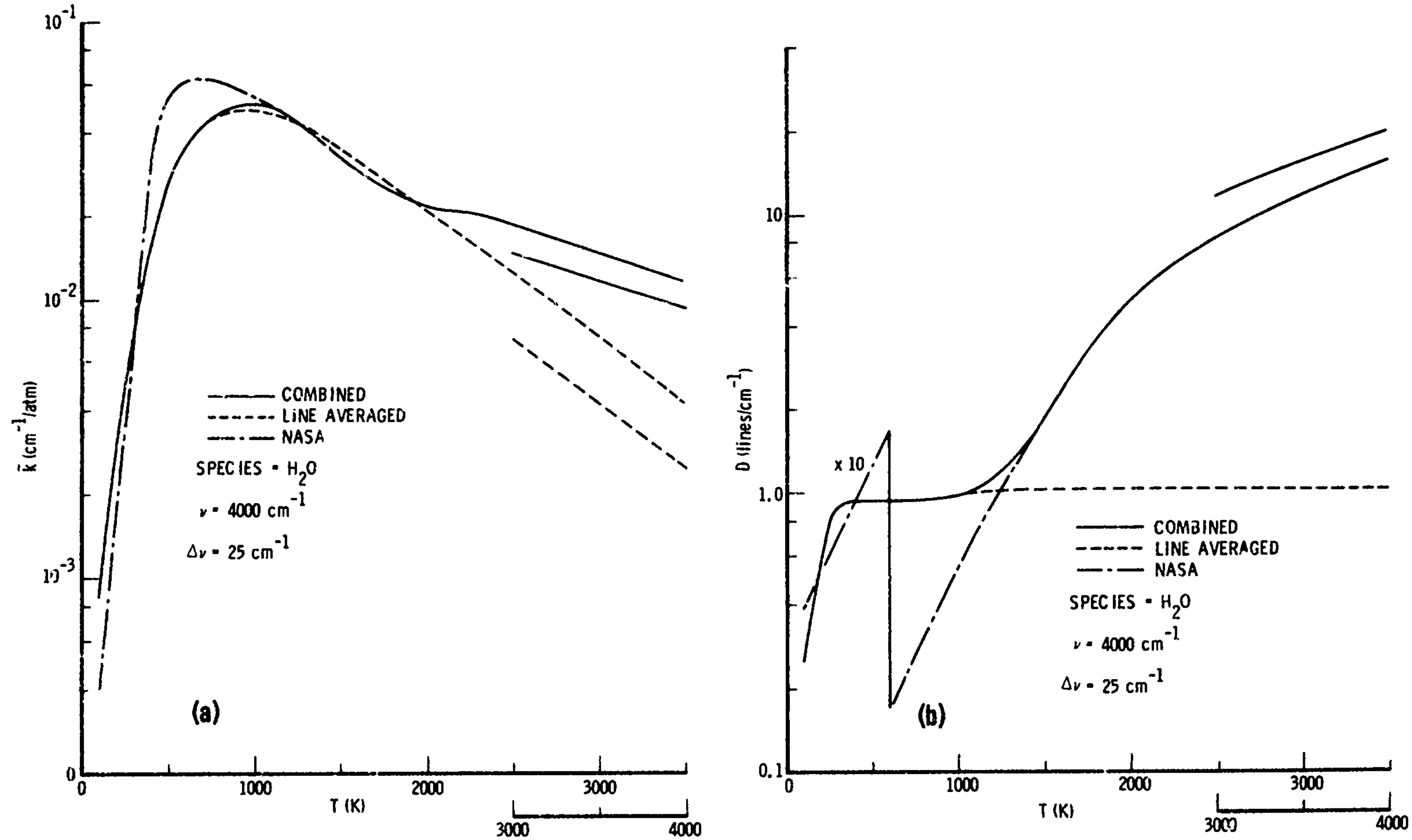

Fig. 59. Band Model Parameters for H_2O. (a) Mean absorption parameter; (b) Line density parameter

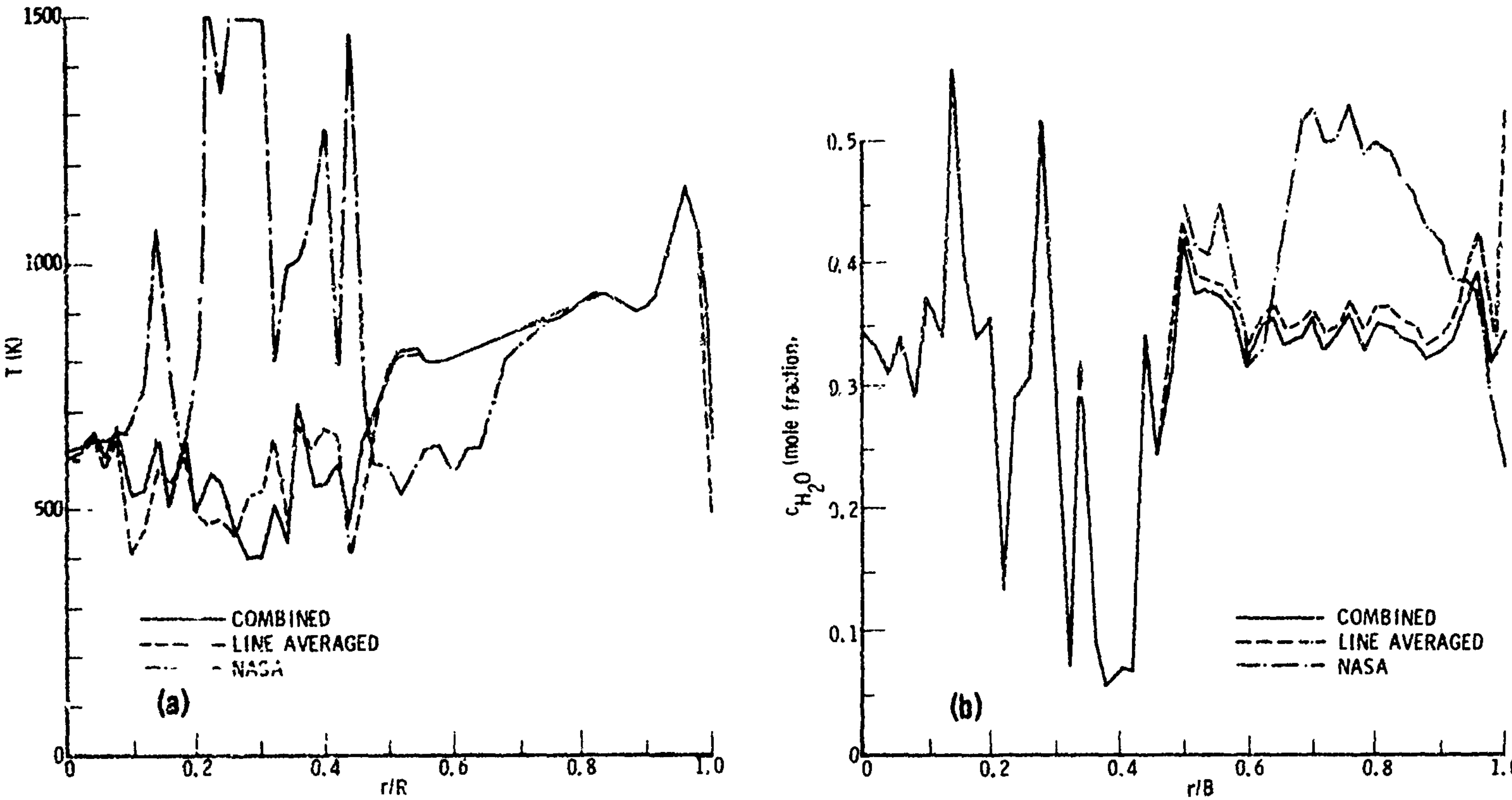

Fig. 60. Inversions for Engine Test Case 11 with Three Band Model Parameter Sets. (a) Temperature; (b) H_2O concentration.

The temperature in this region is roughly 750 K. Reference to Fig. 59 shows that this is precisely the temperature region where the NASA parameters differ significantly from the combined parameters. At 750 K, in fact, the two parameter sets vary by $\Delta\bar{k}/\bar{k} \sim 0.3$. The inversion error in $0.5 \le r/R \le 0.7$ is also ~ 0.3, thus supporting the simple analytical result obtained earlier.

The inversion results for H_2O concentration are shown in Fig. 60b. Again, the results obtained with the combined and line-averaged parameters are comparable while the result obtained with the NASA parameter set is quite different. This difference is as readily explained as for temperature although the difference occurs in a slightly different r/R region. Here, an average error of ~35% obtains in the 0.65 → 0.85 region. The temperature is roughly 900 K and the percentage difference in $\bar{k}$ is ~25%.

C. Effect of Pressure Profile

As discussed in Section IIIA, it is not possible to invert the two independent E/A transverse profiles to get all three of the radial pTc profiles. One of the radial profiles has to be assumed. In all of the inversions treated so far, T and c have been assumed to be the unknown radial profiles. The pressure profile has been taken as its true value. In a realistic application, p would not be known. (However, pressure is the one variable that can be reliably predicted *a priori* with standard combustion/nozzle codes.) A test was made to assess the importance of knowing p. This test was carried out on the engine test Case 4. The uniform source conditions are given in Table 5 and the computed transverse E/A profiles in Fig. 22. Both profile generation and inversion were performed with the Voigt line shape. In inversion, the value of pressure was varied ± 20% from the value used in profile generation. The result was that when p was 20% too low, the inverted result for c was 20% too high. Similarly, when p was 20% too high, c was 20% too low. The variation on p had no effect on the inverted temperature. The important result is that regardless of the uncertainty in p (at least up to ± 20%), the *partial pressure* of the active species, that is, the product cp is retrieved with essentially no error. These results are summarized in Table 8.

Table 8. Pressure Variation Results (Case 4)

Inversion Pressure P (atm)	$\bar{c}$ (mole fraction)[1]		$\bar{c}P$ (atm)		% Error from true[2]	
	H_2O	CO_2	H_2O	CO_2	H_2O	CO_2
0.6320 (-20%)	0.4670	0.07507	0.2951	0.04744	-0.1	+0.6
0.7900 (True)	0.3708	0.05969	0.2929	0.04716	-0.6	0
0.9480 (+20%)	0.3071	0.04953	0.2911	0.04695	+1.2	-0.4

(1) $\bar{c}$ = mean value of c in $0 \leq r \leq R$.

(2) True values: $c_{H2O} = 0.373$ $\quad Pc_{H2O} = 0.2947$

$c_{CO2} = .04716$ $\quad Pc_{CO2} = 0.0597$

D. Effect of Lineshape

Again using Case 4 as an example, the error that could be introduced by assuming a radiation model based on a pure Lorentz profile was examined. In this case, the transverse E/A profiles generated with the Voigt profile were inverted with the Lorentz profile. The results are tabulated in Table 9. As for the effect of pressure profile variation, the variation of lineshape had no effect on the result for temperature retrieval. The result for H_2O concentration was 4.2% higher than the true value, and the CO_2 concentration was 2.7% higher than its true value. Case 4 is a high pressure example, and these small inversion errors would be expected. For low pressure cases, larger errors would occur.

E. Effect of Nonuniformity Approximation

The effect of nonuniformity approximation on E/A profile prediction is evident from the nonuniform source engine test case results (Cases 8-12) presented in Figs. 26-30. In all cases, the DR approximation predicts a larger radiance and absorptance than the CG approximation.

An assessment of the error inherent in inversion using the CG or DR radiation model was made for Case 10. This case was chosen because of its one, well-isolated and strong nonisothermality feature at $r/R \simeq 0.35$ (see Fig. 16a). The inversions were performed on the 2.5-μm transverse emission/absorption profiles generated with the DR approximation and with no superimposed errors. Inversion of these profiles with the DR approximation gave temperature and concentration profiles that agreed exactly with the true radial profiles. The results obtained by inverting the DR transverse profiles with the CG approximation are shown in Fig. 61. The significant result is that the CG approximation failed to reproduce the temperature dip at $r/R \simeq 0.35$. Agreement with the exact profile for larger r ($r/Z \geqslant 0.5$) is very good and adequate for smaller r ($r/Z \leqslant 0.1$). The error near $r/R \simeq 0.35$ is ~400 K.

Table 9. Lineshape Variation Results -- Case 4 Inversion

Inversion Lineshape	λ (μm)	$\overline{T}$ (K)	$\overline{c}_{H_2O}$	% Error from 0.373	$\overline{c}_{CO_2}$	% Error from 0.0597
Voigt	2.5	1728.2	0.3708	+0.6	---	---
Lorentz	2.5	1728.1	0.3888	+4.2	---	---
Voigt	4.4	1728.2	---	---	0.05969	~0
Lorentz	4.4	1728.2	---	---	0.06132	+2.7

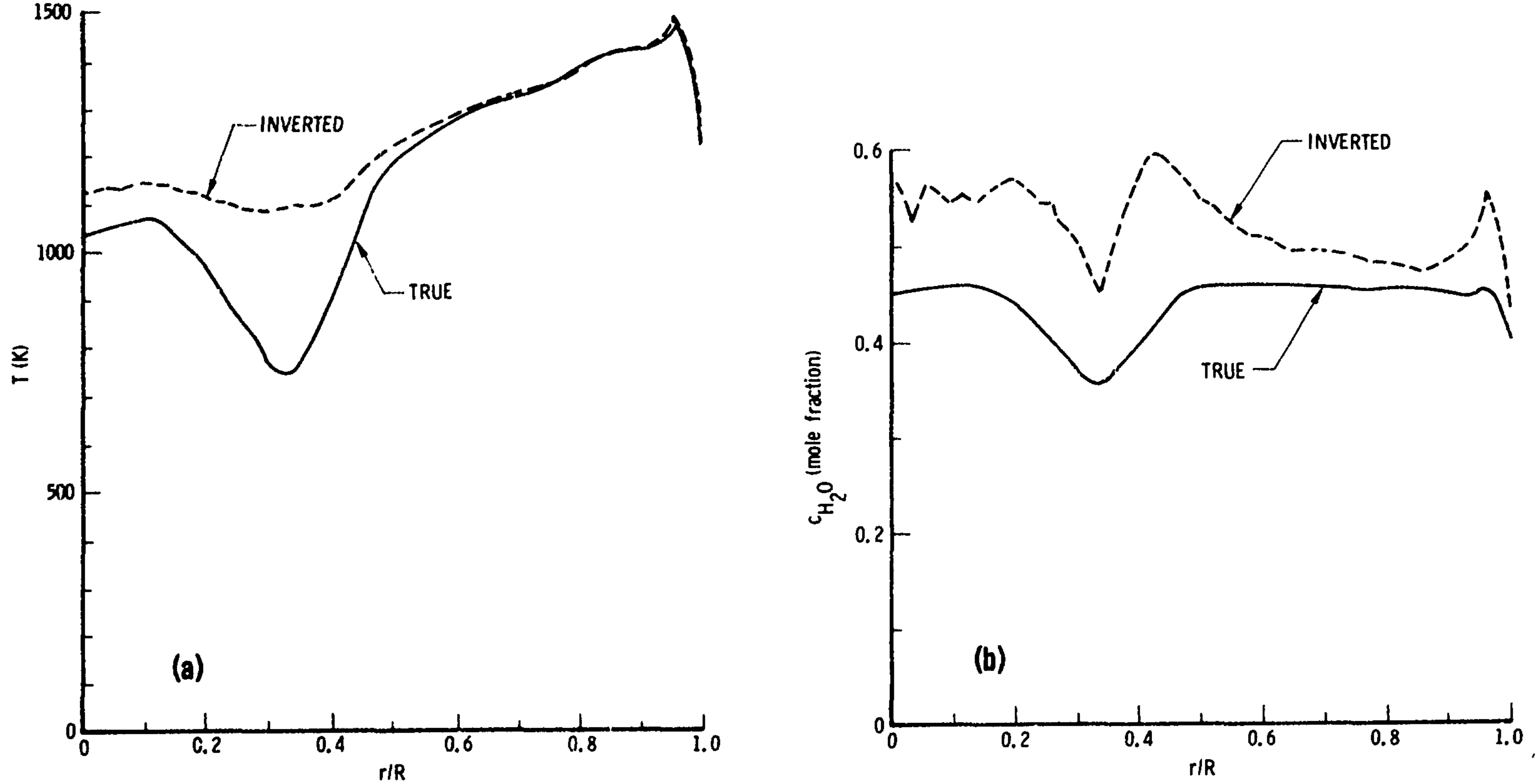

Fig. 61. Effect of Nonuniformity Approximation on Inversions for Engine Test Case 11. (a) Temperature; (b) H_2O concentration.

F. Effect of Finite Field of View

The assessment of FOV on inversion was carried out for the Case 4 nozzle conditions. These conditions are representative of the ERASE 100 lb (6/1 Cone) test and are uniform with R = 4.178 cm, p = 0.790 atm, T = 1728 K, c_{H_2O} = 0.373, and c_{CO_2} = 0.0597. CO_2 emission/absorption profiles were generated for these conditions and then convolved with rectangular FOV slits of width $\Delta z/R$ = 0.04, 0.08, and 0.16. The true and convolved profiles for radiance and transmittance with $\Delta z/R$ = 0.16 are shown in Fig. 62. The only discernable difference between the true and convolved profiles lies in a region $\Delta z/R$ wide around z/R = 1. These convolved profiles were then inverted in order to see how the deduced temperature and concentration differed from the true profiles. The results for temperature and concentration are shown in Fig. 63. The inversions were performed with effective nozzle radii $R' = R + \Delta z/2$ rather than with the true value R.

Even for $\Delta z/R$ as large as 0.16, no effect is seen on the inversion for temperature within the true boundary value z = R. Even over the extended region $z = R + \Delta z/2$, deviations from the true profile occur only at the end point, and these are not large. The effect of FOV on concentration is qualitatively different than on temperature. Here, the effect propagates a distance $\Delta z/2$ from R into the true source region. The slight overshoot at $R - \Delta z/2$ amounts to a maximum value of only ~10%. At z = R, on the other hand, the concentration for all cases is approximately one-half the true value. The conclusion for this one case then, is that the effects of FOV up to 16% of R are inconsequential to temperature inversion and significant to concentration only in the region $R - \Delta z/2$ to R.

In a sense, this assessment for a uniform source is a worst case condition. If, for example, the source were nonuniform with a temperature/concentration minimum near r = 0, then the transverse emission/absorption profiles would be even flatter around z = 0 than those for a uniform source. While this condition causes serious problems in the inversion itself, it does mean that there is less difference between the true and FOV convolved profiles.

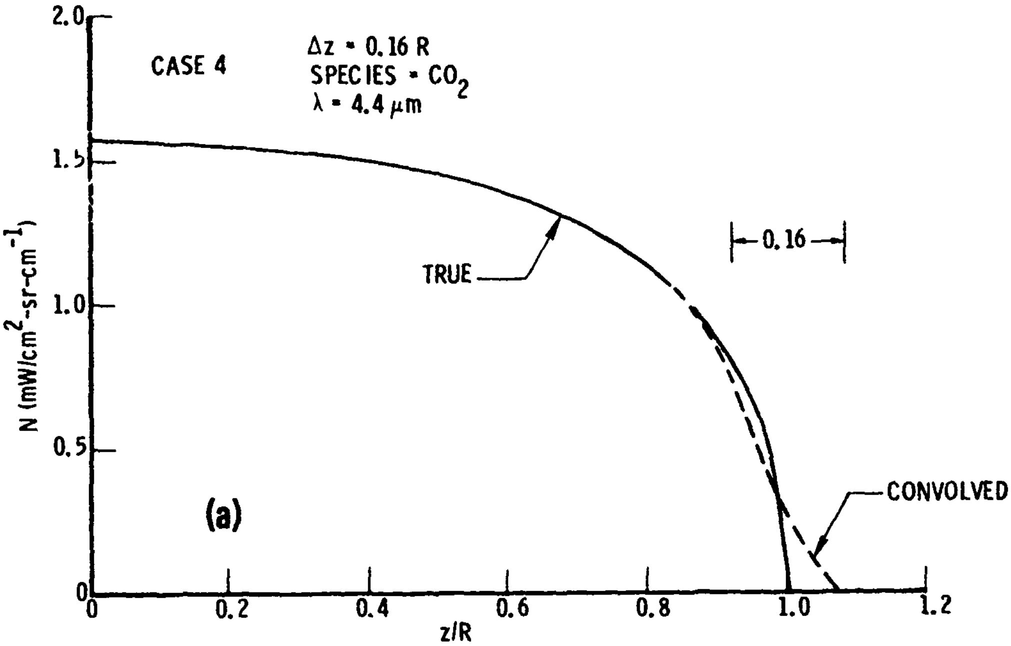

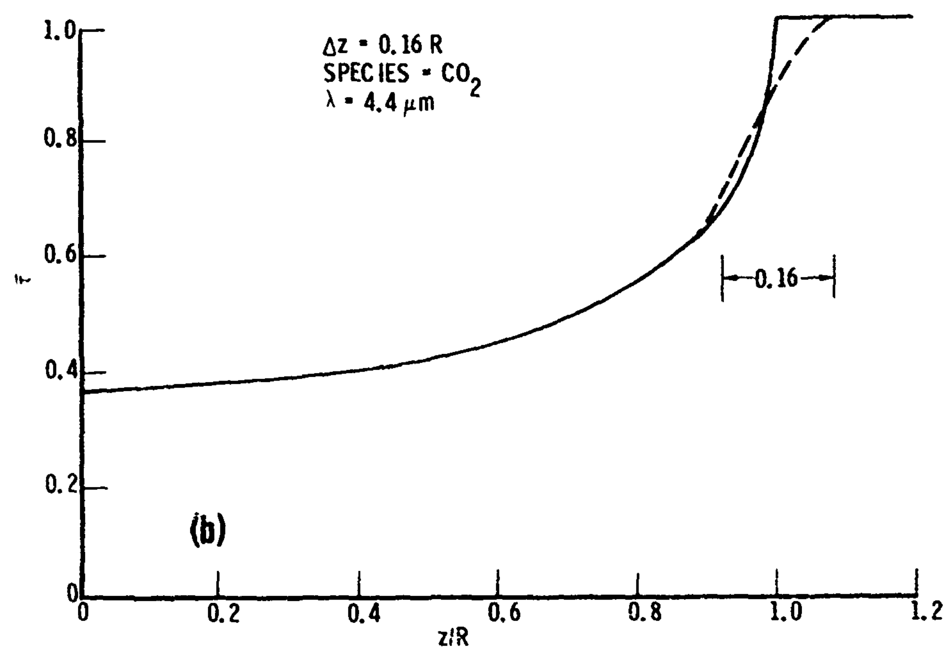

Fig. 62. Convolutions of Transverse E/A Profiles with a Rectangular Field-of-View Slit Function. (a) Radiance; (b) Transmittance.

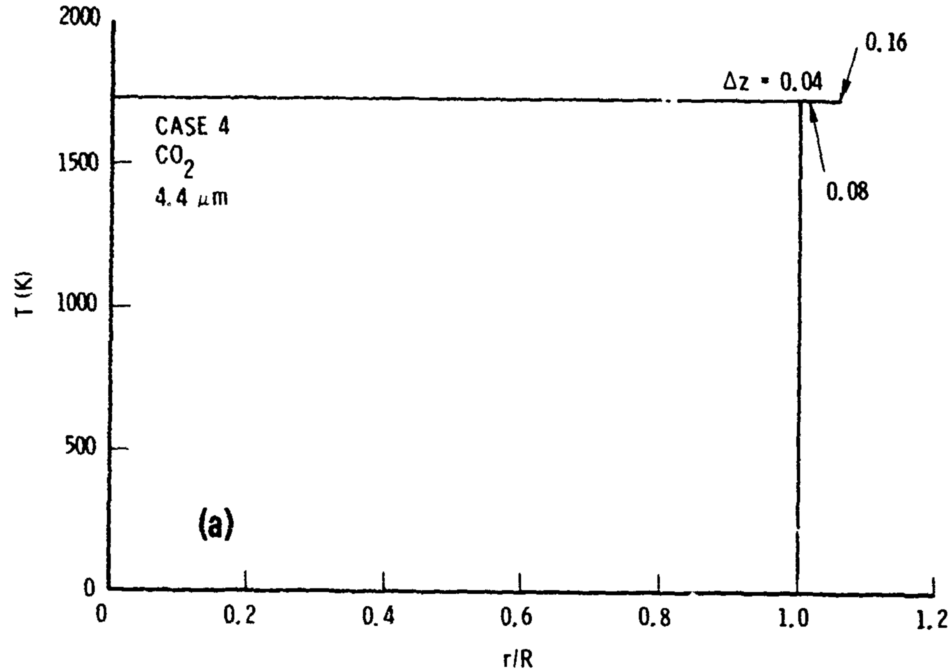

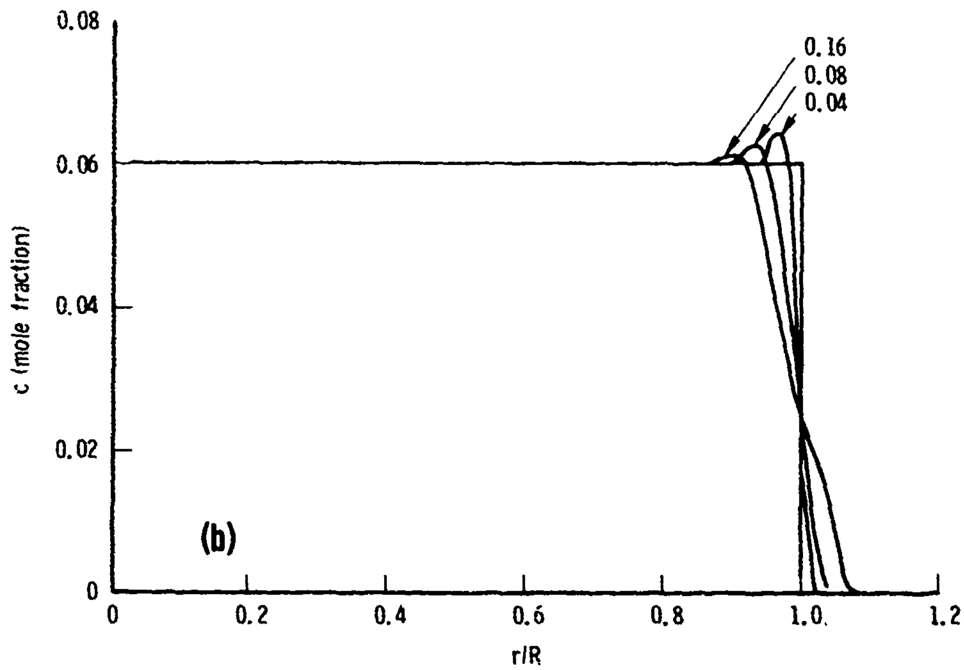

Fig. 63. Effect of Field-of-View Convolution on Inversion. (a) Temperature; (b) CO_2 concentration.

X. TRANSTAGE DATA INVERSION

A. Introduction

Twelve test cases from the NERD Phase I measurements program were selected for inversion analysis. The E/A measurements were made at AEDC* on the Transtage engine operating with three different injector designs and three O/F ratios. Eight cases were for CO_2 and four were for H_2O. The case numbering, engine operating conditions, and spectral bandpass are given in Table 10. The three principal operations of data preparation, profile inversion, and random error analysis are described below in detail in Sections B, C, and D, respectively. Revised inversions for selected cases are discussed in Section E.

B. Data Preparation and Smoothing

The first step in data preparation consisted of plotting the raw transtage E/A data so that zero levels for radiance and absorptance and effective source radii could be selected. These data plots are shown in Figs. 64 through 75. The dashed lines of these figures indicate the zero level selected, and these values are given in Table 11. In all cases, this level was determined by eye from the signal level beyond the experimental source radius of $R_e = 60.8$ cm. Radiance data were adjusted by subtracting the zero level from all data across the profile. Absorptance data were adjusted by a constant multiplicative value that forced the transmittance to unity outside the source region. For both radiance and absorptance and for all twelve cases, the plots allowed a selection of $R = 62$ cm as a reasonable apparent source radius.

For each profile, data points for which $r < 0$ (obtained experimentally because the transverse scanning mechanism could cross the center line) and $r > R = 62$ cm were discarded. The profiles (each consisting of

*These data were supplied by ARO, Inc., in card deck form and through appropriate Air Force channels.

Table 10. Transtage Engine Operating Conditions.

Case No.	Injector	C/F	Species	Spectral Filter
1	Baseline	1.7	CO_2	NERD CO_2
2	↓	2.0	↓	↓
3	↓	2.3	↓	↓
4	↓	2.0	H_2O	NERD H_2O Narrow
5	ITIPCUM2	1.7	CO_2	NERD CO_2
6	↓	2.0	↓	↓
7	↓	2.3	↓	↓
8	↓	2.0	H_2O	NERD H_2O Wide
9	ITIPCUM3	1.7	CO_2	NERD CO_2
10	↓	2.0	↓	↓
11	↓	2.3	↓	↓
12	↓	2.0	H_2O	NERD H_2O Wide

Table 11. Zero Levels for Correction of Transtage E/A Data

Case No.	$\Delta N (W/cm^2\text{-}sr\text{-}\mu m)$	$\Delta\bar{\alpha}$
1	0.0050	0.004
2	0.0025	-0.004
3	0.0075	0.004
5	0.005	0
6	0.0075	0.012
7	0.005	0.008
9	0.005	0.014
10	0.005	0.004
11	0.005	-0.004
4	0.001	0.002
8	0.008	0.002
12	0.003	0.001

~ 200 to 300 points across the transverse position and for an unequal grid) were then smoothed using the general smoothing algorithm of Section IIID. The σ versus λ plots for this procedure are presented in Figs. 76 through 79. The CO_2 cases for common injector are shown together and the three H_2O cases are shown together since these groupings display common smoothing characteristics.

Discussions presented in Section VIII on the analysis of artificially constructed noisy data brought out two criteria for the selection of an appropriate smoothing parameter: (1) γ should be selected so that $\sigma \sim \varepsilon$ where ε is an estimate of experimental rms random error; and (2) γ should be selected from the right hand side of the plateau region. Inspection of Figs. 76 through 79 indicate that whereas most of the absorptance smoothing curves display a reasonably well-defined plateau (cases 7 and 9 being exceptions), few of the radiance smoothing curves do (cases 3, 4, 7 and possibly 8 being exceptions). Thus, use of the second criterion alone would not be adequate for determining the radiance smoothing parameters. However, used in conjunction with the first criterion, it is usually possible to identify a hint of a plateau in the radiance smoothing curves near $\sigma \sim \varepsilon$ and thus to make a plausible selection of γ. The estimated rms errors in the raw data are indicated in Figs. 76 through 79 in order to facilitate the identification of these quasi-plateaus. An initial selection of γ values was made on the basis of these two criteria and smoothed curves were generated. These were compared with the raw data and a subjective assessment of the fit was made. In some cases, a noticeable under- or oversmoothing was evident. These cases were rerun with appropriately increased or decreased smoothing parameter. The final selected set of smoothing parameters are tabulated in Table 12 and comparisons between the final smoothed curves and raw data are shown

Table 12. Smoothing Parameters for Transtage E/A Data

Case No.	γ_E	γ_A
1	100	1000
2	100	1000
3	100	1000
5	100	200
6	100	200
7	100	200
9	100	200
10	100	200
11	100	200
4	1000	10,000
8	1000	10,000
12	1000	10,000

in Figs. 64 through 75. In all cases where γ was revised on the basis of the subjective judgement of goodness of fit of the smoothed curve to the data, the revised γ was still a reasonable value according to the initial selection criteria. For the most part, the smoothed curves fit the data quite well. Where the fit is not as good as one might expect by eye, the tendency is toward oversmoothing.

C. Inversion Results

The smoothed curves of Figs. 64 through 75 were defined on an equal interval grid with N = 100 and used as the basic input for inversion. Inversions were carried out with the Voigt line shape (modified NASA model), the DR nonuniformity approximation, and N = 50 zones. For each case, the band model parameter sets appropriate to the bandpass notation of Fig. 10 were used. The pressure profile used for all inversions was taken from combustion/nozzle calculation for O/F = 2.0,* and is shown in Fig. 80. Iteration convergence was deemed complete when the rms temperature difference between successive iteration results was $\leqslant 50$ K and the concentration difference was $\leqslant 0.001$.

The inversion results are shown in Figs. 81 through 83 for CO_2 and in Fig. 84 for H_2O. Cases 7 and 10 failed to yield an inversion because of indeterminate results in the initiating Abel inversion, and no additional smoothing was applied to the input profiles for these cases in an attempt to obtain an inversion.

The general quality of these inversion results is good for $r/R \gtrsim 0.4$. Below this value, serious fluctuations and gross inconsistencies between cases are often evident. This effect is attributed to the flatness of the

*Data supplied by Lt. Zlotkowski, AFRPL.

input transverse profiles for $z/R \lesssim 0.3$ and has been discussed in Section VIIID.

The results for temperature profile above $r/R \simeq 0.4$ are remarkably consistent from CO_2 case grouping to grouping and with the H_2O cases. Although a slight structure can be discerned from the figures, the profile is nearly flat with value $T \simeq 1400 \pm 200$ K. The results for CO_2 concentration above $r/R \simeq 0.4$ are also reasonably consistent. Here, however, a definite structure is evident. The overall tendency is for a value of $c \simeq 0.02$ near $r/R = 0.4$, a rise to $c \simeq 0.07$ near $r/R = 0.8$, and a decrease to $c \simeq 0.01$ at the source boundary. Cases 9 and 11 (Fig. 83b) show an additional valley near $r/R \simeq 0.7$, and cases 5 and 6 hint at a valley near the same point. H_2O concentration for $r/R \gtrsim 0.4$ has a structure similar to that of CO_2. With $c \sim 0.4$ at $r/R \simeq 0.4$, an increase to $c \sim 0.6$ at $r/R \sim 0.7$ and a decrease to $c \sim 0.05$ at the boundary are evident.

Although these general tendencies above $r/R \sim 0.4$ are clear enough, the quality of the results is judged not good enough to make any sure statements on the variation of radial profiles due to engine O/F or injector change. Whether or not the quality of these results is good enough to evaluate the adequacy of combustion/nozzle codes is the subject of a separate AFRPL in-house project.*

D. Random Error Analysis

The random error analysis of these Transtage inversions was carried out as in Section VIII by assuming radial pTc profiles, generating transverse E/A profiles, adding artificial random noise, smoothing, inverting, and comparing the retrieved radial profiles with the assumed profiles.

*The AFRPL point of contact for this effort is Dr. Dwayne McCay.

The assumed radial profiles for temperature and concentrations are shown in Fig. 85. (The pressure profile from Fig. 80 is retained). Above $r/R \simeq 0.4$, the temperature profile is the mean value of the actual Transtage inversions for both CO_2 and H_2O. The structure of the profile below $r/R \simeq 0.4$ was selected to be consistent with predictions of TDK nozzle codes, and the magnitude was selected to match the profile above $r/R \simeq 0.4$. The concentration profiles were constructed in a similar manner, but the added constraint that c_{H_2O}/c_{CO_2} should fall in the range $3 \longrightarrow 8$ (the range of values for the 12 engine test cases of Section VI) was imposed below $r/R \simeq 0.4$. The transverse E/A profiles generated from these radial profiles are shown in Fig. 86 and are seen to be quite reasonable simulations of the actual Transtage data of Figs. 64 through 75.

Tables of 201 random normal numbers were generated and used to construct simulated noise profiles from the smooth transverse profiles. Different tables were used for radiance and absorptance in order to eliminate any chance of correlated noise between the profiles. The rms magnitude of fluctuation was set at a fixed percentage of peak profile value. For CO_2 radiance, CO_2 absorptance, H_2O radiance, and H_2O absorptance, respectively, the percentages were 3%, 5%, 13%, and 20%. These values are characteristic of the actual Transtage data. These profiles were then smoothed according to the standard procedures outlined earlier. Both the noisy data simulation and smoothed profiles are shown in Fig. 86. The smoothed profiles were then inverted in order to retrieve the radial pTc profiles. The process of noise addition, smoothing, and inversion was carried out five times for each species, each time with different tables of random normal numbers. The inversion results are shown in Fig. 87.

Qualitatively, these results confirm the earlier suspicion that the inversion results become less trustworthy for $r/R \lesssim 0.4$. All of the error analysis temperature and concentration inversions display an increasing scatter below this level. The H_2O results display the most scatter as would be expected from the greater magnitude percentage error superimposed on the synthetic transverse data profiles. The rms scatter of the inversion curves are shown in Fig. 88 at $r/R = 0, 0.2, 0.4, 0.6, 0.8$ and 1.0. Again, a sharp rise below $r/R \simeq 0.4$ is evident.

Quantitatively, the results do not display as large a magnitude of fluctuations as is suggested by the actual Transtage inversion results of Fig. 81. One obvious explanation is that the error analysis treats idealized data that does not contain the subtle foibles and idiosyncrasies of real data. Another possibility is that the enhanced scatter of the Transtage inversions is indeed due to the variation of O/F and injector from case to case. The third, and most likely possibility is that only random error has been addressed in either the Transtage inversions or error analysis. Inspection of Fig. 81 (particularly the three H_2O cases and the CO_2 cases 9, 10 and 11) reveals an oscillatory variation of wavelength $\lambda \sim 5$-10 cm. This noise has been identified by ARO to be a deterministic noise which should be removed (by a Fourier analysis) from the data before inversion. The fact that it was not removed in the present analysis nor simulated in the error analysis is most likely the major cause of the apparent discrepancy between the observed and predicted inversion scatter.

At the same time, this argument does not invalidate the error analysis results concerning random error. That is, in the inversion of a real Transtage data case, the rms error curves of Fig. 88 provide a reasonable estimate of the inversion error due to <u>random</u> experimental error in the measured transverse profiles.

E. Revised Inversions

Three sets of Transtage data were selected for further analysis. Two of these cases are repeats of Cases 2 and 8 considered above, but with the deterministic noise removed. This noise has been identified as due to a "bouncing" of the scanning arm that carries the photometer and emission source apparatus across the plume. This noise was removed by a subtraction of the peak in the Fourier transform of the transverse profiles at the arm-bouncing frequency. In addition, corrections to account for background radiation were made. This background has been attributed to scattering of radiation from the engine nozzle which was inadvertently in the sensor field of view. An empirical correction in time and position was applied.* The third case (designated as Case 13) is a CO_2 scan made during the Phase III portion of the AEDC NERD measurements program. All appropriate corrections to these data were also made.

The raw transverse scans (after corrections) for these three cases are shown in Figs. 89-91 and the variable smoothing curves in Figs. 92-94.** A listing of the smoothing parameters selected is given in Table 13, and the final smoothed curves shown in Figs. 89-91. All of the original Transtage inversions employed a radius R = 62 cm. This constant value was not appropriate for the revised cases. Here, the selections R = 67, 65 and 65 cm were made for Cases 2, 8 and 13, respectively. The pressure curve of Fig. 80 was extrapolated smoothly to 0.0337 atm at 67 cm for these inversions.

*Both the deterministic noise and background radiation correction analyses were made by ARO.

**A comparison of Fig. 90b with Fig. 71b shows that the high-frequency noise of the H_2O absorptance spectrum is missing. These data are as received from ARO. Resolution of this discrepancy was not made in time for publication of this report. However, the absence of this noise is not particularly important since it would have been suppressed in smoothing in any event.

Table 13. Smoothing Parameters for Revised Transtage E/A Data

Case No.	γ_E	γ_A
2 (revised)	100	500
8 (revised)	500	1000
13	10	100

The inversion results for temperature and concentration are shown in Figs. 95-97. The results for Cases 2 and 8 are not substantially different from the results obtained in the previous section (compare Fig. 95a with 81a, 95b with 81b, 96a with 84a, and 96b with 84b). The inversion results for the Phase III CO_2 case (Case 13, Fig. 97) is also qualitatively similar to those for the previous CO_2 cases and the revised Case 2. In this case, however, the results for $r/R \leqslant 0.16$ are meaningless due to an inversion instability. This instability is undoubtedly due to the valley in the region $z \leqslant 15$ cm evident in both the transverse radiance and absorptance profiles (Fig. 91).

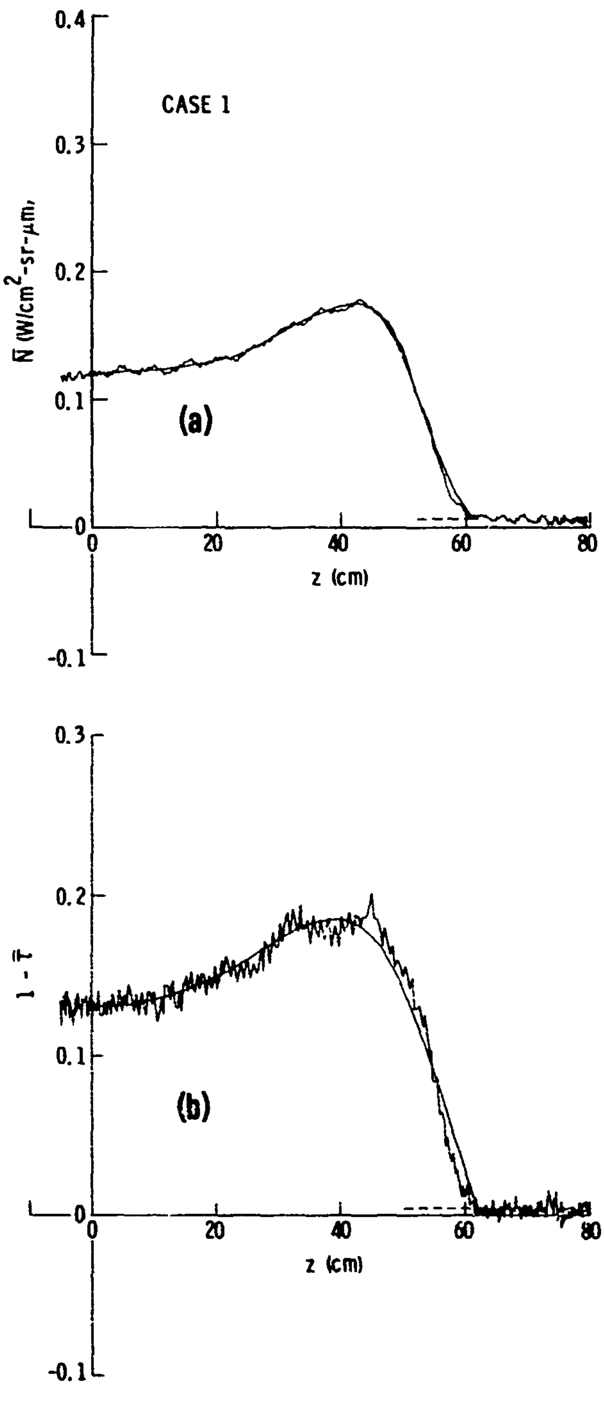

Fig. 64. Transverse E/A Profiles for Transtage Case 1. (a) Raw and smoothed radiance data; (b) Raw and smoothed absorptance data. Dashed lines indicate zero levels.

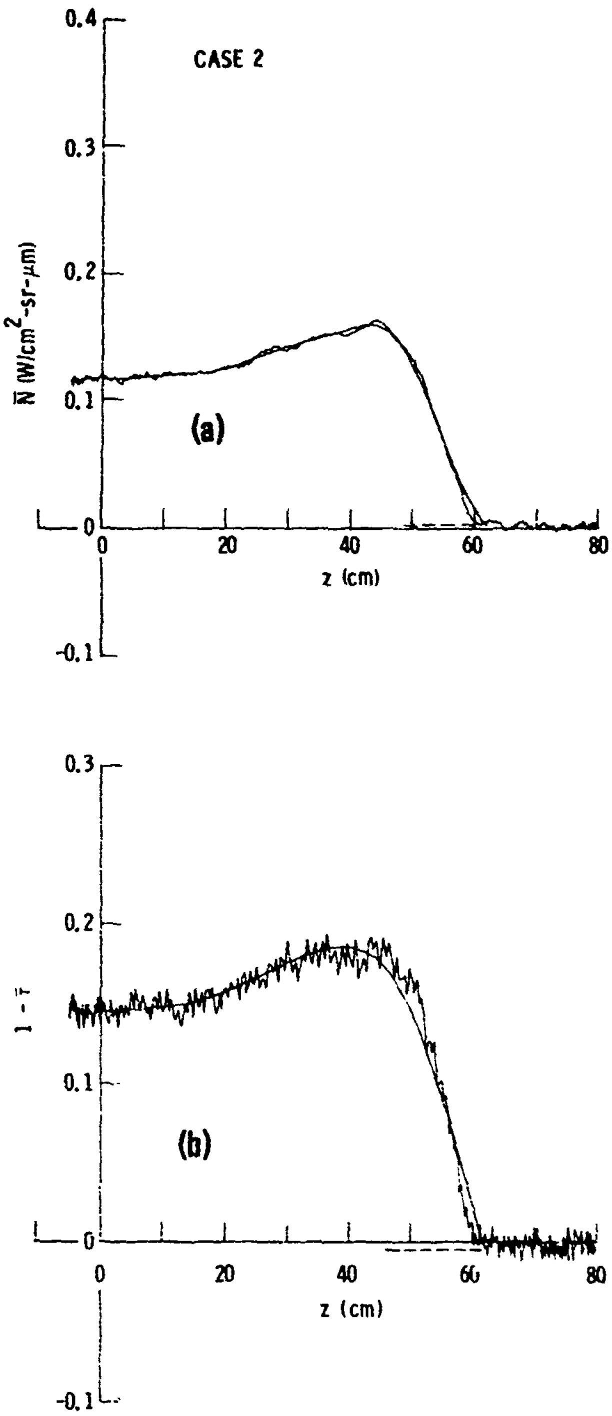

Fig. 65. Transverse E/A Profiles for Transtage Case 2. (a) Raw and smoothed radiance data; (b) Raw and smoothed absorptance data. Dashed lines indicate zero levels.

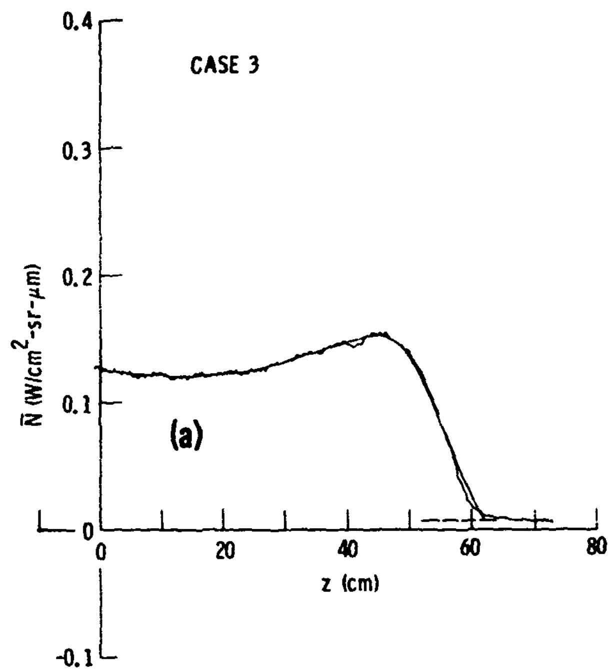

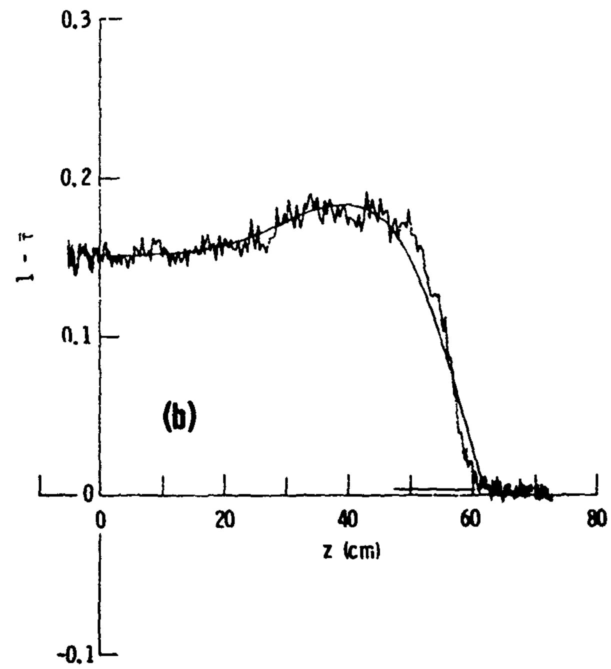

Fig. 66. Transverse E/A Profiles for Transtage Case 3. (a) Raw and smoothed radiance data; (b) Raw and smoothed absorptance data. Dashed lines indicate zero levels.

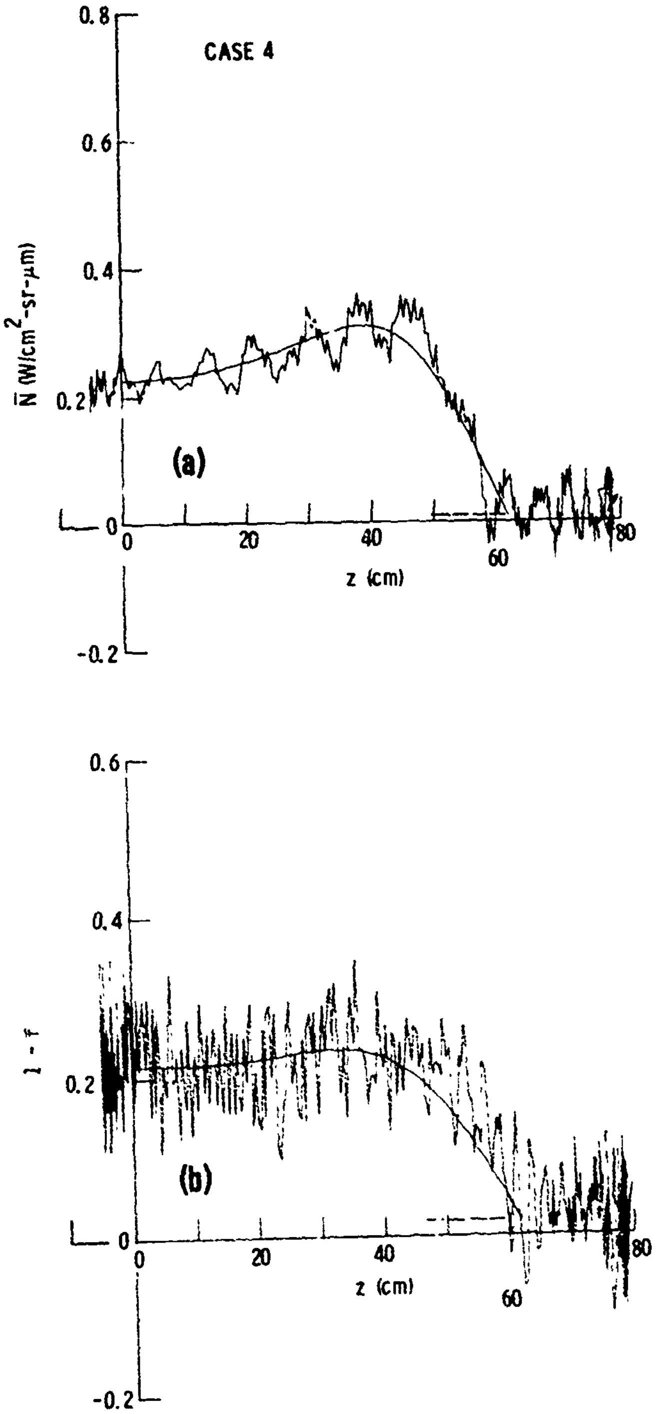

Fig. 67. Transverse E/A Profiles for Transtage Case 4. (a) Raw and smoothed radiance data; (b) Raw and smoothed absorptance data. Dashed lines indicate zero levels.

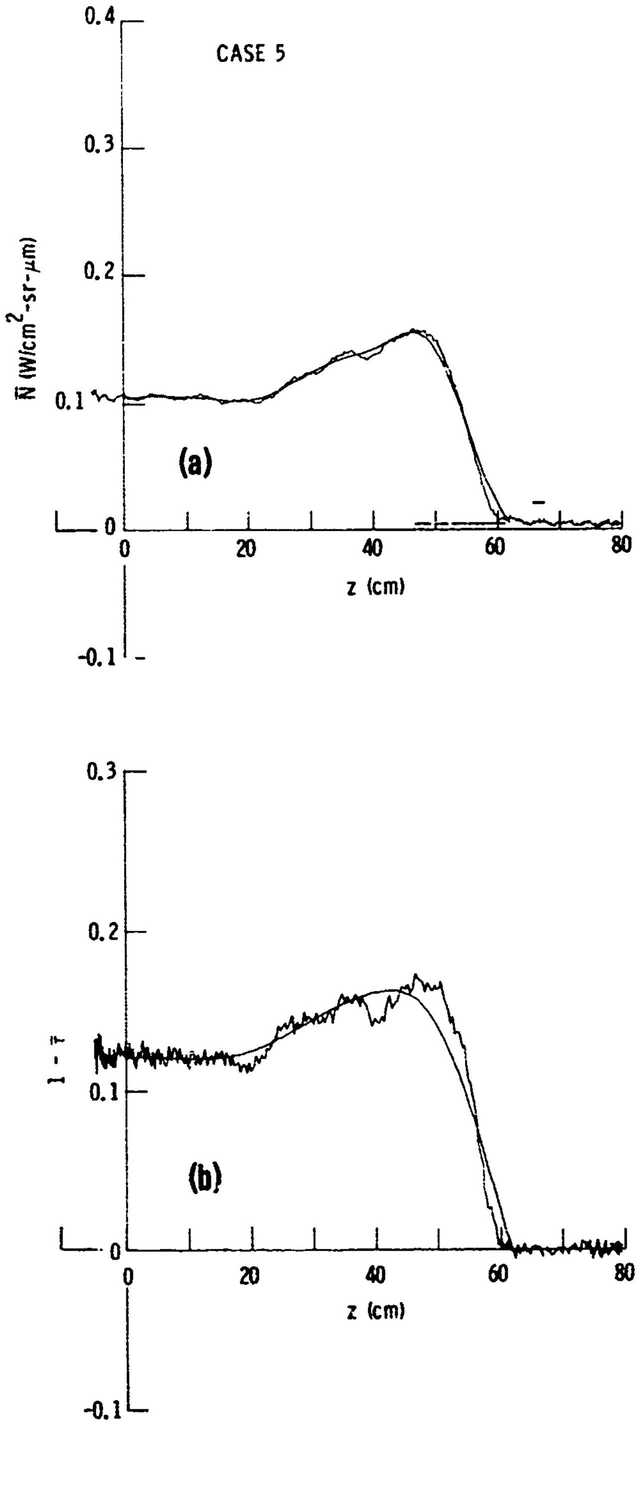

Fig. 68. Transverse E/A Profiles for Transtage Case 5. (a) Raw and smoothed radiance data; (b) Raw and smoothed absorptance data. Dashed lines indicate zero levels.

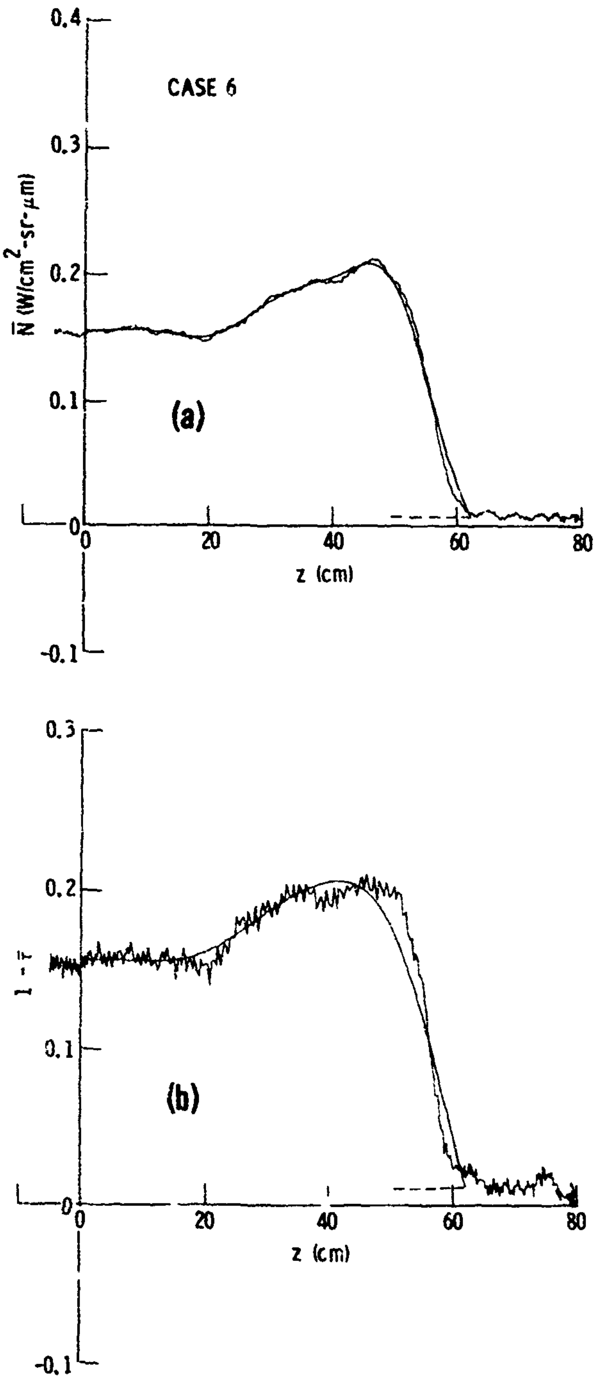

Fig. 69. Transverse E/A Profiles for Transtage Case 6. (a) Raw and smoothed radiance data; (b) Raw and smoothed absorptance data. Dashed lines indicate zero levels.

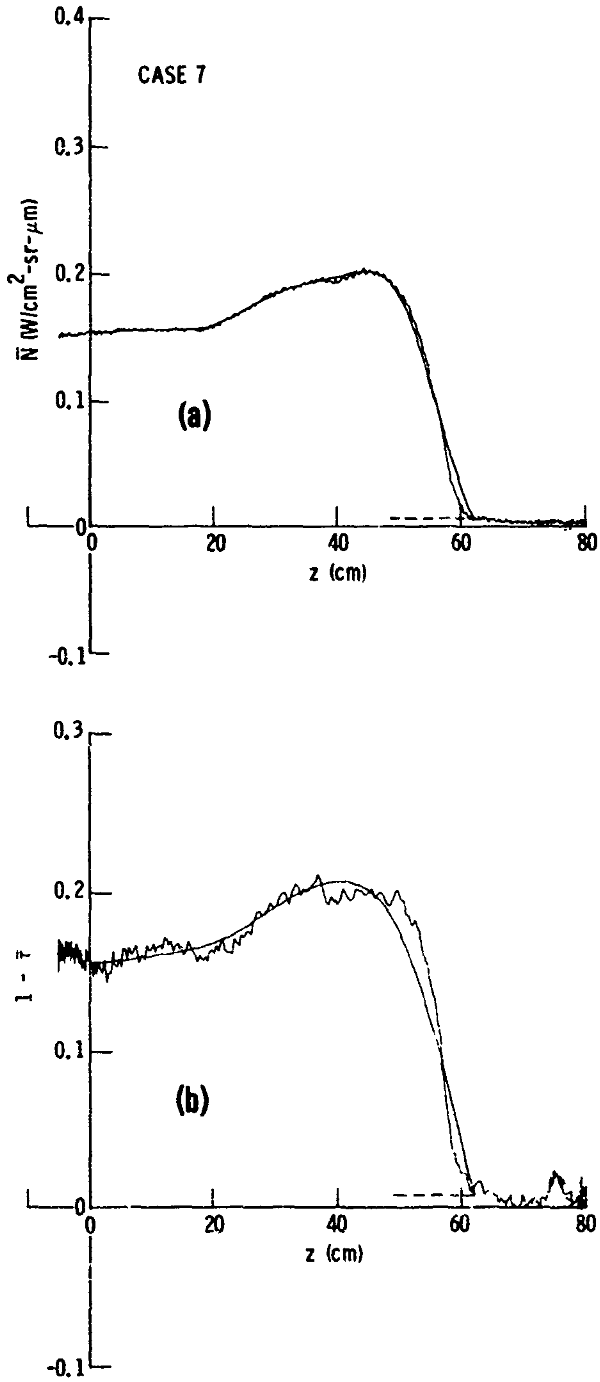

Fig. 70. Transverse E/A Profiles for Transtage Case 7. (a) Raw and smoothed radiance data; (b) Raw and smoothed absorptance data. Dashed lines indicate zero levels.

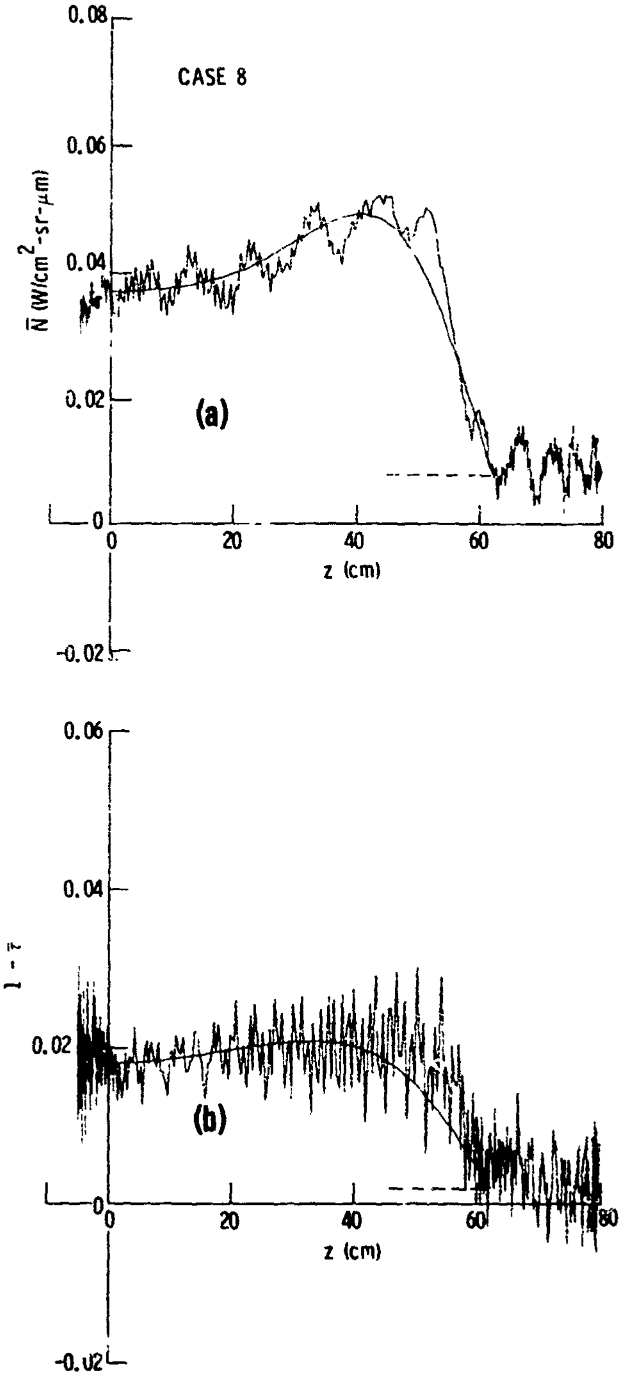

Fig. 71. Transverse E/A Profiles for Transtage Case 8. (a) Raw and smoothed radiance data; (b) Raw and smoothed absorptance data. Dashed lines indicate zero levels.

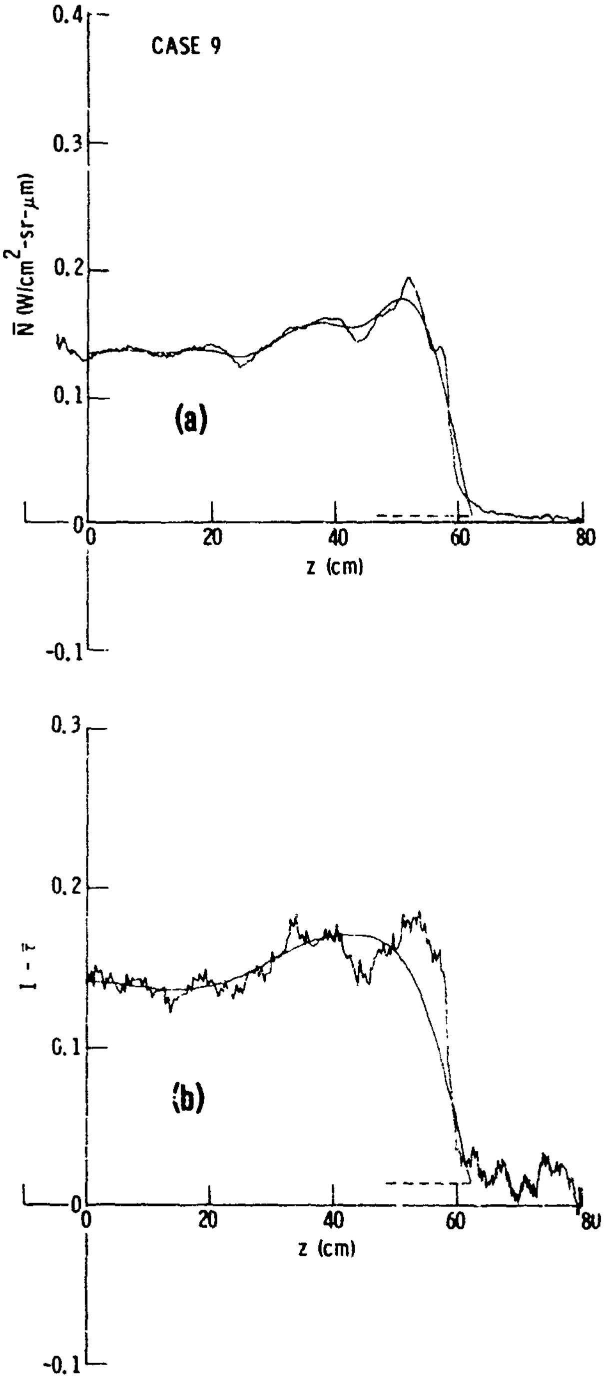

Fig. 72. Transverse E/A Profiles for Transtage Case 9. (a) Raw and smoothed radiance data; (b) Raw and smoothed absorptance data. Dashed lines indicate zero levels.

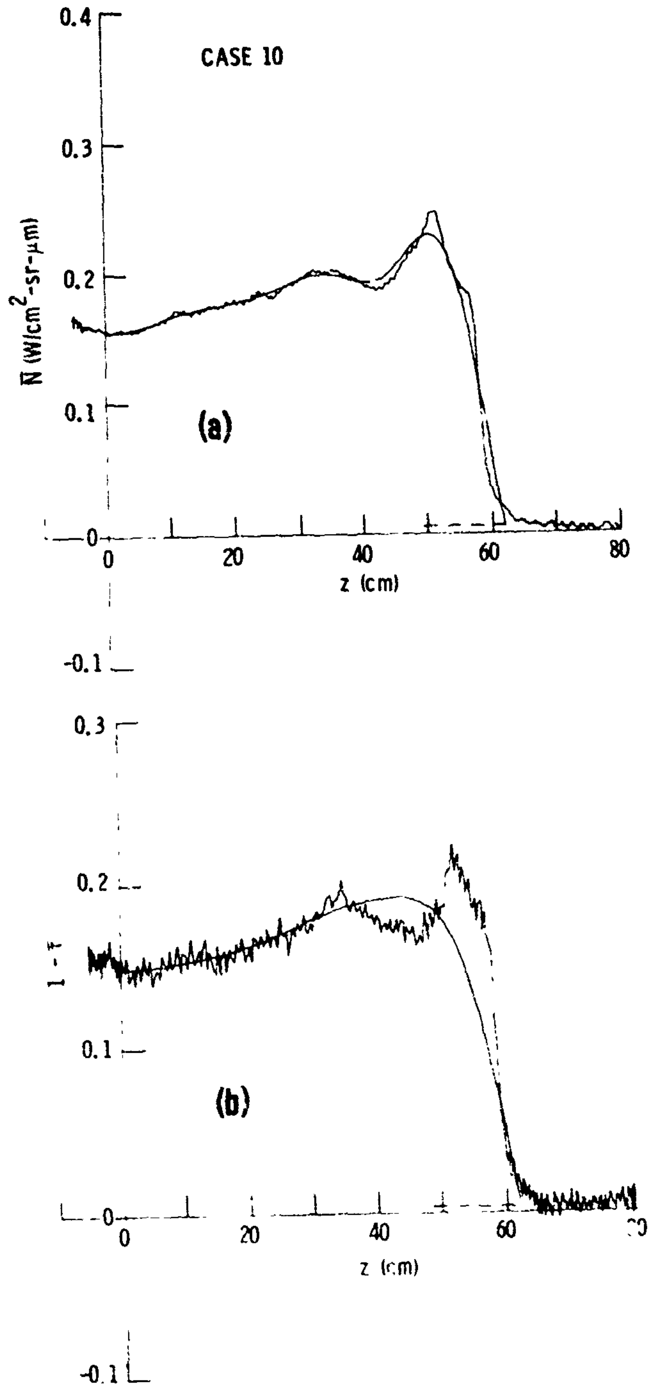

Fig. 73. Transverse E/A Profiles for Transtage Case 10. (a) Raw and smoothed radiance data; (b) Raw and smoothed absorptance data. Dashed lines indicate zero levels.

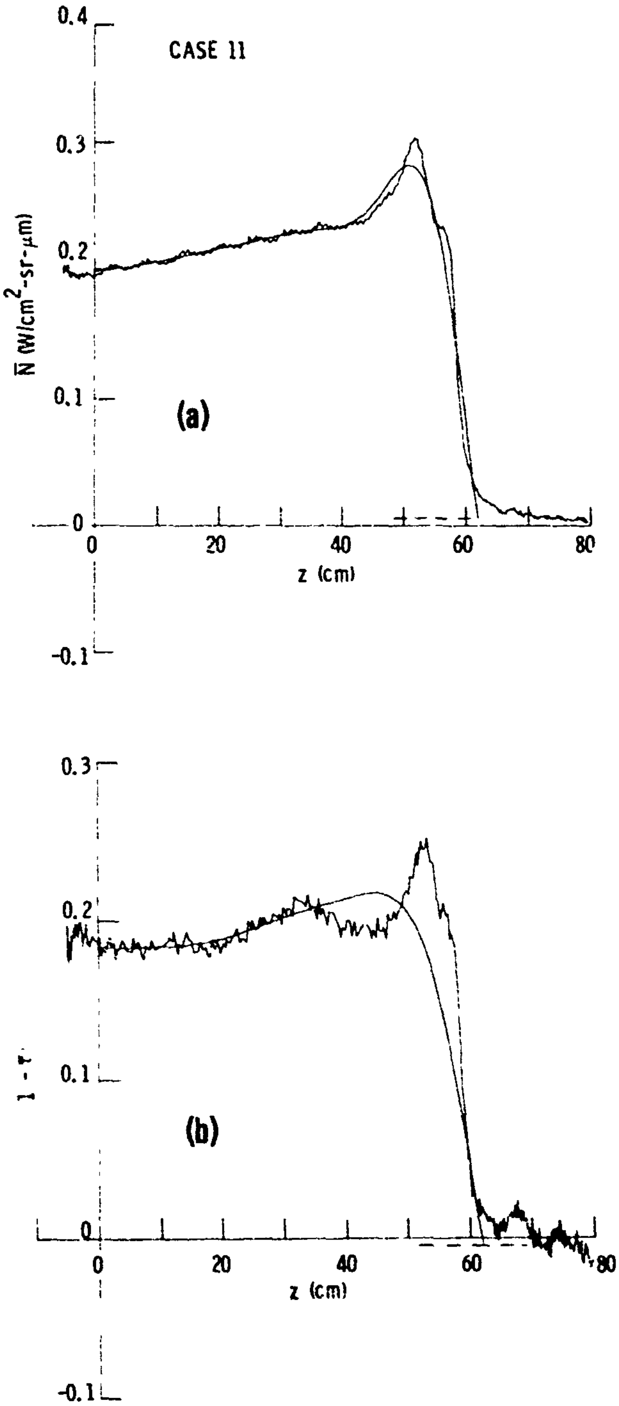

Fig. 74. Transverse E/A Profiles for Transtage Case 11. (a) Raw and smoothed radiance data; (b) Raw and smoothed absorptance data. Dashed lines indicate zero levels.

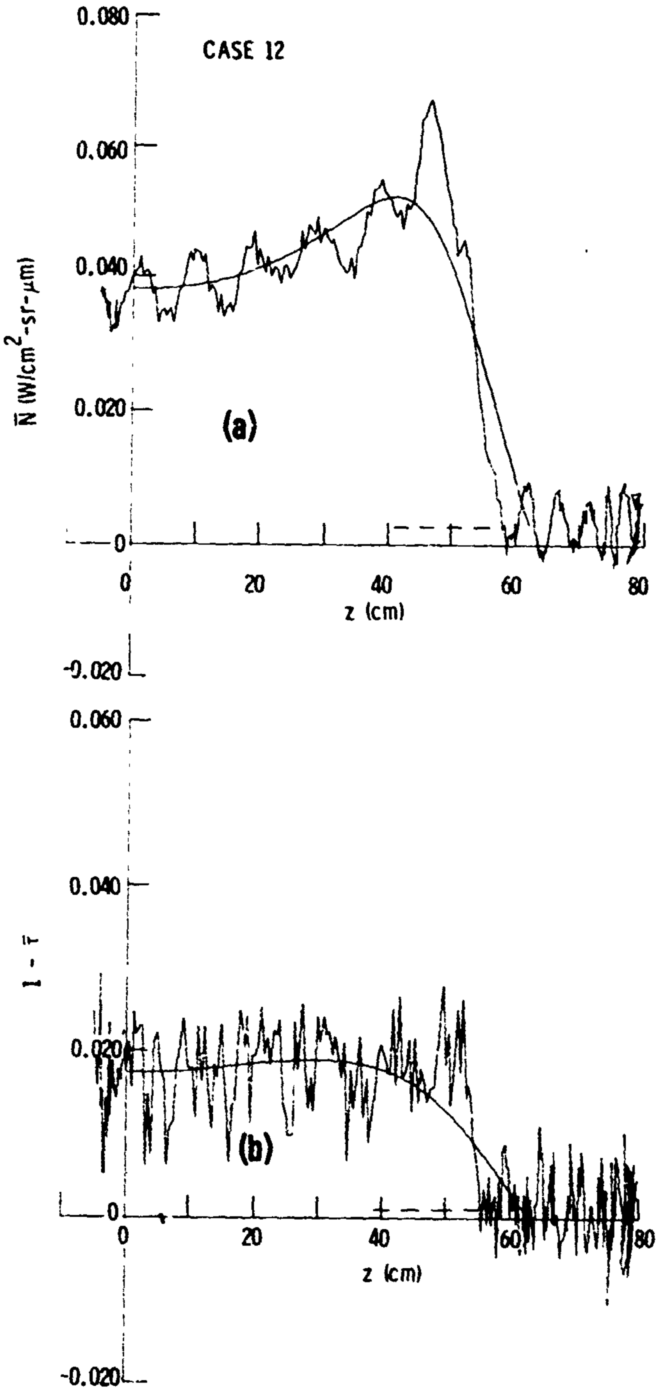

Fig. 75. Transverse E/A Profiles for Transtage Case 12. (a) Raw and smoothed radiance data; (b) Raw and smoothed absorptance data. Dashed lines indicate zero levels.

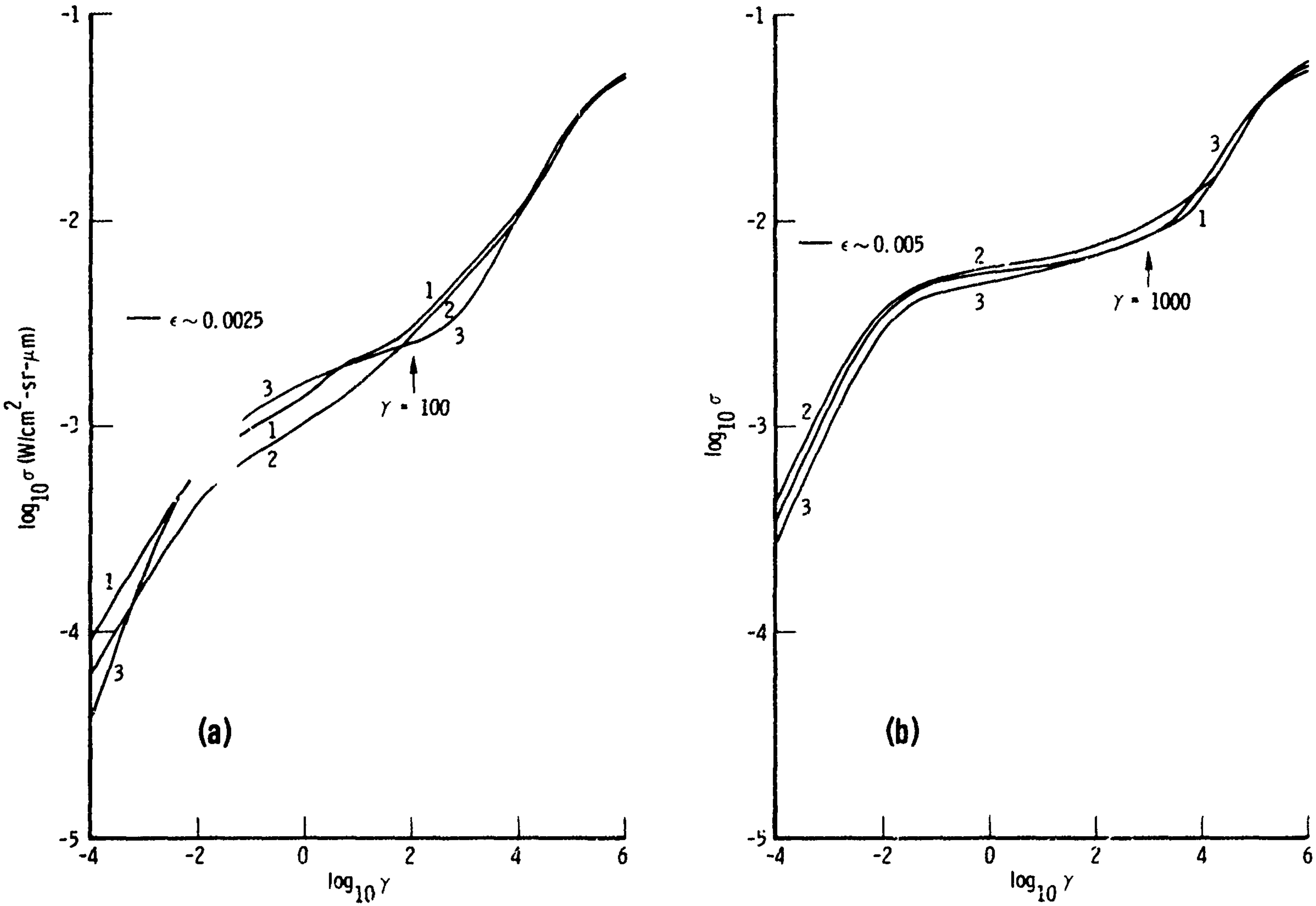

Fig. 76. Smoothing Curves for Transtage Cases 1, 2 and 3. (a) Radiance; (b) Absorptance.

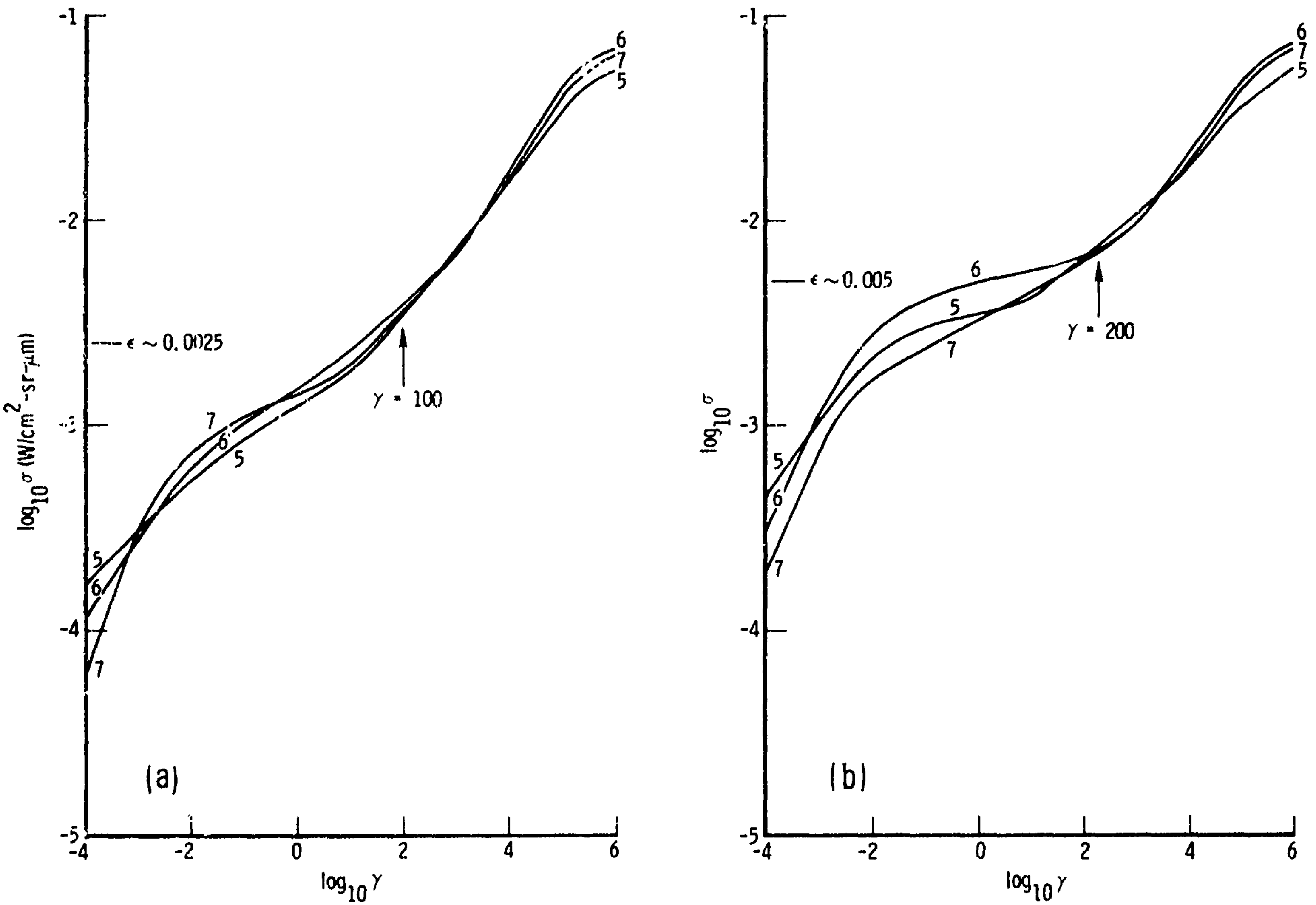

Fig. 77. Smoothing Curves for Transtage Cases 5, 6 and 7. (a) Radiance, (b) Absorptance.

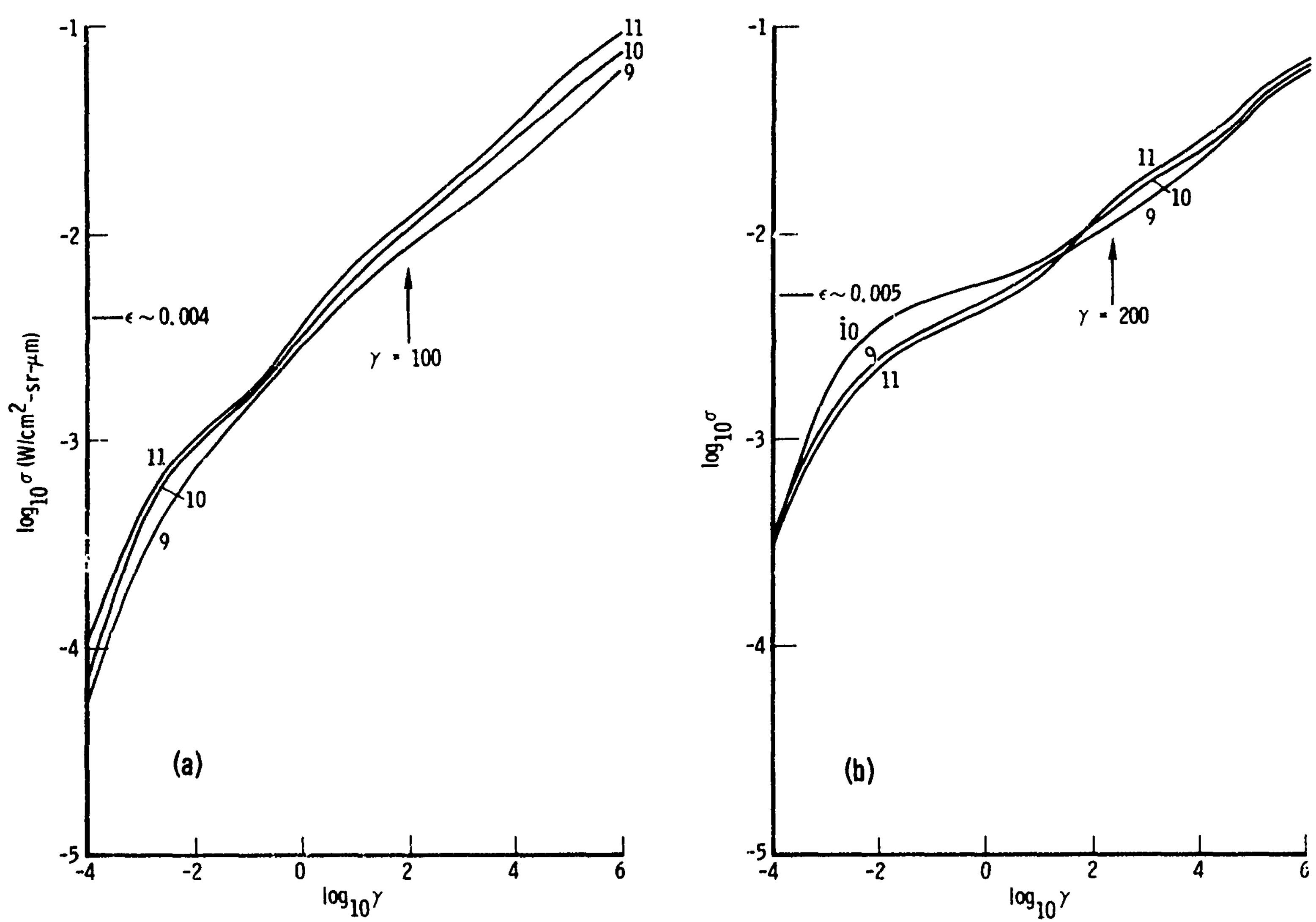

Fig. 78. Smoothing Curves for Transtage Cases 9, 10 and 11. (a) Radiance; (b) Absorptance.

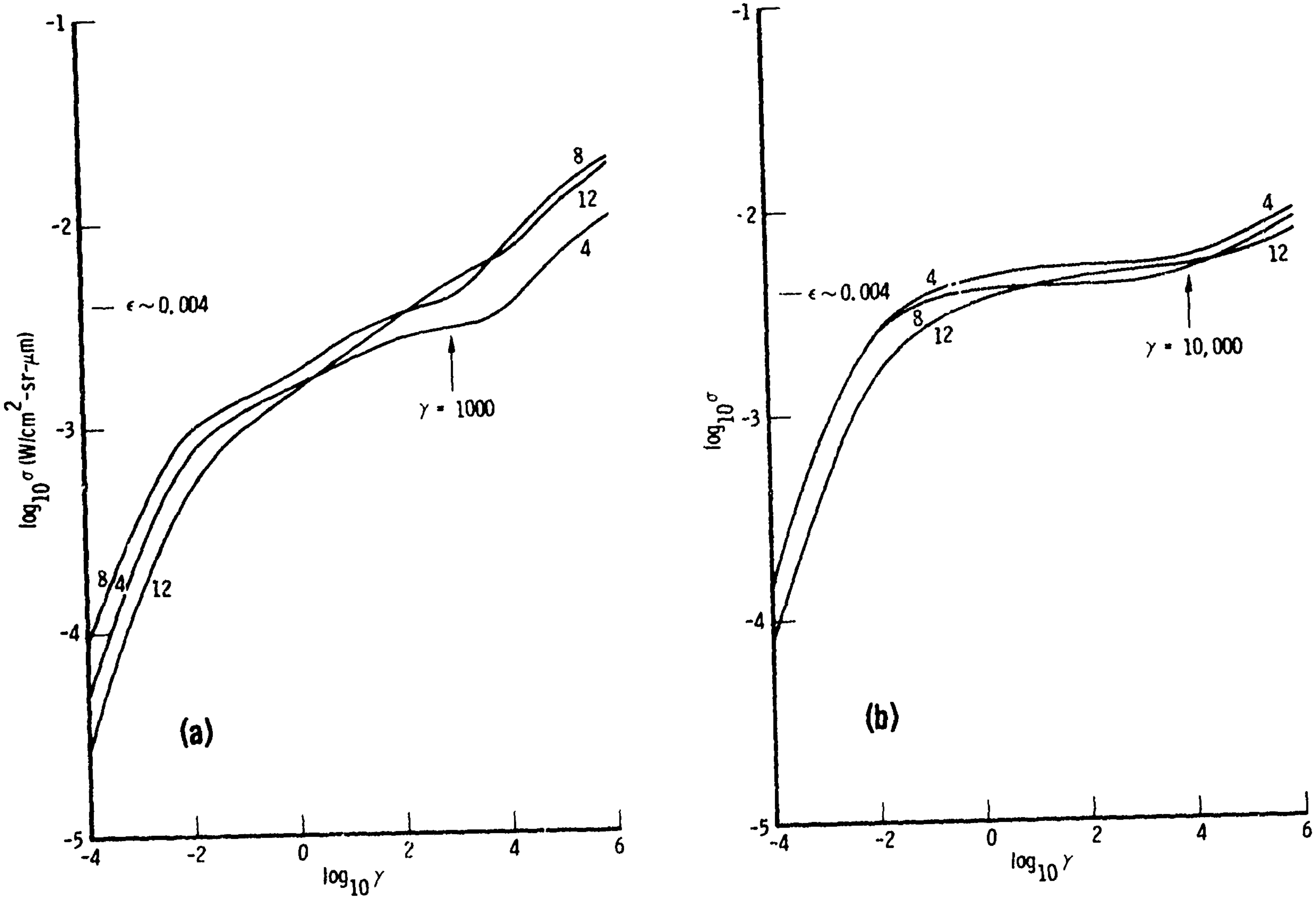

Fig. 79. Smoothing Curves for Transtage Cases 4, 8 and 12. (a) Radiance; (b) Absorptance.

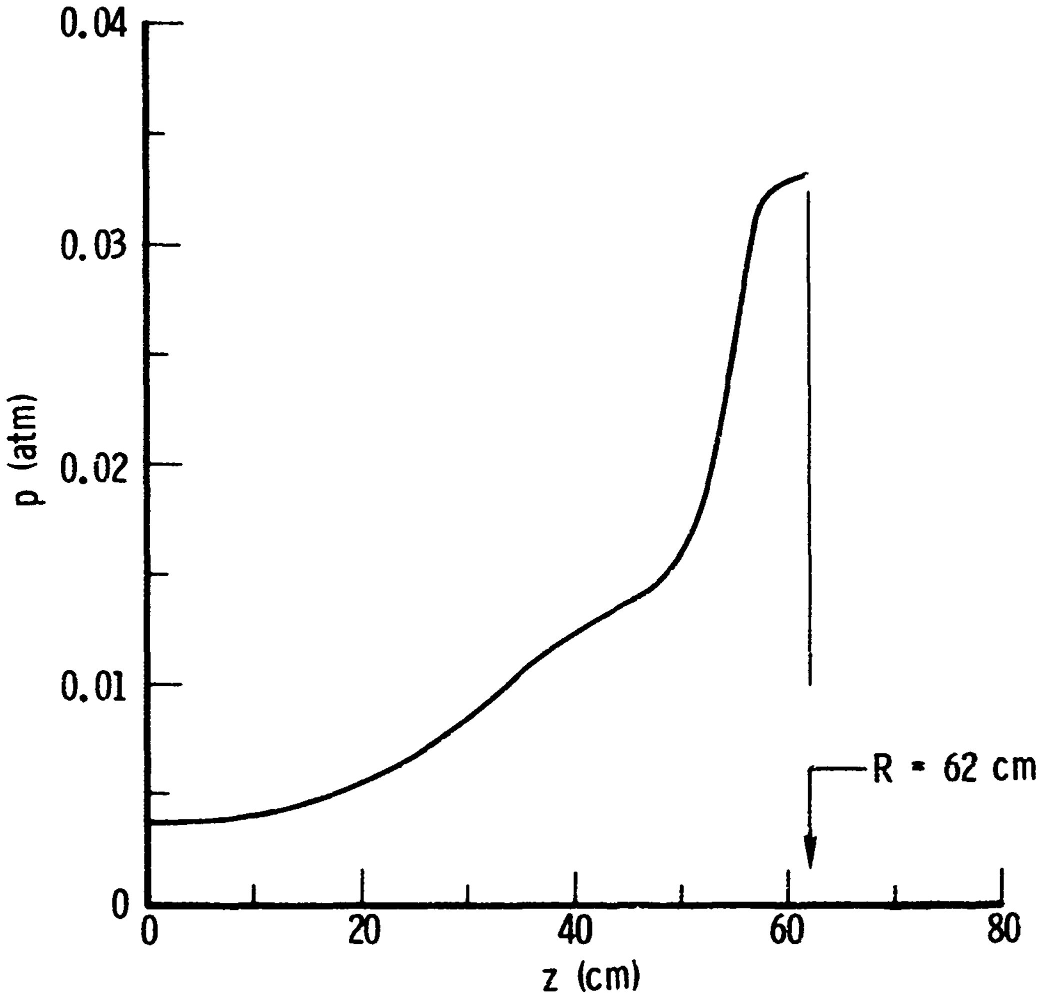

Fig. 80. Pressure Profile for Transtage Inversions.

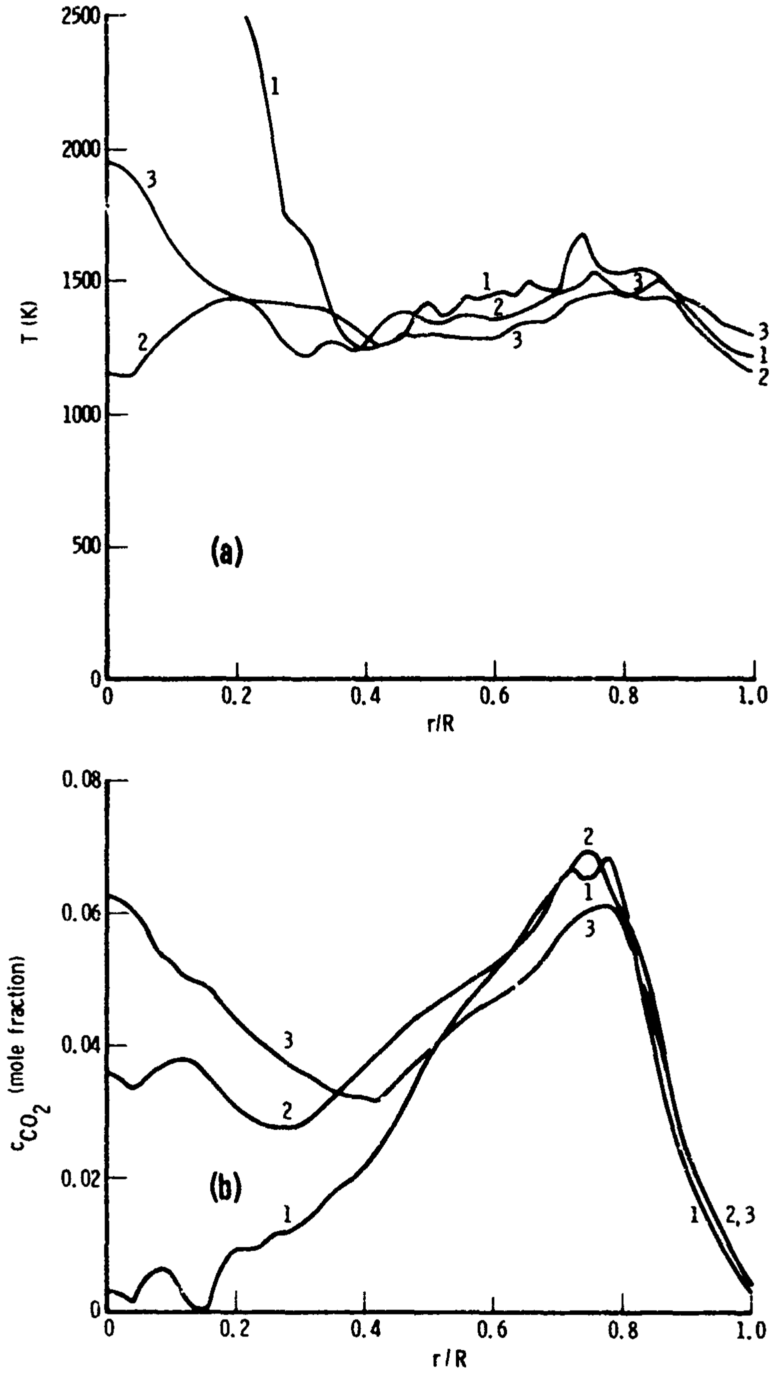

Fig. 81. Transtage Inversion Results for Cases 1, 2, and 3. (a) Temperature; (b) CO_2 concentration.

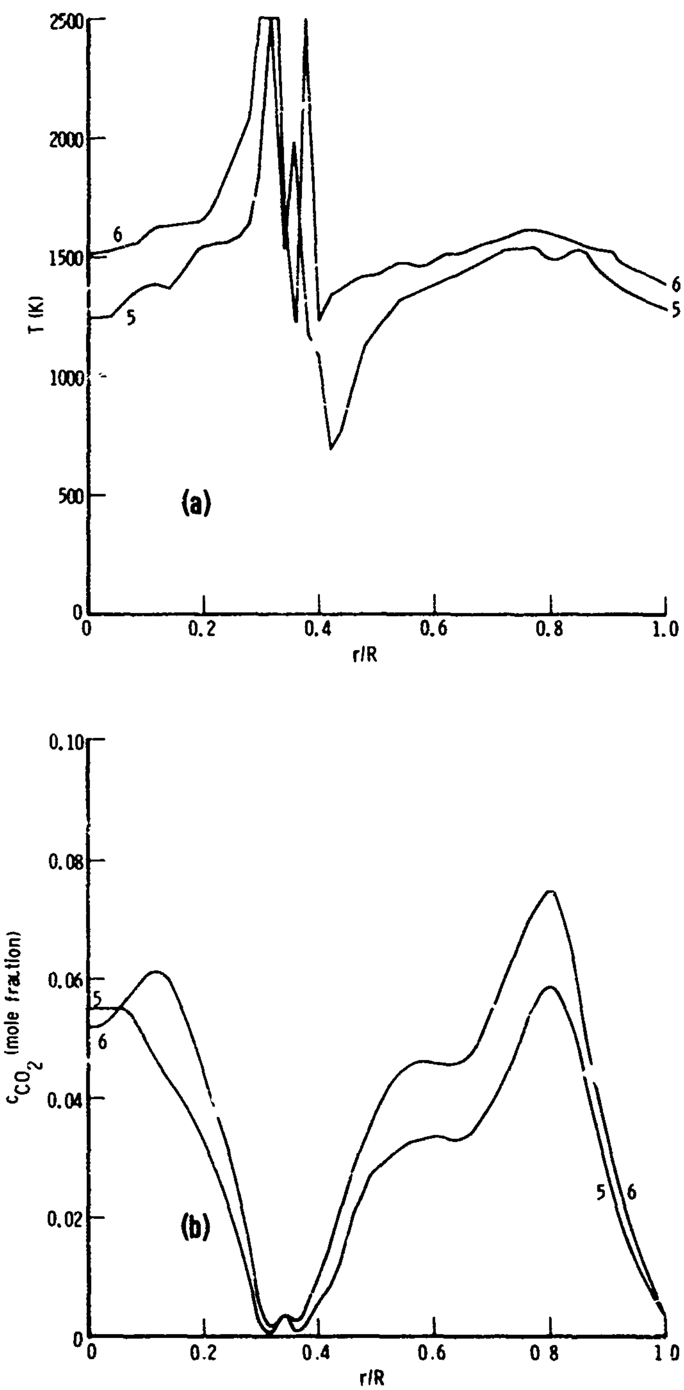

Fig. 82. Transtage Inversion Results for Cases 5 and 6. (a) Temperature; (b) CO_2 concentration.

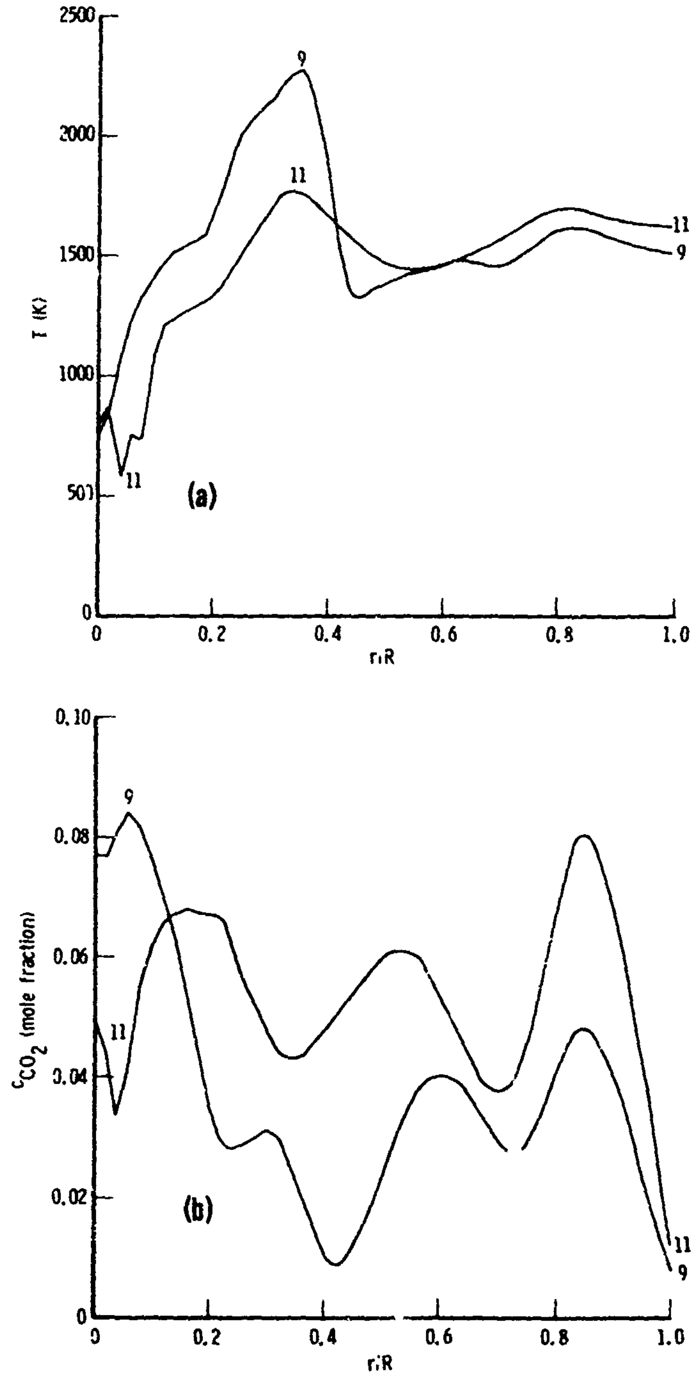

Fig. 83. Transtage Inversion Results for Cases 9 and 11. (a) Temperature; (b) CO_2 concentration.

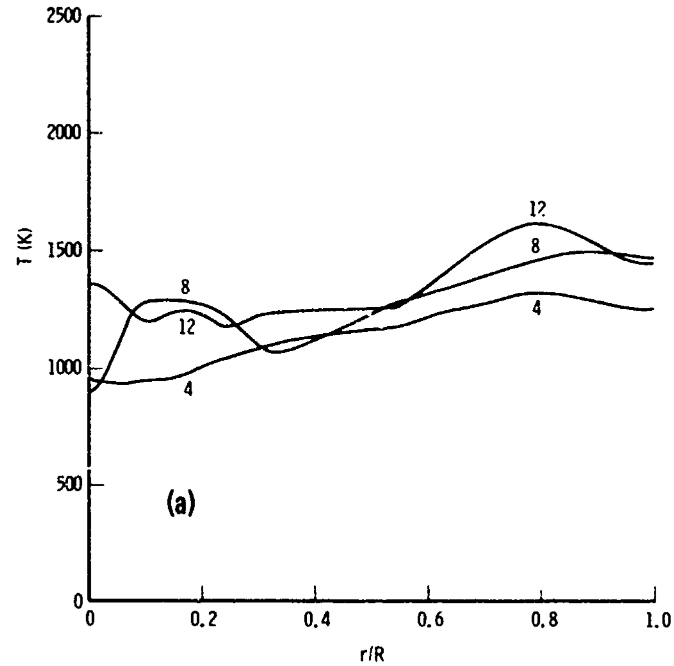

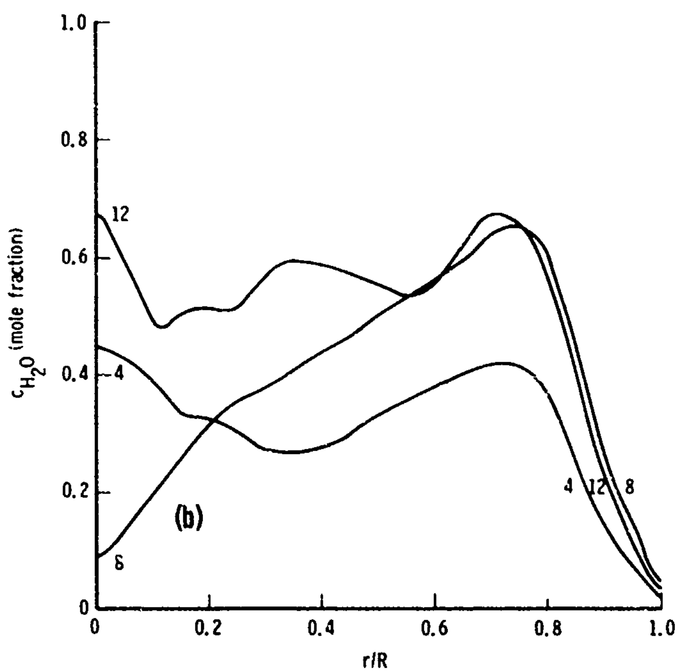

Fig. 84. Transtage Inversion Results for Cases 4, 8 and 12. (a) Temperature; (b) H_2O concentration.

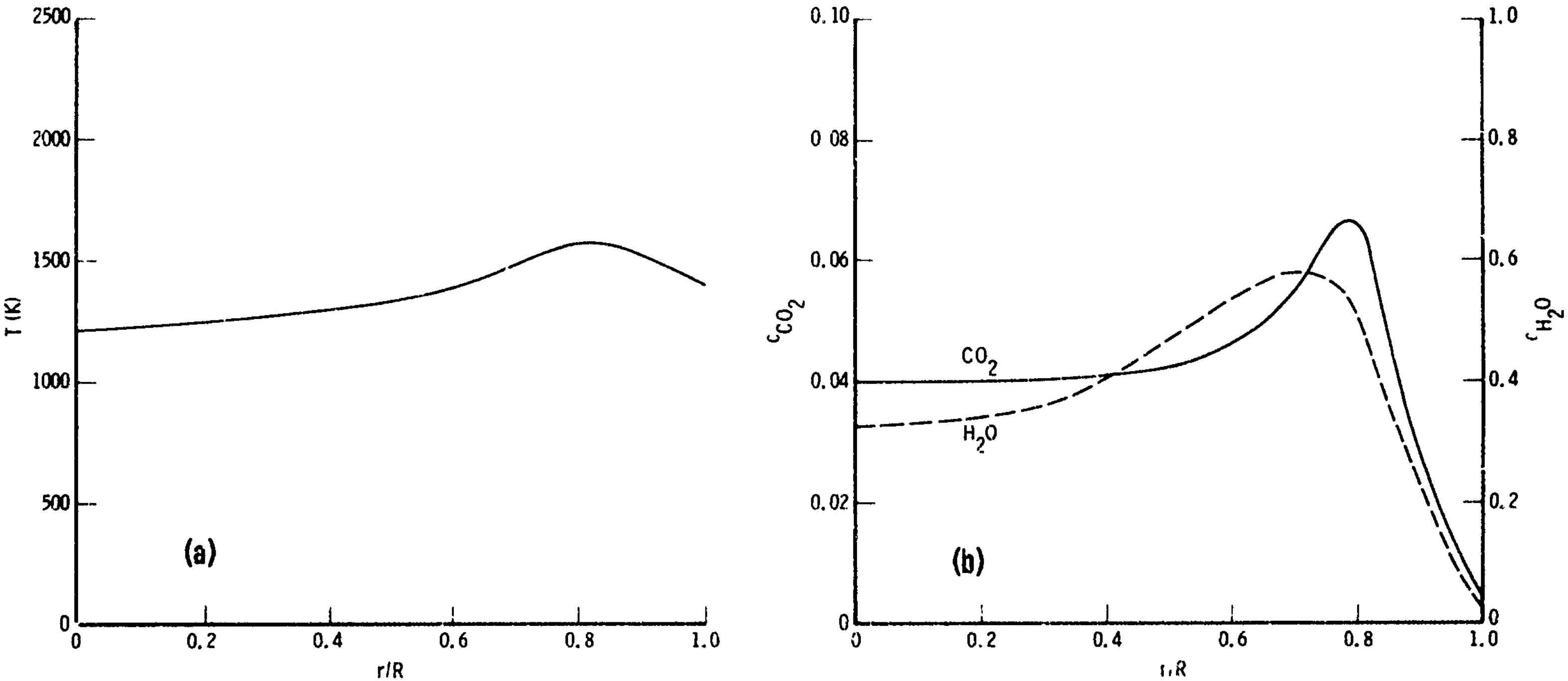

Fig. 85. Radial Profiles for Transtage Random Error Analysis. (a) Temperature; (b) Concentration.

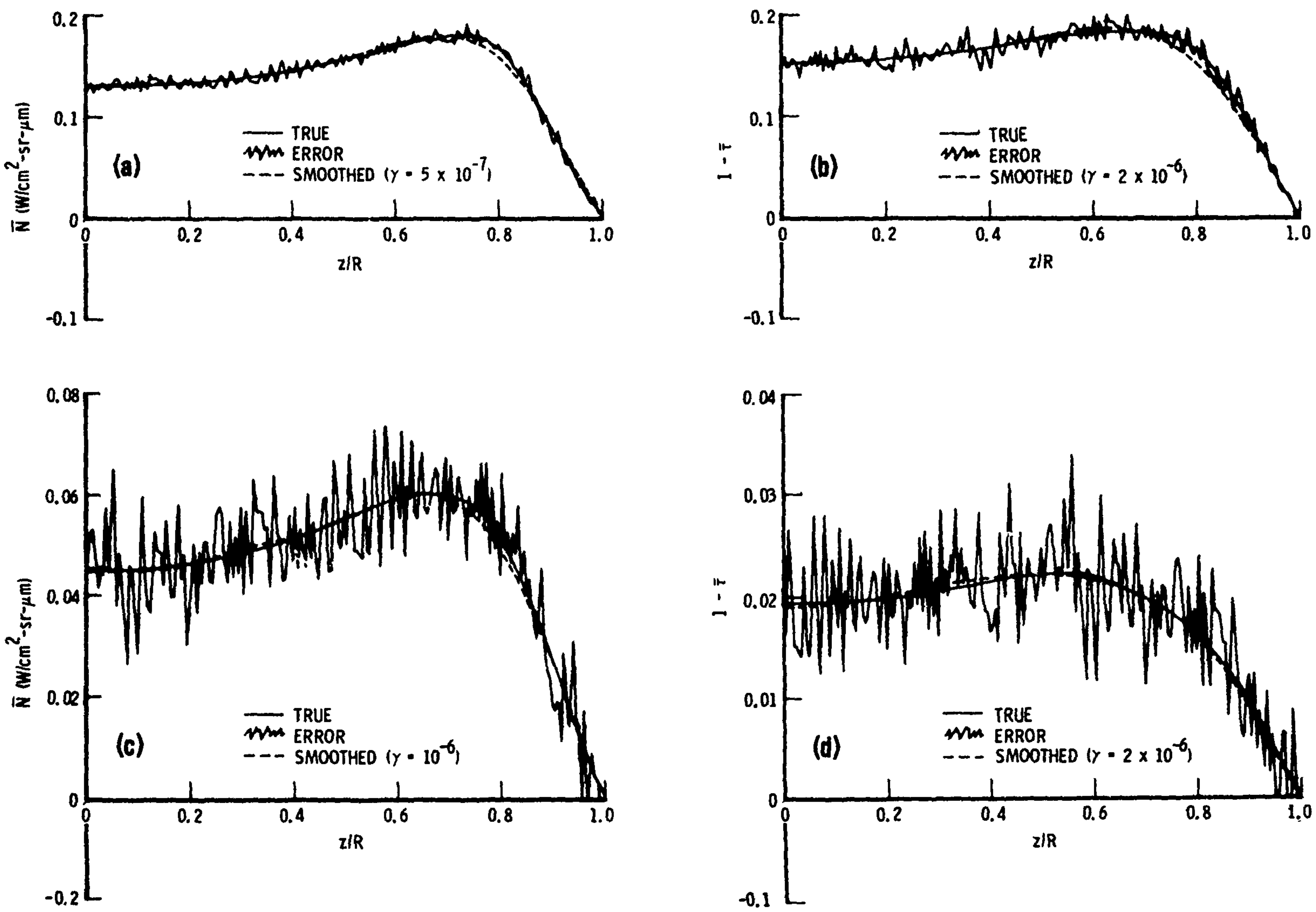

Fig. 86. Transverse E/A Profiles for Transtage Random Error Analysis. (a) CO_2 radiance; (b) CO_2 absorptance; (c) H_2O radiance; (d) H_2O absorptance.

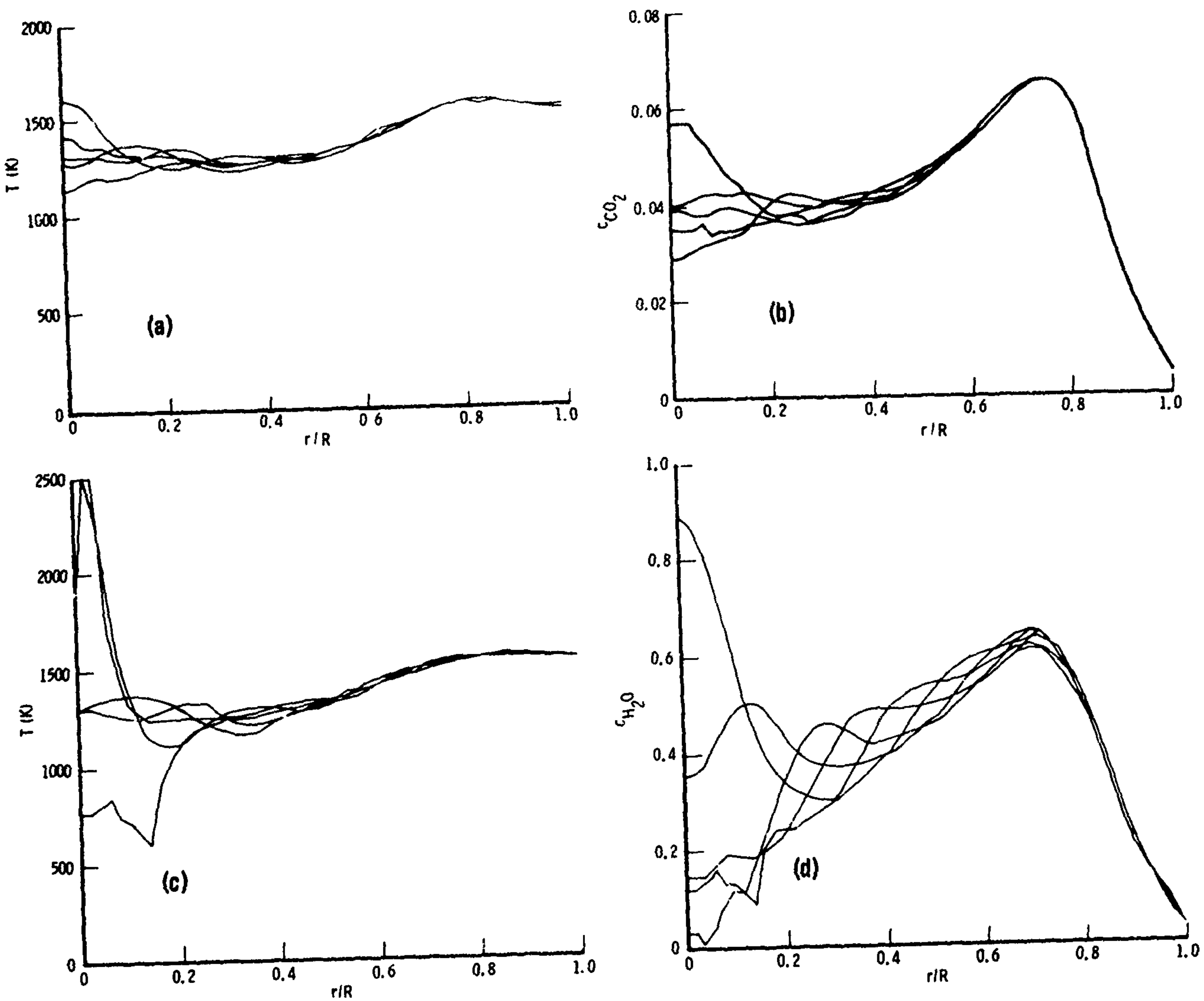

Fig. 87. Inversion Results for Transtage Random Error Analysis. (a) Temperature from CO_2 data; (b) Temperature from H_2O data; (c) CO_2 concentration; (d) H_2O concentration.

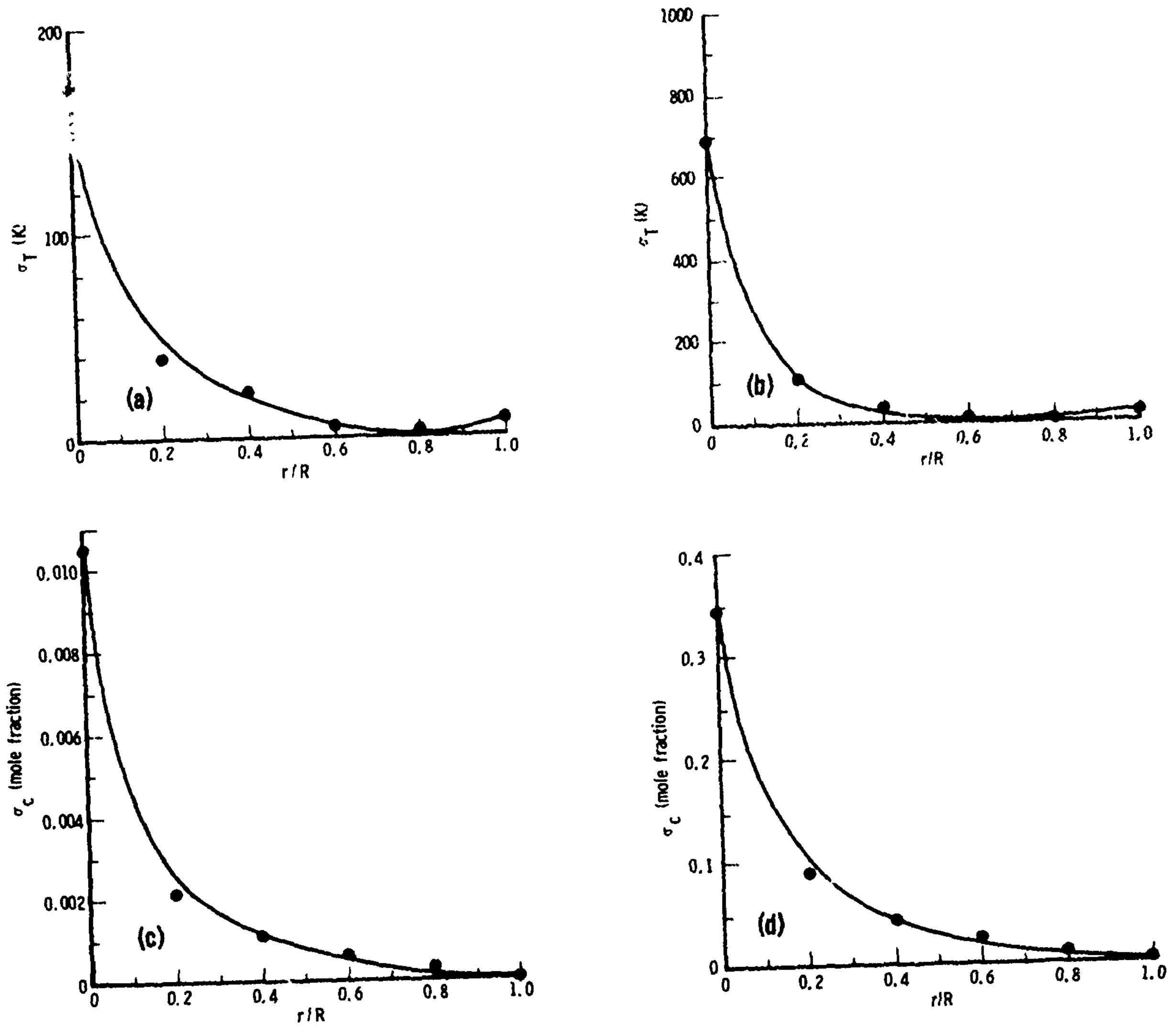

Fig. 88. Radial Error Curves for Transtage Inversion. (a) Temperature from CO_2 data; (b) Temperature from H_2O data; (c) CO_2 concentration; (d) H_2O concentration.

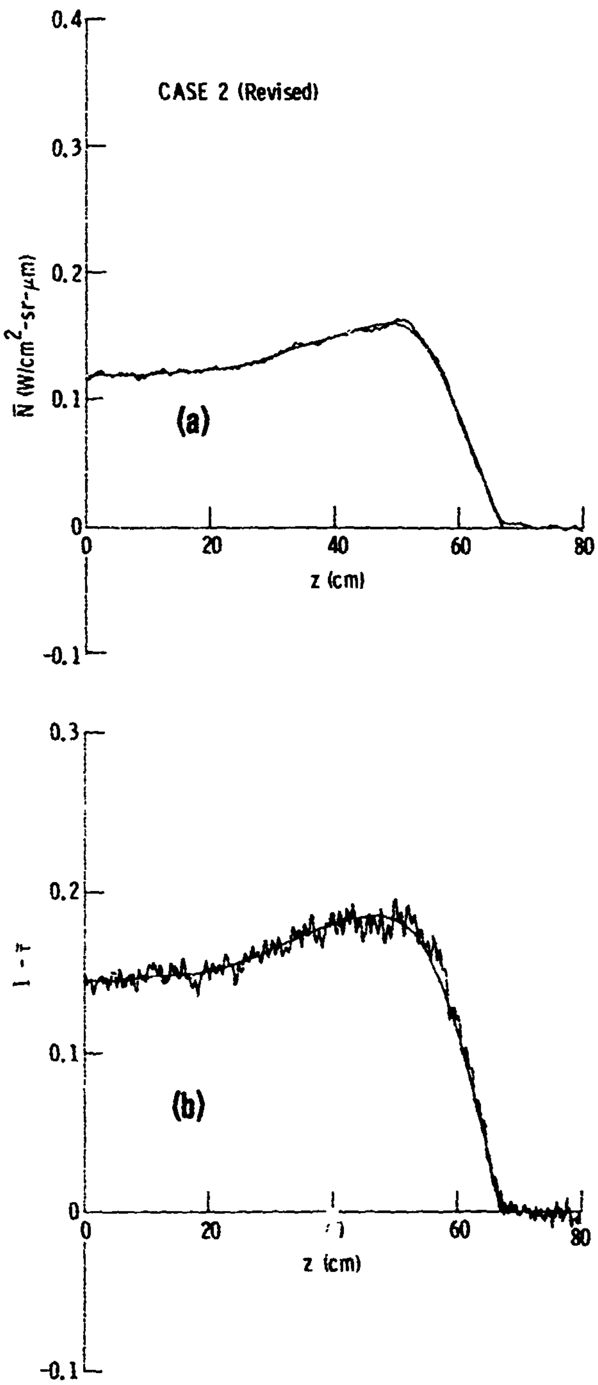

Fig. 89. Transverse E/A Profiles for Transtage Case 2 (Revised). (a) Raw and smoothed radiance data; (b) Raw and smoothed absorptance data.

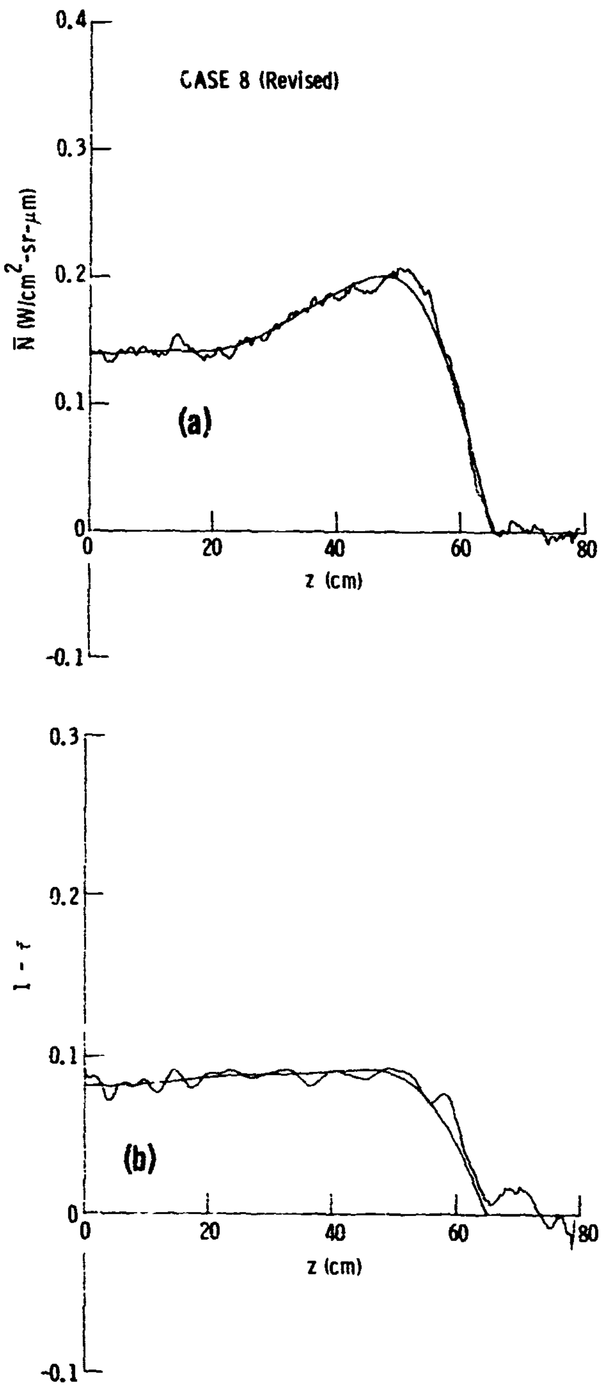

Fig. 90. Transverse E/A Profiles for Transtage Case 8 (Revised). (a) Raw and smoothed radiance data; (b) Raw and smoothed absorptance data.

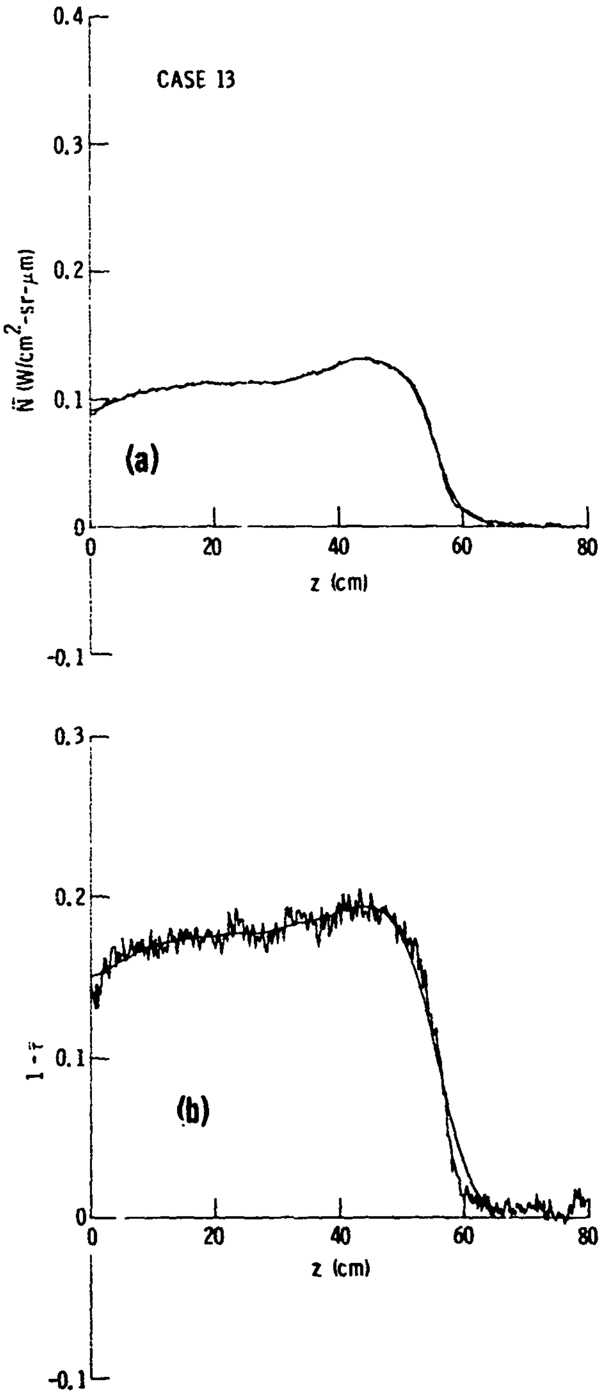

Fig. 91. Transverse E/A Profiles for Transtage Case 13. (a) Raw and smoothed radiance data; (b) Raw and smoothed absorptance data.

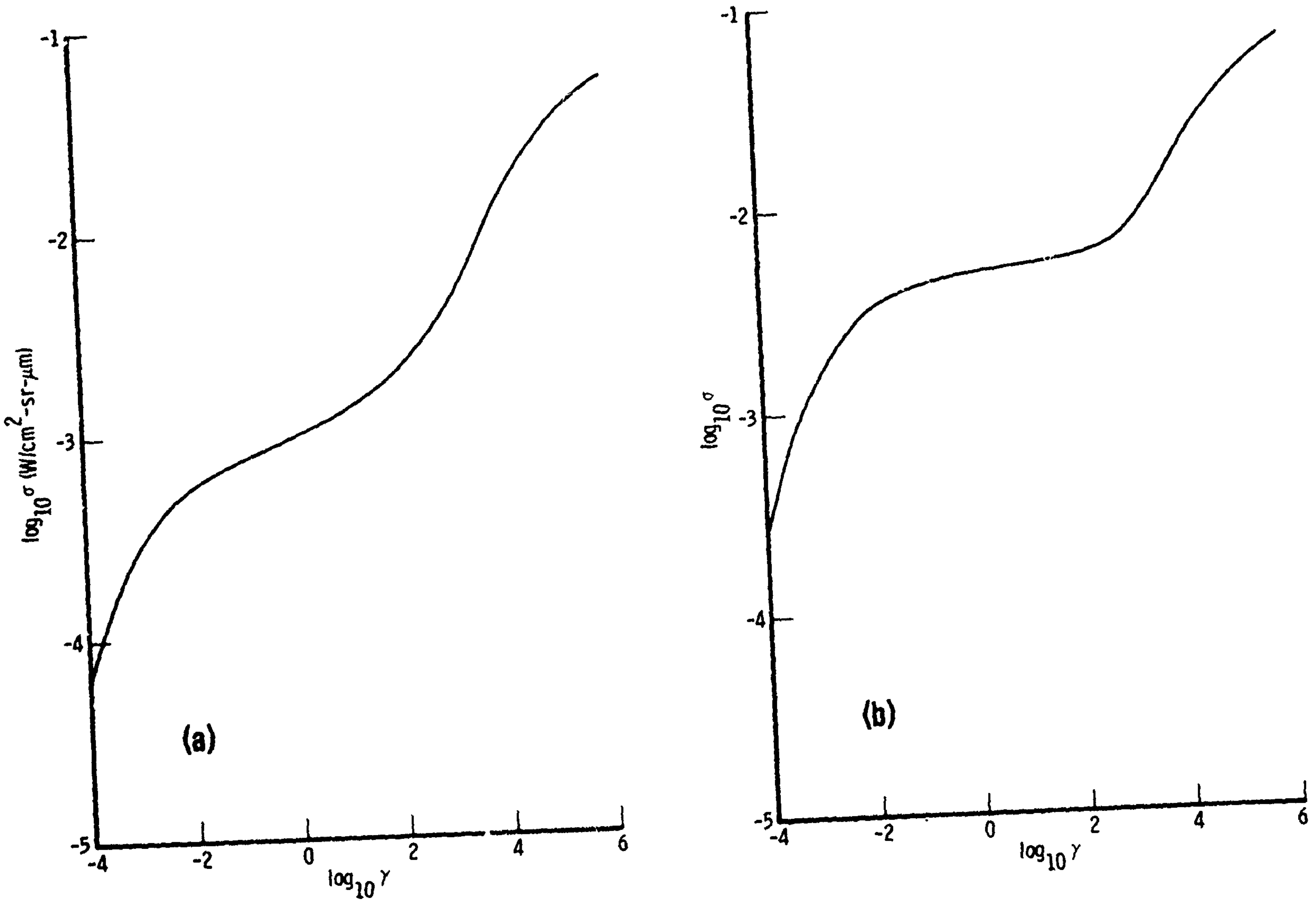

Fig. 92. Smoothing Curves for Transtage Case 2 (Revised). (a) Radiance; (b) Absorptance.

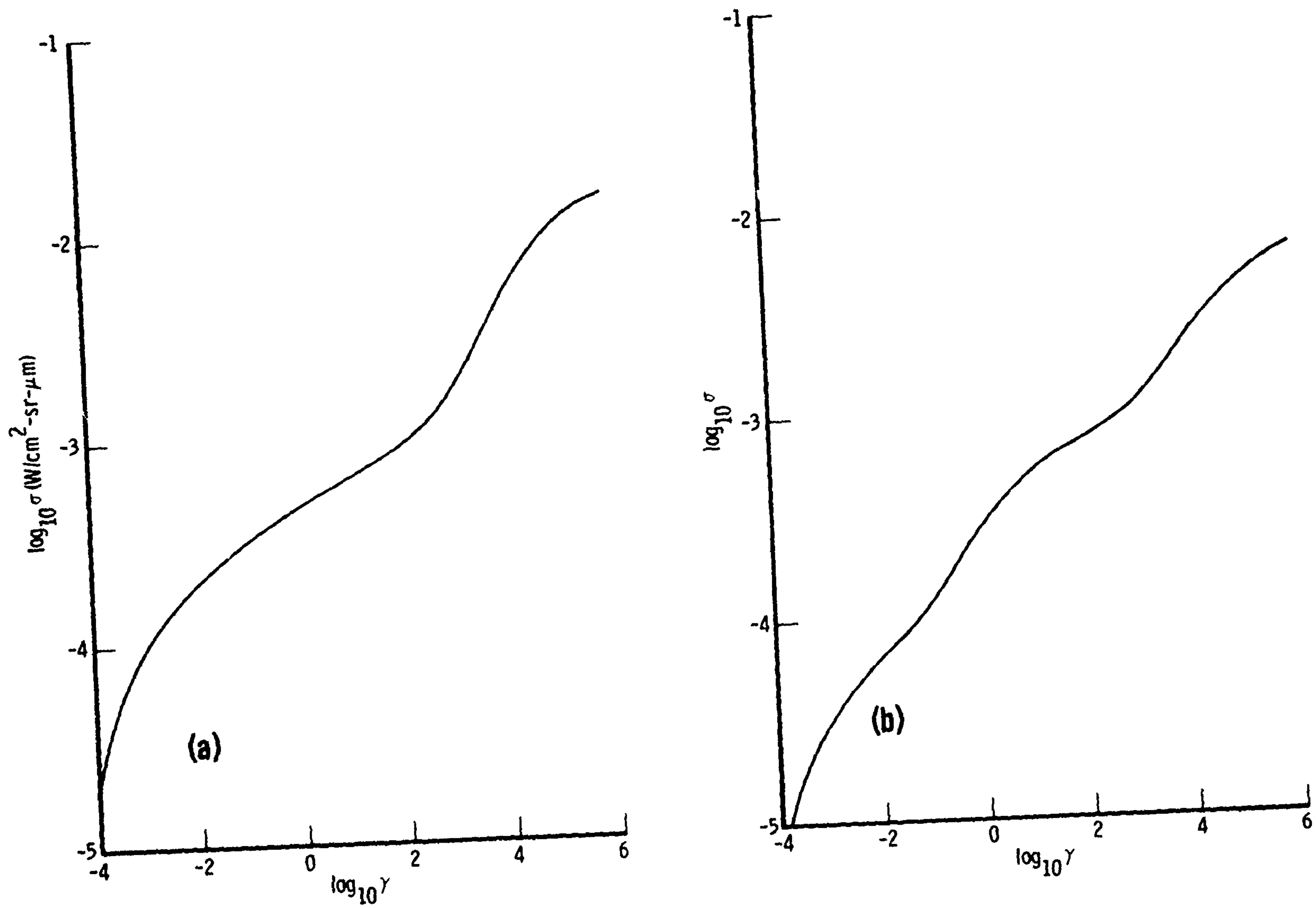

Fig. 93. Smoothing Curves for Transtage Case 8 (Revised). (a) Radiance; (b) Absorptance.

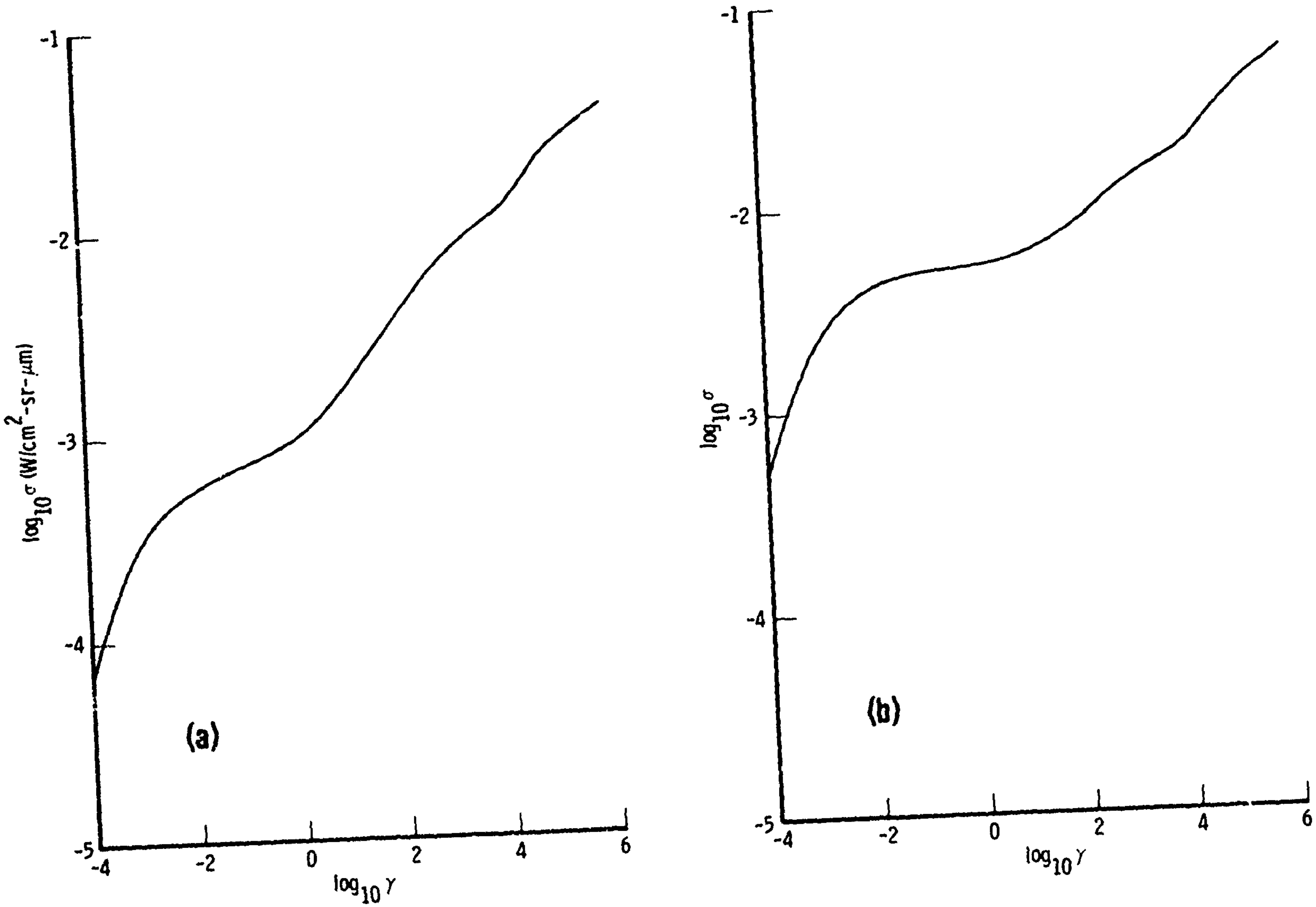

Fig. 94. Smoothing Curves for Transtage Case 13. (a) Radiance; (b) Absorptance.

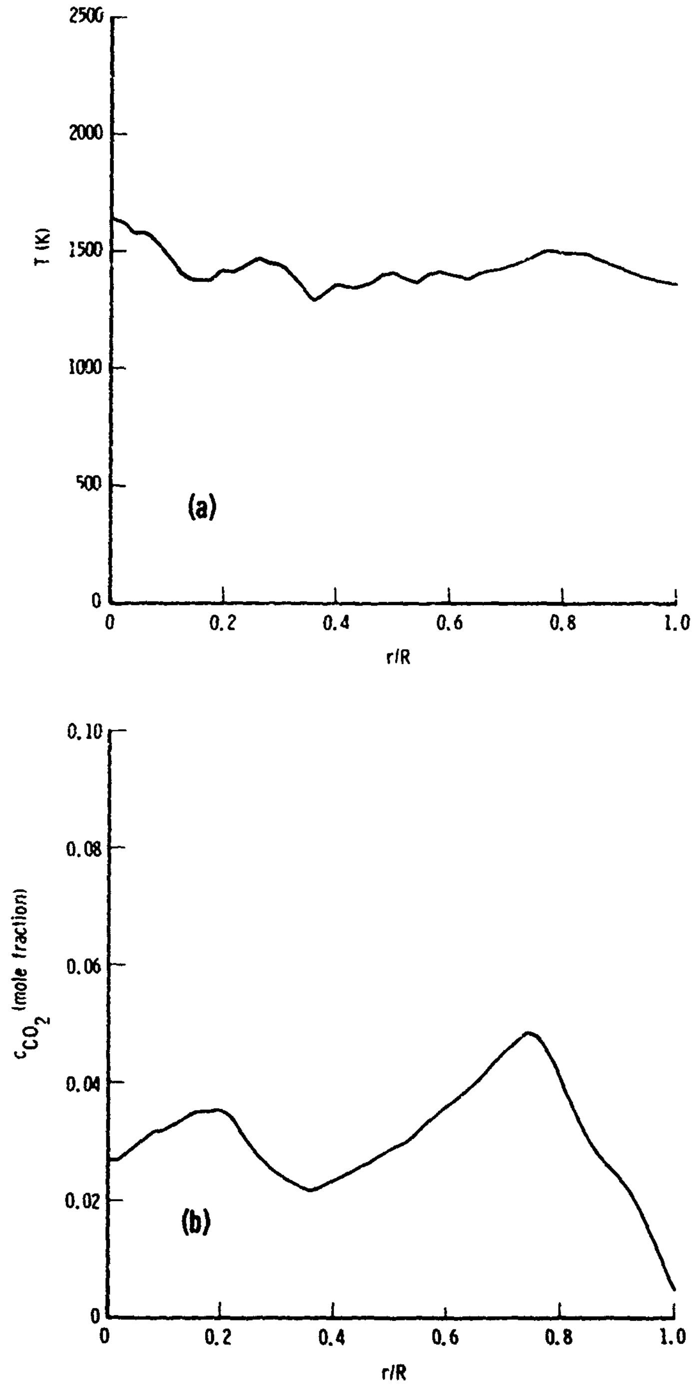

Fig. 95. Inversion Results for Transtage Case 2 (Revised). (a) Temperature; (b) CO_2 concentration.

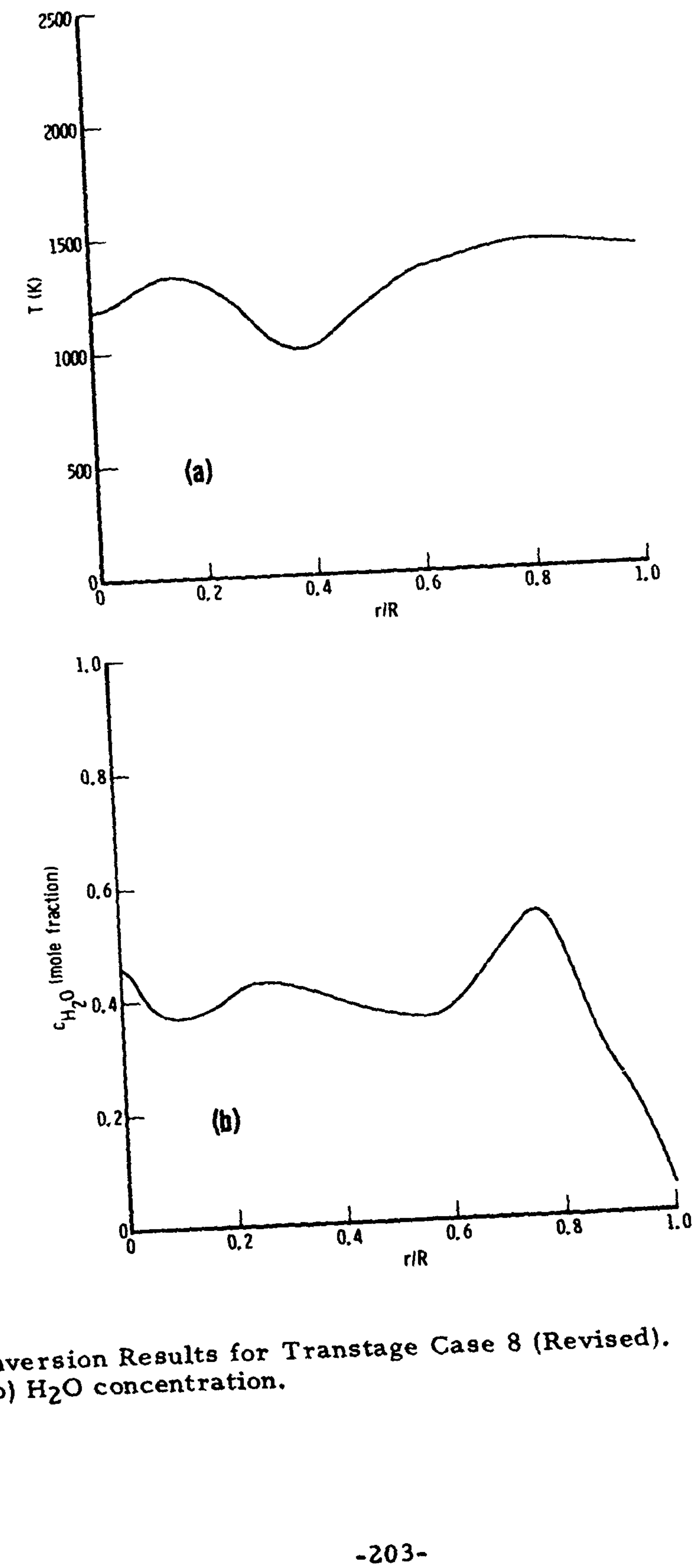

Fig. 96. Inversion Results for Transtage Case 8 (Revised). (a) Temperature; (b) H_2O concentration.

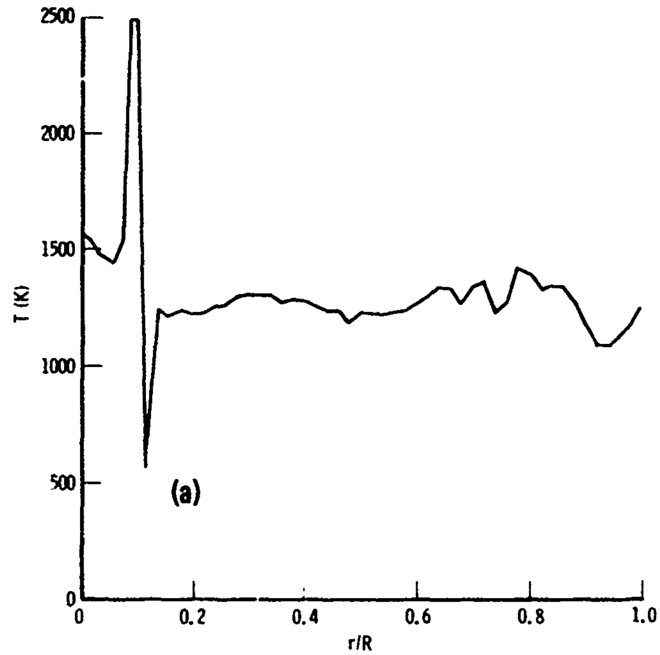

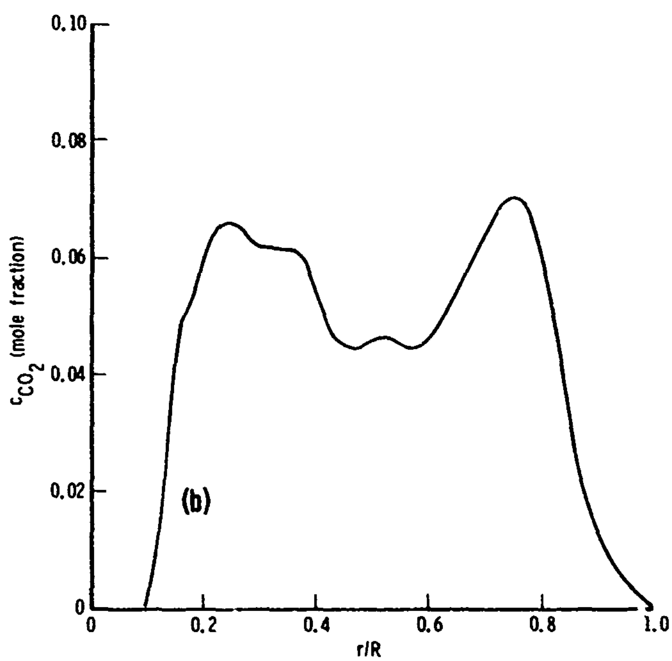

Fig. 97. Inversion Results for Transtage Case 13. (a) Temperature; (b) CO_2 concentration.

XI. SUMMARY AND CONCLUSIONS

The overall objective of this work is to clarify the problem of whether or not multi-position E/A inversion can give pTc profiles with sufficient accuracy for propulsion applications (e.g., evaluation of combustion/nozzle code prediction capabilities and assessment of rocket engine performance). This objective is both general enough and subjective enough that it can only be answered with qualification. The overall impression obtained in this work is that such inversions can <u>at least</u> provide a valuable guide as to the validity of code predictions <u>if</u> sufficient care is taken to obtain good E/A data and <u>if</u> the application is to certain types of test engines. The discussions presented in this section attempt to quantify this conclusion.

The accuracy of E/A inversion depends on: (1) the accuracy of the mathematical and inversion models; and (2) the quality of the input E/A data. The question of data quality is taken up later. Here we consider the validity of the models comprising the overall inversion scheme, these being the band radiation model, the smoothing model and the actual inversion algorithm. The last of these needs little discussion. The results of Section VII clearly display the unique and correct convergence characteristics of the Iterative Abel scheme to arbitrary accuracy.

The accuracy of the band radiation model depends primarily on the accuracy of the fundamental band model parameters, the accuracy with which optical path nonuniformities are handled and the accuracy with which Doppler broadening effects are modeled. The model used in the present work incorporates the most recent developments of band model theory and is capable of predicting E/A profiles for the NERD CO_2 and H_2O bandpasses to an overall accuracy of 15% or better for most all realistic plume conditions. In inversion, errors introduced by the radiation model are of the nature of bias errors and, to a first approximation, can introduce errors in the inverted temperature and concentration profiles of the same order. Specific analyses for variations in bandmodel parameters, line profile and nonuniformity approximation are presented in Sections IXB, IXD, and IXE, respectively.

Any number of procedures can be used for data smoothing. The method employed here is the rational approach of presmoothing the input profiles by fitting the data with the curve having the smallest possible mean square second derivative consistent with the constraint that the rms difference between the smoothed and unsmoothed profiles σ should not be much more than the estimated rms fluctuations of the data ϵ. When applied to synthetic data (that is, data that has been generated artificially by superimposing random fluctuations on smooth profiles), the smoothing procedure is highly objective; optimum smoothing can be effected without recourse to subjective judgment solely by selecting the smoothing parameter γ in the plateau region of the σ versus γ curve. When applied to real experimental data, the procedure is only quasi-objective. Often, the σ versus γ curve fails to display a well-defined plateau, and some subjective judgment is often required in order to effect a good smoothing. The error introduced by smoothing is difficult to judge, and probably not relevant in any event since the principal effect of smoothing is to suppress random errors so that an inversion can be performed. On the other hand, it is evident that some error must be introduced since when the best overall smoothed curve is determined, the fit at local points on the profile is not as good as what one might think it should be by inspection. An example of this phenomenon is given in Fig. 73b where the best overall smoothed curve fails to follow the peak structure at $z \simeq 50$ cm. To the extent that the smoothing of the Transtage data (Figs. 67-75) is typical, the smoothing procedure may introduce local errors of the order of 10%. A plausible solution to this problem is an application of the smoothing procedure used here in a piece-wise manner across the transverse profile.

The most detrimental aspect of E/A inversions is the propagation of random errors. Even the slightest of random fluctuations on the transverse profiles can be amplified in inversion to such an extent that the retrieved radial profiles are meaningless. A smoothing of the input data is almost always required in order to obtain realistic results. Based on the inversions considered in this work, the following crude estimate of final inversion accuracy has been found: Let the percent rms values of fluctuation in the emission and absorption profiles be ϵ_E and ϵ_A, respectively. Then, after an optimum smoothing to damp out these fluctuations, the inversion process will reintroduce errors so that the temperature and concentration profiles will have percent errors of the order of ϵ_E and ϵ_A, respectively.

There are certain qualifications to this rule. Most notably, the error near the center of plumes will be much larger than predicted if there is a pTc valley at r = 0. The result of this valley is relatively flat transverse profiles around z = 0, and, in extreme cases, an actual depression around z = 0. For most of the inversions of this work, this condition obtained.

Aside from this very crude error estimate and the qualification mentioned above, very little can be said about the final error of retrieved radial profiles in general. Specific engine types must be looked at in detail. Some general comments can be made about the conditions that will yield the best inversions. (1) The absorptance must not be so small that the random experimental noise completely hides the signal. (2) At the other extreme, the source cannot be so optically deep that the absorptance is near unity. Then, the percent error of the signal is small, but there is no information in the signal. (3) The transverse E/A profiles should be monitonically decreasing functions with z. This condition ensures that there is not a depression in the pTc profiles at r = 0. In the case of rocket engines employing conical nozzles, this is indeed the case so long as uniform mixture ratio conditions prevail.

For the specific case of the Transtage inversions, more quantitative statements can be made concerning the error of inversion. Consider the revised Case 2 and Case 8 inversions of Section XE. Inspection of the raw data curves of Figs. 89 and 90 (and Fig. 71b for H_2O absorptance) gives the following rough measure of the percent (of maximum profile value) rms fluctuations in the data.

CO_2 radiance	1%
CO_2 absorptance	4%
H_2O radiance	3%
H_2O absorptance	20%

The inversions for these two cases yield the following mean radial values for temperature and concentration (Figs. 95 and 96)

$$T \sim 1300 \text{ K}$$

$$c_{CO_2} \sim 0.03$$

$$c_{H_2O} \sim 0.4$$

while the random error analysis of Section XD yields the following errors due to random fluctuations (Fig. 88) at $r/R \sim 0.4$

$$\Delta T_{CO_2} \sim 20 \text{ K} \sim 1.5\% \text{ of } 1300 \text{ K}$$

$$\Delta T_{H_2O} \sim 40 \text{ K} \sim 3\% \text{ of } 1300 \text{ K}$$

$$\Delta c_{CO_2} \sim .001 \sim 3\% \text{ of } 0.03$$

$$\Delta c_{H_2O} \sim 0.05 \sim 13\% \text{ of } 0.4$$

These results indicate the general usefulness of the rule that percent temperature error is roughly equal to the percent radiance error and that percent concentration error is roughly equal to percent absorptance error (actually, the correspondence is surprisingly good for this case). The percent errors are smaller for $r/R \geqslant 0.4$ and larger for $r/R \leqslant 0.4$. The worst case occurs at $r = 0$ for which the inversion errors are approximately (from Figs. 88, 95 and 96)

$$\Delta T_{CO_2} \sim 12\%$$

$$\Delta T_{H_2O} \sim 60\%$$

$$\Delta c_{CO_2} \sim 40\%$$

$$\Delta c_{H_2O} \sim 90\%$$

However, these errors drop quite sharply for $r > 0$.

In addition to these errors due to random fluctuations, the errors due to radiation modeling and smoothing must be added. The former is approximately 15% at worst, and the latter is estimated from the goodness of fit illustrated in Figs. 89 and 90 to be no worse than $\sim 5\%$.

The inversion results for the revised versions of Cases 2 and 8 are repeated in Fig. 98 with the one standard deviation error bounds suggested by this error analysis.

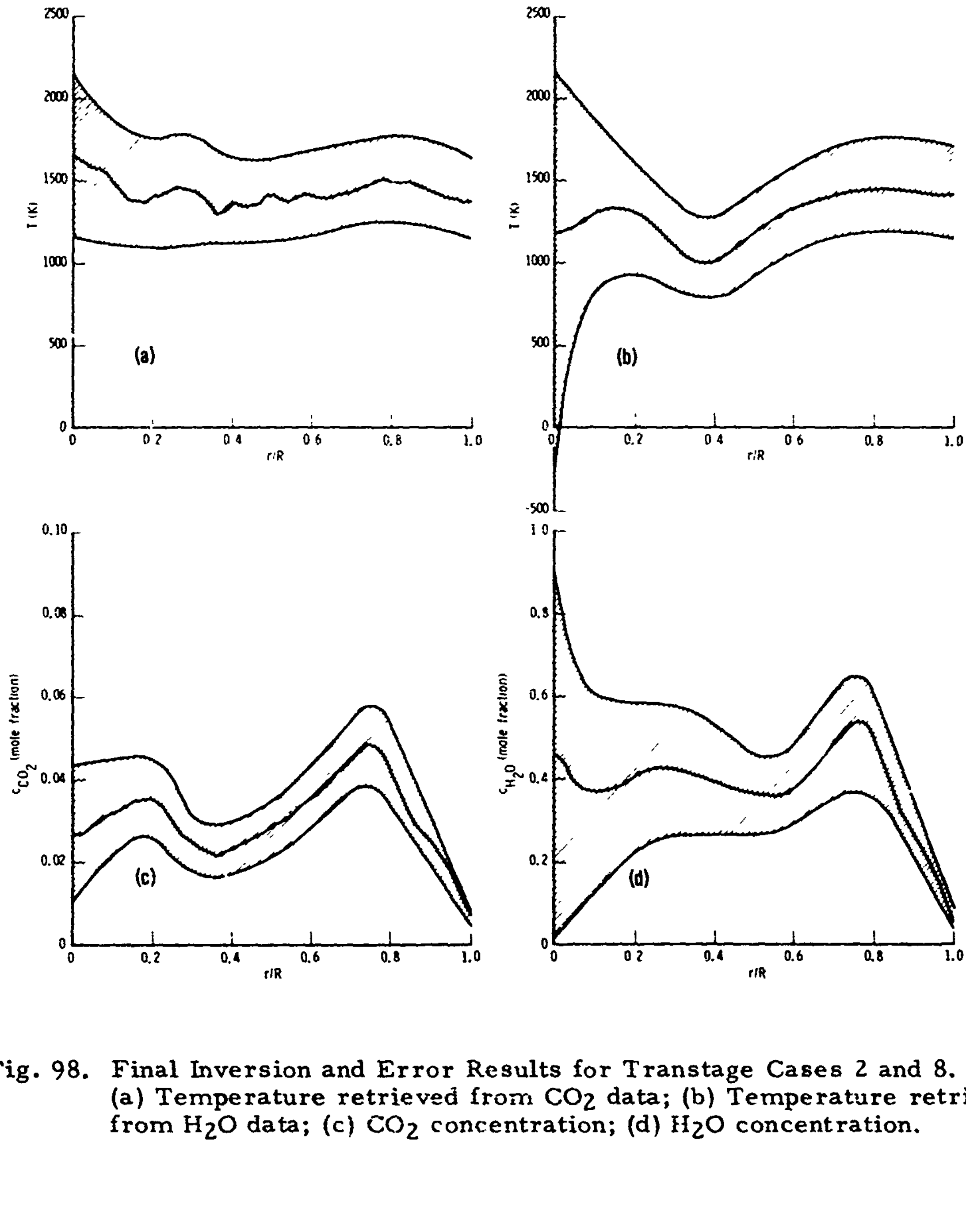

Fig. 98. Final Inversion and Error Results for Transtage Cases 2 and 8. (a) Temperature retrieved from CO_2 data; (b) Temperature retrieved from H_2O data; (c) CO_2 concentration; (d) H_2O concentration.

REFERENCES

1. B. D. Spieth, Computer Models for Predicting Plume Gas Dynamics and Radiation - Background and Overview, AFRPL-TR-76-7, Vol. 1, Air Force Rocket Propulsion Laboratory, Edwards Air Force Base, California, March 1976.

2. B. D. Spieth, Computer Models for Predicting Plume Gas Dynamics and Radiation - Model Descriptions, AFRPL-TR-76-7, Vol. 2, Air Force Rocket Propulsion Laboratory, Edwards Air Force Base, California, March 1976.

3. J. D. Stewart, S. E. Gilles and D. D. Thomas, AFRPL High Altitude Plume Radiation Program Final Report, The Aerospace Corp., El Segundo, California, TOR-0073(3409-01)-1, 31 July 1972 (Secret).

4. L. R. Ring, "Analysis and Correlation of the Gas Dynamic and Radiation Properties Obtained in the Emitted Radiation from Special Engines Test Program," Proc. JANNAF 9th Plume Technology Meeting, CPIA Publication No. 277, February 1976.

5. B. E. Pearce, An Assessment of the "Erase" Fixed-Wavelength Emission/Absorption Measurements and Inversions, The Aerospace Corp., El Segundo, California, TR-0075(5540)-1, 30 September 1975.

6. C. D. Rodgers, "Retrieval of Atmospheric Temperature and Composition from Remote Measurements of Thermal Radiation," Rev. Geophys. Space Phys. 14, 609-624 (1976).

7. B. Krakov, "Spectroscopic Temperature Profile Measurements in Inhomogeneous Hot Gases," Applied Optics 5, 201-210 (1966).

8. F. S. Simmons, H. Y. Yamada and C. B. Blake, Measurement of Temperature Profiles in Hot Gases by Emission-Absorption Spectroscopy, NASA CR-72491, NASA Lewis Research Center, Cleveland, Ohio, April 1969.

9. D. R. Buchele, Computer Program for Calculation of a Gas Temperature Profile by Infrared Emission-Absorption Spectroscopy, NASA TM-73848, NASA Lewis Research Center, Cleveland, Ohio, December 1977.

10. R. D. Cutting and I. McC. Stewart, "Furnace Temperature Profiles: Measurement by Spectroscopic Methods," Applied Optics 14, 2707-2711 (1975).

11. L. E. Brewer and C. C. Limbaugh, "Infrared Band Model Technique for Combustion Diagnostics," Applied Optics 11, 1200-1204 (1972).

12. H. R. Griem, Plasma Spectroscopy, McGraw-Hill Book Company, Inc., New York, 1964.

13. S. J. Young, "Band Model Formulation for Inhomogeneous Optical Paths," J. Quant. Spectrosc. Radiat. Transfer 15, 483-501 (1975).

14. S. J. Young, "Addendum to: Band Model Formulation for Inhomogeneous Optical Paths," J. Quant. Spectrosc. Radiat. Transfer 15, 1137-1140 (1975).

15. S. J. Young, "Nonisothermal Band Model Theory," J. Quant. Spectrosc. Radiat. Transfer 18, 1-28 (1977).

16. S. J. Young, Band Model Calculation of Atmospheric Transmittance for Hot Gas Line Emission Sources. Account of Doppler Broadening, TR-0076(6970)-5, The Aerospace Corp., El Segundo, California (30 July 1975).

17. C. D. Rodgers and A. P. Williams, "Integrated Absorptance of a Spectral Line with the Voigt Profile," J. Quant. Spectrosc. Radiat. Transfer 14, 319-323 (1974).

18. C. B. Ludwig, W. Malkmus, J. E. Reardon, and J. A. L. Thompson, Handbook of Infrared Radiation from Combustion Gases, eds. R. Goulard and J. A. L. Thompson, NASA SP-3080, Marshall Space Flight Center, Huntsville, Ala. (1973).

19. P. Elder, T. Jerrick and J. W. Birkeland, "Determination of the Radial Profile of Absorption and Emission Coefficients and Temperature in Cylindrically Symmetric Sources with Self-Absorption," Applied Optics 4, 589-592 (1965).

20. D. L. Phillips, "A Technique for the Numerical Solution of Certain Integral Equations of the First Kind," J. Assoc. Comp. Mach. 9, 84-97 (1962).

21. S. Twomey, "On the Numerical Solution of Fredholm Integral Equations of the First Kind by the Inversion of the Linear System Produced by Quadrature," J. Assoc. Comp. Mach. 10, 97-101 (1963).

22. System/360 Scientific Subroutine Package (360A-CM-03X) Version III, Programers Manual, H20-0205-3, IBM Technical Publications Department, White Plains, N.Y., 1968.

23. W. L. Barr, "Method for Computing the Radial Distribution of Emitters in a Cylindrical Source," J. Opt. Soc. Amer. 52, 885-888 (1962).

24. S. J. Young, Band Model Parameters for the 2.7-μm Bands of H_2O and CO_2 in the 100-3000°K Temperature Range, TR-0076(6970)-4, The Aerospace Corp., El Segundo, California (31 July 1975).

25. S. J. Young, "Evaluation of Nonisothermal Band Models for H_2O," J. Quant. Spectrosc. Radiat. Transfer 18, 29-45 (1977).

26. S. J. Young, Band Model Parameters for the 4.3-μm Fundamental Band of CO_2 in the 100-3000°K Temperature Range, TR-0076 (6754-03)-1, The Aerospace Corporation, El Segundo, California (19 February 1976).

27. R. A. McClatchey, W. S. Benedict, S. A. Clough, D. E. Burch, R. F. Calfe, K. Fox, L. S. Rothman and J. S. Garing, AFCRL Atmospheric Absorption Line Parameters Compilation, AFCRL-TR-73-006, Air Force Geophysics Laboratory (formerly, Air Force Cambridge Research Laboratories), Hanscomb Air Force Base, Mass. (25 January 1973).

APPENDIX A

OPTIMUM SPECTRAL BANDPASSES

A. Selection of ν and $\Delta\nu$ for H_2O Measurements

Two important criteria on the selection of wavelength and bandpass for multiposition E/A inversion are to make sure that only one active species is being observed and to provide an optimum signal strength. Consider first the 2.7 μm region. The NASA absorption band model parameter $\bar{k}$ for CO_2 and H_2O at T = 1500 K are shown in Fig. A-1. This parameter is a measure of radiance and abosorptance signal strength for thin sources. Also indicated on the figure are the NERD wide- and narrow-bandpasses and the 25 cm^{-1} bandpass used in the 12 engine test case inversions. For H_2O detection, the two criteria of nonoverlap and signal strength leave little option on selection of ν and $\Delta\nu$. Two regions satisfy nonoverlapping: $\nu \gtrsim 3750\ cm^{-1}$ and $\nu \lesssim 3200\ cm^{-1}$. The former is more sure since it lies beyond the CO_2 band head.

Typically, H_2O absorption for plumes of interest is weak. Therefore, we want to choose a region of maximum $\bar{k}$. Thus, in order to ensure non-overlap with CO_2 and to obtain maximum $\bar{k}$, consider only the region above 3750 cm^{-1}. The optimum ν is the peak near 3925 cm^{-1}. The position of this peak changes with temperature as shown in Fig. A-2. Thus, for a general temperature variation within the plume source, an optimum ν cannot be selected a priori. Some estimate of temperature gradiant is required in order to calculate the effective optimum ν, or, more reasonably, this position can be determined experimentally. But even here, the optimum value could change with transverse scan position because the temperature gradient along the line of sight will be different for each transverse position. For the transtage inversions, the plume temperature profile at the nozzle is nearly constant with $T \sim 1400$ K. Thus, from Fig. A-2, an optimum ν of 3925 cm^{-1} is indicated.

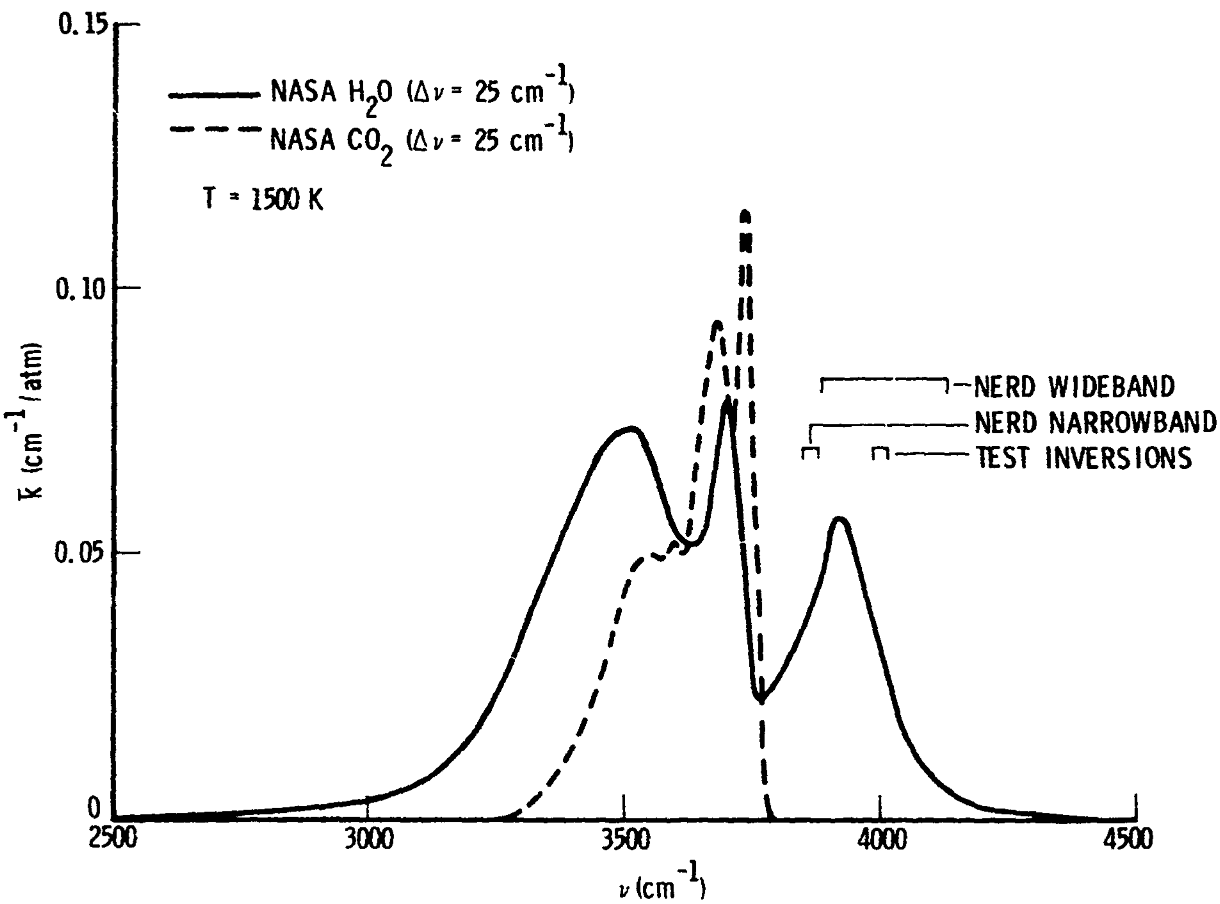

Fig. A-1. Spectral Variation of Absorption Band Model Parameter for H_2O and CO_2 near 2.7 μm

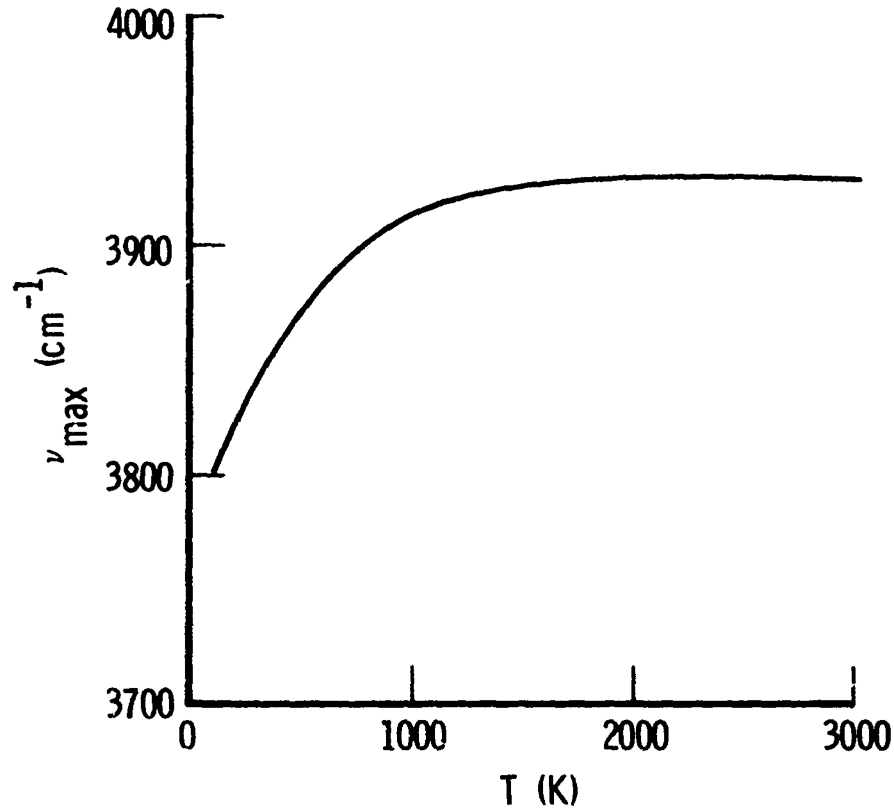

Fig. A-2. Variation of Peak H_2O Absorption Position with Temperature

The selection of an optimum bandpass around ν must involve a trade-off on radiance or absorptance optimization. In order to maximize radiance, a bandpass that covers as much of the peak as possible should be used. That is, the optimum bandpass for radiance is 3800 to ~ 4200 cm^{-1}. In order to maximize absorptance, we want to maximize the mean value of $\bar{k}$ in the bandpass. That is, we should choose a narrow bandpass (~ 20 to 30 cm^{-1}) centered on 3925 cm^{-1}. The overall optimum bandpass must be somewhere between these two extremes. The wide bandpass H_2O filter presently used in the NERD measurements is a very good optimum filter for radiance measurements; it essentially covers the entire H_2O spectral feature around 3925 cm^{-1} and is well isolated from the CO_2 band. The presently used narrow bandpass filter centered at 3866 cm^{-1} would be a better (by about 50%) absorptance measurement filter if moved to 3925 cm^{-1}.

The selection of an optimum filter for simultaneous radiance and absorptance measurements would require a detailed trade-off study of whether noisy absorptance or noisy radiance measurements is more critical in inversion. If absorptance error is the most detrimental, the optimum filter should be weighted toward narrow. If radiance noise is most detrimental, the weighting should be toward wide. Similarly, if more importance is placed on a good inversion for temperature, the band should be wide. If more importance is placed on concentration inversion, the band should be narrow. (This weighting assumes that the system noise is independent of bandpass.)

The evidence obtained so far in the transtage measurements is that absorptance data is more noisy than radiance data, and consequently, that concentration inversions are more uncertain than temperature inversions. These results suggest that future H_2O measurements be made with a narrow band (~ 30 cm^{-1} wide) filter centered on 3825 cm^{-1}.

B. Selection of ν and $\Delta\nu$ for CO_2 Measurements

The complete spectral embedment of the 2.7-μm CO_2 band in the H_2O band precludes CO_2 measurements in this region. The logical region is the 4.3-μm fundamental CO_2 band. Here, however, overlapping with the CO band at 4.7-μm must be considered. The NASA absorption band model parameter $\bar{k}$ for CO_2 and CO at T = 1800 K are shown in Fig. A-3. The NERD and test inversion bandpasses are also indicated. Although both of these bandpasses overlap into the CO band, the effect is probably not important. According to code predictions, the ratio of CO to CO_2 concentration at the nozzle exit plane is not likely to exceed ~ 0.4 for storable missiles (e.g., Titan II). The transtage predictions show ~ 0.4 also. In this case, for the NERD bandpass, the ratio of CO signal to CO_2 signal is only ~ 0.006. Even if the CO/CO_2 ratio were raised to 2.5 (which might obtain for an Atlas), the signal ratio is only 0.04. Nevertheless, since the CO_2 spectrum is reasonably flat, a move to a safer region beyond 2300 cm^{-1} might be prudent.

In complete distinction from the condition for water, the measurements for CO_2 sometimes show too much signal. That is, the source is optically deep, the radiance approaches the blackbody value, and the absorptance is approaches unity. As these limits are approached, the information content of the data is lost. For such cases, a further increase of ν out to the steep slope of the band head may be desirable. However, although $\bar{k}$, and thus radiance and absorptance will be less, an accurate determination of $\bar{k}$ in the bandpass may be difficult because of the steepness of the slope.

Aside from the possibility of trying to reduce the signal strength, the selection of ν and $\Delta\nu$ for CO_2 measurements is straightforward. Assuming a rectangular bandpass for simplicity, it should extend from 2300 to 2375 cm^{-1}.

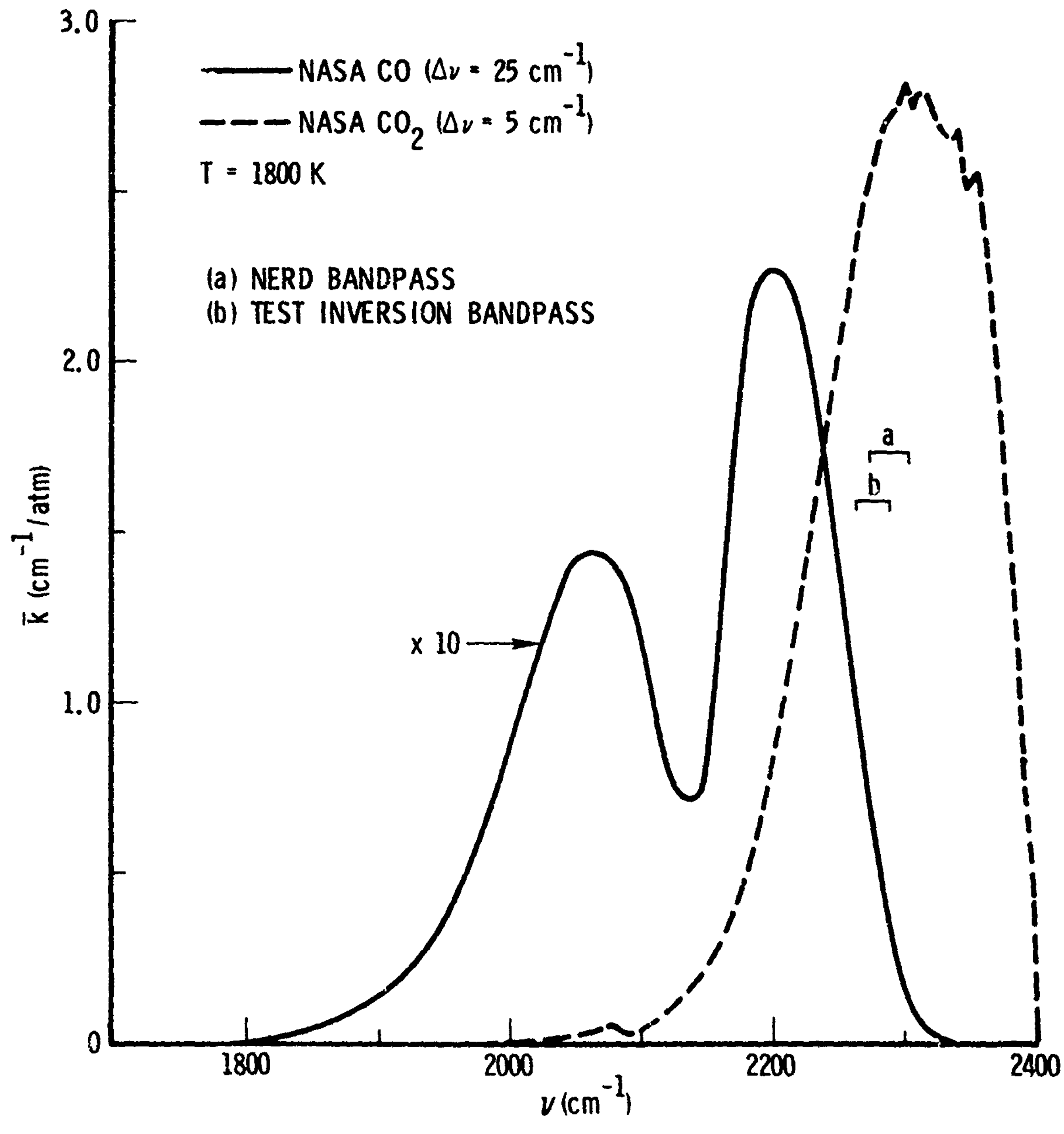

Fig. A-3. Spectral Variation of Absorption Band Model Parameter for CO_2 and CO near 4.3 μm.

APPENDIX B

PHILLIPS-TWOMEY INVERSION METHOD

The method of inversion developed by Phillips (B-1) and Twomey (B-2) has been adapted to the present emission/absorption inversion problem. The method has been used extensively in the inversion of atmospheric sounding data to get atmospheric altitude profiles of temperature and species concentration. A fundamental feature of the method is the explicit account of random errors in the input data. Unlike the iterative Abel inversion method which employs presmoothing of the input data, however, account of random errors is effected by smoothing the output profiles. This smoothing is built into the inversion algorithm and, in effect, smooths the output profiles before they are even generated. In its simplest form, the solution for the function f(r) defined by the integral equation

$$\int_a^b K(z, r)\, f(r)\, dr = g(z) \tag{B-1}$$

or, more accurately, its matrix equivalent

$$\sum_{i=1}^{N+1} w_i\, k_{ji}\, f_i = g_j \tag{B-2}$$

is

$$\overline{f} = (\overline{A^*}\,\overline{A} + \gamma\overline{H})^{-1}(\overline{A^*}\,\overline{g}) \tag{B-3}$$

where $\overline{f}$ and $\overline{g}$ are column matrices with elements f_i ($i = 1, 2, \ldots, N + 1$) and g_j ($j = 1, 2, \ldots, N + 1$), respectively, $\overline{A}$ is a coefficient matrix composed of elements $a_{ji} = w_i k_{ji}$, w_i are the quadrature weights in the summation approximation (B-2) to the integral equation (B-1), (see Section IIIE of main text), $\overline{A^*}$ is the transpose of $\overline{A}$, $\overline{H}$ is a smoothing matrix, and γ is a scalar smoothing parameter. The smoothing matrix $\overline{H}$ is

$$
H = \begin{bmatrix}
5 & -6 & 1 & & & & & & & & & & & \\
-6 & 9 & -4 & 1 & & & & & & & & & & \\
1 & -4 & 6 & -4 & 1 & & & & & & & & & \\
 & 1 & -4 & 6 & -4 & 1 & & & & & & & & \\
 & & 1 & -4 & 6 & -4 & 1 & & & & & & & \\
 & & & & & & & \ddots & & & & & & \\
 & & & & & & & 1 & -4 & 6 & -4 & 1 & & \\
 & & & & & & & & 1 & -4 & 6 & -4 & 1 & \\
 & & & & & & & & & 1 & -4 & 6 & -4 & 1 \\
 & & & & & & & & & & 1 & -4 & 5 & -2 \\
 & & & & & & & & & & & 1 & -2 & 1
\end{bmatrix} \qquad \text{(B-4)}
$$

and is appropriate to the smoothing criterion that the curvature function

$$
C = \sum_{i=1}^{N+1} (f_{i-1} - 2f_i + f_{i+1})^2 \qquad \text{(B-5)}
$$

be a minimum subject to certain restraints. The constraint is that the profiles $g_j^{(C)}$ computed from the solution f_i should deviate from the input data profiles g_j by an amount equal to the estimated rms errors, ϵ, in $g(z)$. That is

$$
N\sigma^2 = \sum_{j=1}^{N+1} [g_j - g_j^{(C)}]^2 = N\epsilon^2 \qquad \text{(B-6)}
$$

The smoothing parameter γ in (B-3) is adjusted until the condition (B-6) is met. The smoothing matrix $\overline{H}$ also incorporates the symmetry and end-point conditions

$$
\begin{aligned}
f_0 &= f_2 \\
f_{N+2} &= 2f_{N+1} - f_N
\end{aligned} \qquad \text{(B-7)}
$$

on the smoothed function.

For the present application, the method must be modified to account for two additional conditions. First, an iterative scheme must be included in order to account for nonthin optical depths, and second, account must be made of the fact that there is not just one integral equation to be inverted, but, in fact, two coupled equations. The two equations are the radiance and absorptance equations [see (81) and (82) of main text)]

$$\overline{N}(z) = 2 \int_z^R J(r)\, w^0(z, r) \frac{r\,dr}{\sqrt{r^2 - z^2}} \tag{B-8}$$

$$\overline{W}(z) = 2 \int_z^R K(r)\, y^0(z, r) \frac{r\,dr}{\sqrt{r^2 - z^2}} \tag{B-9}$$

$\overline{N}(z)$ and $\overline{W}(z)$ are the function $g(z)$ in (B-1) and $J(r)$ and $K(r)$ are the unknown function $f(r)$, $2w^0(z, r)/(r^2 - z^2)^{1/2}$ and $2y^0(z, r)/(r^2 - z^2)^{1/2}$ are the kernel function $K(z, r)$ of (B-1), and $a = z$, $b = R$. In the solution of (B-1), $K(z, r)$ is assumed to be known. The kernels of (B-8) and (B-9), however, are not known because the functions $w^0(z, r)$ and $y^0(z, r)$ are unknown. As for the iterative Abel inversion method, however, we do know that for optically thin sources $w^0 = y^0 = 1$ and we can effect an iteration starting with these values. With the $c(r)$ and $T(r)$ profiles obtained with these initial values for w^0 and y^0, new values for w^0 and y^0 can be computed, and the process continued until convergence is obtained. This iteration scheme is diagramed in Fig. B-1.

The second consideration is that instead of a single constraint of the form (B-6), there are two, and accordingly, there are two smoothing parameters γ that must be varied until the constraints are simultaneously met. This requirement of double variation is a serious defect of the method since a lot of computer time can be spent searching for the proper values of γ.

The Phillips-Twomey method was applied to the moderately-deep inversion example considered in Section VIIB and VIIIB of the main text.

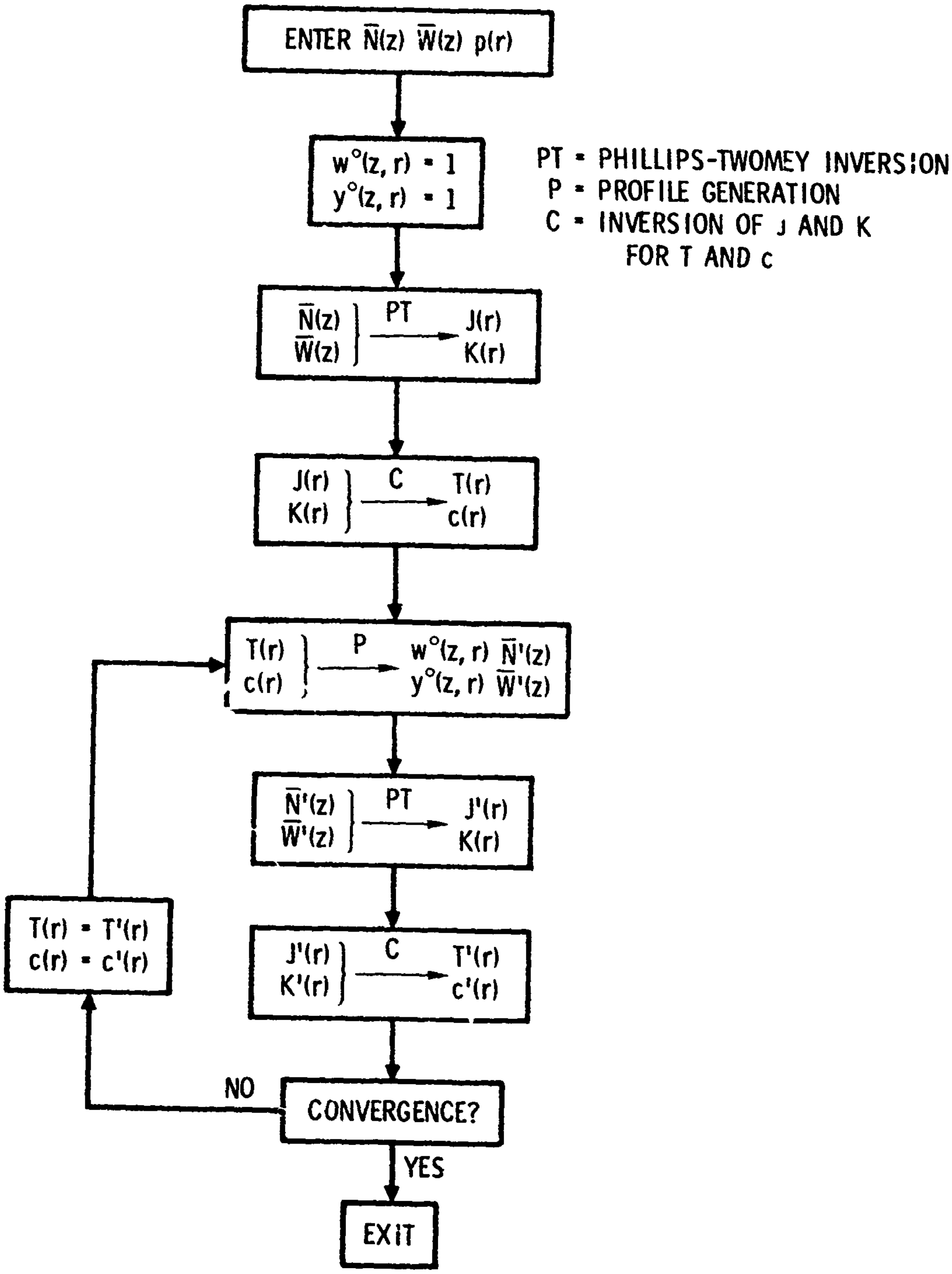

Fig. B-1. Phillips-Twomey Inversion Flow Diagram

When applied to computed transverse E/A profiles with no superimposed random errors, the convergence characteristics are very similar to those of the iterative Abel inversion method. Comparisons between the results of the iterative Abel and Phillips-Twomey inversion methods for the case of five percent superimposed random errors are shown in Fig. B-2. The Phillips-Twomey smoothing parameters were taken as $\gamma_E = \gamma_A = 2000$ in order to achieve σ values near five percent. Except for values near $r/R = 1$, the Phillips-Twomey method is in essential agreement with the iterative Abel method. The Phillips-Twomey results appear, in fact, to be a somewhat smoothed version of the iterative Abel results.

References

B-1. D. L. Phillips, "A Technique for the Numerical Solution of Certain Integral Equations of the First Kind," J. Assoc. Comp. Mach. 9, 84-97 (1962).

B-2 S. Twomey, "On the Numerical Solution of Freedholm Integral Equations of the First Kind by the Inversion of the Linear System Produced by Quadrature," J. Assoc. Comp. Mach. 10, 97-101 (1963).

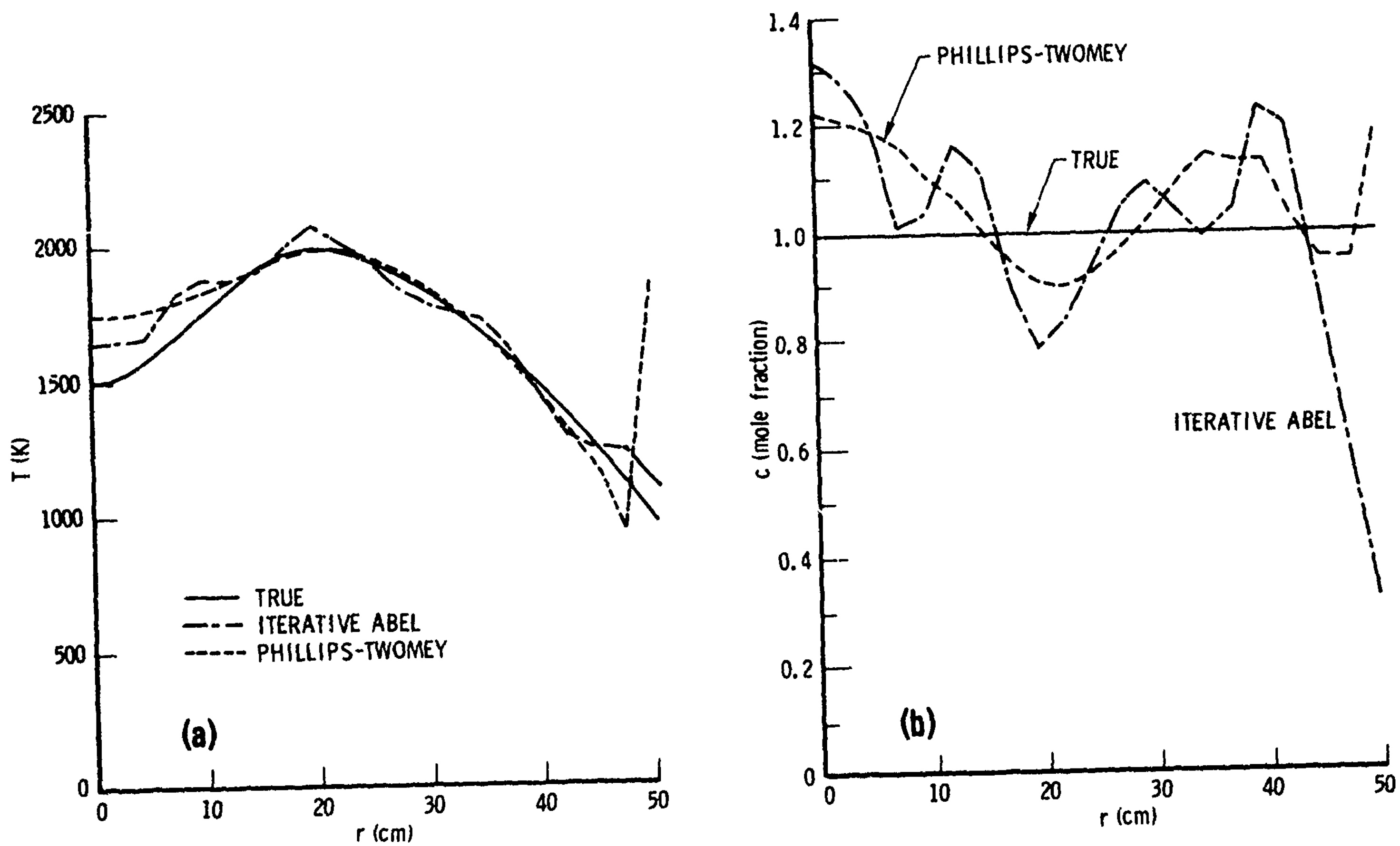

Fig. B-2. Comparison between Phillips-Twomey and Iterative Abel Inversion Results. (a) Temperature; (b) H_2O Concentration.

APPENDIX C
WIDE BAND MODEL PARAMETERS

Within the random band model formulation for an array of Lorentz lines in a spectral interval $\Delta\nu$ centered on ν, the mean transmittance in $\Delta\nu$ for a uniform optical path is

$$\bar{\tau}(\nu) = e^{-\beta(\nu) F[x(\nu)]} \qquad \text{(C-1)}$$

$$x(\nu) = \frac{\bar{k}(\nu) u}{\beta(\nu)}$$

$\left.\begin{matrix}\bar{k}(\nu) \\ \beta(\nu)\end{matrix}\right\}$ = fundamental band model parameters (known for each $\Delta\nu$ over a whole vibration rotation band)

u = optical depth

$$F(x) = \text{curve-of-growth function} \longrightarrow \begin{cases} x & x \longrightarrow 0 \\ \sqrt{2x/\pi} & x \longrightarrow \infty \end{cases}$$

Direct use of this expression for $\bar{\tau}(\nu)$ in an experimental application presupposes detection with a rectangular instrument function of width $\Delta\nu$.

Consider detection over a band pass $\nu_1 \longrightarrow \nu_2$. Let the external radiation source (with which the absorption measurements are made) have a spectral output $S(\nu)$; the detector (less any filter) response be $R(\nu)$; and the filter transmission be $T(\nu)$. The total intensity detected is

$$I = \int_{\nu_1}^{\nu_2} S(\nu) T(\nu) R(\nu) \bar{\tau}(\nu) d\nu$$

Without the intervening gas, the intensity detected would be

$$I_0 = \int_{\nu_1}^{\nu_2} S(\nu)T(\nu)R(\nu)d\nu$$

The apparent wide band transmittance of the gas is then

$$\bar{\tau} = \int_{\nu_1}^{\nu_2} \alpha(\nu)\bar{\tau}(\nu)d\nu \qquad \text{(C-2)}$$

where

$$\alpha(\nu) = \frac{S(\nu)T(\nu)R(\nu)}{\int_{\nu_1}^{\nu_2} S(\nu)T(\nu)R(\nu)d\nu}$$

Substitution of (C-1) into (C-2) gives the exact wideband transmittance function

$$\bar{\tau} = \int_{\nu_1}^{\nu_2} \alpha(\nu)e^{-\beta(\nu)F[x(\nu)]}d\nu \qquad \text{(C-3)}$$

Use of this transmission function in practical applications is quite inconvenient. As an approximation to (C-3), assume that $\bar{\tau}$ can be expressed in the same form as (C-1) but in terms of effective parameters $\bar{K}_e$ and β_e. That is, assume

$$\bar{\tau} = e^{-\beta_e F(x_e)}$$

$$x_e = \frac{\bar{k}_e u}{\beta_e} \tag{C-4}$$

The $\bar{k}_e$ and β_e are to be determined by forcing (C-3) and (C-4) be equal in some limits of absorption. Between these limits, (C-4) is assumed to be a good approximation to (C-3). Setting (C-3) equal to (C-4) gives

$$e^{-\beta_e F(x_e)} = \int_{\nu_1}^{\nu_2} \alpha(\nu) e^{-\beta(\nu) F[x(\nu)]} d\nu \tag{C-5}$$

First consider the so-called weak- and strong-line absorption limits.* These obtain, respectively, as $x \rightarrow 0$ and $x \rightarrow \infty$. For $x \rightarrow 0$, (C-5) reduces to

$$1 - \beta_e x_e = \int_{\nu_1}^{\nu_2} \alpha(\nu)[1 - \beta(\nu)x(\nu)] d\nu$$

$$\bar{k}_e u = \int_{\nu_1}^{\nu_2} \alpha(\nu)\bar{k}(\nu) u d\nu$$

and thus provides the definition for $\bar{k}_e$

---

*An important point must be made clear here. These limits refer to how each line in the array absorb. Even though each line is absorbing strongly, the absorptance effected by the array may still be very small if the lines are well isolated from each other (compared to their width). Thus, the strong line absorption limit does not necessarily correspond to a strong band absorption limit.

$$\bar{k}_e = \int_{\nu_1}^{\nu_2} \alpha(\nu)\bar{k}(\nu)d\nu \tag{C-6}$$

As $x \longrightarrow \infty$, (C-5) reduces to

$$e^{-\beta_e\sqrt{2x_e/\pi}} = \int_{\nu_1}^{\nu_2} \alpha(\nu)e^{-\beta(\nu)\sqrt{2x(\nu)/\pi}}\,d\nu$$

which, when solved for β_e, yields

$$\beta_e = \frac{\pi}{2u\bar{k}_e}\left[-\ell n\left\{\int_{\nu_1}^{\nu_2} \alpha(\nu)e^{-\sqrt{\frac{2}{\pi}\beta(\nu)\bar{k}(\nu)u}}\,d\nu\right\}\right]^2 \tag{C-7}$$

Equations (C-6) and (C-7) provide definitions for the effective band model parameters to be used in (C-4) when the criterion for matching (C-4) to (C-3) is correspondence in the limits of weak- and strong-line absorption.

Two other traditional absorption limits are for overlapping and non-overlapping lines. These limits are obtained, respectively, for $\beta \longrightarrow \infty$, and $\beta \longrightarrow 0$. For $\beta \longrightarrow \infty$, $x \longrightarrow 0$ and (C-5) reduces to

$$e^{-\bar{k}_e u} = \int_{\nu_1}^{\nu_2} \alpha(\nu)e^{-\bar{k}(\nu)u}\,d\nu$$

and yields the definition for $\bar{k}_e$

$$\bar{k}_e = -\frac{1}{u} \ln \left[\int_{\nu_1}^{\nu_2} \alpha(\nu) e^{-\bar{k}(\nu)u} \, d\nu \right] \tag{C-8}$$

For $\beta \longrightarrow 0$, on the other hand, (C-5) reduces to

$$1 - \sqrt{\frac{2}{\pi} \bar{k}_e \beta_e u} = \int_{\nu_1}^{\nu_2} \alpha(\nu) \left[1 - \sqrt{\frac{2}{\pi} \bar{k}(\nu) \beta(\nu) u} \right] d\nu$$

and yields the definition for β_e

$$\beta_e = \frac{1}{\bar{k}_e} \left[\int_{\nu_1}^{\nu_2} \alpha(\nu) \sqrt{\bar{k}(\nu) \beta(\nu)} \, d\nu \right]^2 \tag{C-9}$$

Which two of the four absorption limits are chosen to define $\bar{k}_e$ and β_e should be dictated by the experimental conditions of the application of the model. Consider the Transtage conditions. For a line-of-sight through a full plume diameter, the approximate conditions of Table C-1 obtain for the NERD CO_2 and H_2O (narrow) bandpasses.

The first observation from this table is that the condition of nonoverlapping lines prevails. For H_2O, $\gamma/\bar{\delta} \simeq 0.0013$ and for CO_2, $\gamma/\bar{\delta} \simeq 0.043$. This result strongly suggests the use of (C-9) for the definition of β_e. The second observation is that x never obtains a value so large that the strong line absorption limit can be said to have been achieved. The table entries are for the full line of sight through the plume. In order to perform radiance calculations, $\bar{\tau}$ must be known for all distances into the plume. Although the strong line absorption limit does not obtain for the

Table C-1. Approximate Transtage Conditions

$L \simeq 120$ cm

$T \simeq 1400$ K

$p \simeq 0.013$ atm

Variable	H_2O	CO_2
c	0.4	0.04
u = cpL (atm cm)	0.62	0.062
$\bar{k}$ (cm^{-1}/atm)	0.06	3
$1/\bar{\delta}$ ($1/cm^{-1}$)	2	100
γ/p (cm^{-1}/atm)	0.05	0.033
$\beta = \frac{2\pi\gamma}{\bar{\delta}}$	0.008	0.27
x	4.7	0.69
$F(x) = \frac{1}{\pi}\left[\sqrt{1 + 2\pi x} - 1\right]$	1.4	0.42
$\beta F(x)$	0.012	0.11
$\bar{\tau} = e^{-\beta F(x)}$	0.99	0.89

full distance through the plume, the weak line absorption limit must obtain for small distances into the plume. Therefore, (C-6) is an appropriate definition for $\bar{k}_e$.

For the Transtage conditions, comparisons between (C-7) and (C-9) for β_e gave nearly identical results. [Note, (C-7) was applied with an arbitrarily large u and found to give β_e nearly independent of u.] This result is easily explained by noting that the exponential argument of (C-7) is only ~0.014 for H_2O and ~0.18 for CO_2. Then, first order expansions of the exponential and logarithm are justified, and the resulting expression is (C-9).

ACRONYMS

Facilities

AFRPL	-	Air Force Rocket Propulsion Laboratory
AEDC	-	Arnold Engineering and Development Center
NASA	-	National Aeronautics and Space Administration
AFGL	-	Air Force Geophysics Laboratory

Test Programs

HAPRAP	-	High Altitude Plume Radiation Program
ERASE	-	Emitted Radiation from Special Engines
NERD	-	Nozzle Exit Radiation Determination

Technical

E/A	-	emission and absorption
pTc	-	pressure, temperature and species concentration
EMABIC	-	Emission/Absorption Inversion Code
CG	-	Curtis-Godson nonuniformity approximation
DR	-	derivative nonuniformity approximation
LS	-	Lindquist-Simmons nonuniformity approximation
ML	-	mean line nonuniformity approximation
RW	-	Rodgers and Williams Voigt model
FOV	-	field of view
O/F	-	oxidizer-to-fuel ratio

LABORATORY OPERATIONS

The Laboratory Operations of The Aerospace Corporation is conducting experimental and theoretical investigations necessary for the evaluation and application of scientific advances to new military concepts and systems. Versatility and flexibility have been developed to a high degree by the laboratory personnel in dealing with the many problems encountered in the nation's rapidly developing space and missile systems. Expertise in the latest scientific developments is vital to the accomplishment of tasks related to these problems. The laboratories that contribute to this research are:

Aerophysics Laboratory: Launch and reentry aerodynamics, heat transfer, reentry physics, chemical kinetics, structural mechanics, flight dynamics, atmospheric pollution, and high-power gas lasers.

Chemistry and Physics Laboratory: Atmospheric reactions and atmospheric optics, chemical reactions in polluted atmospheres, chemical reactions of excited species in rocket plumes, chemical thermodynamics, plasma and laser-induced reactions, laser chemistry, propulsion chemistry, space vacuum and radiation effects on materials, lubrication and surface phenomena, photosensitive materials and sensors, high precision laser ranging, and the application of physics and chemistry to problems of law enforcement and biomedicine.

Electronics Research Laboratory: Electromagnetic theory, devices, and propagation phenomena, including plasma electromagnetics; quantum electronics, lasers, and electro-optics; communication sciences, applied electronics, semiconducting, superconducting, and crystal device physics, optical and acoustical imaging; atmospheric pollution; millimeter wave and far-infrared technology.

Materials Sciences Laboratory: Development of new materials; metal matrix composites and new forms of carbon; test and evaluation of graphite and ceramics in reentry; spacecraft materials and electronic components in nuclear weapons environment; application of fracture mechanics to stress corrosion and fatigue-induced fractures in structural metals.

Space Sciences Laboratory: Atmospheric and ionospheric physics, radiation from the atmosphere, density and composition of the atmosphere, aurorae and airglow; magnetospheric physics, cosmic rays, generation and propagation of plasma waves in the magnetosphere; solar physics, studies of solar magnetic fields; space astronomy, x-ray astronomy; the effects of nuclear explosions, magnetic storms, and solar activity on the earth's atmosphere, ionosphere, and magnetosphere; the effects of optical, electromagnetic, and particulate radiations in space on space systems.

THE AEROSPACE CORPORATION
El Segundo, California

• • •